*Final Report*

# Development of P-Y Curves for Large Diameter Piles/Drilled Shafts in Limestone for FBPIER

UF Project No.: 4910450487812

Contract No.: BC 354 RPWO-59

*By*:
M. C. McVay, Professor, and Lila Niraula, Graduate Student
University of Florida
Civil and Coastal Engineering Dept.

*Submitted to*:

Richard Long
Research Center
Florida Department of Transportation
605 Suwannee Street, MS 30
Tallahassee, FL 32399-0450
(850) 414-4614
and
Peter Lai
Florida Department of Transportation
605 Suwannee Street, MS 33
Tallahassee, FL 32399
(850) 414-4306

UNIVERSITY OF FLORIDA

Department of Civil and Coastal Engineering, College of Engineering
365 Weil Hall, P.O. Box 116580, Gainesville, FL 32611-6580
Tel: (352) 392-8697 SunCom: 622-8697 Fax: (352) 392-3394

**September 2004**

**Technical Report Documentation Page**

| 1. Report No. | 2. Government Accession No. | 3. Recipient's Catalog No. |
|---|---|---|
| Final Report | | |

| 4. Title and Subtitle | 5. Report Date |
|---|---|
| Development of P-Y Curves for Large Diameter Piles/ Drilled Shafts in Limestone for FBPIER | September 2004 |
| | 6. Performing Organization Code |
| 7. Author(s) | 8. Performing Organization Report No. |
| M. C. McVay and Lila Niraula | 4910-4504-878-12 |
| 9. Performing Organization Name and Address | 10. Work Unit No. (TRAIS) |
| University of Florida,<br>Dept. of Civil and Coastal Engineering<br>365 Weil Hall/ P.O. Box 116580<br>Gainesville, FL 32611-6580 | 11. Contract or Grant No.<br>BC 354, RPWO #59 |
| 12. Sponsoring Agency Name and Address | 13. Type of Report and Period Covered |
| Florida Department of Transportation<br>Research Management Center<br>605 Suwannee Street, MS 30<br>Tallahassee, Florida 32301-8064 | **Final Report**<br>Nov. 1,2001 - Sept. 2004 |
| | 14. Sponsoring Agency Code |

15. Supplementary Notes

Prepared in cooperation with the Federal Highway Administration

16. Abstract

Currently, drilled shafts embedded in Florida Limestone are modeled with P-Y curves when subject to lateral loading. Users currently use either the soft or stiff clay models in FB-Pier, or the Reese and Nyman curve in Lpile to characterize Florida Limestone. Little if any, data exists for lateral load tests carried to failure for typical rock strengths in Florida. Moreover, most current software models lump the axial skin friction developed on the side of a shaft into lateral resistance, (P-Y) when the shaft is subject to lateral loading.

This study conducted 19 instrumented centrifuge tests: 12 lateral, and 7 axial on drilled shafts embedded in Florida Limestone. Strengths varied from 10 tsf, 20 tsf, & 40 tsf, shaft diameters varied from 6' to 9', and shaft embedment, L/D, ranged from 2 to 4. The axial centrifuge tests, i.e. axial T-Z curves, which compared favorably with earlier field results, were used to separate the moment from shear on opposite faces of the shaft from lateral resistance of the rock. Back computed P-Y curves, which disallowed side shear on shafts, were found to be 30% lower than curves that included shaft side shear. Normalized P-Y curves were developed for Florida Limestone for a range of shaft diameters, and rock strengths. None of the curves were found to be a function of the shaft's embedment depth. Prior employed P-Y curve's, i.e., Reese & Nyman, as well as the stiff and soft clay models were found to be very conservative. The report recommends that further field-testing of drilled shafts be undertaken to validate the proposed P-Y curves.

| 17. Key Word | 18. Distribution Statement |
|---|---|
| Drilled shafts, limestone, lateral resistance: P-Y curves, Axial skin friction: T-Z, centrifuge testing | No restrictions. This document is available to the public through the National Technical Information Service, Springfield, VA, 22161 |

| 19. Security Classif. (of this report) | 20. Security Classif. (of this page) | 21. No. of Pages | 22. Price |
|---|---|---|---|
| Unclassified | Unclassified | 158 | |

## TABLE OF CONTENTS

## LIST OF FIGURES

Page

FIGURES

## LIST OF TABLES

Page

TABLES

# CHAPTER 1

# INTRODUCTION

## 1.1 BACKGROUND

Prior to 1980, most Florida Department of Transportation (FDOT) bridges were founded on small diameter pre-stressed concrete piles. However, in the past 20 years, the use of drilled shaft foundations as an alternative to driven piles for supporting bridges and buildings has become increasingly popular. The main reasons for their use are fivefold: 1) presence of shallow limestone, 2) the need to resist large lateral loads such as wind loads (hurricanes tornados etc.) and ship impacts, 3) right of way constraints which require minimal foundation footprints, 4) need to minimize construction noise and vibrations in urban areas and 5) the economy of replacing large number of piles with a single or few drilled shafts with out pile caps. With the introduction of larger and more autonomous equipment, the shaft diameters have been getting larger and larger. Shaft diameters in excess of 8 ft are now common in Florida.

## 1.2 CURRENT DRILLED SHAFT DESIGN IN FLORIDA LIMESTONE

Currently, the FDOT design of bridge pier foundations for extreme events from lateral loading (e.g., ship impact) is done with the finite element code FB-Pier. In FB-Pier, pile or drilled shaft's soil-structure interaction is characterized with non-linear T-Z and P-Y springs. The vertical non-linear springs (T-Z) transfer the axial pile/shaft loads to the soil/rock while the horizontal non-linear springs (P-Y) transfer the pile/shaft shear loads. In addition, the P-Y and T-Z springs are attached to the pile/shafts' beam element at the element's centerline, as shown in Figure 1.1.

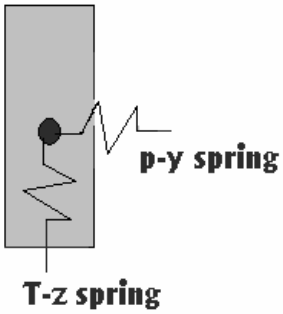


Figure 1.1 Current FB-Pier load transfer model in soil/rock.

However, in the field, the actual transfer of axial load from the pile/shaft occurs at the soil/rock interface and not at the centerline of the pile/shaft, as shown in Figure 1.2. Because the side shear transfer occurs with opposite signs (shaft rotation), and at a distance, a moment or couple (τ-D, Fig. 1.2) develops. This moment may be significant, especially for strong material or in the case of large diameter pile/shafts.

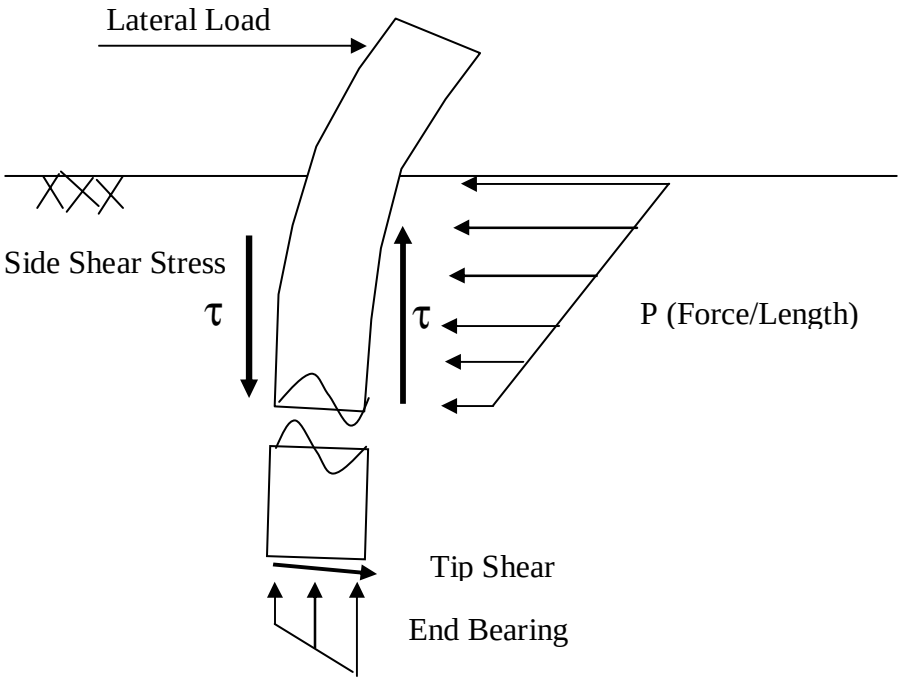


Figure 1.2 Field load transfer in soil/rock.

In the case of short shafts, the tip of the shaft will undergo lateral translation and rotations. The latter results in variable unit end bearing and tip shear, Fig. 1.2, along with moments within the shafts. However, for long shafts, little if any lateral translation occurs at the shaft tip, resulting in uniform end bearing, and no tip shear. This research focuses on the latter case, i.e., effects of side shear, $\tau$, Fig. 1.2 and associated couple ($\tau$ D) in long shafts, as well as the rock's P-Y resistance as a function of rock strength, qu.

## 1.3 MODIFIED FB-PIER MODEL

In order to represent the moment contribution due to the axial shear (Fig 1.2), it is proposed that in an additional rotational spring be attached at the pile/shaft centerline as shown in Figure 1.3. The moment resistance due to the shear transferred at the walls (M), Figure 1.2, is a function of shaft diameter, rock/soil strength (secant stiffness of the T-Z curve), and the angle of rotation ($\theta$) of the pile/shaft. The rotational secant stiffness, $K_{\theta\theta,}$ of the spring (Figure 1.3) is $M/\theta$. Note that the new rotational stiffness for the shaft/pile nodes below the ground surface requires no new material characterization (or parameters).

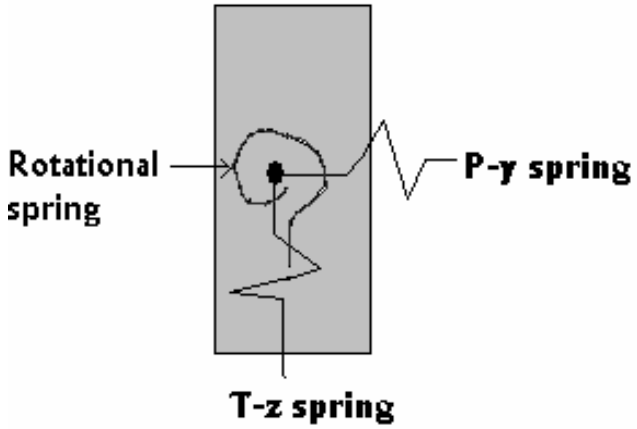


Figure 1.3 Proposed FB-Pier model.

## 1.4 VALIDATION OF PROPOSED FB-PIER MODEL

In order to validate the new model, both axial and lateral load test data is required. Due to limited availability of this data from the field, it was decided that both lateral and axial tests should be carried out in the centrifuge. Specifically, the axial tests will study side shear not end bearing. In the centrifuge, the field loading and stress conditions can easily be reproduced and the soil/rock parameters can easily be controlled. It was also proposed that the tests be carried out on rock since the axial moments will be larger due to the strength of rock vs. soil. In addition, little if any P-Y information is available for Florida Limestone. Consequently, in addition to developing rotational springs (M-θ), testing Florida Limestone will allow development of representative P-Y curves for rock.

Florida limestone is highly variable in both the horizontal and vertical directions. Moreover, there are over ten specific formations in Florida (Tampa, Ocala, etc.). In addition, since the experiments will have both lateral and axial loading carried out on the same rock (i.e., strength, density etc.), as well as repeated several times (i.e., verification), it was believed that field samples could not be employed. Consequently, it was decided to use synthetic rock to perform the centrifuge tests. The latter has been shown to be homogeneous, isotropic, with properties of similar to those of the natural Florida limestone. Synthetic rock with the required strength was made by mixing ground up limestone, cement and water in various proportions.

## 1.5 SCOPE OF WORK

In order to develop both the P-Y curves, as well as validate the Rotational Spring Model (Fig. 1.3), three different strengths of rock were tested: weak, medium, and strong to cover the range of Florida Limestone. Based on the previous research (Kim, 2001) as well as FB-Pier modeling, it was decided to vary the unconfined strengths from 10 tsf to 40 tsf. For lateral

loading, two rock strengths, qu, were considered, 10 tsf and 20 tsf, whereas for axial, three were tested: 10 tsf, 20 tsf, and 40 tsf. The highest strength was not tested for lateral because of the small expected lateral movements in the rock, and the large variation over small vertical distance (top one diameter of shafts). The lateral results were later extrapolated for strengths both below 10 tsf and above 20 tsf.

For each rock strength, the following were varied:

1. Loading (Axial and Lateral)

Axial tests were needed to validate the existing T-Z curves as a function of rock strengths. Lateral tests were required to back compute P-Y curves, as well as estimate the axial moment-rotation (rotational springs) curves along a shaft's length.

2. Shaft Diameter

Two different diameters were tested to investigate the effect of diameter on the rotational springs. Diameters of 6ft and 9ft were used, as they are representative of the typical large diameter shafts in Florida.

3. Length to Diameter (L/D) Ratio

For each shaft diameter 2 L/D ratios were considered to investigate the effect of embedment depth. L/D ratios for different rock strengths and shaft diameters have been chosen based on field experience (Kim, 2000).

Table 1.1 below shows the nineteen centrifuge tests which were used to calculate T-Z and P-Y curves, as well as validate the proposed rotational spring model. A number of other tests (axial and lateral) were performed, but the data in Table 1.1 was repeatable and subsequently used in this research.

Table 1.1 Centrifuge tests performed.

| Rock $q_u$ tsf | Shaft Dia. ft | Shaft Length ft | L/D ratio | Loading Type | No of Tests |
|---|---|---|---|---|---|
| 10 | 6 | 18 | 3 | axial | 3 |
| | 6 | 18 | 3 | lateral | 4 |
| | 6 | 24 | 4 | lateral | 2 |
| | 9 | 27 | 3 | lateral | 2 |
| 20 | 6 | 18 | 3 | axial | 2 |
| | 6 | 18 | 3 | lateral | 1 |
| | 6 | 24 | 4 | lateral | 1 |
| | 9 | 18 | 2 | lateral | 2 |
| 40 | 6 | 18 | 3 | axial | 2 |

# CHAPTER 2

# CENTRIFUGE MODELING AND REPRESENTATION OF FLORIDA LIMESTONE WITH SYNTHETIC ROCK

## 2.1 CENTRIFUGE BACKGROUND

The UF centrifuge used in this study was constructed in 1987 as part of a project to study the load-deformation response of axially loaded piles and pile groups in sand, Gill (1988). Throughout the years several modifications have been undertaken to increase the payload capacity of the centrifuge. Currently, electrical access to the centrifuge is provided by four 24-channel electrical slip-rings and the pneumatic and hydraulic access is provided by a three port hydraulic rotary union. The rotating-arm payload on the centrifuge is balanced by fixed counter-weights that are placed prior to spinning the centrifuge. Aluminum C channels carry, i.e., support both the pay-load and counter-weights in the centrifuge.

On the pay-load side (Figure 2.1), the aluminum C channels support the swing-up platform, through shear pins. The latter allows the model container to rotate as the centrifugal force increases with increasing revolution speed (i.e., rpm). The platform (constructed from A36 steel), and connecting shear pins were load tested with a hydraulic jack in the centrifuge. The test, concluded that both the swing up platform and shear pins were safe against yielding if the overall pay-load capacity was less than 12.5 tons (Molnit 1995).

### 2.1.1 Theory of Similitude

Laboratory modeling of prototype structures has seen a number of advances over the decades. Of interest are those, which reduce the cost of field-testing as well as reduce the time of testing. Additionally, for Geotechnical Engineering, the modeling of insitu stresses is extremely

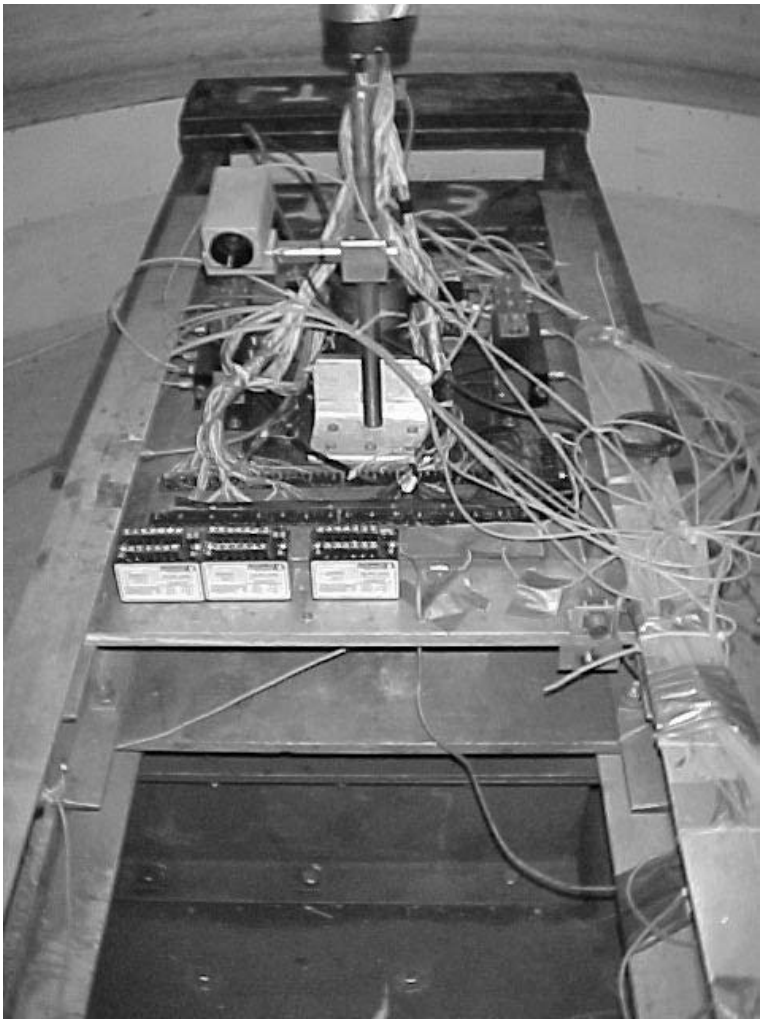

Figure 2.1 The UF geotechnical centrifuge.

important due to soils' stress dependent nature (stiffness and strength). One way to reproduce the latter accurately in the laboratory is with a centrifuge.

A centrifuge generates a centrifugal force, or acceleration based on the angular velocity that a body is traveling at. Specifically, when a body rotates about a fixed axis each particle travels in a circular path. The angular velocity, $\omega$, is defined as $dq/dt$, where q is the angular position, and t is time. From this definition it can be implied that every point on the body will have the same angular velocity. The period T is the time for one revolution, and the frequency f,

is the number of revolutions per second (rev/sec). The relation between period and frequency is f = 1/T. In one revolution the body rotates $2\pi$ rads or

$$\omega = 2\pi \div T = 2\pi f \qquad \text{(Eq. 2.1)}$$

The linear speed of a particle (i.e., v = ds/dt) is related to the angular velocity, $\omega$, by the relationship $\omega$ = dq/dt = (ds/dt)(1/r) or

$$v = \omega r \qquad \text{(Eq. 2.2)}$$

An important characteristic of centrifuge testing can be deduced from Eqs. 2.1 and 2.2: all particles have the same angular velocity, and their speed increase linearly with distance from the axis of rotation (r). Moreover, the centrifugal force applied to a sample is a function of the revolutions per minute (rpm) and the distance from the center of rotation. In a centrifuge, the angle between the gravitational forces, pulling the sample towards the center of the earth, and outward centrifugal force is 90 degrees. As the revolutions per minute increase so does the centrifugal force. When the centrifugal force is much larger than the gravitational force the normal gravity can be neglected. At this point the model will in essence feel only the "gravitational" pull in the direction of the centrifugal force. The earth's gravitational pull (g) is then replaced by the centrifugal pull ($a_c$) with the following relationship;

Centrifugal acceleration $$a_c := r \cdot \left(\frac{\pi \cdot rpm}{30}\right)^2 \qquad \text{(Eq. 2.3)}$$

where $$rpm := \frac{30}{\pi} \cdot \sqrt{\frac{a_c}{r}} \qquad \text{(Eq. 2.4)}$$

Scaling factor; $$N := \frac{a}{g} \qquad \text{(Eq. 2.5)}$$

$$N := \frac{\sqrt{a_c^2 + g^2}}{g} \qquad \text{(Eq. 2.6)}$$

if $a_c >> g$, $$N := \frac{a_c}{g} \qquad \text{(Eq. 2.7)}$$

where a equals the total acceleration

g equals the normal gravitational acceleration

$a_c$ equals the centrifugal acceleration

rpm number of revolutions per minute

r equals distance from center of rotation.

The scaling relationship between the centrifuge model and the prototype can be expressed as a function of the scaling factor, N (Eq. 2.5). It is desirable to test a model that is as large as possible in the centrifuge, to minimize sources of error (boundary effects, etc.), as well as grain size effects with the soil. With the latter in mind, and requiring the characterizing of foundation elements with 18 to 27 ft of embedment in the field, the following rationale was employed to determine the appropriate centrifuge g level and angular speed ω.

The maximum height of the sample container was 12 inches, the longest foundation to be modeled (27 ft embedment) if tested at 67 gravities would require a model depth of 4.84 inches, which would ensure that the bottom of the foundation model had seven inches of rock beneath (i.e., minimizing end effects). Spinning the centrifuge at higher or lower gravities would imply the model would either have to be smaller, or too large to fit in the container.

Knowing that the desired scaling factor N, was 67 gravities, and that the distance from the sample center of mass to the centrifuge's center of rotation was 1.3 meters (51.18 inches), it is possible to then compute the angular speed of the centrifuge, ω from Eq. 2.4,

$$\omega = \frac{30}{\pi} \bullet \sqrt{\frac{67 \times 9.81\ \mathrm{m/s^2}}{1.3\,\mathrm{m}}} = 215 \text{ rev/min} = 3.58 \text{ rev/sec} \qquad \text{(Eq. 2.8)}$$

The actual Scaling factor, N from Eq. 2.6 is:

$$N = \frac{\sqrt{(67 \times 9.81)^2 + 9.81^2}}{9.81} = 67.01 \qquad \text{(Eq. 2.9)}$$

Based on Eq. 2.5, a number of important model (centrifuge) to prototype (field) scaling relationships have been developed (Bradley, 1984). Shown in Table 2.1 are those, which apply to this research.

Table 2.1 Centrifuge scaling relationships (Bradley, 1984).

| Property | Prototype | Model |
|---|---|---|
| Acceleration ($L/T^2$) | 1 | N |
| Dynamic Time (T) | 1 | 1/N |
| Linear Dimensions (L) | 1 | 1/N |
| Area ($L^2$) | 1 | $1/N^2$ |
| Volume ($L^3$) | 1 | $1/N^3$ |
| Mass (M) | 1 | $1/N^3$ |
| Force ($ML/T^2$) | 1 | $1/N^2$ |
| Unit Weight ($M/L^2T^2$) | 1 | N |
| Density ($M/L^3$) | 1 | 1 |
| Stress ($M/LT^2$) | 1 | 1 |
| Strain (L/L) | 1 | 1 |
| Moment ($ML^2/T^2$) | 1 | $1/N^3$ |

Based on Table 2.1, two of significant scaling relationships emerge:

- Linear Dimension are scaled 1/N (prototype length = N∗model length)
- Stresses are scaled 1:1.

The first significantly decrease the size of the experiment, which reduces both the cost and time required to run a test. The second point, ensure that the insitu field stresses are replicated one to one. Note, the effective stress controls both the stiffness and strength of the soil and rock.

### 2.1.2 Slip Rings and Rotary Union

A total of 96 channels are available in the centrifuge through four slip rings (24 channels each) mounted on the central shaft, Figure 2.2. Each channel may be accessed from the top platform above the centrifuge, and used to obtain readings from instrumentation being used to monitor the model, or the centrifuge itself.

For this particular research, several channels were used to send voltages (power-in), and obtain readings (signal-out) from a 1000-lb load cell, two Linear Variable Differential Transducers (LVDT's to measure deformation), and one camera. Power was also supplied, through slip rings to solenoids, which controlled air supply to the air pistons (point load source, etc), and to an amplifier, which boosted the signal (LVDTs, etc.) coming out. To minimize noise, cross

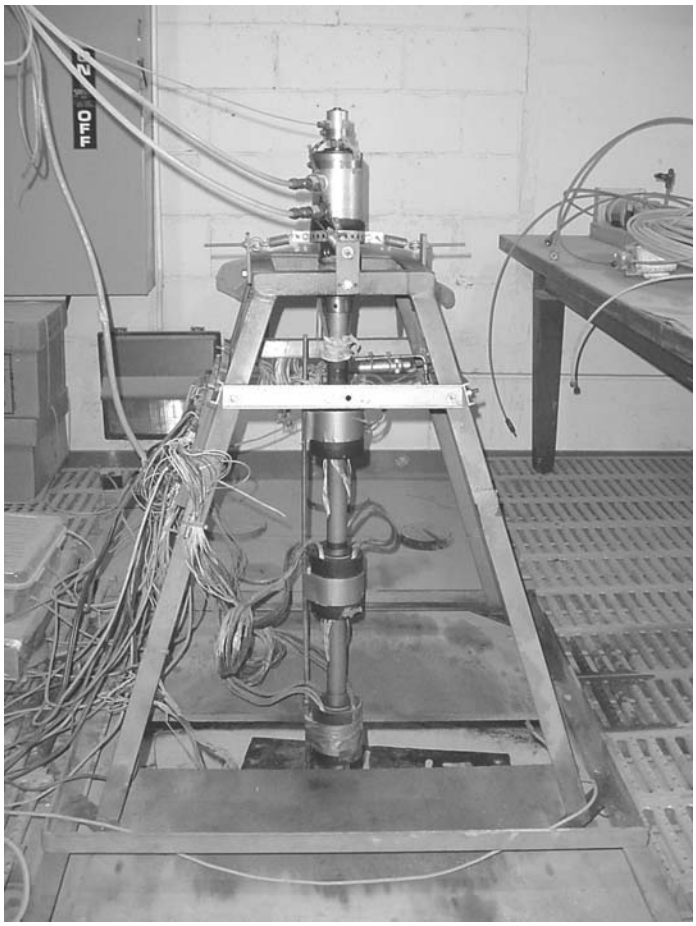


Figure 2.2 Slip rings, rotary union, and connection board (left).

talk, etc., low voltage out devices was kept on different sets of slip rings than the higher voltage power input. For instance, the voltage-in for the load cell was 5 volts, however, the signal (voltage-out) coming from the instrument ranged from 0 to 20 milivolts.

The pneumatic port on the hydraulic rotary union was used to send air pressure to the air pistons acting on the model. The air-line was then connected on the centrifuge through a set of solenoids, Figure 2.3, located close to the center of rotation. Solenoids have the advantage that they may be operated independently of each other, allowing the application of air pressure to a large number of pistons in any combination required. The solenoids required an input voltage of 24 volts of direct current and opened or closed values depending if voltage was supplied or not.

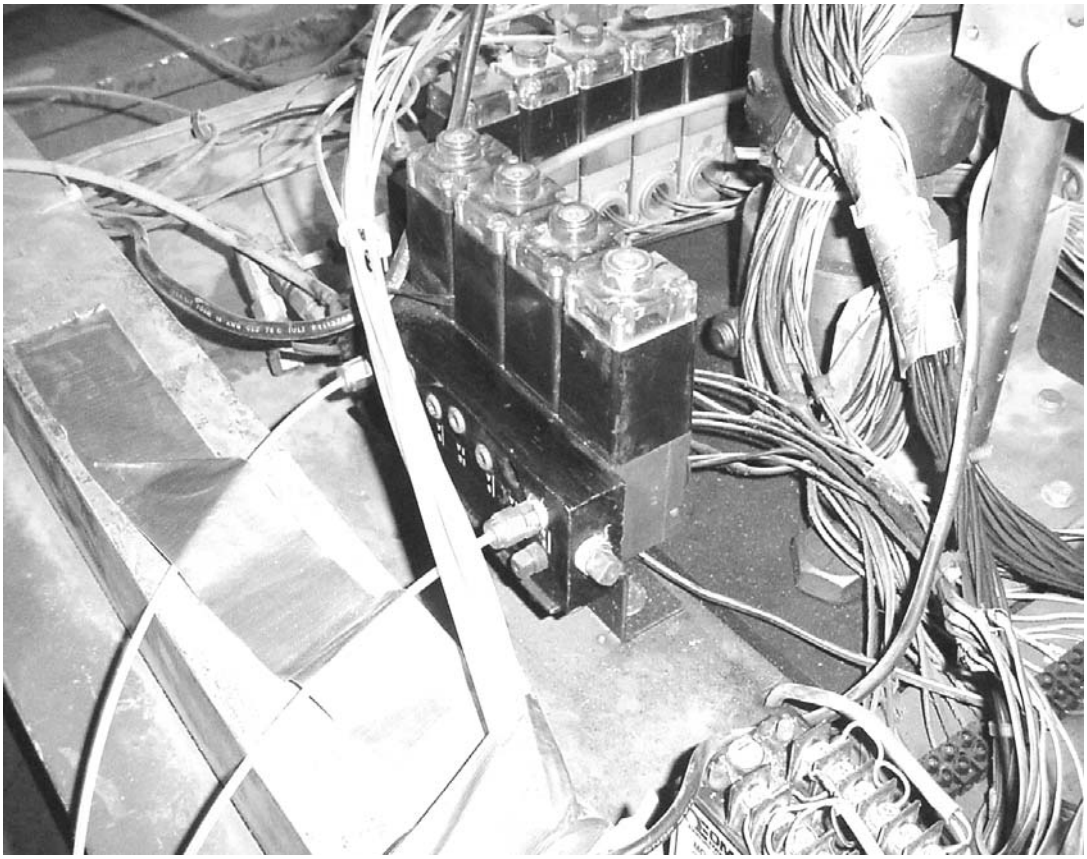

Figure 2.3 Solenoids.

## 2.2 SYNTHETIC ROCK

It was readily recognized from the variability of Florida Limestone, and the difficulty of cutting and placing rock cores within the centrifuge container, that an alternative approach was needed. To replicate the stress-strain and strength characteristic of Limestone, it was decided to use a combination of ground up limestone, cement and water, i.e., synthetic rock.

Synthetic limestone (Gatorock) was developed by mixing ground up limestone sieved through a No 10 standard sieve (max particle diameter of 2 mm), Portland cement and water. The proportion of these constituents can be varied to achieve different strengths. An extensive program of preparation and testing was carried out with different amounts of constituents in order to achieve 3 strengths ranging from about 10 to 40 tsf. Once the desired strength was achieved the test was repeated 3 to 5 times to quantify repeatability. It was found that when the water content was at least 20% by weight of the cement aggregate mix, the strengths were repeatable. Unconfined compressive strength of the final test samples varied by only 10%. However, specimens with less than 20% water had greatly increased strength variability. This strength variability is most probably due to improper mixing of the constituents at lower water content. Table 2.2 shows 14-day unconfined compressive strengths and Figure 2.4 shows rock samples ready for testing.

Table 2.2 Percentage of constituents for different strength synthetic rock.

| Strength | Percentage (by weight) of | | |
|---|---|---|---|
| qu (tsf) | Limestone | Cement | Water |
| 5 | 77.5 | 2.5 | 20 |
| 10 | 75 | 5 | 20 |
| 20 | 72.5 | 7.5 | 20 |
| 30 | 70 | 10 | 20 |
| 40 | 60 | 15 | 25 |

Figure 2.4 Synthetic rock samples.

### 2.2.1 Raw Materials

Limestone Products Inc. provided the crushed limestone used in "Gatorock" from their quarry in Newberry, Florida, west of Gainesville. The quarry mines limestone from the Ocala formation, which outcrops in this region. The FDOT Research and Materials Office in Gainesville transported the material in bulk to UF.

The crushed limestone contained oversized particles, which had to be removed in order to obtain uniform strength and consistency. This was done by first drying the material in oven for at least 24 hours and sieving it through a standard No. 10 sieve. Material retained on the No. 10 sieve was removed for a well graded particle distribution (see Figure 2.5).

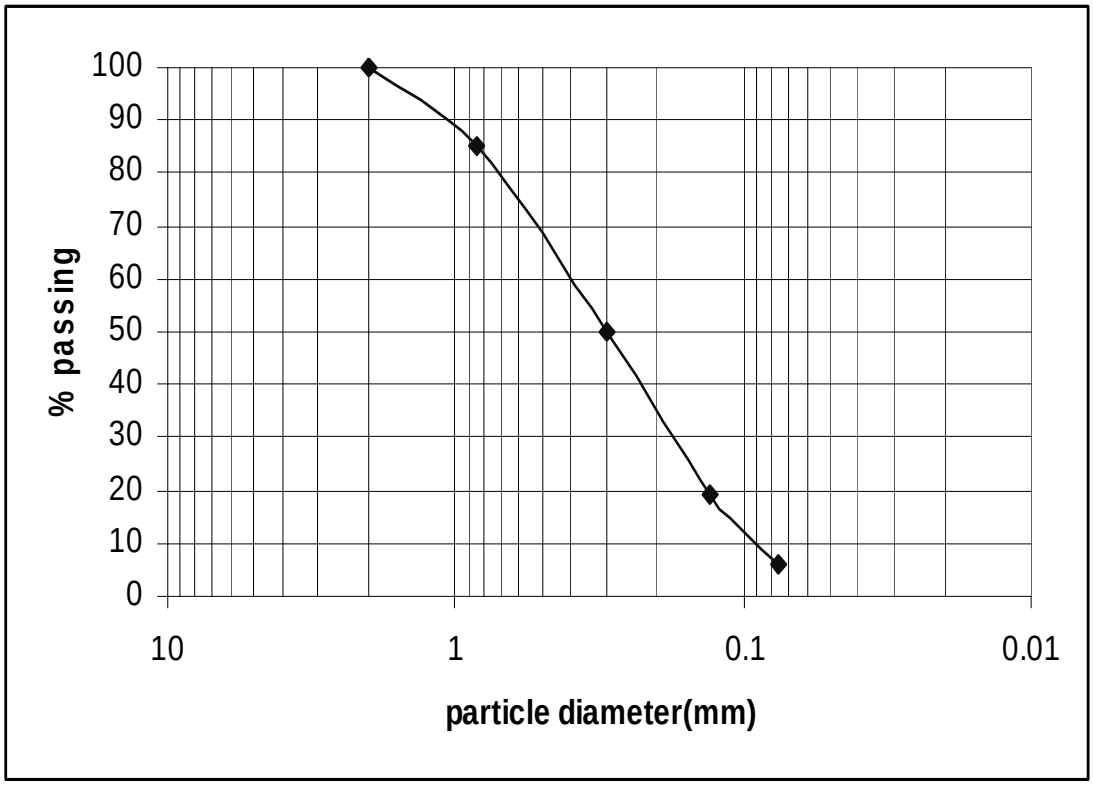

Figure 2.5 Grain size distribution for the limestone aggregates used in the synthetic rock.

### 2.2.2 Mixing and Curing

As part of any mix, cylindrical samples (2 in diameter 4 in high) were cast by hand. First the required weight of the aggregate (dry, sieved limestone) was weighed. Then the percentage of cement (Quickrete type I cement), based on the weight of the dry aggregate and percentage of water based on the sum of the weights of aggregate and cement was determined. For example, suppose that samples containing 10% cement and 20% water was required for 40 tsf strength. If the desired weight of aggregate for a batch of samples is 4 lb then the weight of cement used was 0.4 lb (10% of 4 lb) and the weight of water was 0.88 lb (20% of 4.4 lb). After mixing the mixture was compacted into brass molds (2 in. diameter and 4 in. high) and cured at room temperature for 14 days before testing for its unconfined compressive strength.

The synthetic rock samples used for the axial and lateral load testing in the centrifuge were much bigger (1.8 $ft^3$) and they required use of a concrete mixer for their preparation. A drum mixer manufactured by Constructional Machinery Co, Iowa, with a rotational speed of 19 rpm was used. This mixer, with the capacity of 3.5 $ft^3$, allowed the specimen to be prepared in a single batch. The sample containers used in the centrifuge were steel cylinders measuring 18 in. diameter and 12 in. high. Limestone aggregate and cement were mixed dry in the mixer and water was gradually added so that the mixture formed was uniform. The mixture was then emptied into the sample container and compacted using a vibratory probe.

## 2.3 TESTING OF SYNTHETIC ROCK SAMPLES

Two kinds of samples of synthetic rock were tested during this project to determine their unconfined compression and split tensile strengths. First, small trial mixes were made and cast in cylindrical samples (2 in diameter by 4 in high) and tested for their unconfined compressive strength. The testing was done using Humboldt loading frame located at UF geotechnical laboratory, purchased for tri-axial testing of soil samples. If the mix was satisfactory then large batches were made for the centrifuge bucket. For the centrifuge batches, small cylinders (2" by 4") were cast for later testing. Generally, the cylinders were tested under unconfined loading on the day of the centrifuge test. In addition, cores were taken from the centrifuge containers after the completion of axial and lateral testing of the model drill shafts. The small cores were tested in both unconfined compression and split tensile loading conditions. Figures 2.6 and 2.7, respectively, show the set up of the samples for unconfined compression and split tensile tests.

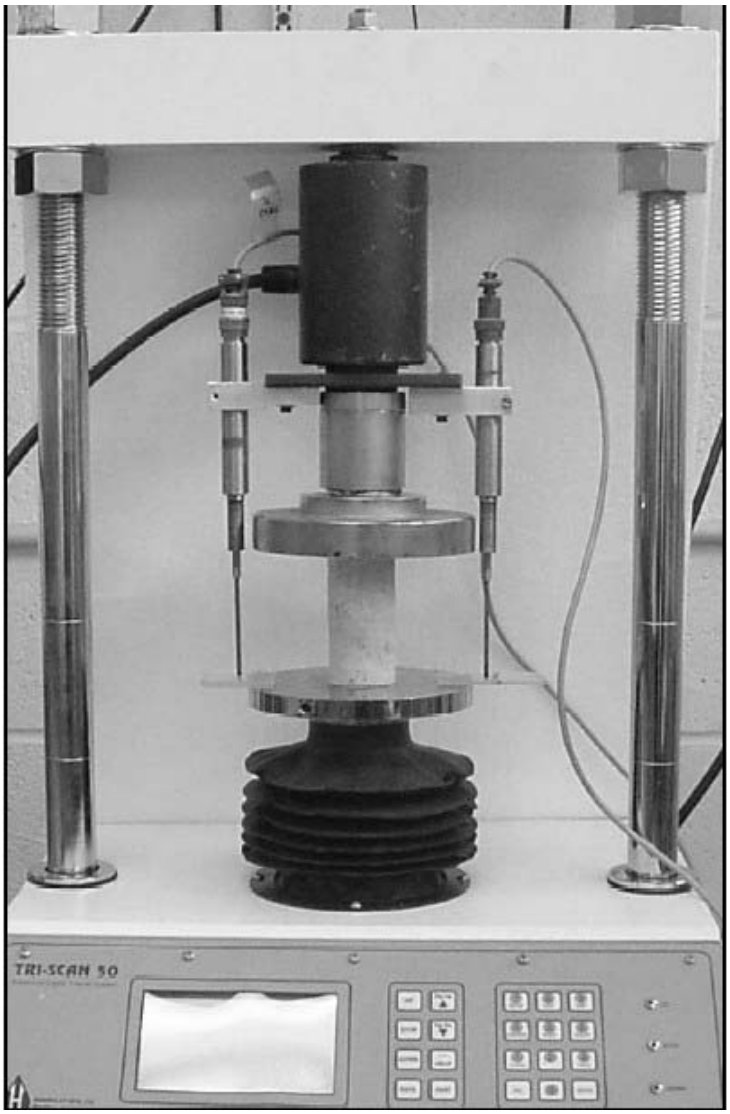


Figure 2.6 Synthetic rock sample set up for unconfined compression test.


Figure 2.7 Synthetic rock sample set up for a split tensile test.

## 2.4 FB-PIER ANALYSIS OF PROPOSED DRILLED SHAFTS EXPERIMENTS

In order to determine the rock strengths for testing, properties of concrete for the shaft as well as the capacity of the load cell needed to measure the axial and lateral loads on the shaft, a FB-Pier analysis was performed. The analysis also gave the maximum depths that the moments and the shear forces would be transferred, determining shaft lengths, as well as instrumentation placement. In the analysis, a drilled shaft was modeled as a single shaft and tested for the maximum lateral as well as axial load before the rock failed. In the present FB-Pier software the axial behavior in rock is modeled by its own T-Z curve but the lateral P-Y characterization must be modeled as either soft or stiff clay with rock properties. Analysis was performed using both models. In general it was found that the soft clay model gave much higher capacities. Using a 9 ft diameter shaft with rock strengths varying from 10 tsf to 45 tsf it was found that the maximum lateral load required to fail 45 tsf rock was approximately 6000 kips. This translates to a force of 1.3 kips in the centrifuge model, spinning at a centrifugal acceleration of 67 g. The axial capacity of the shaft was tested with and without tip resistance. With the tip resistance included it was seen that the maximum axial capacity of the shaft could be over 40,000 kips (9 kips in the model). Ignoring tip resistance, i.e., skin friction only, the maximum axial capacity of the shaft was about 17,500 kips which corresponds to a force of 4 kips in the model. For the latter representation, placing a layer of styro-foam at the bottom of the shaft would eliminate the tip resistance. Hence it was decided that a load cell of 10 kips capacity would be sufficient for both types of tests. Both axial and lateral loading would be provided through a Bimba air cylinder with a 2,500 lb capacity.

The analysis also gave the depth below ground for which no more moment and shear force is transferred from the shaft to the rock (tip cut-off depth). It was found that this depth

depended on the strength of the rock as well as the diameter of the shaft. In general it was observed that moments and shears could be transferred deeper in weaker rock and with larger diameter shaft. Table 2.3 summarizes the results of the FB-Pier analysis of the drilled shafts.

Table 2.3 Results of FB-Pier modeling.

| Rock $q_u$ (tsf) | Max Lateral Load (kips) | | Max Axial Load (kips) | | Tip Cut-Off Depth (Diameters) | |
|---|---|---|---|---|---|---|
| | (Prototype) | (Model) | (Prototype) | (Model) | 6 ft dia shaft | 9 ft dia shaft |
| 10 | 3000 | 0.7 | 3500 | 0.8 | 4 | 5 |
| 25 | 5000 | 1.1 | 10000 | 2.2 | 4 | 5 |
| 35 | 5500 | 1.2 | 13000 | 2.9 | 3 | 3 |
| 45 | 6000 | 1.3 | 17500 | 4 | 3 | 3 |

The analysis suggests that for shaft diameters ranging from 6 to 9 ft the cut off depths should vary from 3 to 5 diameters. Hence, the L/D ratio was kept less than 5 and varied depending on the rock strength and the shaft diameter, giving the longest possible shaft length of 45 ft. The latter resulted in 8 in. long shaft at an acceleration of 67 g. The analysis also suggested that the maximum depth to which moments and shear forces are transmitted would not exceed 3 diameters even for rock with unconfined strengths higher than 40 tsf. It was therefore decided to conduct tests on rock strengths of 10 and 20 tsf. It was decided to use the result obtained from the tests to extrapolate to lower and higher strength rock.

## 2.5 REDUCTION OF qu AND qt TESTS

For unconfined compression loading, the axial load, P and vertical deformation, $\Delta$ are recorded. To obtain $q_u$, the P-$\Delta$ data has to be converted into stress (q) and strain ($\varepsilon$) results. The following equations were used to calculate q and $\varepsilon$ from P and $\Delta$.

$$q_u = P/A \quad \text{(Eq. 2.10)}$$

$$\varepsilon = \Delta/L \quad \text{(Eq. 2.11)}$$

Where A is the average initial cross sectional area and L is the initial length of the sample, and $\Delta$ is the sample deformation.

The split tensile tests were reduced in accordance with ASTM D 3967 using the following equation.

$$q_t = 2P/\pi Ld \quad \text{(Eq. 2.12)}$$

Where P = maximum applied load, L = sample length and d = sample diameter.

Shown in Table 2.4 are the average results from the unconfined compression and split tensile tests for the various mix design. Each testing sequence (i.e., strength) was repeated three to five times for repeatability.

Table 2.4 Percentage of constituents for different strength synthetic rock.

| Strength | Percentage (by weight) | | |
|---|---|---|---|
| qu (tsf) | Limestone | Cement | Water |
| 5 | 77.5 | 2.5 | 20 |
| 10 | 75 | 5 | 20 |
| 20 | 72.5 | 7.5 | 20 |
| 30 | 70 | 10 | 20 |
| 40 | 60 | 15 | 25 |

## 2.6 MODEL SHAFT DESIGN AND CONSTRUCTION

### 2.6.1 Concrete

Since rock strength evaluated in the tests were to be as high as 20 tsf, the concrete strength had to be of sufficient strength to ensure rock failure instead of the concrete. FB-Pier

modeling (section 2.4) was performed with 5 ksi concrete (360 tsf). The latter are typical strengths reported in design plans for drilled shafts in Florida. Because of the small size of the model shaft (9 feet diameter prototype = 1.62 in diameter modeled in the centrifugal acceleration at 67 g) it was not possible to use large aggregates. In addition, the curing time had to be limited because the shaft had to be ready for testing in about 2 weeks. Leaving the concrete in the shaft to cure longer would result in increased strength of the synthetic rock above the target values.

Initially, many different types of ready mixes were tried but the highest strength reached was 3,000 psi. It was evident that the target strength of 5000psi was not viable from ready mixes. Next, silica sand and ordinary Portland cement mixes were tried but the highest strengths achieved were approximately 4,000 psi. Subsequently, granite sand and Portland cement mixes were found to give strengths higher than 4,000 psi. Adding silica fume to the granite sand cement mix and reducing the water to cement ratio through synthetic super-plasticizer resulted in compressive strengths of over 5,000 psi. Note, the addition of silica fume and reduction of water not only increased strength but also reduced undesirable shrinking of the concrete.

### 2.6.2 Steel Reinforcement

It was decided that two different prototype (field) shaft diameters would be tested – 6 ft and 9 ft (model diameters of 1.08 in and 1.62 in). For the model shafts, 0.75 in and 1.3 diameter steel pipes were used above the rock surface, and below the ground surface, the pipes were slotted to provide steel ratios ($\rho$) of 6.4% and 7.5%. The latter reinforcement were required to carry the expected moments transferred to the rock. Winding a 0.0625-inch tie wire round the pipe provided shear reinforcement. The concrete cover for the reinforcing steel in both cases was approximately 0.1 inch, which is equal to 6.7 inches in the prototype shafts. Figure 2.8

shows the drilled shaft steel reinforcement along with attached strain gauges. The gauges were attached in pairs on opposites sides of the reinforcement.

Figure 2.8 Instrumented rebar cages for 6 ft and 9 ft model shafts.

# CHAPTER 3

# TEST EQUIPMENT AND PROCEDURE

## 3.1 SAMPLE CONTAINER

For this research, the original sample container built by Molnit (1995) from aluminum alloy 6061 with rectangular dimensions of 18 inches long, 10 inches wide and 12 inches deep was to be used. It was the largest container available at the start of the research. Since other research was using the container, as well the need for long curing times (rock, shaft, etc.), it was recognized that the synthetic rock could not be cast directly in the container. Both the synthetic rock and the model-drilled shaft were prepared external to the container and subsequently placed in it for testing. However, preliminary testing of shafts constructed this way failed. Due to small unavoidable gap between the container and the sample, a crack, Figure 3.1, developed across the rock mass, in the direction perpendicular to loading. Although the gap between the container wall and the rock was filled with fine sand and compacted, this did not prevent cracking in the rock mass. The latter cracking was attributed to loss of confinement, which would not exist in the field.

It was hence decided to build new sample containers for this project. The new containers (3) were constructed from 0.5 inch thick steel pipes with inside diameter of 17 inches and overall length of 12 inches as shown in Figure 3.2. The hooks or ears were used in lifting the new containers with the cast insitu rock.

The new sample containers offered three distinct advantages over the old sample container. First as the synthetic rock was cast directly into an individual container and not removed prior to testing, the container provided sufficient rock confinement which eliminated rock

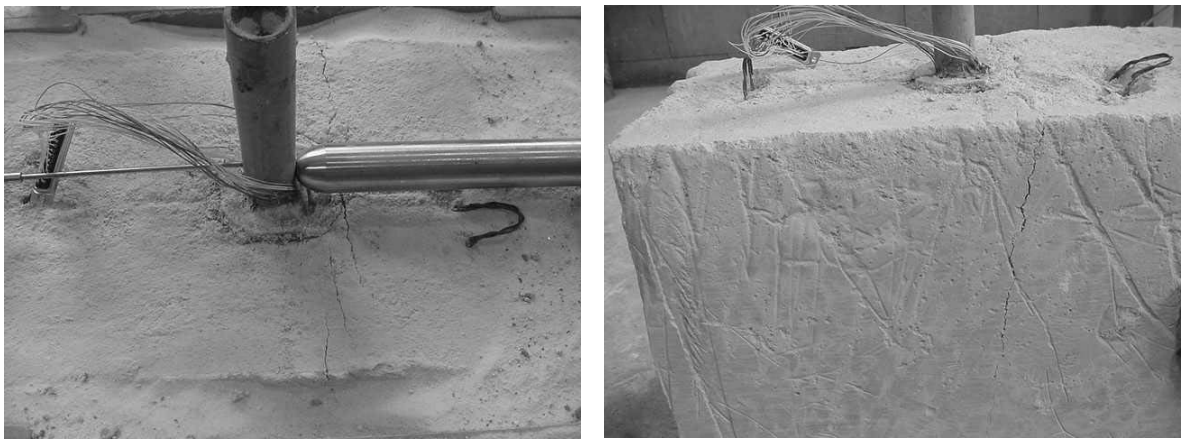

Figure 3.1 Cracking of synthetic rock in the old rectangular container.

Figure 3.2 New cylindrical sample container with aluminum loading frame and base plate.

cracking during lateral loading. Secondly, the larger area of rock in the new containers made it possible to conduct multiple tests within the same rock sample. Finally, construction of more than one container allowed samples of rock to cure while others were being set up for centrifuge testing, i.e., staggered construction and testing.

## 3.2 LOADING FRAME AND THE BASE PLATE

Since the old rectangular sample container was replaced with a new cylindrical shape, the arrangement for loading and displacement measurement had to be modified. It was thought that instead of attaching the loading air piston directly to the container, a loading frame independent of the container would be a better arrangement to minimize boundary effects. In addition, the single frame should be capable of providing loading for both axial and lateral scenarios.

The frame was constructed out of square aluminum tube 2in by 2in in cross section and reinforced with 0.5 in diameter steel rods to prevent buckling during loading. The frame is bolted to a 21in by 21in aluminum base on which the sample container would be attached. The base plate is 0.5 in thick and reinforced on the underside with aluminum angles in order to prevent buckling. Figure 3.2 shows the loading frame together with the new sample container and the base plate.

## 3.3 STRAIN GAGES AND THE BRIDGE COMPLETION CIRCUITS

### 3.3.1 Strain Gages

In order to monitor the moments, shear and rock lateral resistance along each shaft, multiple pairs of strain gages were attached to opposite sides of the shaft. To obtain moments, shears, etc., along the shaft, 6 pairs or sets of strain gages were attached at 6 elevations along the shaft. For accurate strain measurements, the gauges were attached to the steel reinforcement in each shaft. The strain in the reinforcement was subsequently translated to the strain on the out side surface of the shaft, then to rotations and finally to moments. The rock lateral resistance (P-Y) was obtained by double differentiating the moment distribution along the shaft at a given elevation.

Because of the small size of the model shafts, the strain gages had to be small in size. However, strain gages smaller than 3 mm are very difficult to install. Consequently, a compro-

mise was found (lab testing) using a gage length of 3mm. After an extensive search of suitable strain gages it was decided to use CEA-06-125UN manufactured by Measurements Group, Inc. A gage length of 1/8 in and a narrow geometry together with large solder pads for connecting wires made this strain gage ideal for this research. The gages have a gage factor (GF) of 2.1 with an excitation voltage of 10 volts. A gage resistance of 350 ohms was selected vs. 120 ohms, giving a higher output voltage from the bridge, which is more sensitive to strain changes.

### 3.3.2 Bridge Completion Circuits

Each strain gage was connected to its own separate quarter bridge circuit. Since each gauge generates its own strain, then separate computation of axial, shear and moment values at a given cross-section is possible.

Lead wire effect (change in resistance of the lead wires due to heating, stretching etc) is a source of error in quarter bridge circuits. Using a three-wire quarter bridge circuit, Figure 3.3, instead of two wires will reduce this effect. In a two-wire circuit, both lead wires are in series with the strain gage, in one arm of the Wheatstone bridge. In the three-wire circuit, the first lead wire remains in series with the strain gage but the second lead wire is in series with the dummy resistor $R_4$ between the negative input and the output corners of the bridge. If these two wires are the same type, length and exposed to same temperature and stretching, their resistances will be the same and the bridge balance will be unaltered by any change in the two wires.

## 3.4 LOAD AND DISPLACEMENT MEASURING DEVICES

A load cell with a 10000 lb capacity was used to measure the applied load during either axial or lateral testing. Load was provided through a “Bimba” air cylinder. The air cylinder–load cell assembly was mounted on the loading frame either horizontally or vertically for either lateral or axial loading.

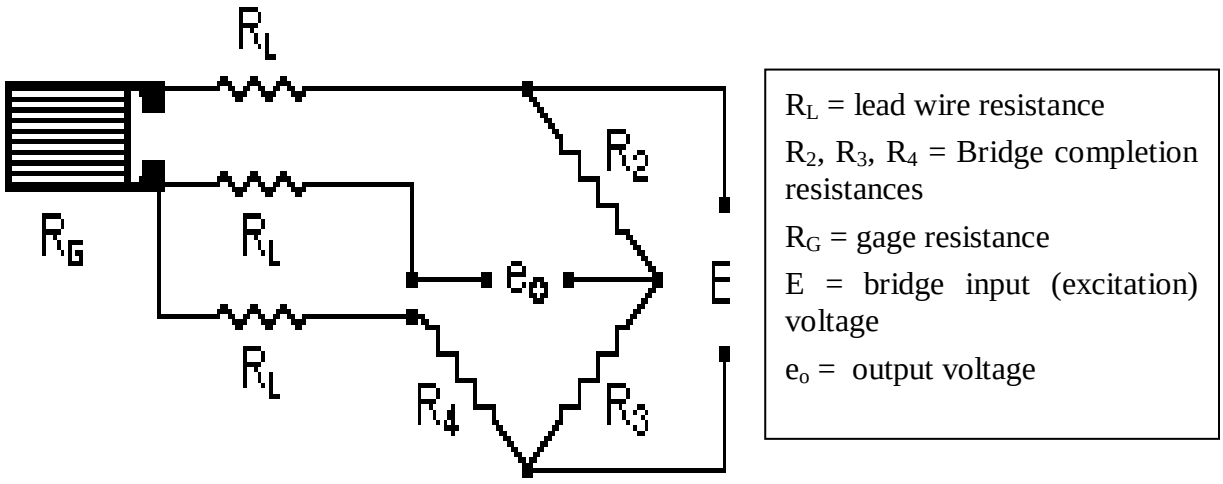


Figure 3.3 Three-wire quarter bridge circuit.

Two LVDTs with 0.5 inch of travel were used to measure the displacements of the top of the shaft for lateral loading. The LVDTs were attached to the top of the centrifuge sample container, Figure 3.2. They devices were fixed 1 inch apart, and measured lateral displacements at two separate points above the surface of the rock. Figure 3.4 shows the devices used for both loading and monitoring of force and displacement on each shaft.

Figure 3.4 Devices for loading and load and displacement measurement.

## 3.5 DATA ACQUISITION SYSTEM

The outputs from the 12 strain gages, one load cell and two LVDTs were collected by a National Instrument data acquisition card (NI 6034E) and processed and monitored by LabView. Since the raw output voltage from the strain gage bridges were very small (i.e., millivolts), they had to be amplified prior to passing through centrifuge slip rings to increase their signal to noise ratio. Amplification was done by an Omega EXP-20 amplifier/multiplexer, Figure 3.5, which could amplify the signals 800 times.

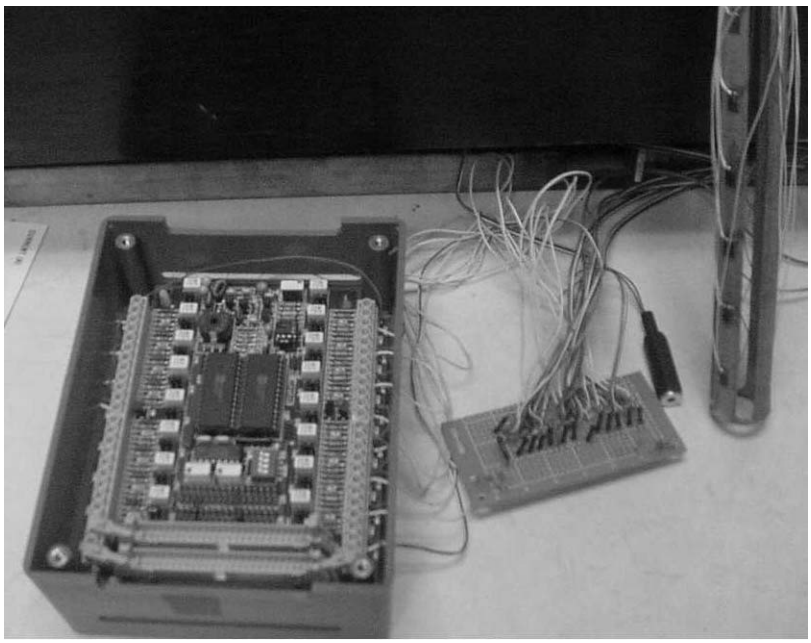

Figure 3.5 EXP-20 with instrumented shaft and bridge completion circuit.

The signals from the strain gage bridges were connected to 12 different input terminals of the EXP-20 and the amplified output was multiplexed into a single channel of the NI 6034 card in the computer. The output from the load cell (20 mV max) was also amplified before the signal was sent through the centrifuge slip rings. This was done using an Omega DMD-465 bridge sensor and amplifier with amplified the signal of 1000 times. The signal from the LVDT

(40V/in) did not need amplification and was connected to the NI6034 directly. Figure 3.6 shows the overall schematic of the data acquisition system, amplifiers, and instrumentation.

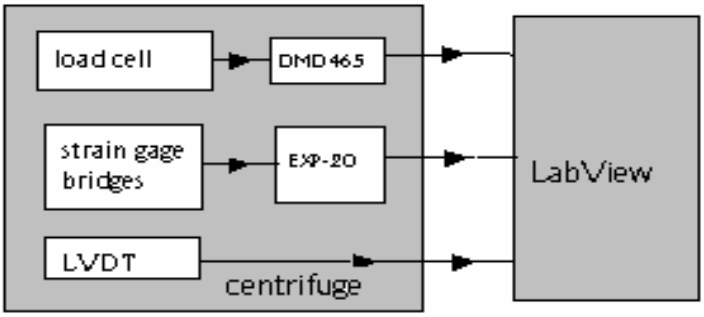


Figure 3.6 Data acquisition system.

The LabView Virtual interface (VI), which converts the load cell and LVDT voltages into force and displacement, is shown in Figure 3.7. The amplified output voltages from the 12 strain gauges and load cell are later stored by LabView in a Microsoft EXCEL worksheet file. The EXCEL worksheets have VB interface to convert the voltages into strains and loads. LabView also displays a graph of load vs. top displacement of the top of the shaft for control the "Bimba" air cylinder during the test.

## 3.6 TEST PROCEDURES

### 3.6.1 Preparation of the Model Shaft

Preparation of the model shaft involved the following steps:

1. Strain Gaging

   Before casting the shaft in rock, the rebar cage for model was instrumented with strain gages along its length. The steel pipe (with slots cut in it) representing the rebar cage was first ground flush with abrasive paper and then cleaned with acetone. This removed the grease, dust etc. from the bonding area to present the placement of the strain gages. Next, lines were marked with a scriber on the cleaned steel where the strain gages were to be bonded. The strain gages were then bonded the steel surface using Cyano-acrylate adhesive and thumb pressure for approximately one minute to cure.

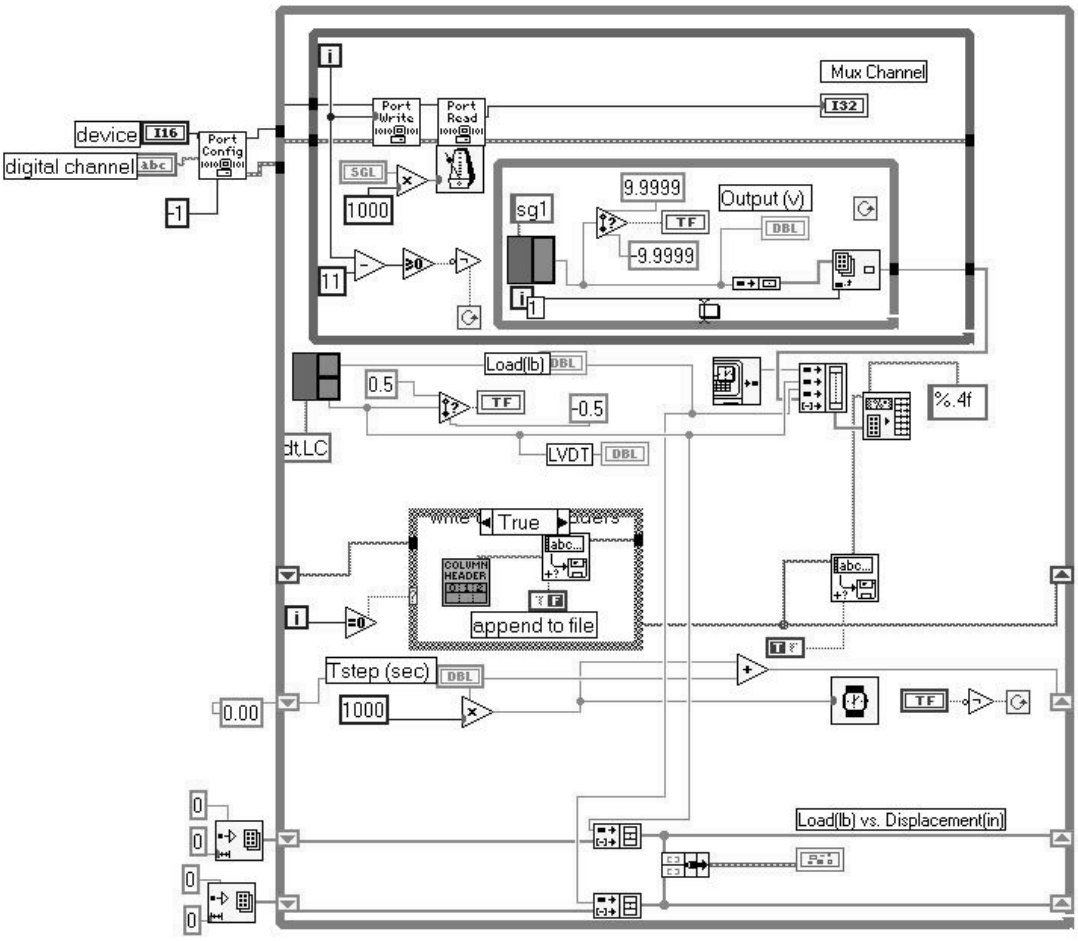


Figure 3.7 LabView VI for reading and processing data.

2. Wiring Strain Gages

Next, lead wires were soldered to the exposed strain gage solder tabs to connect them to their respective bridge circuits. Each strain gage has two terminals (solder tabs) for wiring. One wire was attached to the first terminal and two wires to the second so that the gage could be connected to a 3-wire quarter bridge circuit, Figure 3.3. A 25 pin connector provided the connection from the strain gages on the model shaft to the bridge completion circuit located on the centrifuge arm.

3. Coating Strain Gages

Since the shaft rebar cage and strain gages were to be embedded in concrete, the strain gages had to be protected well against moisture and other chemicals in the concrete. A variety of coating substances are available depending on the nature of the environment in which the gages are used. In the field, strain gages and lead wires are protected against such harsh conditions by many thick layers of different materials. However, the small size of the model did not allow thick multiple layers to be used and it was necessary to use a single thin layer. In the early tests, a single component: xylene coating (M-coat A) supplied by Vishay Measurements group was used but it was soon found to be ineffective. It was observed that moisture and other chemicals from the wet concrete could easily penetrate the coating and soften the Cyanoacrylate adhesive between the steel and the gages. For instance, the results from several early tests had to be discarded as the strains did not go high enough, possibly because of de-bonding of the gages from the steel of the rebar cages.

Other materials were tried to determine the most suitable coating to protect the strain gages and it was finally decided to use a two component epoxy coating (M-Bond AE-10) from the same supplier. This worked well as it is highly resistant to moisture and most other chemicals. No de-bonding of strain gages was detected on shafts with this coating.

4. Model Shaft Installation

The synthetic rock was prepared as described in Chapter 2. After curing the rock for about 10 days, the model drilled shaft was installed in the rock mass (see Figure 3.8). The process is described as follows:

A hole of required diameter (1.08 in for 6 ft prototype and 1.62 in for 9 ft prototype) was drilled at the desired location on the surface of the synthetic rock sample. Initially, this was done

Figure 3.8 Installation of the model shafts in the synthetic rock.

using a "Hilti" hand drill. However, it was discovered that the diameter of the hole constructed this way was not uniform and decreased with depth. This was attributed to the difficultly of keeping the drill perfectly vertical while drilling. Subsequently, it was decided to use a drill press to create the shaft hole. This greatly improved the quality of the hole, although there was still some variation in diameter due to wobbling of the drill bit and shaking of the rock sample during drilling. Typically, the difference in diameter between the top and bottom of a 3 inch deep hole was 0.01 inches which is equal to 0.67 inches in the prototype hole which is typical.

Before placing the instrumented rebar cage in the hole, it was coated with a thin layer of bentonite slurry. The bentonite slurry was prepared by adding 3% by weight of dry bentonite powder in water and mixed using an electric mixer. The slurry was poured into the hole and kept there for few minutes before pumping it out. This formed a thin slurry cake on the wall.

In the actual drilled shaft construction, bentonite slurry is used to maintain the wall stability of the drilled hole in caving soils. The purpose of the slurry here was to provide a separating layer between the shaft concrete and the rock. Without this separating layer, the con-

crete in the model shaft was forming a chemical bond with the synthetic rock. This resulted in extremely high axial and lateral capacity of the model shaft as the synthetic rock and the shaft concrete were behaving as a single material. In practice, the bond between the shaft concrete and rock is of a mechanical nature, with no chemical bonding. The bentonite layer was kept very thin so that its effect on the axial shear capacity of the shaft/rock interface was minimal.

Next, the instrumented rebar cage was lowered into the hole with the strain gages aligned in the direction of loading. Concrete (prepared as described in Chapter 2) was poured into the hole and compacted with a small steel rod by layers. The rebar cage was kept at the middle of the hole in the concreting process with a wood template placed on the top of the rock surface. The shaft was then left to cure and gain strength for 4-5 days before testing began in the centrifuge.

### 3.6.2 Centrifuge Test Setup

When the model shaft was ready for testing, the sample container was bolted to the base plate and the loading frame attached to it, Figure 3.2. The Bimba pneumatic air cylinder with a 1000 lb capacity load cell was then mounted to the loading frame. Depending on the type of test (axial or lateral) the air cylinder was placed either vertically or horizontally with a stainless steel rod extending from the load cell to the model shaft, Figure 3.9. In the case of lateral tests, the loading occurred at 0.8 to 1 inch above the rock surface. It was desirable to load the shaft as close to the rock surface as possible in order to avoid large moments developing on the shaft above the rock and to transfer high moments into the rock. The size of the load cell allowed the minimum distance to be about 0.8 inches. For the axial tests, the load-measurement assembly was mounted on a horizontal member (vertical LVD attached), which applied axial load at the top of the shaft about 3 inches above the rock surface.

Figure 3.9 Test set up for axial and lateral tests.

Two LVDTs monitored the displacements in both the lateral vertical loaded shaft tests. In the axial set up, the LVDTs were attached to a horizontal bar clamped to the top of the model shaft (Fig. 3.9), with the tips of the LVDTs resting directly on the rock surface. For the lateral set up, the LVDTs were placed horizontally with their tips pushing against the shaft about 1 inch apart. They were mounted on a horizontal bar, which was clamped to two points on the edge of the sample container. It was decided to place the LVDTs as close to the rock surface as possible to compare with integrated strain displacements. Because of size and space constraints, the distance from the surface to the lower of the two LVDTs was 0.5 inches. In both loading scenarios, the system of displacement measurement was independent of the loading frame. The latter was important, since the frame was expected to deflect under loading.

### 3.6.3 Centrifuge Balance Calculations

Before spinning, the balance condition of the centrifuge arms was checked. This involved comparing the sum of moments from the payload vs. sum of moments on the counterweight side about the centre of rotation of the arm. The moments on each side were calculated by multiplying the weight of each component by the distance from its centroid to the center of

rotation of the arm. The difference in the total moments between the two sides is called the out of balance moment and the value had to be less than one percent of total applied moment. To correct any unbalance, additional weights were either added or removed from either the payload (experiment) or counterweight side of the centrifuge. For each rock sample, the total weight of the sample container was slightly different (i.e., 340–345 lbs) which made it necessary for the additional weight to be added or removed for each test. A spreadsheet was used to tabulate weights and distances from the centre of rotation for each major component of the centrifuge.

### 3.6.4 Centrifuge Testing

The assembled sample container was lowered unto the centrifuge sample platform with the aid of a crane. The base plate was fixed to the platform with four 3/4 inch steel bolts. The airline was connected to the Bimba air cylinder. The LVDTs, load cell and the strain gages were connected to their respective plugs which provided both power as well as monitored output signals from the devices with the LabView software.

The testing consisted of spinning the centrifuge at 215 revolutions per minute (RPM) giving a centrifugal acceleration of 67 g at the rock surface (1.3 m from the axis of rotation) and loading (axially or laterally) the shaft to failure while recording the load, displacements and the strain data. In both types of test, failure was indicated by a large increase in displacement with very small or no increase in load.

Before spinning the centrifuge, all electrical connections were checked carefully, any loose wires were attached to the centrifuge arm with duct tape and the floor was cleaned to remove any loose material. All the electrical outputs (12 strain gages, LVDTs and the load cell) were measured with a digital voltmeter and verified with the corresponding readings shown by LabView in the computer. This was especially important for the strain gage bridge and the load

cell outputs as they were small (few millivolts) and had to be amplified before sending them to the computer. This also ensured that the amplifiers were functioning properly.

The centrifuge was started and accelerated to 215 RPM. When all the readings (strain gage bridges, LVDTs, load cell) were stable, loading was initiated by slowly applying pressure to the air cylinder by turning the control knob located in the control room. The air pressure was increased in steps of about 1 psi until the model shaft failed. As the shaft was loaded, load, deflection and the strain gage outputs were observed on the computer monitor.

LabView plotted a graph of load versus deflection of the shaft during the test. As described earlier, LabView also stored an EXCEL worksheet of raw voltages from the strain gages, LVDTs and load cell. Reduction of data to obtain T-z and P-Y curves is described in the Chapter 4.

# CHAPTER 4

# DATA REDUCTION

## 4.1 AXIAL LOAD TESTS

Instrumented axial load tests provide both axial force and displacement along a shaft as a function of applied load. Of interest is the side shear, $\tau$ vs. axial displacement (z), i.e., T-z curves. The latter curves are important in the development of the rotational springs (Chapter 1), as well as moment equilibrium at a cross-section.

Initially, it was planned to instrument the model-drilled shaft with six pairs of strain gages as in the case of lateral loading. From each pairs of strain gages, a compressive strain for each applied axial load state is found. Subsequently, each strain may be converted into stress ($\sigma$) or compressive force (Q). The difference between the compressive forces between adjacent pairs of strain gages is the force (T) transferred from the shaft to the rock. Dividing this force by the area of the shaft between the two sets of strain gage locations gives the unit skin friction ($\tau$) at the middle of the shaded element. The axial displacement (z) of the shaft at that location is obtained by subtracting the sum of all the strains to that location from the axial displacement of the top of the shaft. Hence, graphs of $\tau$ vs. z (T-Z curves) could be plotted at five elevations along the shaft.

However, since the synthetic rock was uniform with depth, the skin friction was not expected to vary with depth. Furthermore, the use of Styro-foam at the bottom of the shaft eliminated end bearing, Fig, 1.2. Hence, the T-Z curve was obtained without the use of any strain gages (see Figure 4.1) as follows:

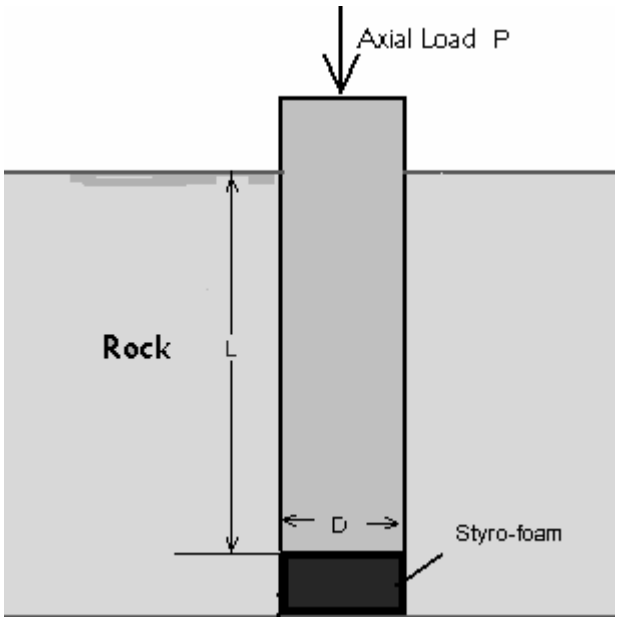


Figure 4.1 Axial loading with no strain gages.

1. Using the applied load on top of the shaft (P) and zero axial force at the bottom (Styro-foam – 0 end bearing) the total load transferred to the rock (T) is equal to the applied load (P).
2. The shear stress on the shaft wall (skin friction, $f_s$) is then given by

$$f_s = T/\pi DL \qquad \text{(Eq. 4.1)}$$

where, D = shaft diameter and L = length of shaft embedded in rock.

3. A plot of $f_s$ against the measured axial displacement (z) of the shaft is the T-Z curve.

In the method described above, axial compression of the shaft has been ignored as it was found to be negligible.

## 4.2 LATERAL LOAD TESTS

The goal of the lateral load tests was to obtain P-Y curves for rock at various unconfined strengths. Two types P-Y curves were back computed; 1) Current FB-Pier small diameter

pile/shaft curves which are not corrected for shaft friction effects, and 2) Proposed FB-Pier model, P-Y curves corrected for the side shear. The theory for the back computation of the latter curves is presented in 4.2.3. In order to calculate, the P-Y curves, the moment at a given cross-section must first be computed from the strain gage data.

The model shaft was instrumented with 6 pairs of strain gages as shown in Figure 4.2. The raw data from each lateral load test consist of load and displacement at the top of the model drilled shaft and the 12 strain gage bridge outputs (voltages) along its length. The reduction of raw data to obtain P-Y curves involves numerous steps as described bellow.

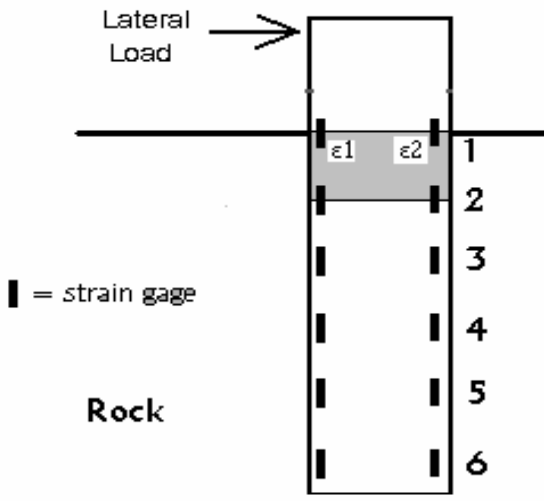


Figure 4.2 Strain gage layout for lateral tests.

### 4.2.1 Strain from Bridge Output

The strain for a single strain gage quarter bridge (see Figure 3.3) can be calculated using the following equation,

$$\varepsilon = \frac{4\Delta V}{GE} \qquad \text{(Eq. 4.2)}$$

where, $\varepsilon$ = strain

$\Delta V$ = change in bridge output voltage

G = gage factor

E = bridge excitation voltage.

This equation assumes a linear variation of strain with change in strain gage resistance and is obtained from the following relationship,

$$\varepsilon = \frac{\Delta L}{L} = \frac{\Delta R}{R G} \qquad \text{(Eq. 4.3)}$$

where, R = unstrained strain gage resistance

$\Delta R$ = change in resistance due to strain,

G = gage factor.

### 4.2.2 Determination of Bending Moments from Strains

Calculation of bending moments from strains involved the following steps:

#### *4.2.2.1 Fitting trend lines to raw strain data –*

After calculating strains for all 12-strain gages, the strains were plotted against the lateral load on the top of the shaft, as shown in Figure 4.3. The strains from the gages on the opposite sides of the shaft are plotted. The positive strains are tension and the negative strains are compression. Plots similar to Figure 4.3 were computed for all six locations along a shaft, Figure 4.2. Appendix A plots all the strain vs. load for the 12 lateral tests (Chapter 1) conducted.

Evident from Figure 4.3, the strain–lateral load relation is linear initially and then becomes highly non-linear. Analysis with FB-pier and observations, Figure 4.3, suggest the strains become non-linear at about 130 micro-strains. The latter corresponds to the initiation of concrete cracking. Cracking results in the movement of the shaft's neutral axis resulting in non-symmetrical strains assuming that plane sections remain plane.

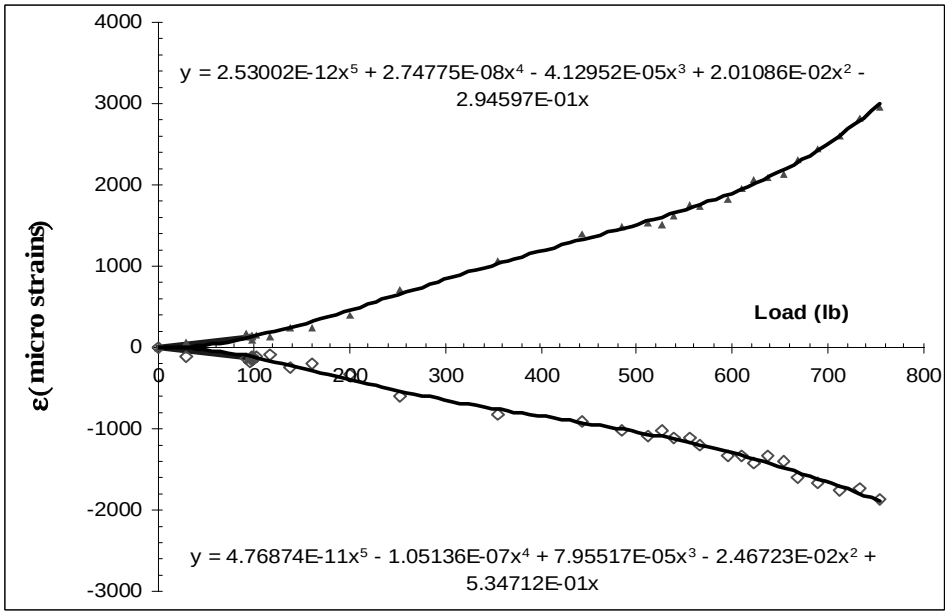

Figure 4.3 Strains from a pair of gauges vs. applied lateral load.

The plot of lateral load vs. strain was used two ways. First, the plot identifies any irregularities in the strains. For instance, non-continuous strain profiles (i.e., jump discontinuities) are strong indicator of either broken or slipping strain gages. Second, from the plot of strain vs. load, a trend line or relationship may be established to compute moments for any lateral load of interest. Also note, the output voltage contained noise due to centrifuge slip rings, wiring, etc. The trend lines were subsequently used in computing the bending moments. Figure 4.3 shows the trend-lines together with their equations (generally $5^{th}$ order) for each strain gage.

#### *4.2.2.2 Calculation of bending strains -*

At each strain gage location, the total strain consists of an axial and bending component. Of interest is the bending strain, $\varepsilon_b$ at any given section of the shaft,

$$\varepsilon_b = \frac{\varepsilon_1 - \varepsilon_2}{2} \qquad \text{(Eq. 4.4)}$$

where, $\varepsilon_1$ and $\varepsilon_2$ are the values of the strain on the opposite sides of the shaft. Figure 4.4 shows in detail how the bending strains are obtained from the measured strains.

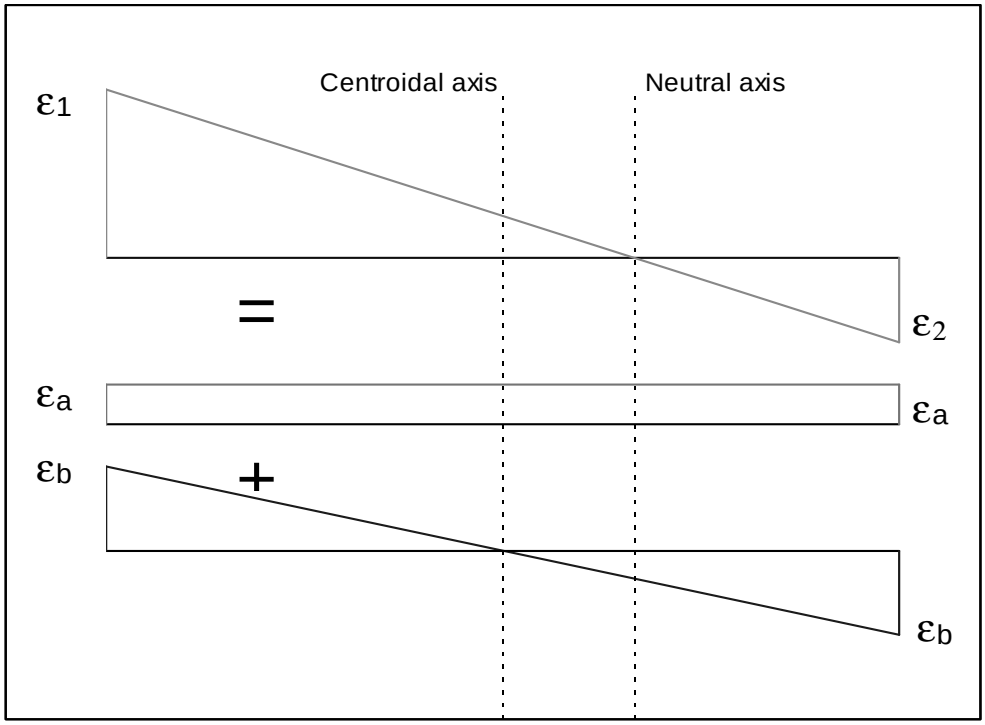


Figure 4.4 Total, axial and bending strains on cross-section.

#### *4.2.2.3 Development of Moment-Curvature relation -*

For small bending strains, the moments can be calculated as follows

$$M = E I \frac{\varepsilon_b}{r} = EI\phi \qquad \text{(Eq. 4.5)}$$

where, E = Young modulus, I = second moment of area, r = shaft's radius and $\phi$ is the curvature of the cross-section given by $\phi = \varepsilon_b/r$.

As identified earlier, the maximum strain for which relationship, Eq. 4.5, applies (i.e., constant EI) is strains up to 130 micro-strains, Figure 4.2. Above that strain level, the stress-strain behavior of concrete is nonlinear (E not constant), and the concrete cracks in tension,

shifting the neutral axis (I not constant). Therefore, a non-linear Moment (M) and curvature ($\phi$) relationship is needed to calculate the bending moment. The relationship still has the form M = B $\phi$, where the curvature, $\phi$, is still given by $\varepsilon/r$, but EI is no longer constant and must be replaced by the variable B. The non-linear M- $\phi$ relation was developed in 3 different ways and compared to ensure the appropriate bending moment diagram along the shaft in order to obtain the P-Y curves.

For a shaft of given cross-section (geometry) and properties (stress-strain, strength, etc.), the relation between moment and curvature may be obtained from a FB-Pier analysis. The FB-pier fiber model considers the nonlinear stress-strain behavior of both concrete and steel and is capable of generating both a moment-curvature as well as biaxial bending diagram for any cross-section. To perform the analysis, a column with a given cross-section is specified. Next, springs of very high stiffness (both in translation and rotation) are applied to the bottom of the shaft with various moments applied to the top of the shaft, Figure 4.5. As the moment is constant along the length of the column, curvature, $\phi$, is also constant and can be calculated as $\phi = \theta/L$, where L is the length of the column, and $\theta$ is rotation of cross-section, Figure 4.5. By changing the applied moment, M, a series of corresponding $\phi$ values or M vs. $\phi$ may be obtained. Figures 4.6 and 4.7 are the M vs. $\phi$ plots for the 6' and 9' prototype shafts used in this research.

To validate the analytical Moment-Curvature relationship, M-$\phi$ (Figures 4.6 and 4.7), model drilled shafts of same cross-section and properties were constructed with several pairs of strain gages, Figure 4.8. Only the bottom portion of the models, which did not contain instrumentation were cast into the rock. A point load was applied to the top of each shaft. From Eqs. 4.4 and 4.5, the Moment-Curvature, M-$\phi$, was computed and plotted in Figures 4.6 and 4.7.

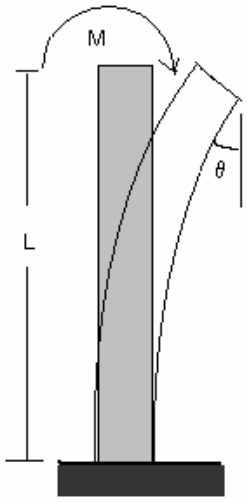


Figure 4.5 FB-Pier column analyses for moment-curvature.

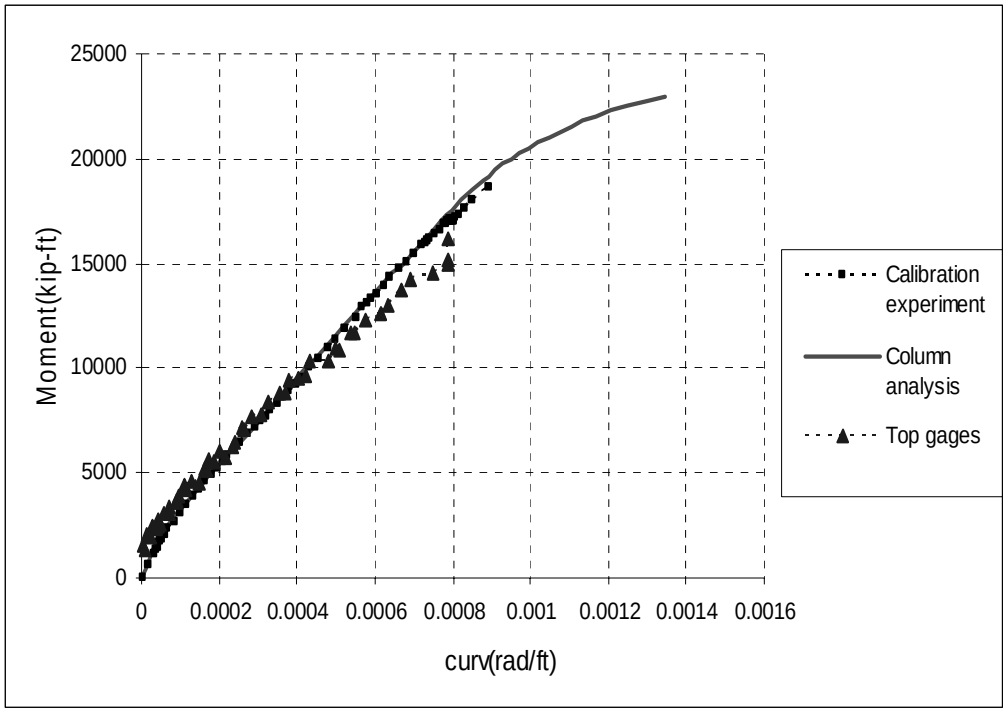


Figure 4.6 Moment-Curvature relationship for 6 ft diameter shaft.

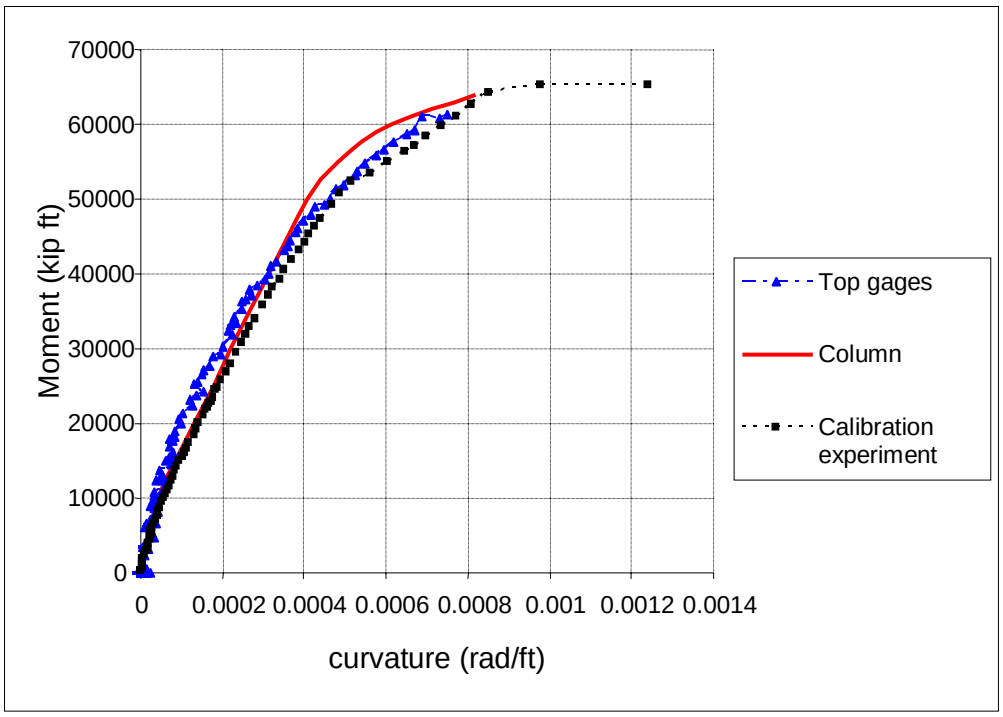


Figure 4.7 Moment-Curvature relationship for 9 ft diameter shaft.

To ensure similar Moment-Curvature relationship, M-ϕ, for each lateral load test, one pair of the 6 pair of strain gages, Figure 4.2, was located above the rock surface. As there was no rock at the top gage level, there was no contribution from skin friction to the moment and the moment was simply equal to the applied load times the distance from top gauges to the load cell. Again, the Moment-Curvature relationship, Figures 4.6 and 4.7, were determined from Eqs. 4.4 and 4.5.

Evident from Figures 4.6 and 4.7, the Moment-Curvature, M-ϕ relationships obtained from all of the experimental methods were close. The latter suggested the shaft reinforcement, instrumentation, and construction process were very repeatable. It was found that the FB-Pier column analysis was very sensitive to the properties of concrete and steel, as well as the location of the steel. The properties of the steel and concrete were varied in the column analysis until a good agreement was found between the M–ϕ plots from all three methods. The same properties will be used subsequently in FB-Pier to verifying the calculated P-Y curves for the rock.

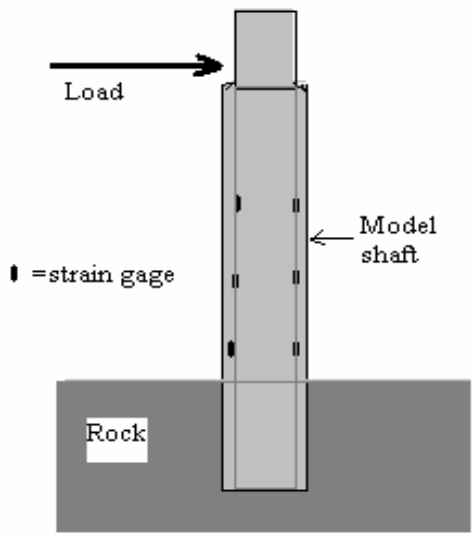


Figure 4.8 Instrumented shaft layout for moment-curvature determination.

#### *4.2.2.4 Fitting trend-lines to Moment–Depth graphs –*

Having established a Moment-Curvature relationships, moments at each strain gage location was determined by first computing bending strains, Eq. 4.4, followed by curvature, Eq. 4.5 which gives moment from Figures 4.6 and 4.7. For each load case, the moment along the shaft was plotted with depth (z), Figure 4.9. Evident from the plot, the moment at the top of shaft (point where load is applied) is zero and increases linearly with depth until the rock surface is reached. The moment below the rock surface increases to a maximum and then diminishes to zero at the tip of the shaft. The location of maximum moment corresponds to zero shear (i.e., shear reversal) and is the point of rotation of the shaft within the rock.

A trend-line was fitted to each M-Z graph. The trend line was required because the back computed P-Y curve is obtained from a second order derivative of the M-Z graph. Several different trend-lines were considered for the moment depth graph but it was decided to use a third order polynomial. Higher order polynomials gave better fits to the experimental data; however their differentiation resulted in very odd looking shear and rock P values. The third order

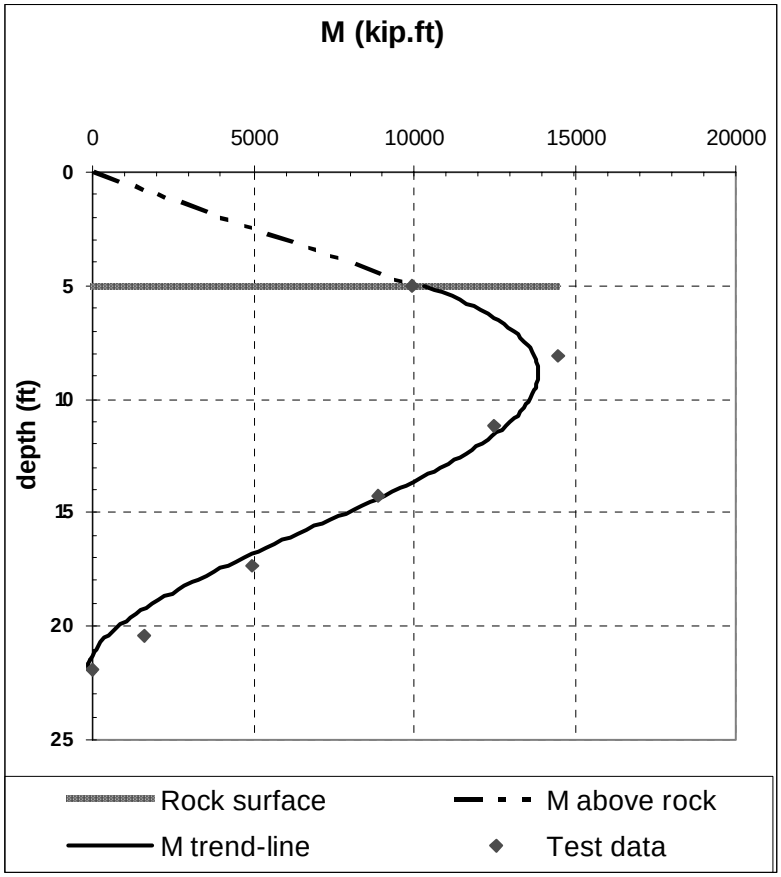

Figure 4.9 Moments vs. depth for a given applied lateral load.

moment distribution gives a quadratic shear distribution and a linear rock resistance (P) with depth. Figures 4.10 and 4.11, respectively, show the distribution of shear force and lateral rock resistance (P) with depth, for the moment distribution presented in Figure 4.9. In addition to satisfying the calculated moments along the length of the shaft, the moment distribution had to satisfy the condition of applied shear at the top and zero shear at the tip. The use of styro-foam at the tip guaranteed a zero shear force at the shaft tip.

### 4.2.3 Rock's Lateral Resistance P(F/L) Form Bending Moments and Skin Friction

The difference in the moment at two different elevations is caused by rock's lateral (P force/length) and axial force (T force/length) resistance at the rock-shaft interface (see Figure 1.2

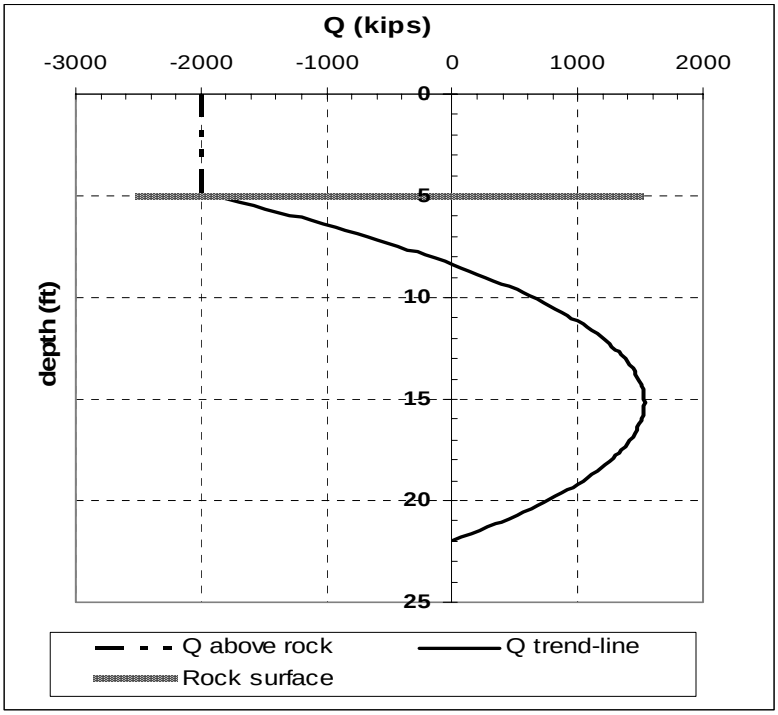


Figure 4.10 Shear force distribution with depth.

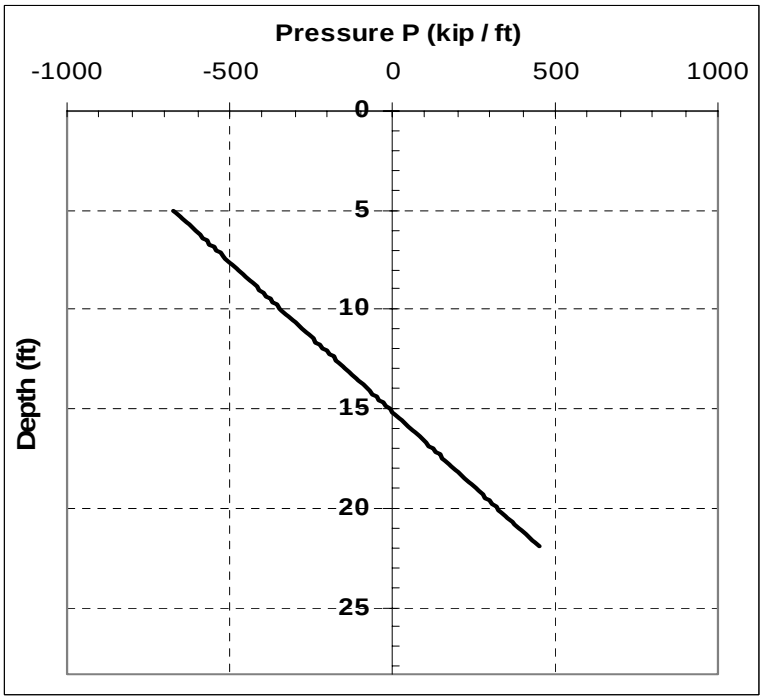


Figure 4.11 Rock resistance, P with depth for given applied lateral load.

Chapter 1). The contribution to moment in the case of the latter is a function of shaft diameter, and the rock's T-Z curve as well as the rotation of the shaft. Current Software (FB-Pier, LPILE, etc.) neglect the contribution of T, Figure 4.12, in the Moment Equilibrium for the resulting Shear, V at a cross-section,

$$V = dM/dz \qquad \text{(Eq. 4.6)}$$

Consequently, from lateral force equilibrium, Figure 4.12, the soil lateral P (force/length) is found as

$$P = dV/dz = d^2 M/dz^2 \qquad \text{(Eq. 4.7)}$$

If the side shear, T (Figure 4.12), is taken into account, then moment equilibrium results in

$$dM/dz = V + TD/\Delta z \qquad \text{(Eq. 4.8)}$$

or

$$dM/dz = V + M_s \qquad \text{(Eq. 4.9)}$$

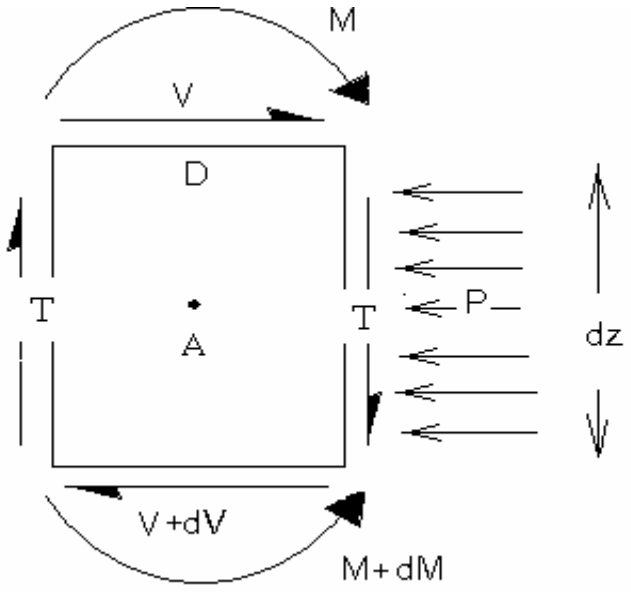


Figure 4.12 Forces acting on a shaft element of length dz.

where, M = moment on cross-section and $M_s$ = moment per unit shaft length from the side shear force, T.

Evoking horizontal force equilibrium,

$$P = dV/dz \qquad \text{(Eq. 4.10)}$$

Substituting Eq. 4.9 into Eq. 4.10, then the rock lateral resistance, P, is obtained:

$$P = d^2M/dz^2 - d(M_s)/dz \qquad \text{(Eq. 4.11)}$$

Evident from Eq. 4.11 vs. Eq. 4.7, the side shear on the shaft will reduce the rock's lateral resistance, P, calculation. The latter suggest that for large diameter drilled shaft field tests in stiff rock, the back computed P-Y curve from Eq. 4.7 may be un-conservative.

The moment/unit length, $M_s$, of the side shear is obtained from the T-Z curve for the rock. The value of T requires the displacement, z, at a point on the shaft. From the strain gage data, the angle of rotation ($\theta$) will be determined and then the axial displacement (z) will be computed using the shafts diameter. Also for the development of the P-Y curve, the lateral displacement, Y, is needed. The latter will be found from the shaft rotation, $\theta$, and the top shaft displacements. The computation of $M_s$ used to find P is undertaken next.

### 4.2.4 Moment Due to Side Shear, $M_s$

Lateral loading causes a rotation of the shaft at any given cross section. The shaft rotation is resisted through skin friction, T, and lateral rock resistance, P, acting on the sides of the shaft. In the case of the unit skin friction, a Moment/length resistance, $M_s$, may be computed at any cross-section. The value of $M_s$ is a function of the unit skin friction at the periphery of the shaft, which varies around the shaft's circumference. To estimate the moment due to side shear ($M_s$), the shaft cross section was divided into slices as shown in Figure 4.13. For this idealiza-

tion, the shaft is loaded in direction AC. All the points to the left of line BD move up while those on the right of BD are assumed to move down. Next, the cross-section of the shaft was cut into 10 slices, Figure 4.13. $R_i$ is the distance from the center of shaft to the center of slice i. For example $R_1$, is the distance from the center of the shaft to the middle of slice 1 (shaded).

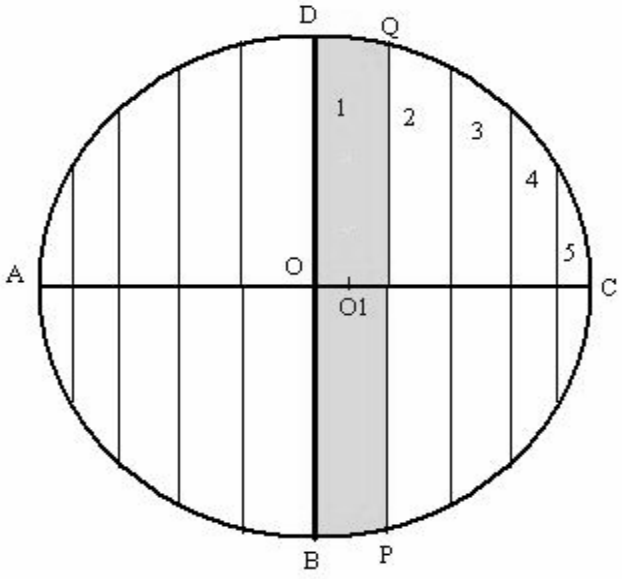


Figure 4.13 Shaft cross-section divided into slices to calculate $M_s$.

Next, the sum of arc lengths BP and DQ is referred to as $C_1$ where subscript 1 refers to slice 1. Note, both arcs are summed together, i.e., BP or DQ, since the shear stress, $\tau$, is assumed constant on both sides of the slice. The value of shear stress, $\tau_i$, is a function of vertical displacement, $z_i$, which is a function of the rotation, $\theta$, and the distance from the center of cross-section to the center of the slice, $R_i$.

If $z_1$ is the average axial displacement of slice 1 and $\tau_1$ (obtained from T-z curve knowing $z_1$) then the side shear force/unit length, $T_1$, acting on slice 1 is given by

$$T_1 = \tau_1.C_1 \qquad \text{(Eq. 4.12)}$$

The moment per unit shaft length about O, $M_{s1}$ , is found by multiplying $T_1$ by the distance to the cross-section centroid, $R_1$, as

$$M_{s1} = T_1.R_1 = \tau_1.C_1.R_1 \qquad \text{(Eq. 4.13)}$$

The total moment per unit length may be found by summing the moments acting on all the slices:

$$M_s = \sum_{1}^{n} \tau_i C_i R_i \qquad \text{(Eq. 4.14)}$$

where n = number of slices.

In the above estimation of $M_s$, it is assumed that the neutral axis (i.e., center of rotation) of the shaft remains at the center of the cross section. Although this assumption is not the case for large strains, the effect of changing the position of neutral axis was found to be small on P estimation. For instance, an analysis of a 9 ft diameter shaft with an applied lateral load of 5000 kips at 7 ft above rock surface with FB-Pier showed a maximum movement of the neutral axis of 10 inches. Subsequent calculation of $M_s$ with the cross-section's center of rotation at the centroid or at the neutral axis made only a 1% difference in the calculation of P (force/length).

The $M_s$ was developed (Eq. 4.14) at every strain gage location along with a trend line with depth. Using Eq. 4.11 with trend lines for both M and $M_s$ , the rock's lateral resistance, P (F/L), was determined as function of applied lateral load.

### 4.2.5 Lateral Deflections, Y for a Given Rock Resistance, P

Having obtained the rock resistance, P, the corresponding lateral displacement, Y, is required to obtain a P-Y curve. The distribution of Y with depth (i.e., the deflected shape of the shaft) was determined as follows.

Figure 4.14 shows the deflected shape of a shaft for a given applied lateral load at the top of the shaft. With depth on the sides of the shaft are pairs of strain gages labeled B to G, Figure

4.14. At the top of the shaft, A (Fig. 4.14) the lateral displacement from LVDT measurement is known. Also at some depth below the rock surface there is point on the shaft which undergoes no lateral displacement, y = 0, Figure 4.14. That is above this point, the shaft is moving in one direction, and below this point, the shaft is moving in the opposite direction. Referred to as the point of zero deflection, y = 0, it corresponds to zero lateral resistance, P, in Figure 4.11, which is known.

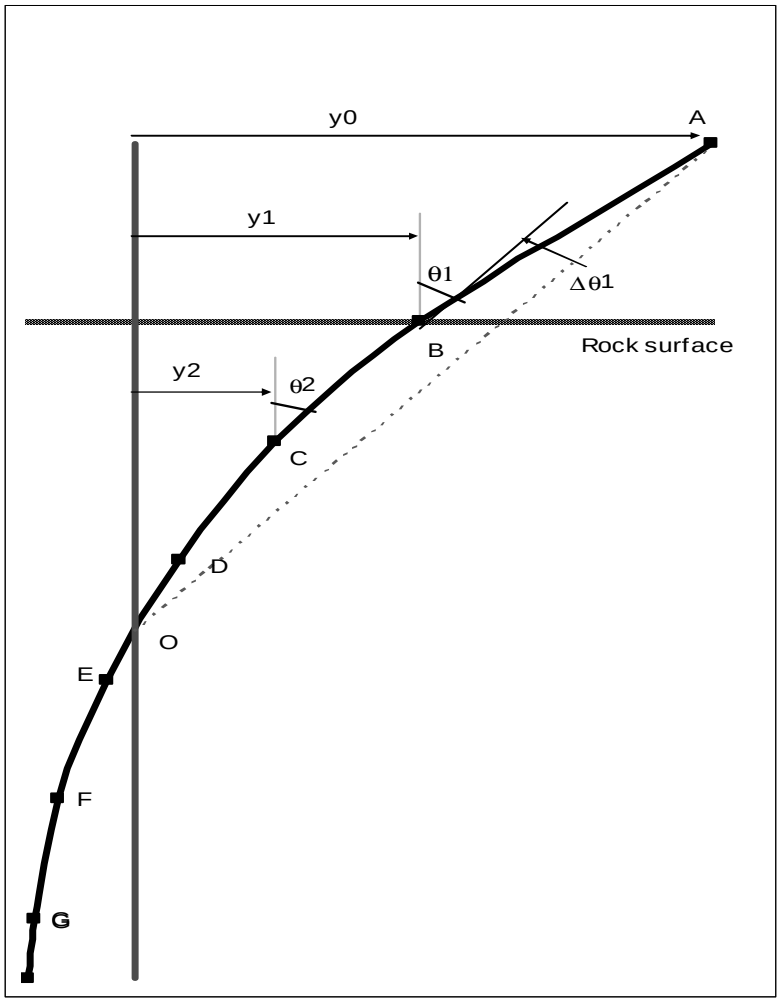


Figure 4.14 Computing deflected shape of the shaft with depth.

Next, from the strains at individual cross-sections B, C, …G, the rotations are found, and the average rotation of segments, BC, CD, … FG ($\Delta\theta_1$ through $\Delta\theta_5$, Fig. 4.14) was determined,

$$\Delta\theta = \frac{\varepsilon_{bt} + \varepsilon_{bb}}{2r} \times L \qquad \text{(Eq. 4.15)}$$

where, $\varepsilon_{bt}$ and $\varepsilon_{bb}$ are the bending strains at the top and the bottom of each segment respectively, r is the shaft radius and L is the segment length. The quantity $\frac{\varepsilon_{bt} + \varepsilon_{bb}}{2r}$ represents the average curvature over a segment and when multiplied by the segment length gives the average change in angle over the segment.

For the lateral displacement calculation, at least one absolute value of θ (i.e., relative to fixed reference) is needed in order to calculate the absolute value of θ at all 6 strain gage positions. Two LVDTs were used to measure lateral displacements at two points above the rock surface. These measured displacements could be used to estimate the angle $\theta_1$ at the rock surface. However, since the difference between these two LVTD readings was small and very sensitive to noise, the lateral deflections calculated from the LVDTs did not always satisfy the condition of zero deflection at P = 0. It was, therefore decided to use only one measured displacement and an iterative method to obtain the lateral deflections. The method used is described:

1) An estimate of shaft rotation at the top strain gage position ($\theta_1$), i.e., rock surface was found by drawing a straight line from point A to the point of zero deflection (O), as shown in Figure 4.14.
2) Using the latter estimate of $\theta_1$, the segment rotations, $\Delta\theta$: Eq. 4.15, the rotations ($\theta_I$) at each point on the shaft, i.e., C to G was calculated (i.e., $\theta_2 = \theta_1 - \Delta\theta_1$, $\theta_3 = \theta_2 - \Delta\theta_2$ and etc.)
3) The computed $\theta_i$ (step 2) at the strain gage positions represent the slopes of the deflected shape at their respective positions ($dy/dz_i = \theta_i$). Hence a smooth line was drawn from point A ($y = y_0$) with slopes at the strain gage positions (B to G) equal to $\theta_i$.

4) Steps 1 to 3 were repeated until the line passed through or was very close to the point O (point of zero deflection and P = 0).

Shown in Figure 4.15 is a typical displacement vs. depth (prototype dimensions) for a shaft using the method described above. The moment, shear and rock lateral pressure are for the same load case as was presented in Figures 4.9 to 4.11.

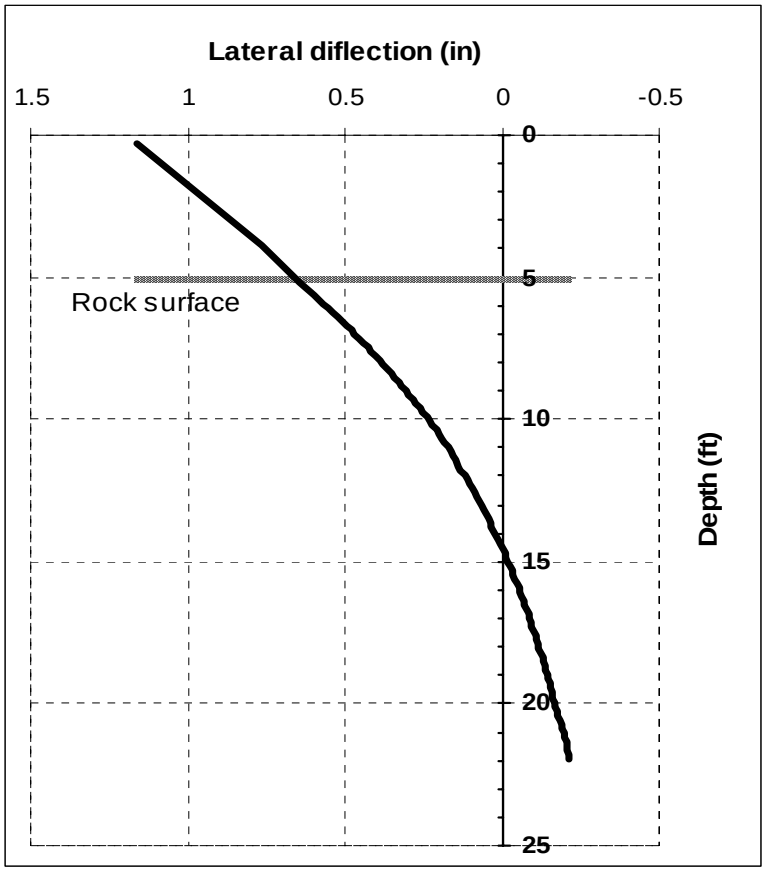


Figure 4.15 Typical lateral deflection (y) vs. depth plot.

# CHAPTER 5

# RESULTS

## 5.1 AXIAL SKIN FRICTION

Axial load tests were conducted on drilled shafts embedded in the rock at 3 different rock strengths: 10 tsf, 20 tsf, and 40 tsf. For the 10 tsf strength rock, the axial load tests were repeated three times (Fig. 5.1), and for the two higher strengths (20 tsf and 40 tsf), the tests were repeated twice (Figs. 5.2 and 5.3). All of the tests were performed on 6' diameter shafts embedded 18' (L/D = 3) into the rock. All of the plots, Figures 5.1 - 5.3 show the load – displacement data which mobilize significant axial resistance with small displacements (i.e., 80% capacities at 0.5% of diameter). Axial load test in lower strength 5 tsf rock, proved unattainable, because the rock mass fractured from the shaft to the boundaries of the bucket.

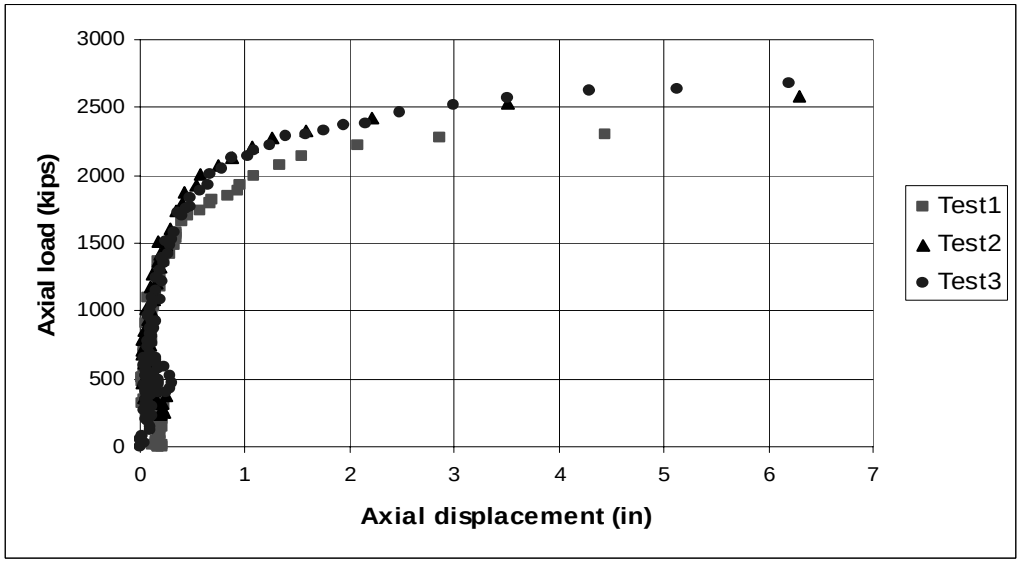


Figure 5.1 Axial load vs. displacement in 10 tsf strength rock.

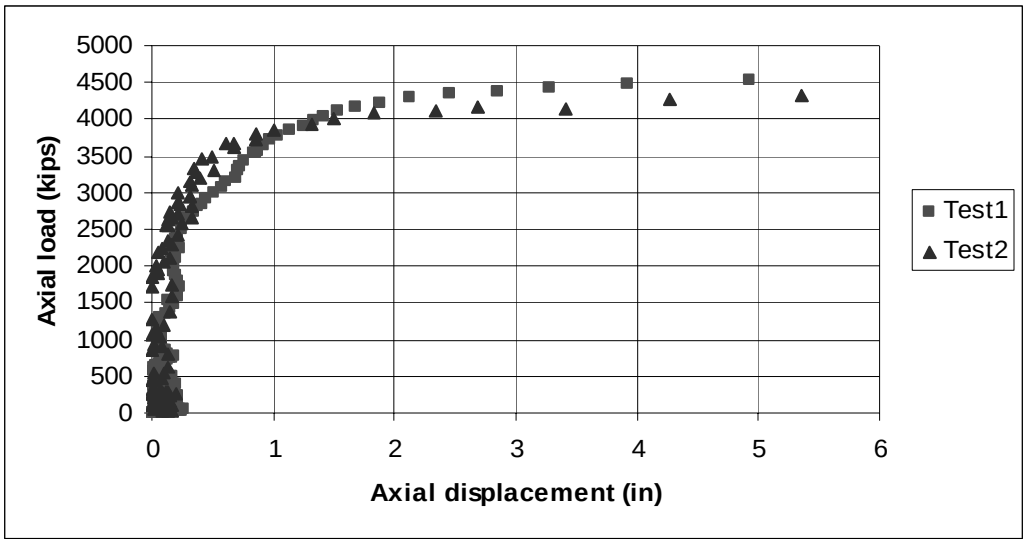


Figure 5.2 Axial load vs. displacement in 20 tsf strength rock.

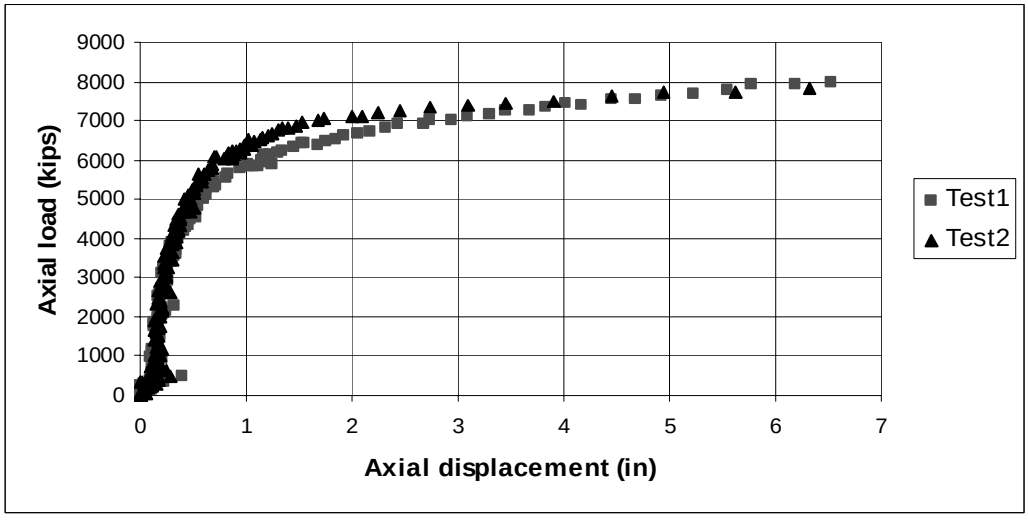


Figure 5.3 Axial load vs. displacement in 40 tsf strength rock.

The load applied at the top of each shaft was subsequently converted into shear stress (skin friction, $f_s$) on the shaft/rock interface by dividing by the shaft area (as described in Chapter 4). Since styro-foam was placed at the shaft tip, the entire load was transferred to the rock through skin friction. Plots of $f_s$ vs. axial displacement (T-z curves) for each strength rock are

shown in Figure 5.4. The data points were obtained by averaging the multiple centrifuge tests for each strength. Also shown in the plot are trend-lines for each rock strength.

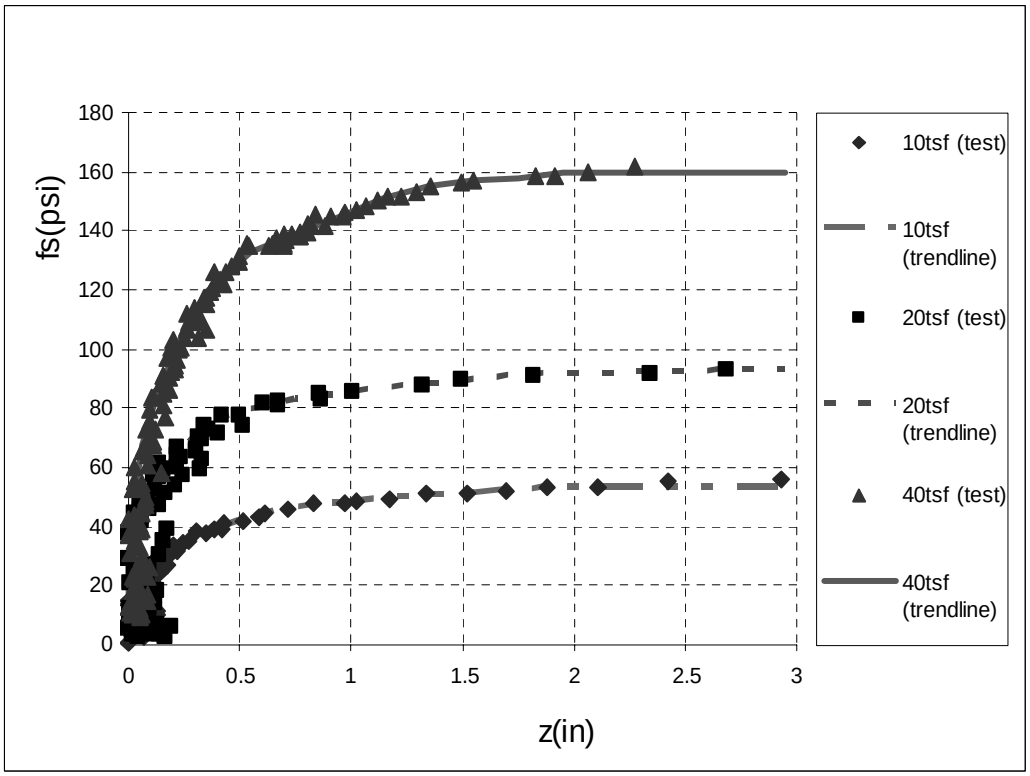


Figure 5.4 T-Z curves for 10, 20 and 40 tsf rocks.

From the T-Z curves, the ultimate unit skin frictions were established from the horizontal tangents. Ultimate unit skin friction of 53 psi, 92 psi and 160 psi, were found for rock strengths of 10 tsf, 20 tsf, and 40 tsf, respectively. Of interest is the comparison of the measured unit skin frictions and those predicted based on FDOT design equation (McVay, 1992)

$$f_s = \frac{1}{2} \bullet \sqrt{q_u \cdot q_t} \qquad \text{(Eq. 5.1)}$$

where $q_u$ and $q_t$ are the unconfined compression and split tensile strengths.

Table 5.1 shows the comparison of the ultimate unit skin friction predicted from Eq. 5.1 with the measured centrifuge values. Evident, from the table, the measured are higher than

Table 5.1 Comparision of measured and predicted ultimate skin friction for synthetic limestone.

| Rock qu (tsf) | Rock qt (tsf) | Ultimate unit skin friction (tsf) | |
|---|---|---|---|
| | | $0.5(qu*qt)^{0.5}$ | Measured |
| 10 | 1.6 | 2.0 | 3.8 |
| 20 | 3.4 | 4.1 | 6.6 |
| 40 | 5.6 | 7.5 | 11.5 |

predicted values from Eq. 5.1. Suggested reasons for their difference are 1) use of synthetic rock vs. Florida Limestone, and 2) method of construction. In the case of the synthetic rock, bentonite slurry was used to separate the shaft concrete from the synthetic rock, which contained cement, which chemically bonded to the shaft. It is postulated that the bentonite coating could have been scrapped off in some zones along the shaft during construction. Further, as identified earlier (Chapter 3), the hole in the synthetic rock for the model construction was always larger (0.03") at the top of the shaft vs. the bottom. The latter through scaling (N=67) is approximately 2" in prototype dimensions. The latter leads to increased horizontal stress and unit side friction on the shaft-rock interface. For computing the P-Y curves, section 5.2, the measured unit skin curves, T-Z were used.

To compute the P-Y curves, T-z curves independent of diameter are required. Shown in Figure 5.5 are the normalized T-Z curves (Fig. 5.4): $f_s$ values were normalized with respect $f_{smax}$ (ultimate unit skin friction) and vertical displacement, Z, was normalized with respect to D (diameter). Evident from the figure, the three normalized curves are quite similar and can be represented by a single curve (shown in bold line), with the following equations:

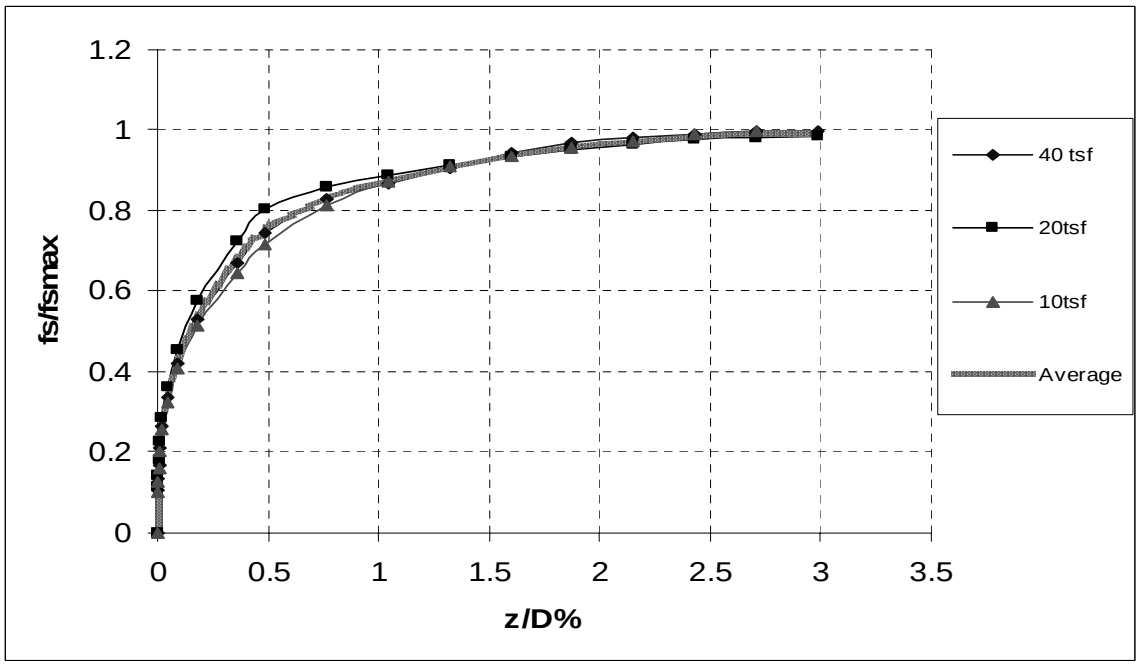

Figure 5.5 Normalized T-Z curves for synthetic rock.

$$\frac{f_s}{f_{s\max}} = 0.96R^{0.33} \qquad 0 \le R \le 0.5 \qquad \text{Eq. 5.2}$$

$$\frac{f_s}{f_{s\max}} = 0.86R^{0.16} \qquad 0.5 \le R \le 3 \qquad \text{Eq. 5.3}$$

$$\frac{f_s}{f_{s\max}} = 1 \qquad 3 \le R \qquad \text{Eq. 5.4}$$

where, R = z/D*100.

Kim (2001) analyzed data from 33 axial load tests (Osterberg) from various bridge sites throughout Florida and recommended the normalized T-Z curve for the natural Florida Limestone given in Figure 5.6. A comparison of Kim's normalized T-Z curve with the synthetic rock curve, Figure 5.5 is also shown in Figure 5.6. Evident from the figure there is a very good agreement between the normalized T-Z behavior of the natural limestone and the synthetic rock. Figure 5.6 will be used in the P-Y curve estimation.

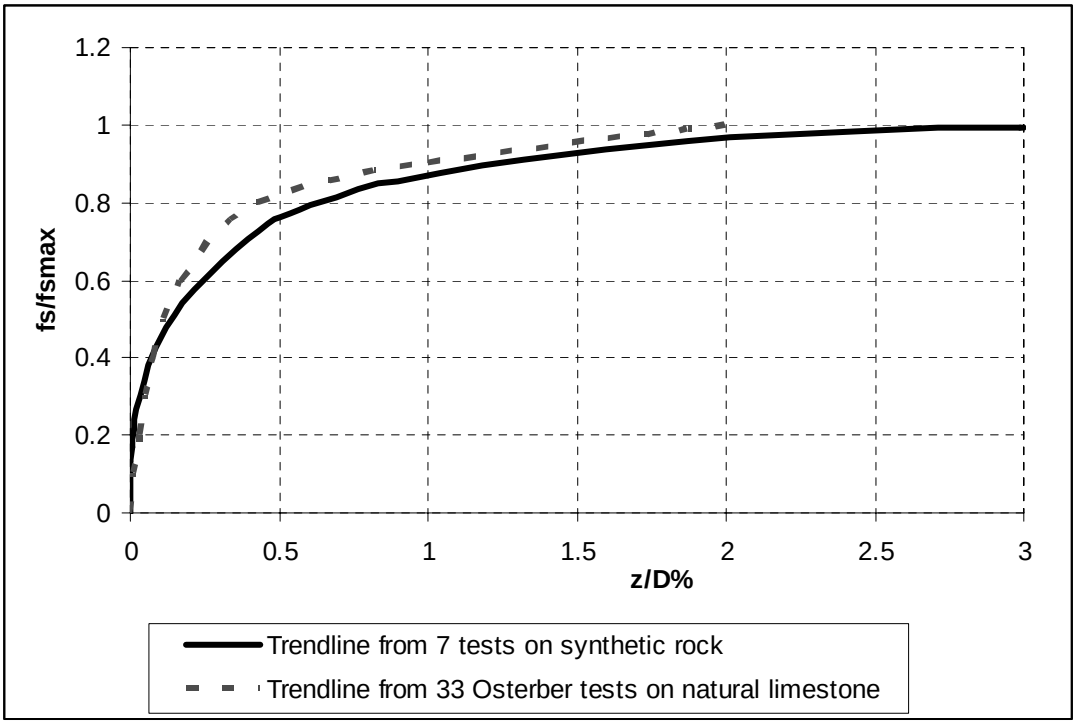

Figure 5.6 Comparison of normalized T-Z curves.

## 5.2 LATERAL P-Y RESISTANCE

The methods and assumptions used in calculating P-Y curves were discussed and presented in Chapter 4. As identified, two types of P-Y curves were back computed: 1) P-Y curves considering unit side shear, Eq. 4.11, and 2) P-Y curves neglecting all side shear on the shafts, Eq. 4.7. All back computed curves were obtained from the 12 lateral load tests performed in the centrifuge with diameters of 6 and 9 ft, embedment (L/D) of 2, 3, and 4 and rock strengths of 10 and 20 tsf. Note each lateral load test gave multiple P-Y curves, which were averaged to obtain a representative curve.

### 5.2.1 Back Computed P-Y Curves Neglecting Side Friction

Figure 5.7(a) shows the typical back computed P-Y curves for a 6 ft diameter shaft embedded in 10 tsf rock. The depth of embedment for this shaft was 18 ft (i.e., L/D ratio of 3).

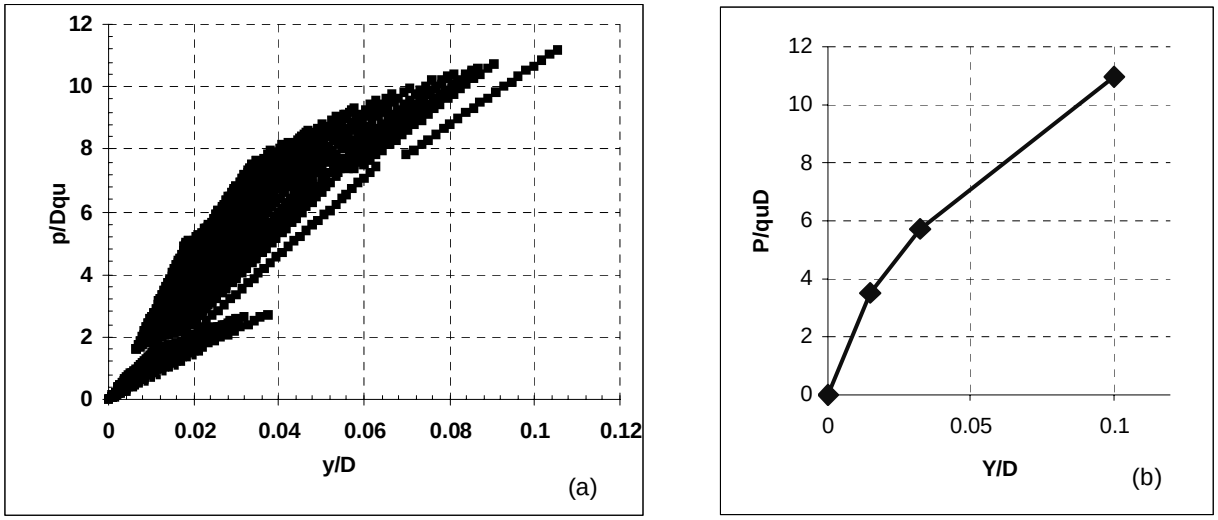


Figure 5.7 (a) P-Y curve calculated from test data, (b) Trend-line for the plot in (a).

The P values have been divided by $q_u D$ (rock compressive strength multiplied by shaft diameter) and the y values by D to make the curves dimensionless. The points that are plotted were calculated for the whole shaft from the rock surface to the shaft tip for each case. As evident in Figure 5.7(a), the points have some scatter with the deeper curves (i.e., not as large p values) being softer than the upper curves (high P values). It is believed the scatter is due to just the third polynomial fit to the moment distribution along the shaft (i.e., linear for P: i.e., secant lines) as well the accuracy of the instrumentation. Consequently, representative trend-line was drawn through the middle of all the points (Figure 5.7(b)).

As part of the P-Y curve development/validation, the curves were inputted to FB-Pier and used to predict the moments, displacements, etc. for each experiment. Note, in addition to the standard P-Y curves such as soft clay model, stiff clay model, FB-Pier has provision for input of custom P-Y curves. It was expected that the back computed P-Y should be able to simulate the results of a centrifuge experiments. The shaft steel and concrete properties used in the modeling were the same as those used to obtain the moment curvature relations for calculating moments

from strain data, i.e., Chapter 4. The resulting deflections of the shaft were compared with the actual deflections obtained from test for different load cases. Figure 5.8 shows the comparison of deflections for the shaft described above, at four different lateral load cases. Evident from the figure, the agreement in displacement was poor at small loads, but gave quite similar response at high loads. In particular, the back computed P-Y curves were too soft initially. The latter could be a result of the accuracy of the approach to estimate the lateral displacement, Y, of the shaft, section 4.2.5 at small lateral displacements.

Consequently, it was decided to adjust the P-Y curves in Figure 5.7b to better fit the measured centrifuge results with FB-Pier. This was done by altering the initial shape of the P-Y curves until FB-Pier gave a good match of deflections. The resulting P-Y curve is given in Figure 5.9 along with the original curve for comparison. The predicted and measured deflections of the shaft under various lateral loading are given in Figure 5.10. The same four load cases of Figure 5.8 were used. Evident from the plots, the agreements between measured and predicted deflections under various loads are excellent. Note, only the initial portion of the P-Y curve was adjusted. Figure 5.11 presents the back computed P-Y curves for the 6' and 9' diameter shafts embedded in the 10 tsf and 20 tsf strength (qu) rock. Evident from the figure, the curves are a function of rock strength.

### 5.2.2 Comparison of Measured and Published P-Y Curves Neglecting Side Friction

Reese and Nyman performed lateral load tests in 1978 on instrumented drilled shafts cast in vuggy limestone in the Florida Keys and developed the P-Y curve of Figure 5-12. The shafts were 4' in diameter, 44' long, with 12' of soil overburden. The rock had an unconfined compressive strength of 15 tsf. Unfortunately, the tests were conducted only to a lateral load of 75 tons, which resulted in a lateral displacement of 0.0213" at the top of the rock. In addition, the

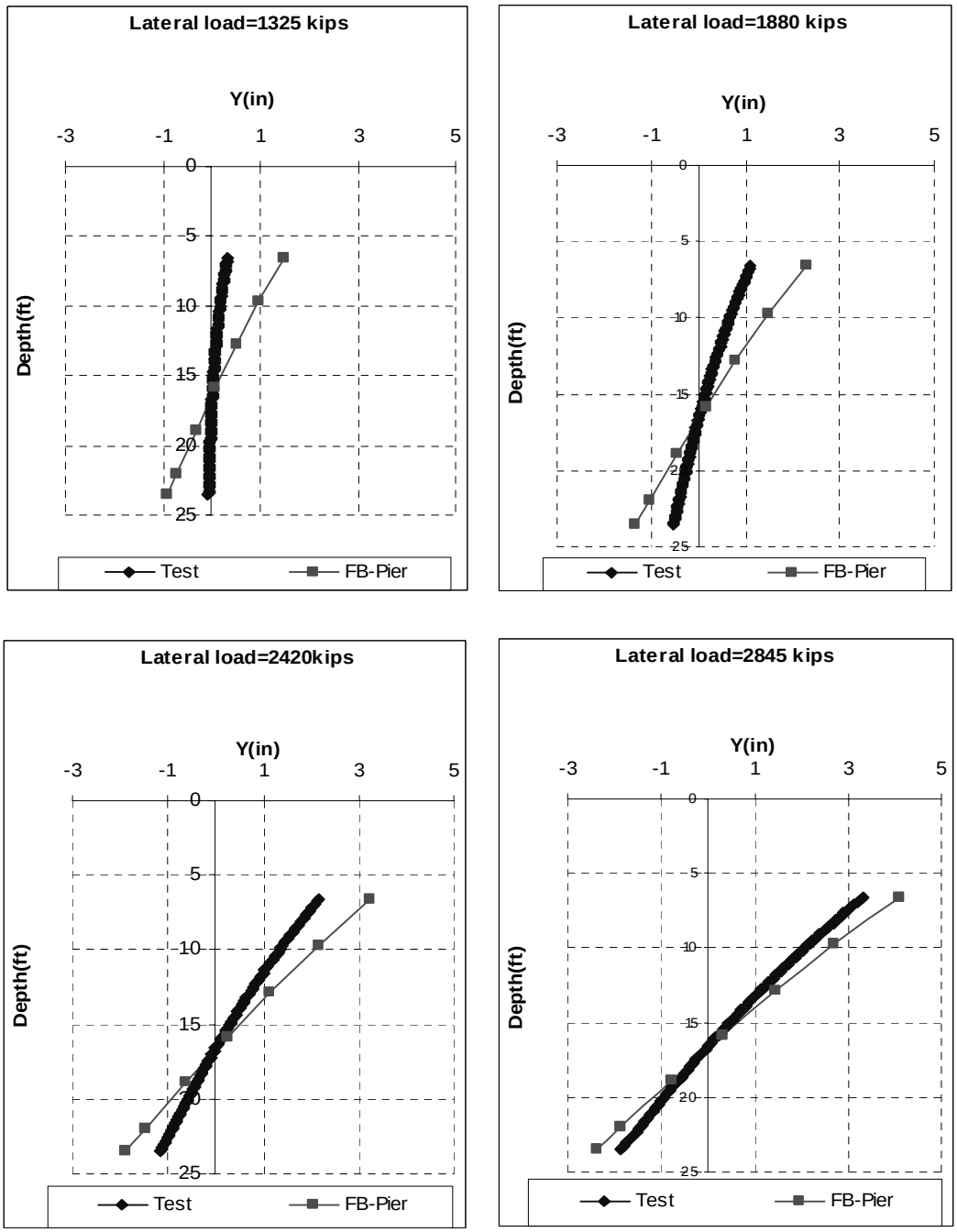


Figure 5.8 Comparison of deflections (Test vs. FB-Pier modeling) for 4 load cases.

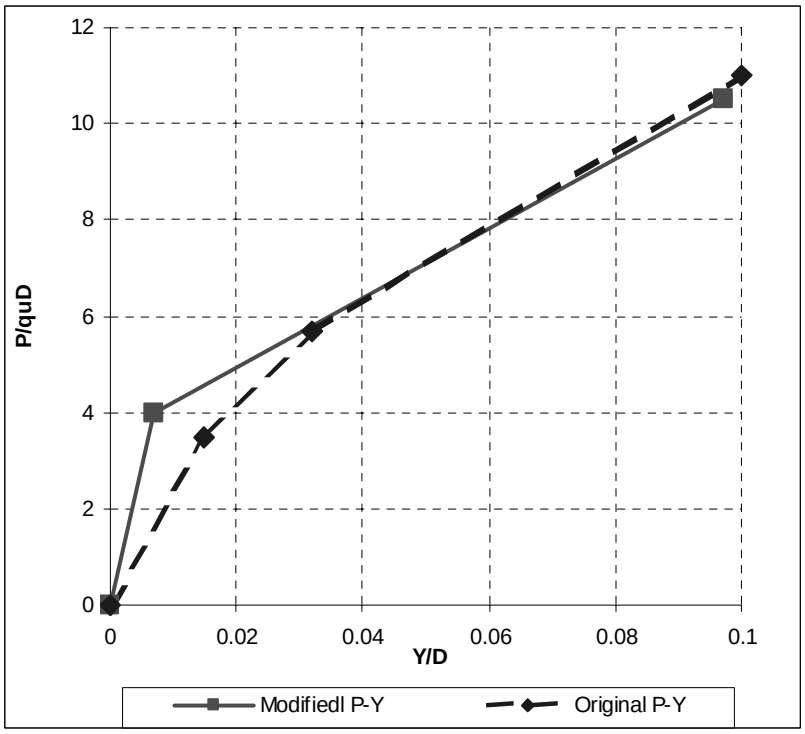

Figure 5.9 Modified and original P-Y curves, without shaft side shear.

shafts were modeled as linear elastic material (i.e., constant M-θ). Figure 5-11 shows the Reese and Nyman predicted P-Y behavior, which terminates well before the measured curve goes nonlinear.

Due to a lack of published P-Y representation for Florida Limestone, a number of consultants have employed either the soft or stiff clay models with the rocks' strength characteristics (i.e., qu and qt). A discussion of each follows along with a comparison with the measured response.

The soft clay model is one of the standard P-Y curves used in FB-Pier to model lateral behavior piles/drilled shafts. The soft clay model, developed by Matlock (1970) uses the following equation to calculate the points on the P-Y curve:

$$\frac{P}{P_u} = 0.5\left(\frac{y}{y_{50}}\right)^{0.33} \qquad \text{for} \quad 0 \le y \le 8y_{50} \qquad \text{(Eq. 5.5)}$$

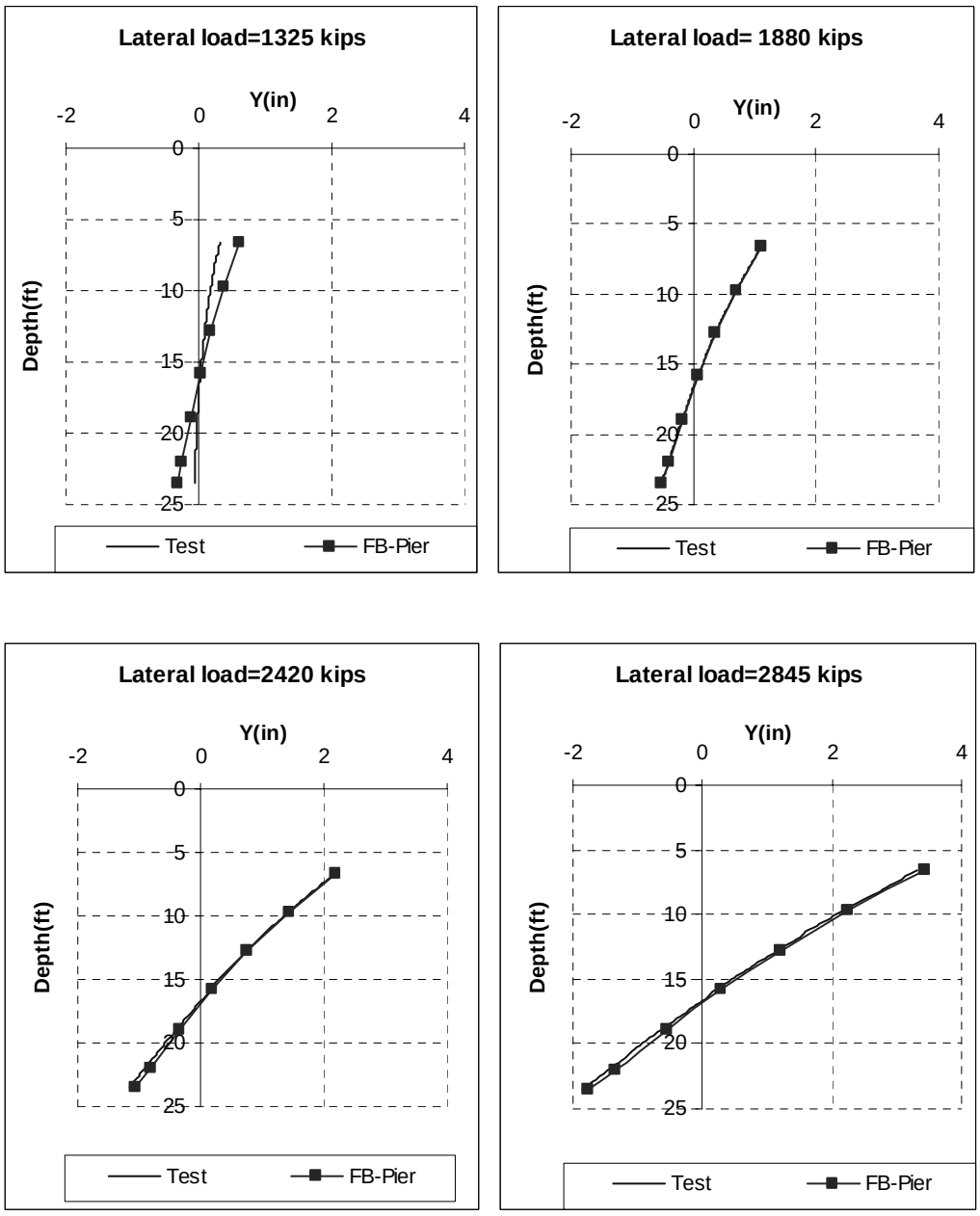


Figure 5.10 Measured and predicted lateral deflections of shafts under load.

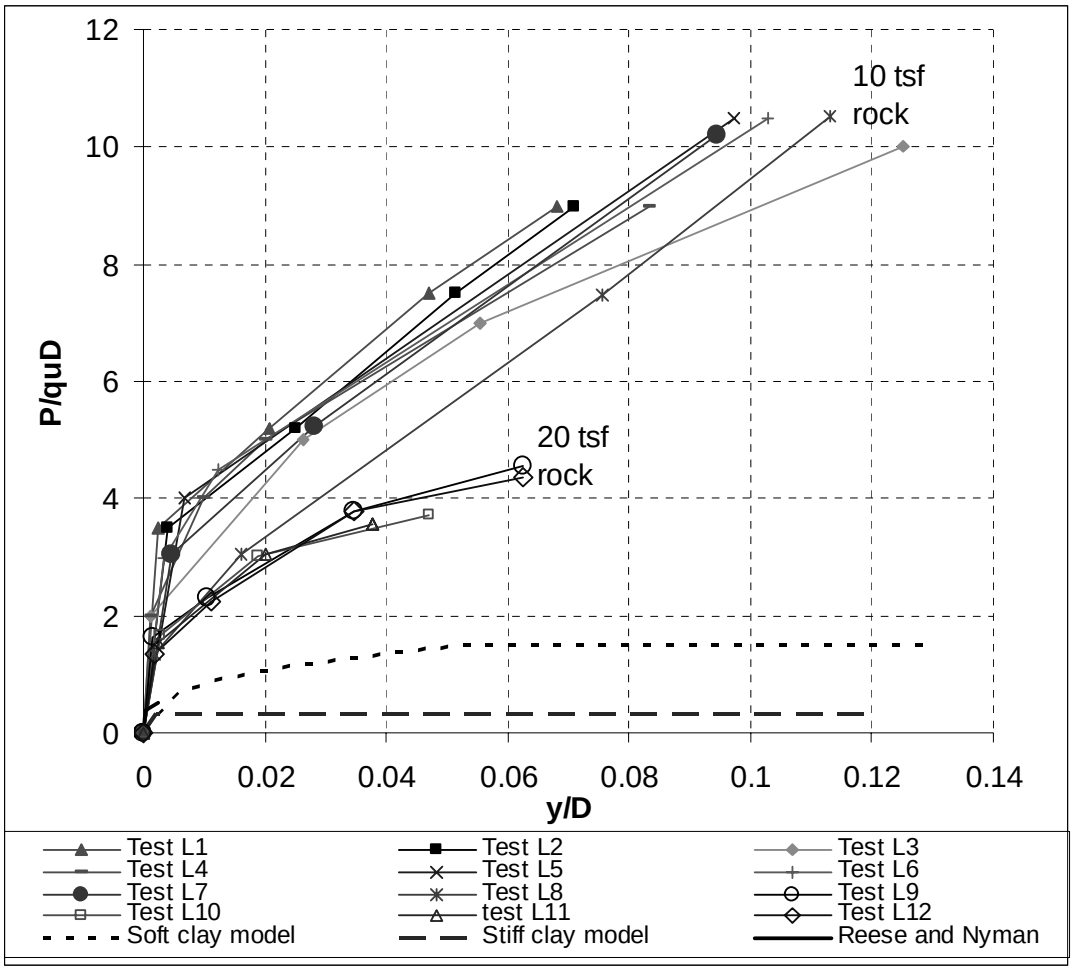


Figure 5.11 Measured and predicted P-Y curves without side shear.

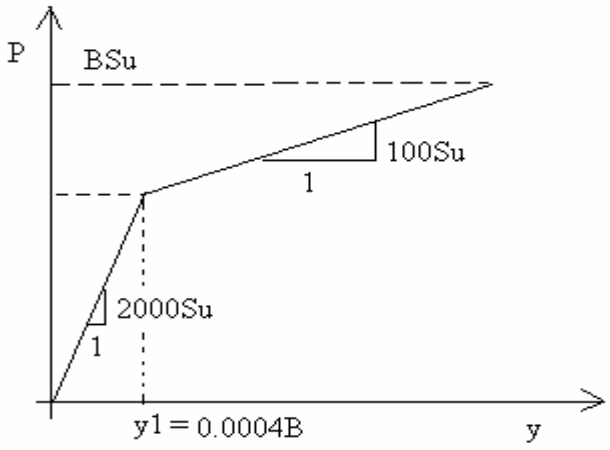


Figure 5.12 P-Y curve for limestone, Reese and Nyman, 1978.

$$\frac{P}{P_u} = 1 \qquad \text{for} \quad y > 8y_{50} \qquad \text{(Eq. 5.6)}$$

Where, $P_u$ = ultimate soil resistance per unit pile/shaft length and is equal to the smaller of the values given by Equations 5.7 and 5.8.

$$P_u = \left(3 + \frac{\gamma'}{C}H + \frac{J}{D}H\right) C\,D \qquad \text{(Eq. 5.7)}$$

$$P_u = 9\,CD \qquad \text{(Eq. 5.8)}$$

and $\gamma'$ = average effective unit weight of soil from ground surface to P-Y curve,

H = depth from ground surface to P-Y curve,

C = shear strength of rock at depth H,

D = pile/shaft width (diameter if circular)

J = 0.25 for stiff clay/rock (found by Matlock, 1970 experimentally).

The Pile/shaft displacement at one half the ultimate resistance ($y_{50}$) is given as

$$y_{50} = 2.5\varepsilon_{50}\,D \qquad \text{(Eq. 5.9)}$$

where, $\varepsilon_{50}$ = strain at half the maximum principal stress difference.

The method of computing P-Y curve for stiff clay was developed by Welch and Reese (1972). The lateral resistance, P, as a function of lateral displacement is

$$\frac{P}{P_u} = 0.5\left(\frac{y}{y_{50}}\right)^{0.25} \qquad \text{for} \quad 0 \le y \le 16y_{50} \qquad \text{(Eq. 5.10)}$$

$$\frac{P}{P_u} = 1 \qquad \text{for} \quad y > 16y_{50} \qquad \text{(Eq. 5.11)}$$

where $P_u$ and $y_{50}$ are given by Equations 5.7, 5.8 and 5.9, respectively.

Figure 5.11 shows both the stiff and soft clay models' predicted P-Y curve using the measured rock strength. Evident both models under predict the Florida Limestone's lateral resistance.

### 5.2.3 Back Computed P-Y Curves Corrected for Side Friction

The process of obtaining P-Y curves from moment data corrected for shaft side friction is described in Chapter 4. Shown in Figure 5.13 is a typical back computed P-Y curve (original) for a 6' diameter, 18' embedded shaft in 10tsf strength rock. The back computed P-Y curve was then used in FB-Pier to predict the experimental results. However, since the current version of FB-Pier does not employ rotational springs representing the shaft's side shear, a moment equal to the side shear (see Equation 4.13, Chapter 4) over the shaft element (section of shaft between strain gages) was inputted. Note, the moment applied along the length of the shaft at the end nodes of each element was varied for each load case. Figure 5.14 shows the lateral displacements along the shaft for various applied lateral loads. Evident, from the figure, the predicted

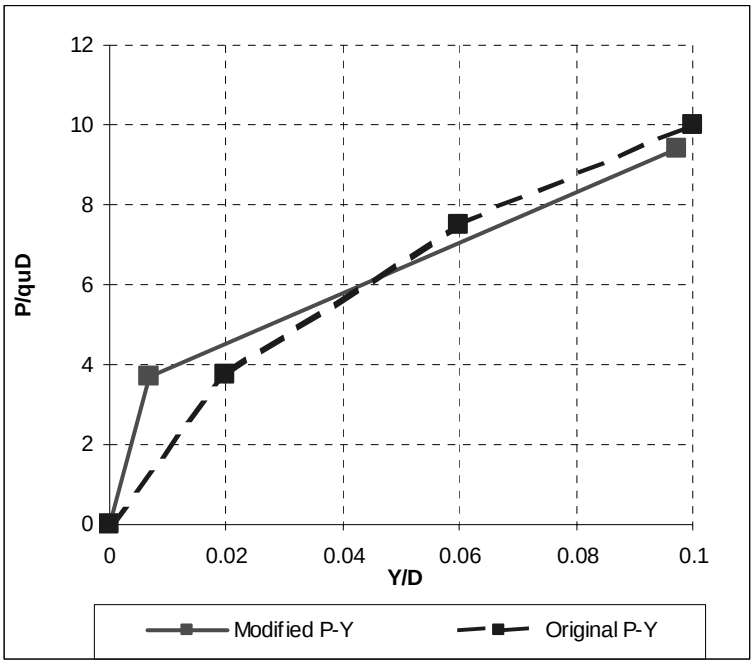


Figure 5.13 Modified and original P-Y curves, with shaft side shear.

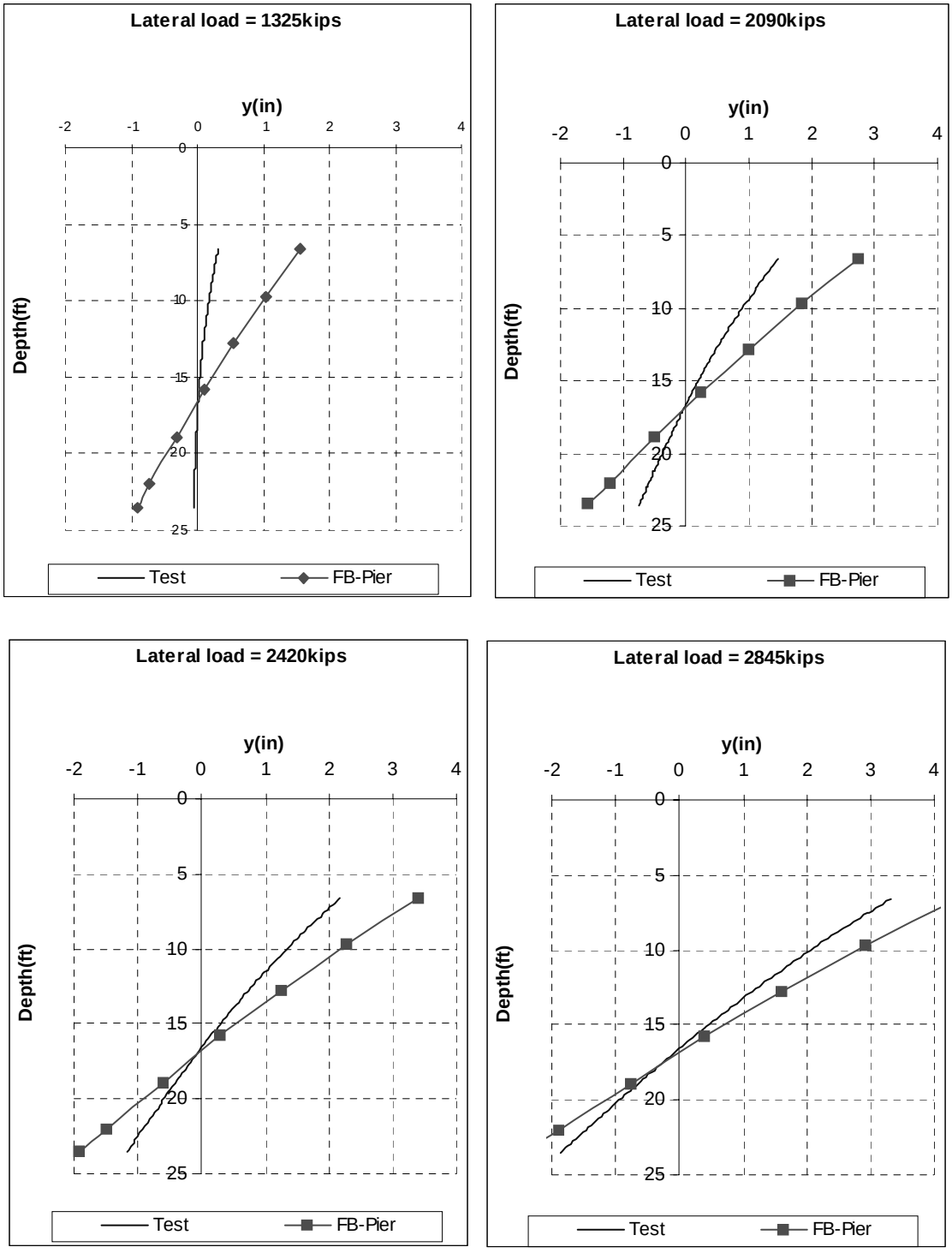


Figure 5.14 Measured and predicted lateral deflections of 6’ diameter shaft.

displacements are too large for small lateral loads and agree well at the higher loads. Consequently the back computed P-Y curve Figure 5.13, was stiffened until better agreement for lower lateral loads (Fig. 5.15) were attained.

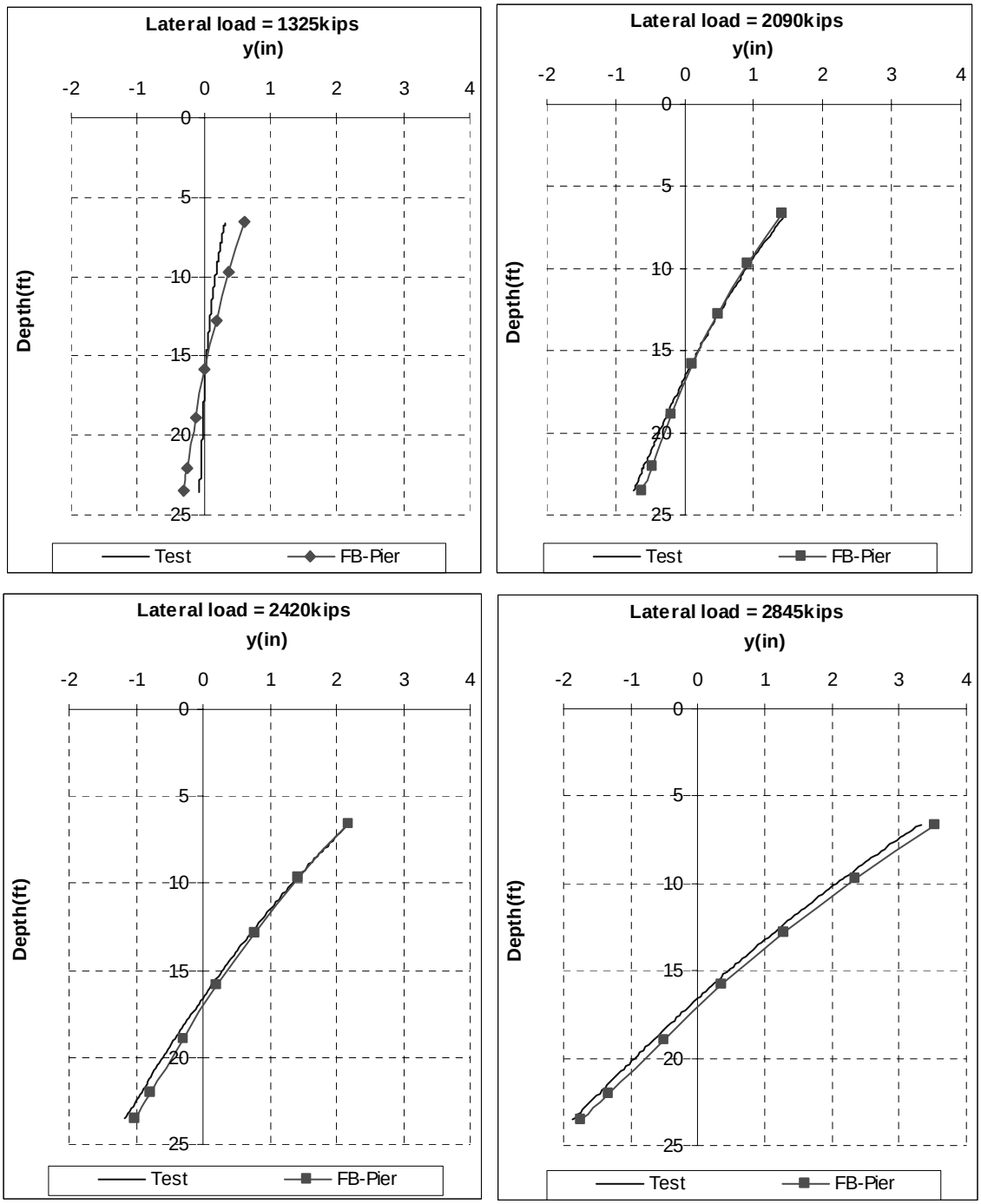


Figure 5.15 Measured and predicted (modified P-Y) lateral deflections of 6' diameter shaft.

A comparison of the adjusted P-Y curves which either ignore, Figure 5.9, or consider unit side shear, Figure 5.13, reveal a reduction in P-Y resistance with side shear for the same strength rock (10 tsf). The latter is expected, since a portion of the shaft's lateral resistance, Figure 5.13 is being carried by unit side shear.

Presented in Figure 5.16 are back-adjusted P-Y curves for all twelve-centrifuge tests with side shear considerations; i.e., two shaft diameters (6' and 9'), three embedment lengths (L/D = 2, 3, and 4) and two rock strengths (10 tsf and 20 tsf). Also shown in the figure are the predicted

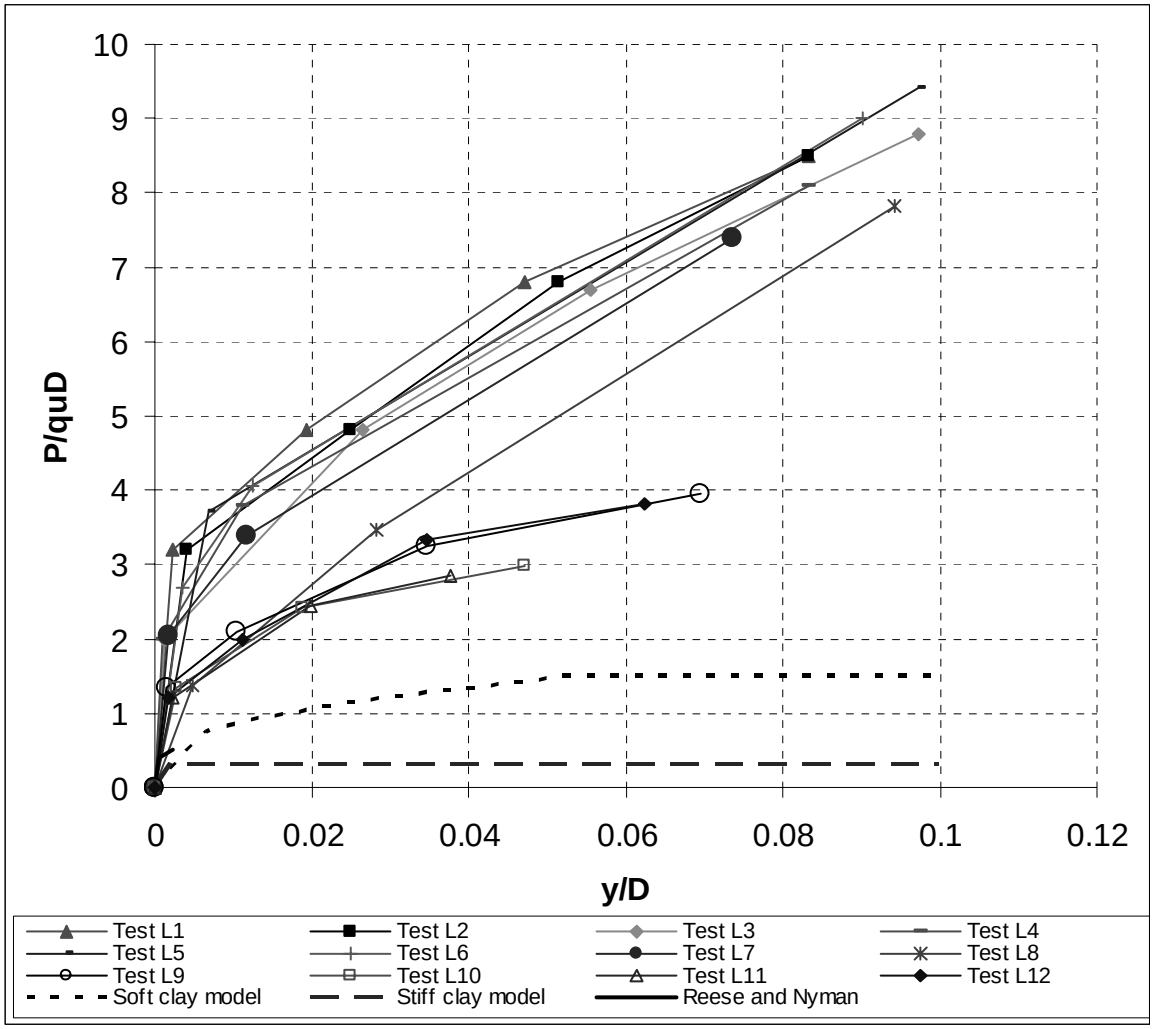


Figure 5.16 P-Y curves from 12 lateral tests corrected for side shear.

P-Y curves for soft and stiff clay models. Evident from the figure, even though the lateral resistance is normalized with rock strength and diameter, there is quite a bit of variability in the P-Y curves. Consequently, an attempt to normalize the P-Y curves was undertaken.

### 5.2.4 Normalized P-Y Curves

It is common practice to normalize P-Y curves with $q_u D$ and D as was done for both the inclusion and exclusion of side friction (Figures 5.11 and 5.16). However, the computed P-Y curves for rock still exhibit significant variability as a function of rock strengths and shaft diameters. Hence, better normalizing functions were needed for both curves, Figures 5.11 and 5.16. After a number of trials, it was found that, the un-corrected, Figure 5.11, and the corrected curves, Figure 5.16, could be represented by a single trend-line if the P values are normalized with $q_u^{0.25} D^{0.9}$ and $q_u^{0.15} D^{0.75}$, respectively. Figures 5.17 and 5.18 present the normalized P-Y curves for Florida Limestone with the inclusion or exclusion of shaft side friction. Note the curves are valid for all the experimental results (i.e., 6' and 9' diameter shafts, different rock strengths, etc.). Note however, the P-Y curves are unit dependent. That is, the rock unconfined compressive strength ($q_u$), the shaft diameter and rock's lateral resistance, P must be in ksf, feet and kips/ft, respectively.

### 5.2.5 Influence of Rock Strength, and Shaft Diameter on P-Y Curves

For this research, the P-Y curves were found from shafts with 6 ft and 9 ft diameters and rock strengths of 20 and 40 ksf. However, with trend-lines given in Figures 5.17 and 5.18, P-Y curves may be reconstructed for any shaft diameter and rock strength representing field conditions. For example, the graphs in Figure 5.19 show P- Y curves reconstructed for 3 ft, 6 ft, 9 ft and 12 ft diameter drilled shafts embedded in 80 ksf rock. The latter diameters are typical in many Florida drilled shaft design/construction projects. Figure 5.20 presents the reconstructed

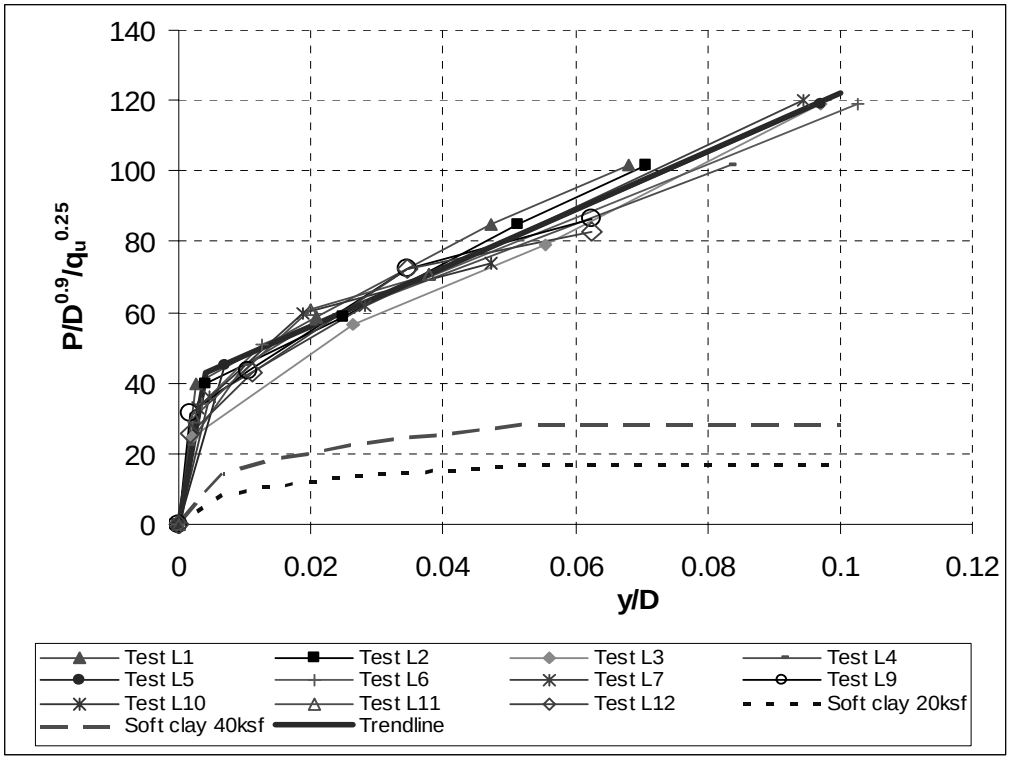


Figure 5.17 Normalized P-Y curves without side shear correction.

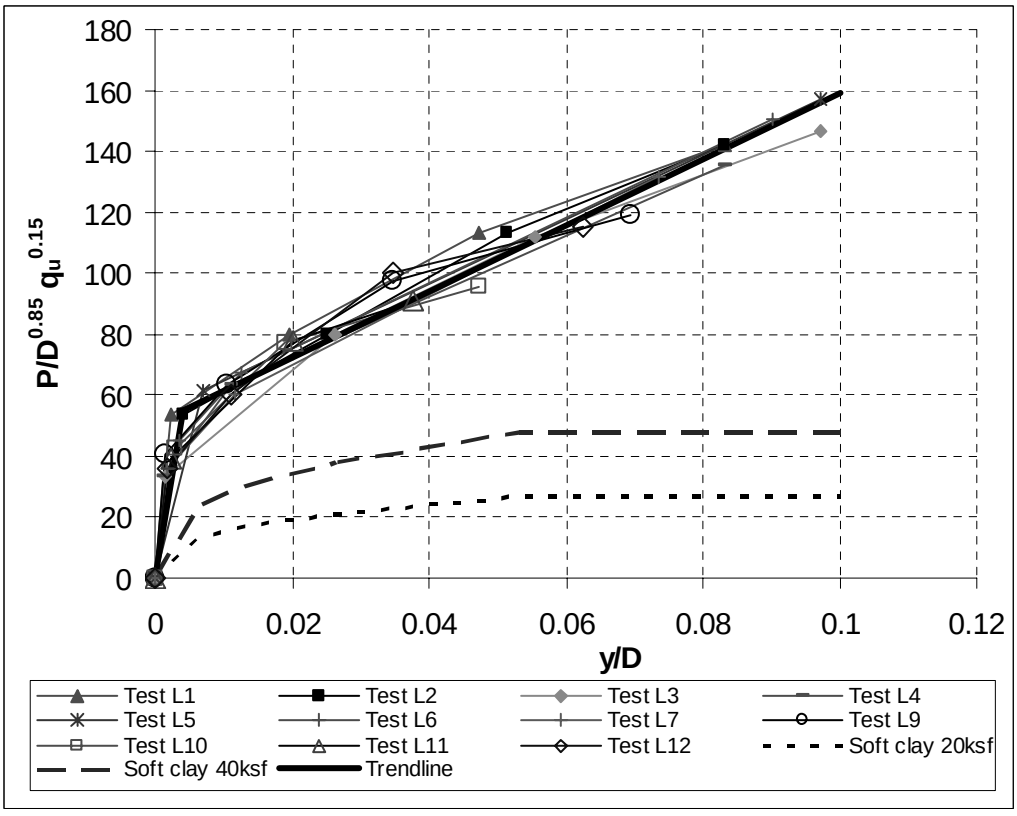


Figure 5.18 Normalized P-Y curves corrected for side shear.

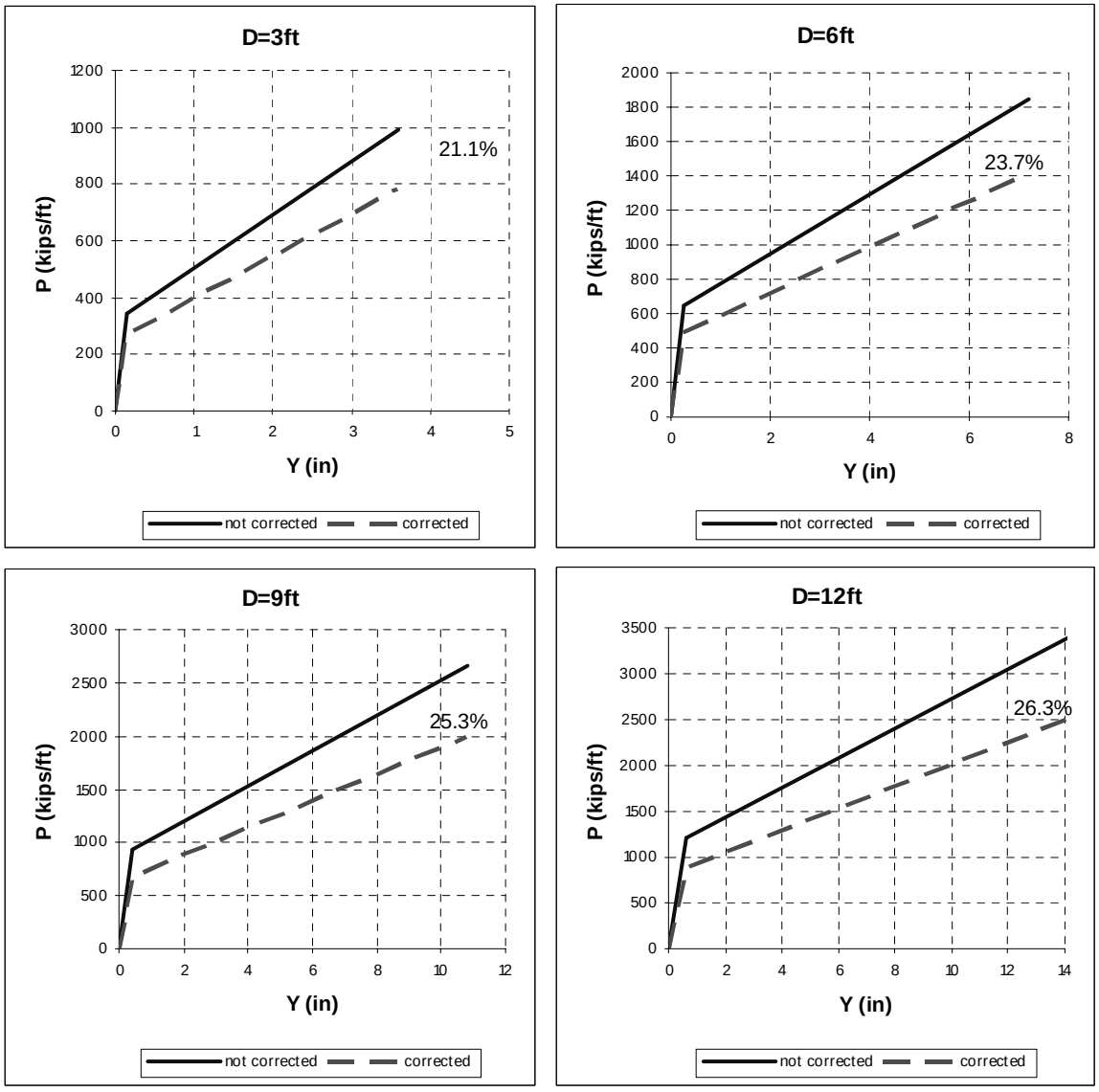


Figure 5.19 Reconstructed P-Y curves for 80 ksf rock.

P-Y curves for a 6 ft diameter shaft embedded in 10, 20, 40 and 80 ksf rock. In both figures, the percentage difference (as percentage of the uncorrected value) between corrected (considers side shear) and uncorrected (neglects side shear) P values are also shown along with the curves. In Figure 5.20, the P-Y curves obtained from the centrifuge tests are plotted for 20 and 40 ksf rock for comparison.

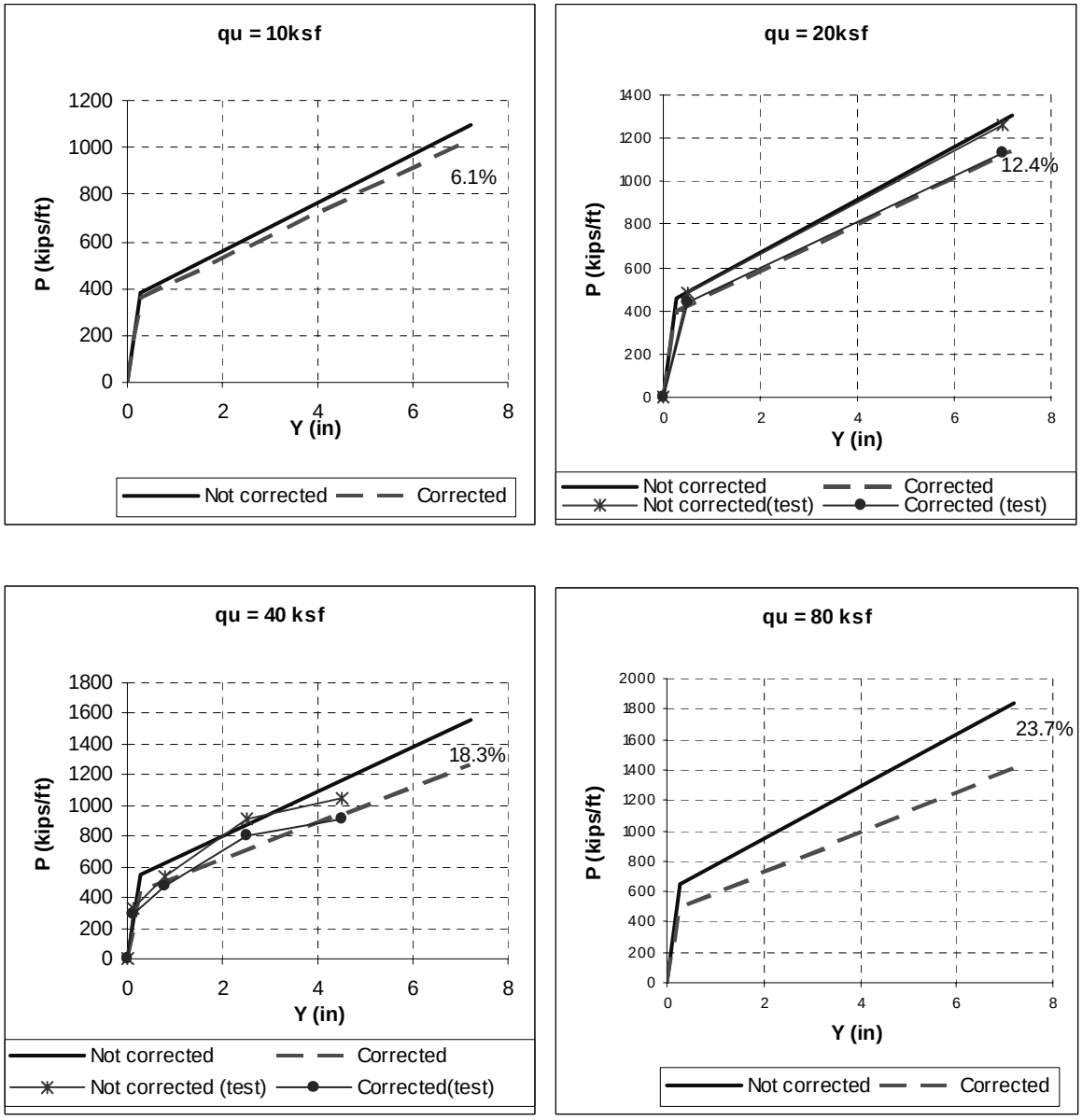


Figure 5.20 Reconstructed P-Y curves of a 6 ft diameter shaft in various strength rock.

It is evident from Figures 5.19 and 5.20 that the reduction in P due to side shear is more dependent on rock strength than on shaft diameter. Increasing the diameter from 3 to 12 ft results in 5% reduction in the P-Y curve, whereas, increasing the rock strength from 20 to 80 ksf reduced the P-Y curve by 12%.

### 5.2.6 Recommended Moment-Rotation Springs for FB-Pier

In the new FB-pier code, it is proposed to model the moment due to axial side shear by rotational springs (M-θ) at the pile/shaft nodes in addition to the existing P-Y and T-Z springs. The process of obtaining P-Y curves involved the calculation of the angle of rotation (θ) and the moment (Ms) per unit shaft length at strain-gage elevations. A plot of Ms against θ is a M-θ curve. M-θ curves for both the 6' and 9' diameter shafts embedded in the 10 tsf and 20 tsf rock are shown in Figures 5.21 and 5.22.

In Figure 5.23 all M-θ curves have been normalized with the maximum available moment ($M_{smax}$), which is related to the ultimate skin friction ($f_{su}$) of rock and the shaft diameter (D). Curves representing all the tests (2 diameters and 2 rock strengths) are plotted and a single curve (trend-line) is drawn, which can be expressed by the following equations:

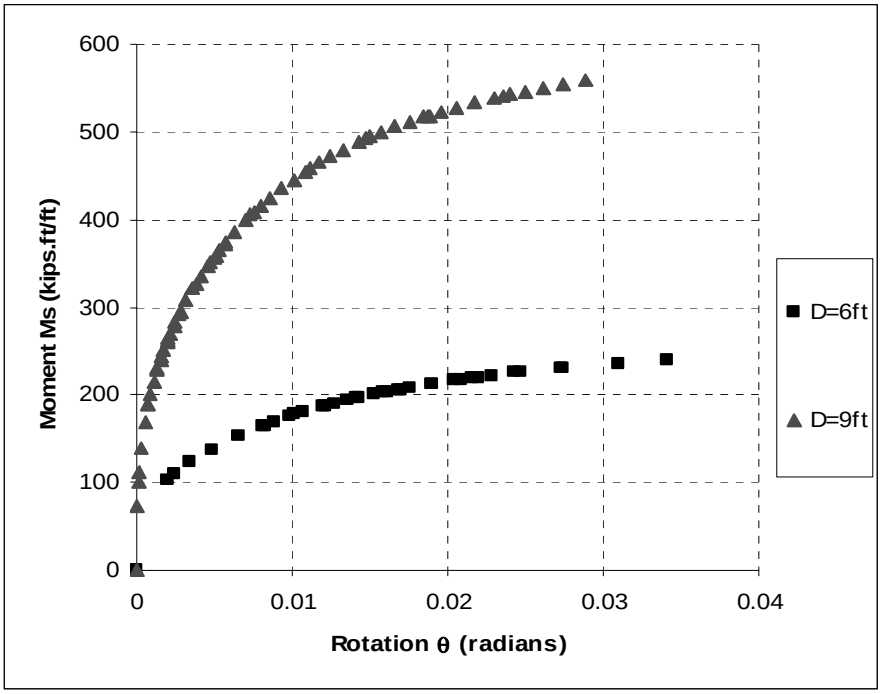


Figure 5.21 Moment from shaft side shear vs. rotation for 10 tsf rock.

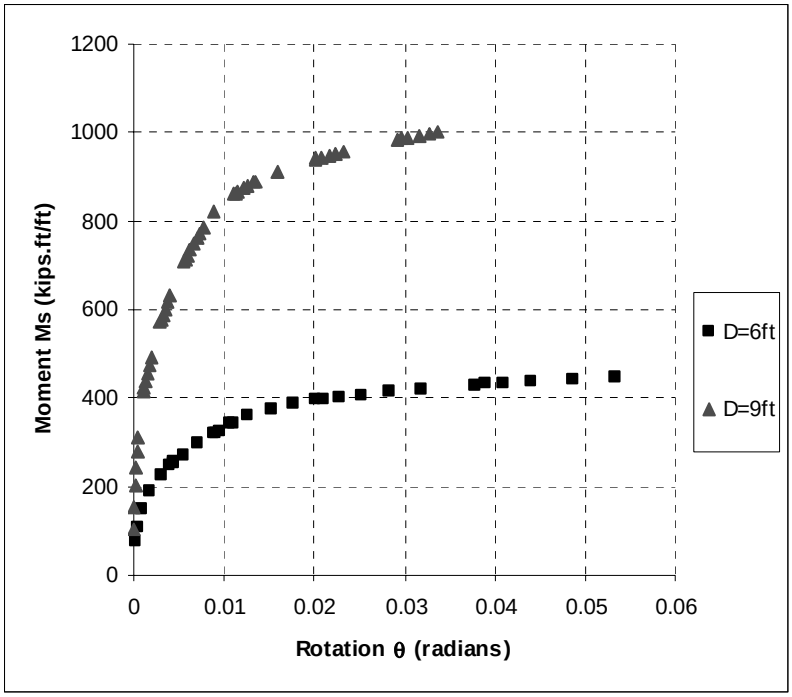


Figure 5.22 Moment from shaft side shear vs. rotation for 20 tsf rock.

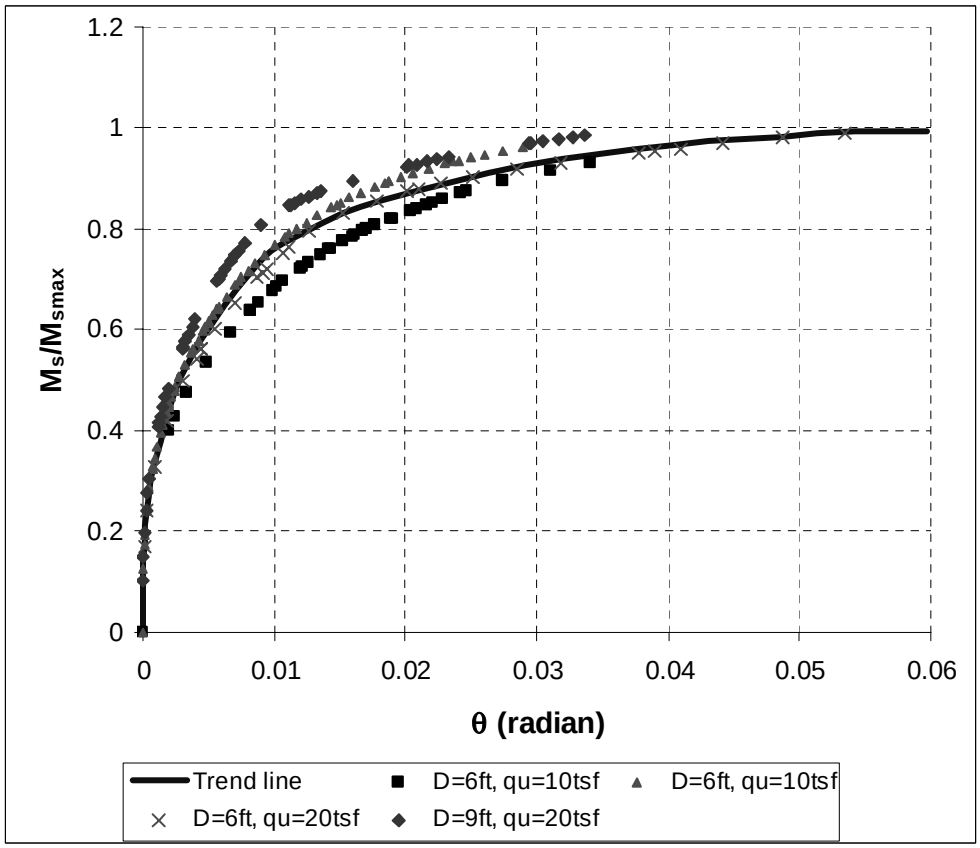


Figure 5.23 Normalized moment (Ms)–rotation (θ) curve.

$$\frac{M_s}{M_{smax}} = 3.49\,\theta^{0.33} \qquad 0 \leq \theta \leq 0.01 \text{ rad} \qquad \text{(Eq. 5.12)}$$

$$\frac{M_s}{M_{smax}} = 1.61\,\theta^{0.16} \qquad 0.01 \leq \theta \leq 0.06 \text{ rad} \qquad \text{(Eq. 5.13)}$$

$$M_{smax} = \frac{f_{su}\,\pi D^2}{3.35} \qquad \text{(Eq. 5.14)}$$

***Note: Figures 5.21 and 5.22 are for no applied axial forces on the shaft. They may be used in combination with Eq. 4.11 to back compute P-Y curves from field lateral load tests to account for shaft side shear. The latter is recommended, since the side shear will reduce back computed P-Y curves by 25% to 30%, making the conventional curves unconservative. It is also recommended that full-scale field tests be employed to validate the P-Y curves developed in Figures 5.17 and 5.18.***

# CHAPTER 6

# CONCLUSIONS AND RECOMMENDATIONS

## 6.1 CONCLUSIONS

For axial loading, T-Z curves characterize the axial skin friction on a drilled shaft as a function of its vertical load and displacement. For many pile/shaft programs, i.e., FB-Pier, LPILE, etc., the side Friction, T (Figure 6.1) is assumed to act through the center of the shaft, i.e., point A. Therefore, in the case of lateral loading, the shear, V, and moment, M, in a segment of shaft (Fig. 6.1) is assumed to resisted by the soil/rock lateral resistance, P (force/unit length) with no contribution of T (Fig. 6.1) occurring.

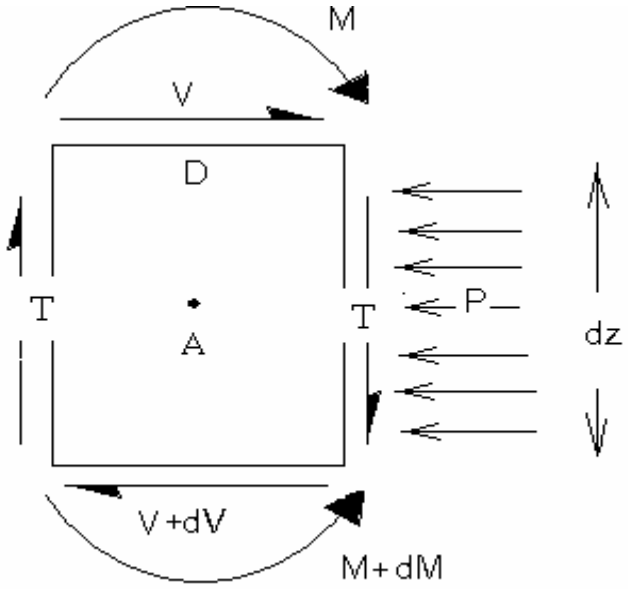


Figure 6.1 Forces and moments acting on segment of drilled shaft.

In the case of large shafts, or strong rock, the side shear, T (Fig 6.1) may develop a significant couple (Moment, $M_s$) depending on rotation, $\theta$, of the cross-section and if T is assumed

to act at the rock/shaft interface, Figure 6.1. The latter may have a significant effect on both the Moment, M, and the back computed P-Y curve for a laterally loaded shaft. The rotational spring, $M_s$ - $\theta$, as well as P-Y curves for Florida Limestone for FB-Pier implementation was the focus of this research.

For this study, 7 axial and 12 lateral tests were conducted in a centrifuge on drilled shafts embedded in variable strength rock to develop typical P-Y, T-Z and $M_s$-$\theta$ curves for Florida limestone. Synthetic limestone was used to ensure repeatability of tests as it was not viable to obtain uniform samples of natural limestone. Synthetic limestone, made by mixing ground up natural limestone, cement and water was believed to be representative of natural limestone. The two have been shown to have similarity in their strength and stiffness characteristics.

Results of the axial tests showed the skin friction of synthetic rock was higher than Florida limestone of similar strength. This was attributed to the construction technique employed in the model construction (e.g., the hole for casting model shaft was narrower at the bottom than at the top) and the chemical properties of the synthetic rock (e.g., bonding of shaft concrete with rock). However, T-Z curves normalized with the ultimate unit friction show a remarkable similarity to the trend observed from the results of 33 Osterberg tests at various sites in Florida.

Results from 12 lateral tests conducted on 2 rock strengths, 2 shaft diameters and 3 L/D ratios were used to back calculate P-Y curves for Florida Limestone. P-Y curves were found if the shaft side friction, T (Fig. 6.1), was considered or not. Subsequently, all the curves were normalized and are shown in Figures 6.1 and 6.2.

The normalized back computed P-Y curve with (Fig. 6.3) and without (Fig 6.2) side friction, show that the current use of either the soft or stiff clay models to characterize Florida

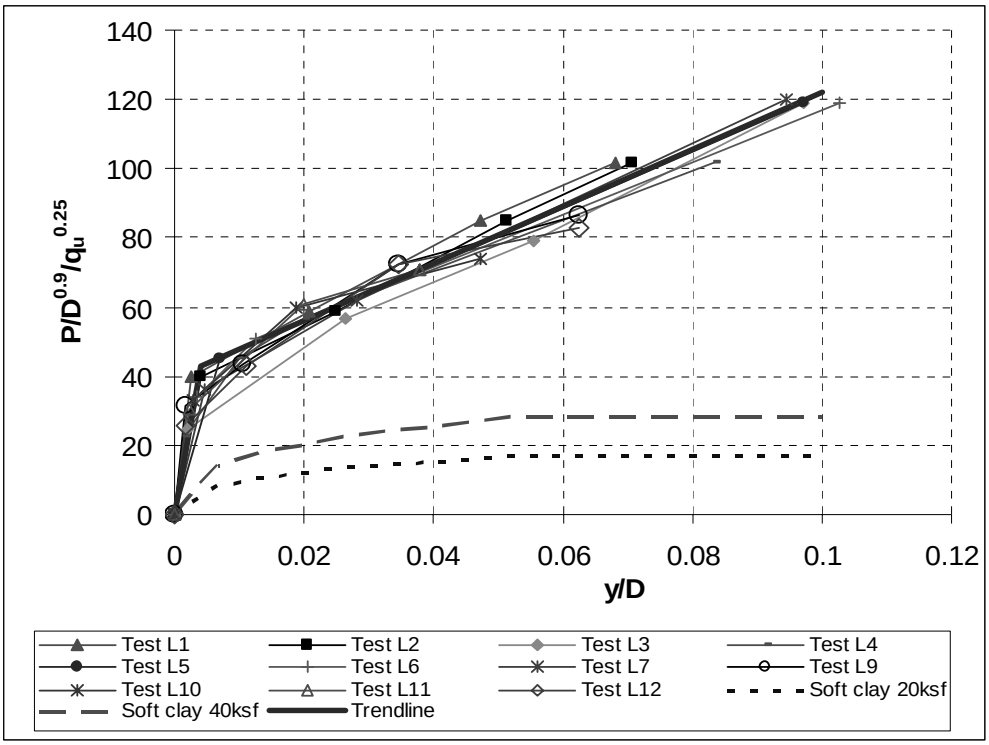


Figure 6.2 Normalized P-Y curves without side shear correction.

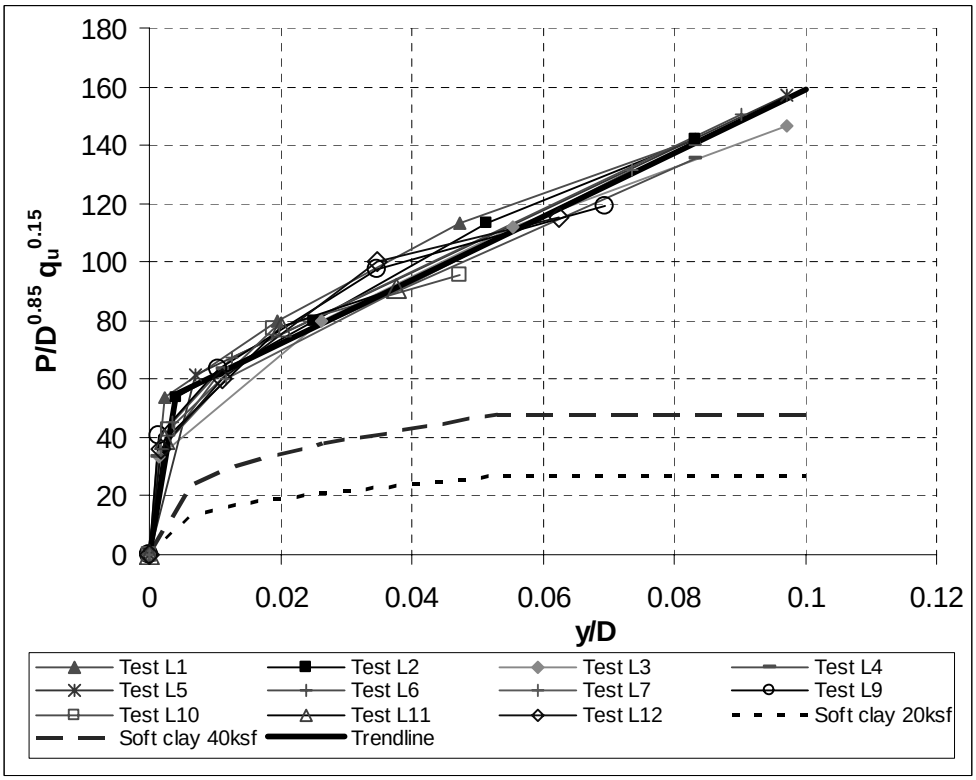


Figure 6.3 Normalized P-Y curves corrected for side shear

Limestone, are conservative. However, the current practice of neglecting side friction in back computing P-Y curves is unconservative as shown in Figure 6.4. The plot shows a typical 6' diameter drilled shaft embedded in 40 tsf rock has a P-Y curve which is 25% too high if side friction is neglected. That is a portion of the P-Y curve or lateral resistance which is assumed to be from rock shear strength, is actually due to axial side shear, T in Figure 6.1, along the shaft. However, if an axial load were to act on the shaft (i.e., structure live and dead loads), then the side friction, T, Figure 6.1, would be mobilized under the axial load acting on the shaft, and would no longer be available to resist the lateral load. In addition, any lateral load test with variable axial load would generate different P-Y curves (Fig. 6.2).

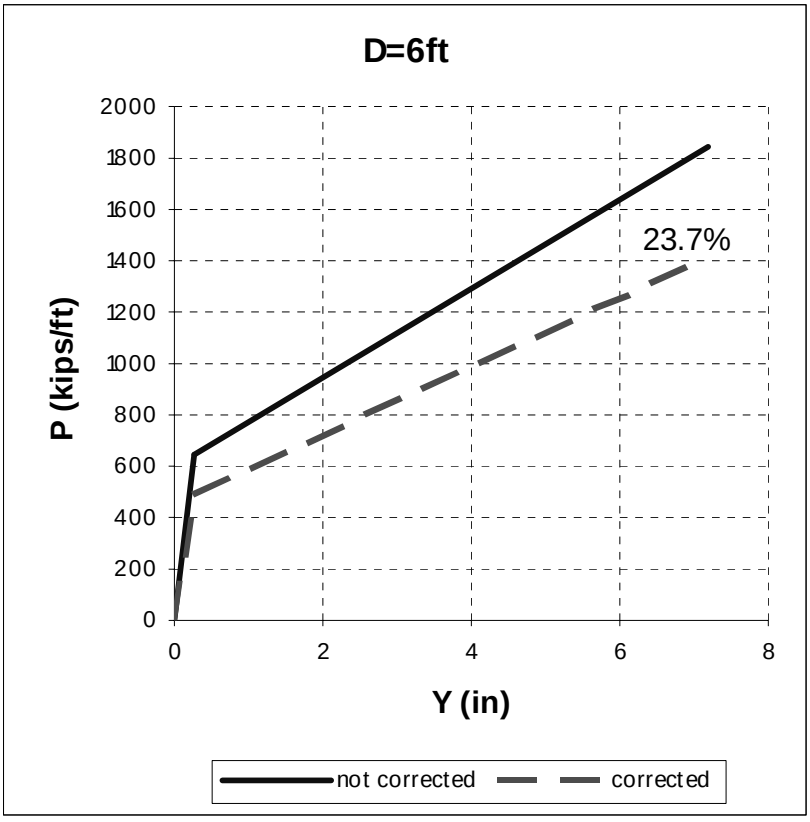


Figure 6.4 P-Y curve for 6' diameter shaft, with and without side friction.

Also evident from Figures 6.2 and 6.3, the normalized P-Y curves are depended on rock strength and shaft diameter but independent of shaft embedment depth, or L/D ratio. The curves were employed in FB-Pier and used successfully to predict all the experimental results. In the case of the P-Y curves, which corrected for side friction, Figure 6.3, a moment resistance as a function of rotation, i.e., $M_s$ vs. $\theta$, applied to each node in the rock. The moment due to side shear, $M_s$, and the rotation of the shaft at strain gage locations were plotted to obtain M-$\theta$ curves for both rock strengths tested as well as shaft diameters. The M-$\theta$ curves closely resemble the T-Z curves and can be derived automatically from T-Z curves if the shaft rotations are known.

To develop a P-Y curve (e.g., Fig. 6.4) for input into LPILE or FB-PIER, the user first selects a point on the trend line in Figure 6.3, and finds the corresponding pair of X and Y values (i.e., axes values). From the X (Y/D) value, the lateral is displacement, Y (ft), is obtained by multiplying the X value by the shaft's diameter in feet. Next, the corresponding P (Kips/ft) is obtained by multiplying the Y value by the [shaft diameter (ft)]$^{0.85}$ and [rock strength, qu (ksf)]$^{0.15}$. Generally, the process is repeated 10 to 20 times to fully describe the P-Y curve of the rock. Note, if the shaft is embedded in rock with multiple strengths, qu along its length, multiple P-Y curves will be required, as a result of the rock's strength variability and its affect on P (Y-axis, Figure 6.3).

## 6.2 RECOMMENDATIONS

P-Y and M-$\theta$ curves obtained in this research are based only on 2 rock strengths and 12 lateral tests. The results must be used with caution, especially outside the range of rock strengths tested. In addition, although synthetic limestone has been proved to be similar to Florida limestone in terms of its physical characteristics, its chemical properties may make it behave differ-

ently. Therefore, it is strongly recommended that field tests be performed to verify the results obtained from this study.

Having verified the results of this research by field study, it is also recommended that the new P-Y curves adjusted for side shear, Figure 6.3, as well as M-θ curves be implemented in the FB-Pier software to model the actual axial and lateral transfer of the pile/drilled shaft to the rock. For conservative design, the adjusted side shear P-Y curves, Figure 6.3 should be used with no M-θ springs. The latter would assume all shaft side shear, Figure 6.1 was being fully mobilized under axial conditions with none available for lateral loading.

# REFERENCES


Bradley, G.S., Townsend, F.C, Fagundo, F.E., and Davidson, J.L (1984). "Centrifuge Scaling Laws for Ground Launch Cruise Missile Shelter" ESL-TR-84-07, Air Force Engineering Services Center, Tyndall Air Force Base, Florida.

Cepero, C. E. (2002). "Insitu Measurement of Rock Modulus and Strength," Master's Thesis, University of Florida, Gainesville Florida.

FHWA (1993). "COM624P Manual" Federal Highway Administration Washington, D.C.

Gill, J.J. (1988). "Development and Testing of a Device Capable of Placing Model Piles by Driving and Pushing in the Centrifuge," Ph.D. Dissertation, University of Florida, Gainesville, Florida.

Hoit, M.I, McVay M.C. (1996). "FB-Pier User's Manual," Department of Civil Engineering, University of Florida, Gainesville, Florida.

Kim, Myoung-Ho (2001), Analysis of Osterberg and Stanamic Axial Load Testing and Conventional Lateral Load Testing," Master's Thesis, University of Florida, Gainesville, Florida.

McVay, M.C., Townsend, F.C. and Williams R.C. (1992). "Design of Socketed Drilled Shafts in Limestone," ASCE Journal of Geotechnical Engineering, 118(10), 1626 – 1637.

Molnit, T. (1995). "Centrifuge Modeling of Laterally Loaded Large Plumb Pile Groups in Sand," Master's Thesis, University of Florida, Gainesville Florida.

National Instruments (1999). "DAQ 6034E/6035E User Manual," National Instruments Corporation, Austin Texas.

Omega (2000). "The Pressure Strain and Force Handbook," Omega Engineering, Inc., Stamford, CT.

Taylor, R.N. (1995). Geotechnical Centrifuge Technology, Blackie Academic and Professional, London, U.K.

# Appendix A

# LATERAL LOAD TEST DATA

This section presents the raw data from the 12 lateral load tests, which were used to back compute P-Y curves. For each test a graph of load vs. displacement and 6 graphs of Load vs. strain are plotted. Each load vs. strain plot consists of strains on the opposite sides of the shaft at a given depth.

The load, displacement and strains shown in the graphs are those for the model shaft. Since the tests were conducted at a centrifugal acceleration of 67g, loads, displacements and strains have to be multiplied by appropriate scaling factors (Table 2.1, Chapter 2) to obtain the values for a prototype shaft as follows:

- Scaling factor N = 67.
- Displacement (linear dimension) is scaled 1:67.
  Therefore, prototype displacement = 67 x model displacement.
- Load (force) is scaled $1:67^2$.
  Therefore, prototype load = 4489 x model load.
- Strain is scaled 1:1.
  Therefore, prototype strain = model strain.

**Lateral Test # L1**

Shaft Information and Load – Displacement Data

| qu (ksf) | 20 | |
|---|---|---|
| Elevation | Model (in) | Prototype (ft) |
| LVDT | | |
| Load | 0 | 0.00 |
| LVDT | 0.050 | 0.28 |
| surface | 0.897 | 5.01 |
| strain g1 | 0.897 | 5.01 |
| strain g2 | 1.448 | 8.08 |
| strain g3 | 1.999 | 11.16 |
| strain g4 | 2.550 | 14.24 |
| strain g5 | 3.102 | 17.32 |
| strain g6 | 3.653 | 20.39 |
| tip | 3.930 | 21.94 |
| Diameters | | |
| Shaft | 1.080 | 6.03 |
| Rebar cage | 0.750 | 4.19 |

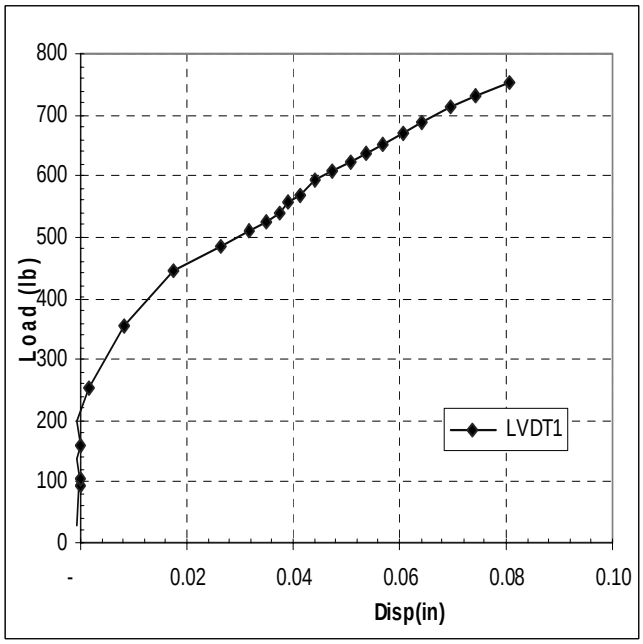


**Load - Strain Data**

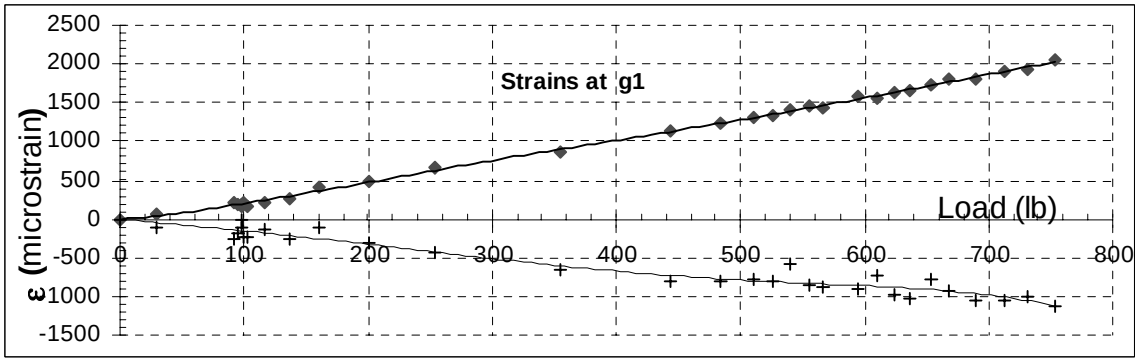


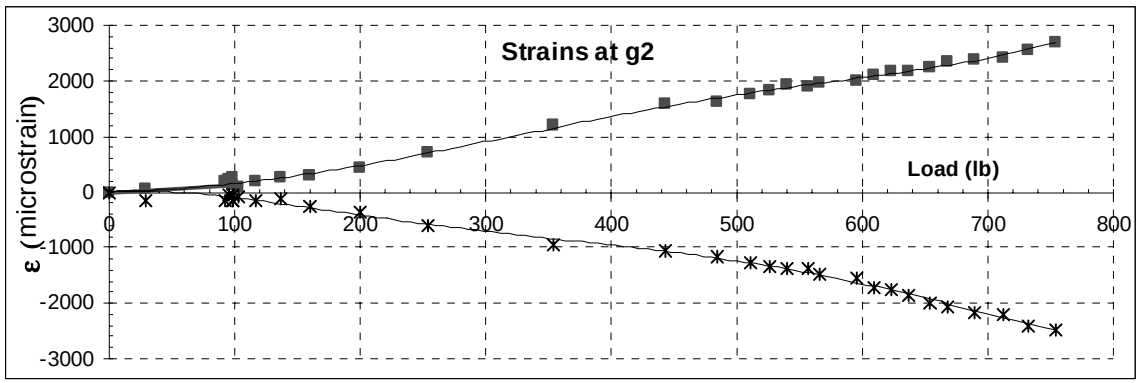

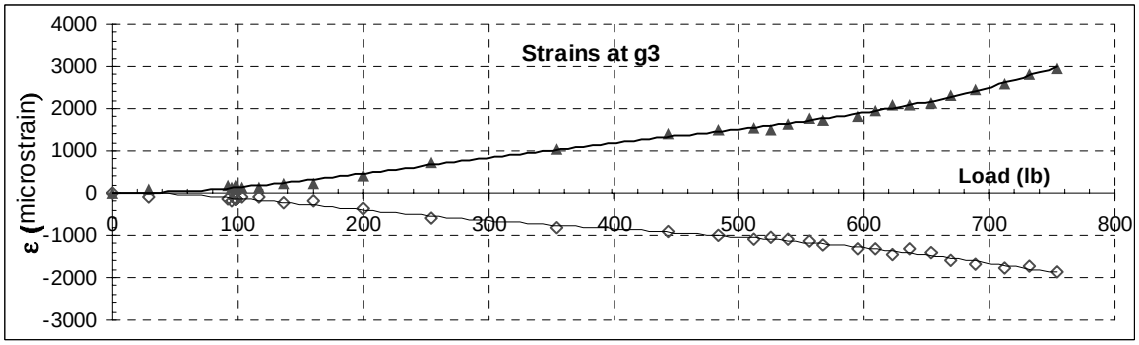
Strains at g3
ε (microstrain)
Load (lb)
4000
3000
2000
1000
0
-1000
-2000
-3000
0
100
200
300
400
500
600
700
800

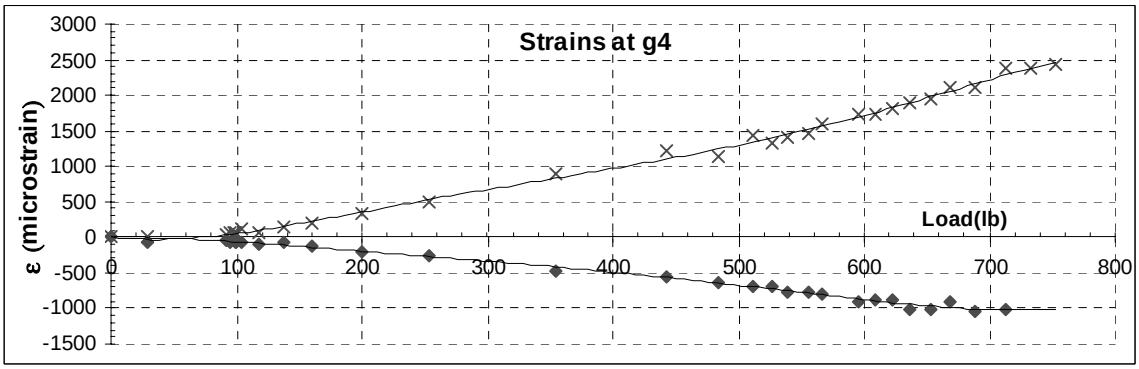
Strains at g4
ε (microstrain)
Load(lb)
3000
2500
2000
1500
1000
500
0
-500
-1000
-1500
0
100
200
300
400
500
600
700
800

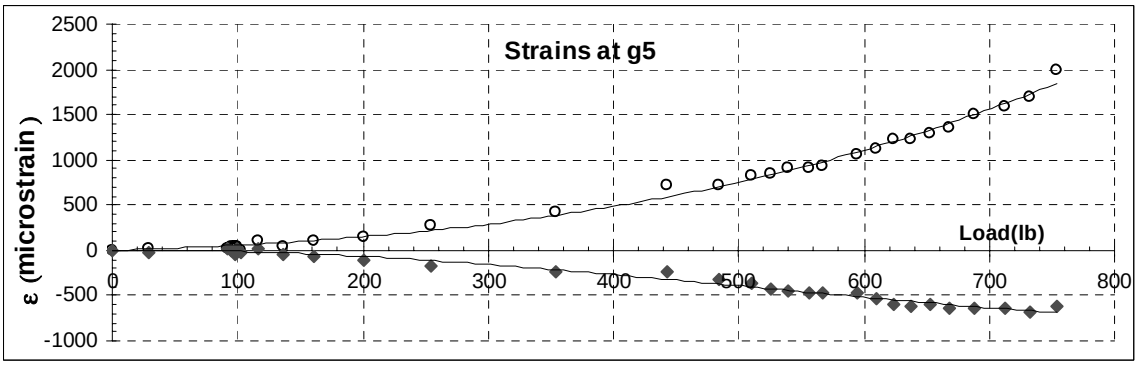
Strains at g5
ε (microstrain)
Load(lb)
2500
2000
1500
1000
500
0
-500
-1000
0
100
200
300
400
500
600
700
800

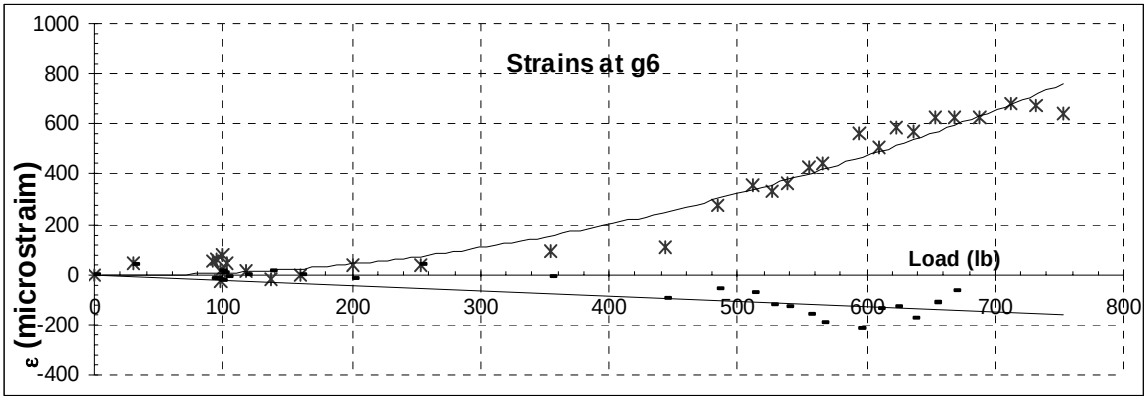
Strains at g6
ε (microstraim)
Load (lb)
1000
800
600
400
200
0
-200
-400
0
100
200
300
400
500
600
700
800

**Lateral Test # L2**

**Shaft Information and Load - Displacement Data**

| qu (ksf) | 20 | |
|---|---|---|
| Elevation | Model (in) | Prototype (ft) |
| LVDT | -0.200 | -1.12 |
| Load | 0 | 0.00 |
| LVDT | 0.050 | 0.28 |
| surface | 0.897 | 5.01 |
| strain g1 | 0.897 | 5.01 |
| strain g2 | 1.448 | 8.08 |
| strain g3 | 1.999 | 11.16 |
| strain g4 | 2.550 | 14.24 |
| strain g5 | 3.102 | 17.32 |
| strain g6 | 3.653 | 20.39 |
| tip | 3.930 | 21.94 |
| Diameters | | |
| Shaft | 1.080 | 6.03 |
| Rebar cage | 0.750 | 4.19 |

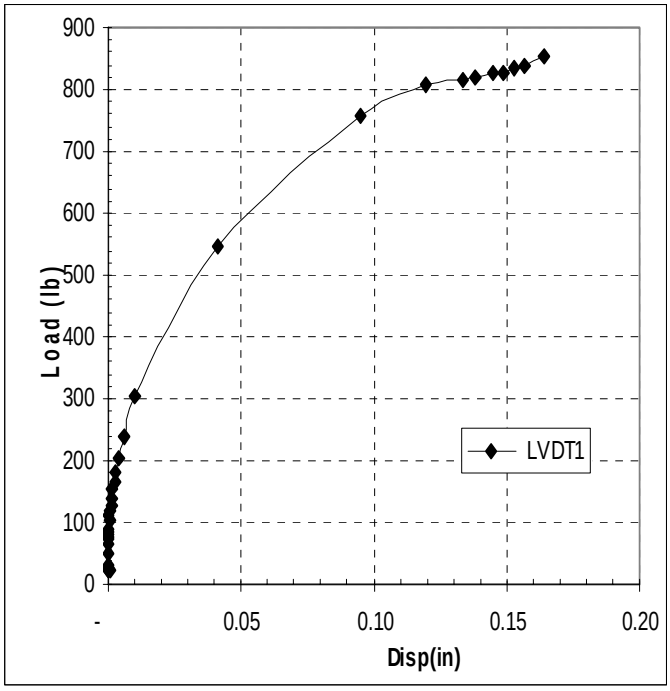


**Load - Strain Data**

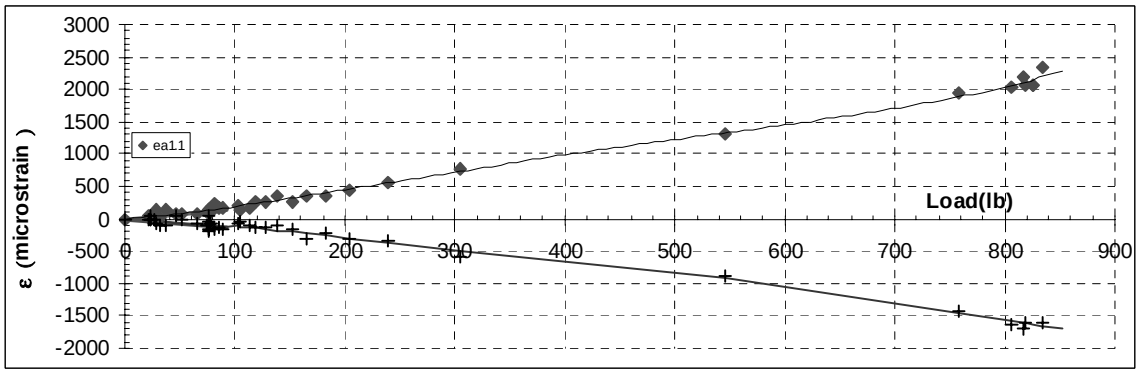


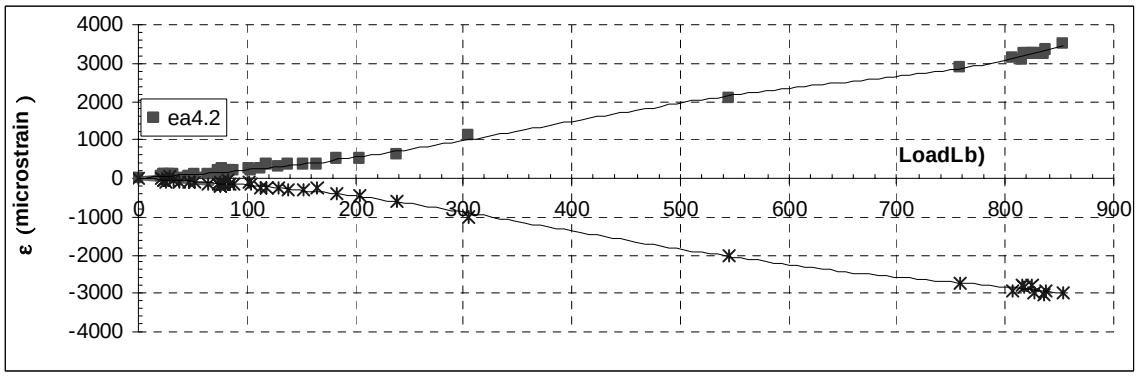

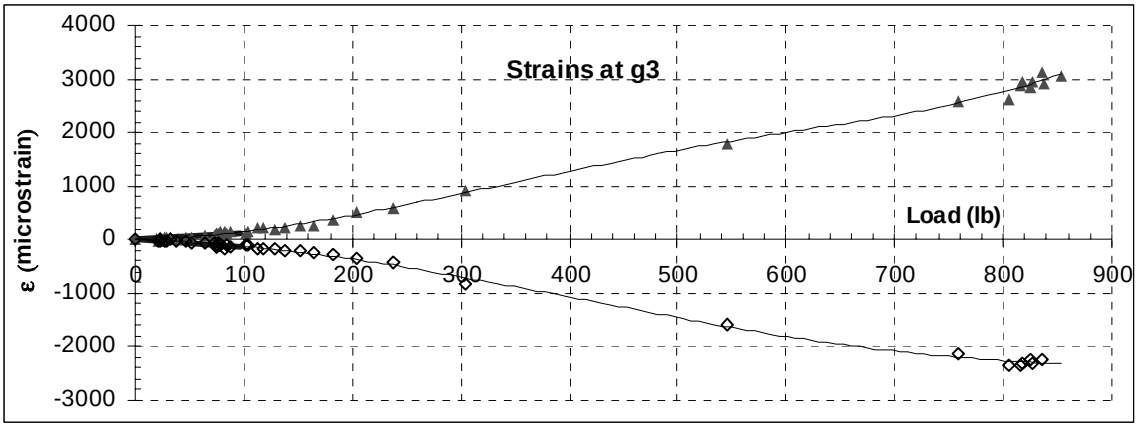
Strains at g3
ε (microstrain)
Load (lb)
4000
3000
2000
1000
0
-1000
-2000
-3000
0
100
200
300
400
500
600
700
800
900

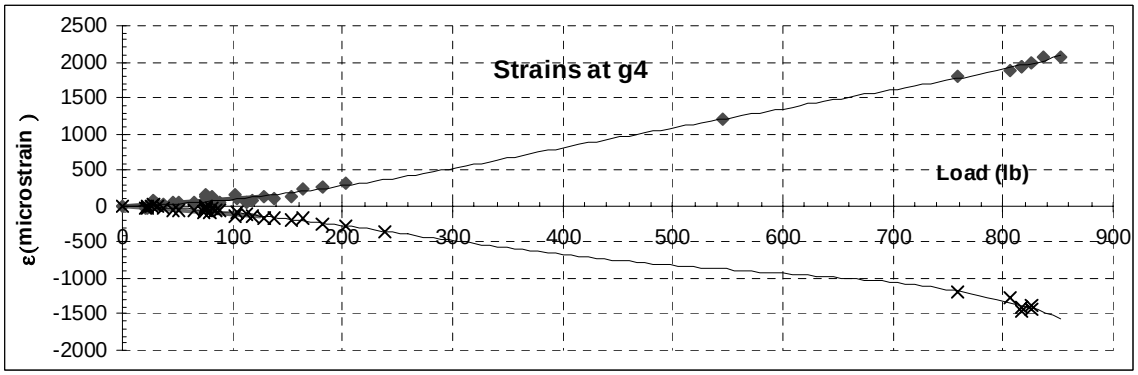
Strains at g4
ε(microstrain )
Load (lb)
2500
2000
1500
1000
500
0
-500
-1000
-1500
-2000
0
100
200
300
400
500
600
700
800
900

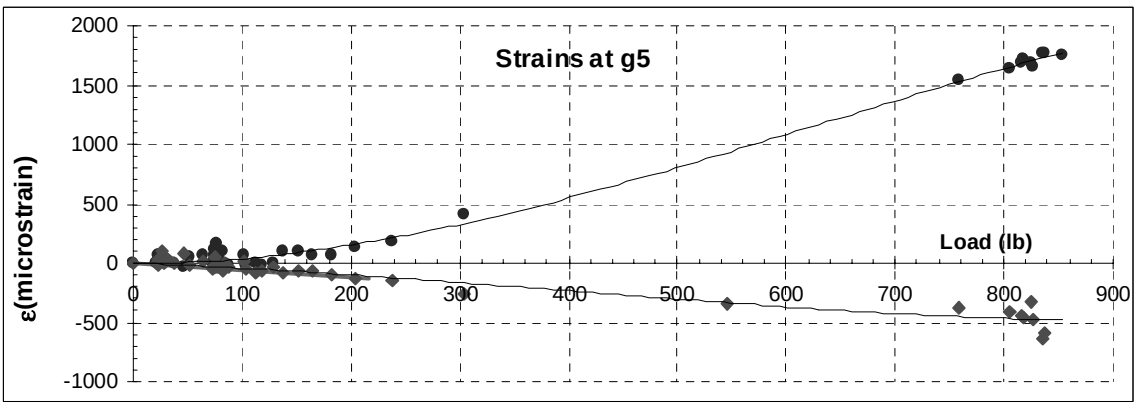
Strains at g5
ε(microstrain)
Load (lb)
2000
1500
1000
500
0
-500
-1000
0
100
200
300
400
500
600
700
800
900

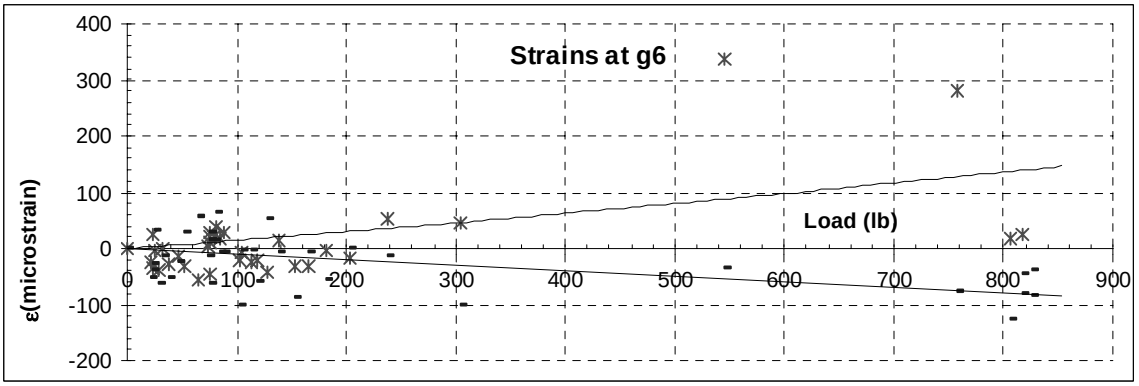
Strains at g6
ε(microstrain)
Load (lb)
400
300
200
100
0
-100
-200
0
100
200
300
400
500
600
700
800
900

**Lateral Test # L3**

**Shaft Information and Load - Displacement Data**

| qu (ksf) | 20 | |
|---|---|---|
| Elevation | Model (in) | Prototype (ft) |
| LVDT | -0.900 | -5.03 |
| Load | 0 | 0.00 |
| LVDT | 0.100 | 0.56 |
| surface | 1.133 | 6.33 |
| strain g1 | 1.133 | 6.33 |
| strain g2 | 1.842 | 10.28 |
| strain g3 | 2.550 | 14.24 |
| strain g4 | 3.259 | 18.20 |
| strain g5 | 3.968 | 22.15 |
| strain g6 | 4.676 | 26.11 |
| tip | 5.031 | 28.09 |
| Diameters | | |
| Shaft | 1.060 | 5.92 |
| Rebar cage | 0.750 | 4.19 |

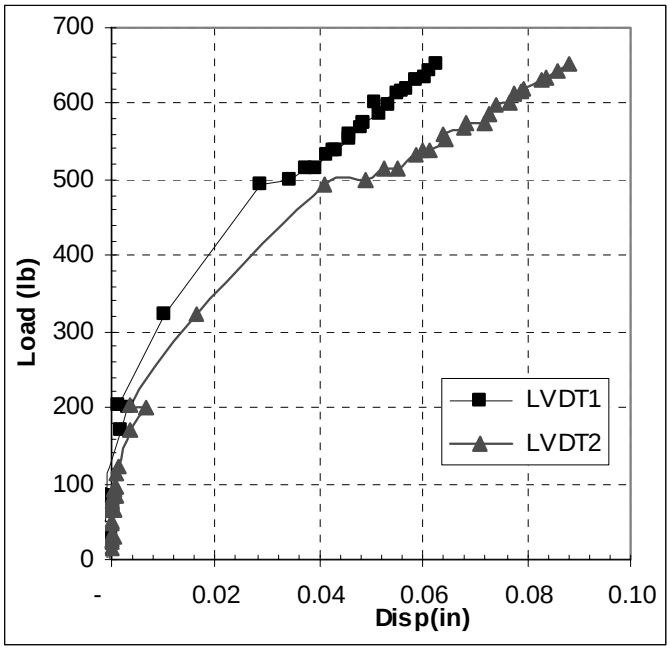


**Load - Strain Data**

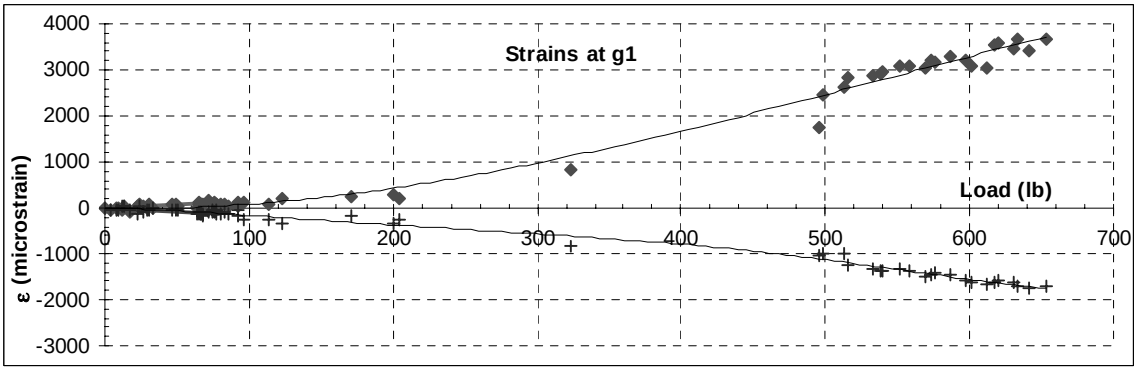


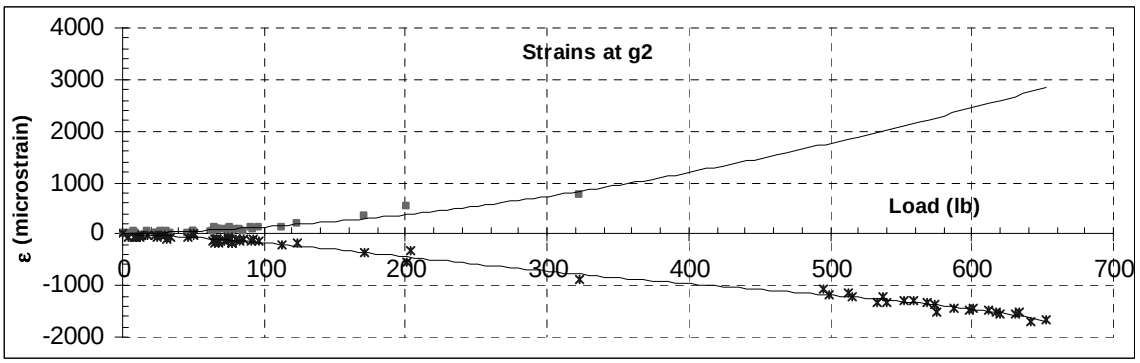

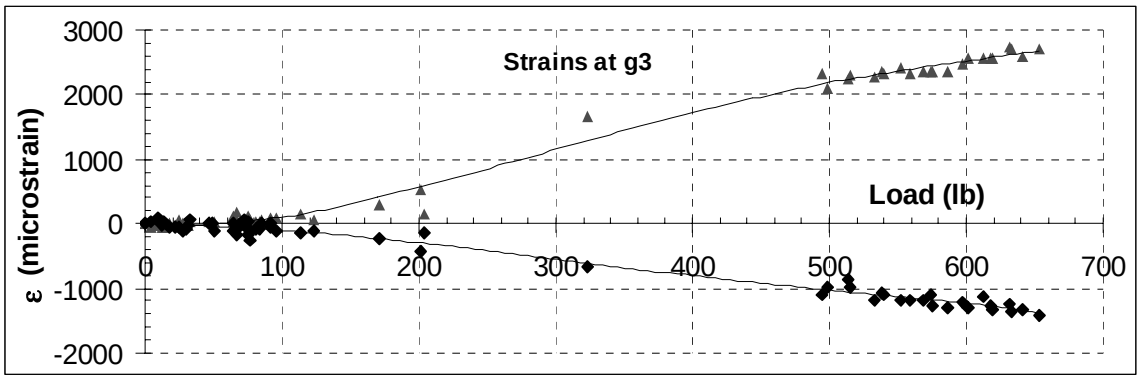
Strains at g3
ε (microstrain)
Load (lb)
3000
2000
1000
0
-1000
-2000
0
100
200
300
400
500
600
700

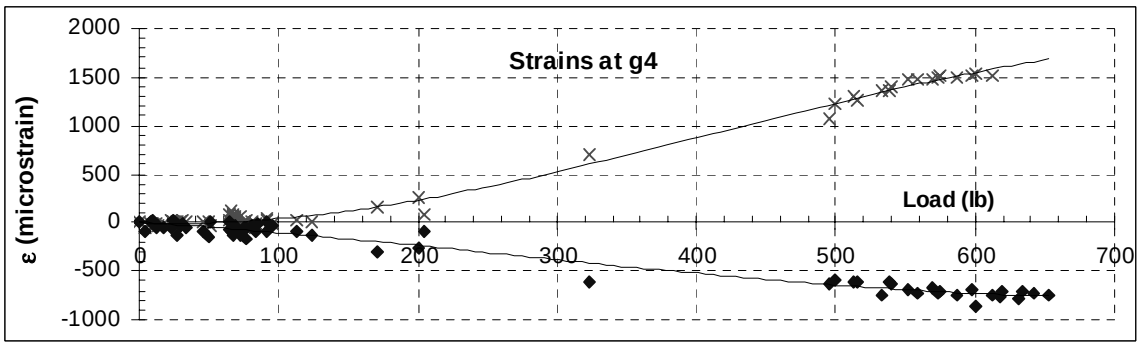
Strains at g4
ε (microstrain)
Load (lb)
2000
1500
1000
500
0
-500
-1000
0
100
200
300
400
500
600
700

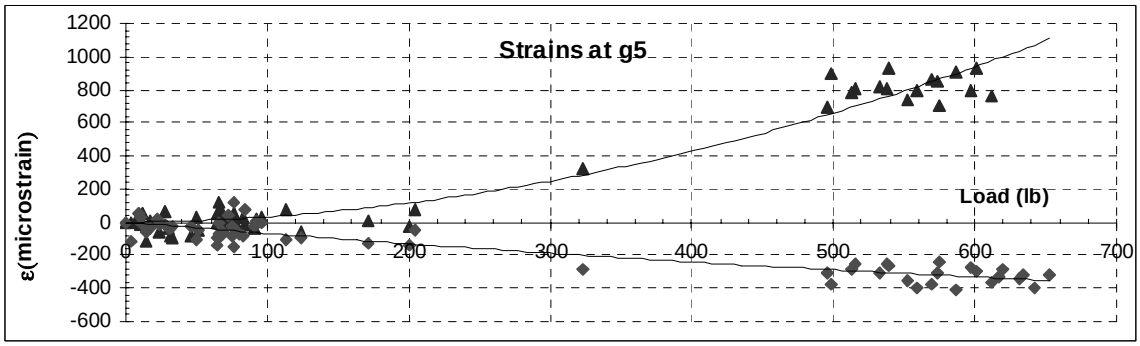
Strains at g5
ε(microstrain)
Load (lb)
1200
1000
800
600
400
200
0
-200
-400
-600
0
100
200
300
400
500
600
700

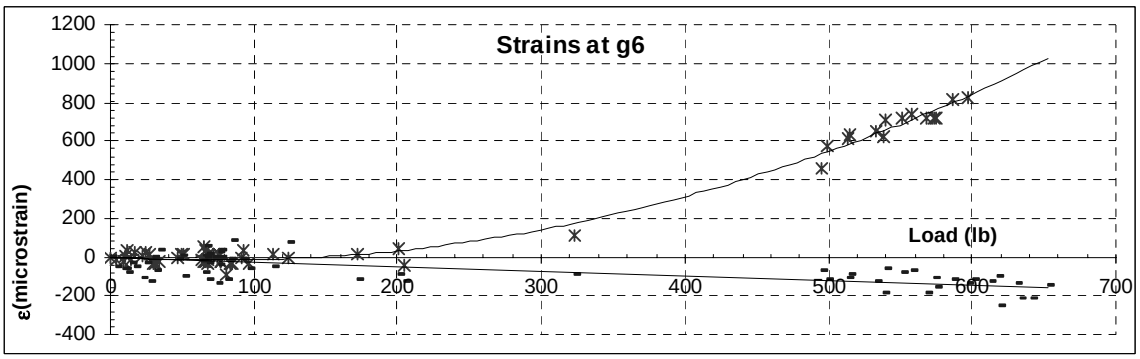
Strains at g6
ε(microstrain)
Load (lb)
1200
1000
800
600
400
200
0
-200
-400
0
100
200
300
400
500
600
700

**Lateral Test # L4**

**Shaft Information and Load - Displacement Data**

| qu (ksf) | 20 | |
|---|---|---|
| Elevation | Model (in) | Prototype (ft) |
| LVDT | -0.900 | -5.03 |
| Load | 0 | 0.00 |
| LVDT | 0.100 | 0.56 |
| surface | 1.133 | 6.33 |
| strain g1 | 1.133 | 6.33 |
| strain g2 | 1.842 | 10.28 |
| strain g3 | 2.550 | 14.24 |
| strain g4 | 3.259 | 18.20 |
| strain g5 | 3.968 | 22.15 |
| strain g6 | 4.676 | 26.11 |
| tip | 5.031 | 28.09 |
| Diameters | | |
| Shaft | 1.060 | 5.92 |
| Rebar cage | 0.750 | 4.19 |

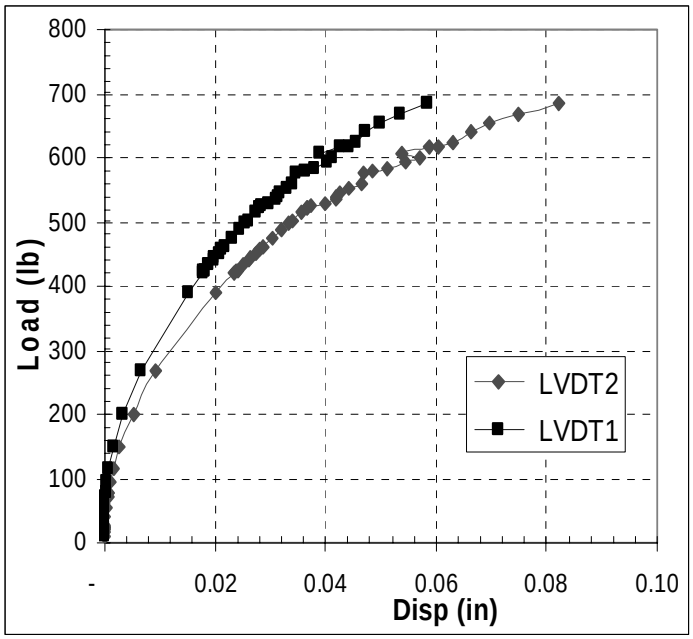


**Load - Strain Data**

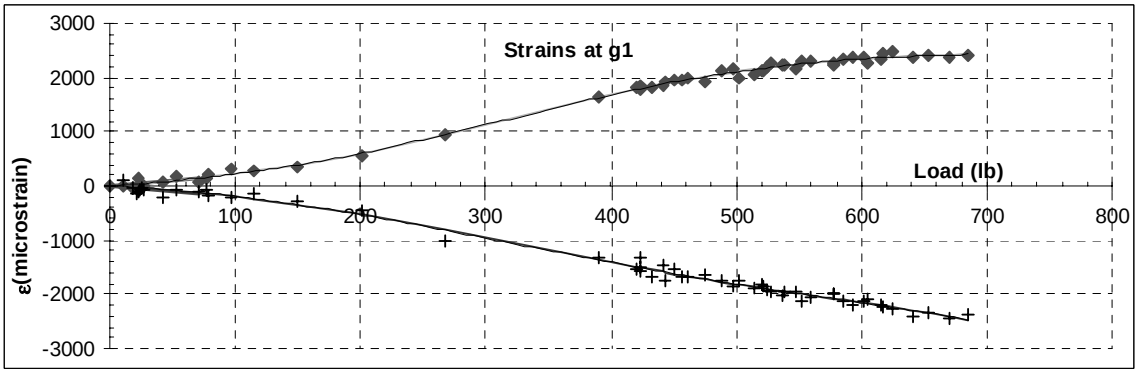


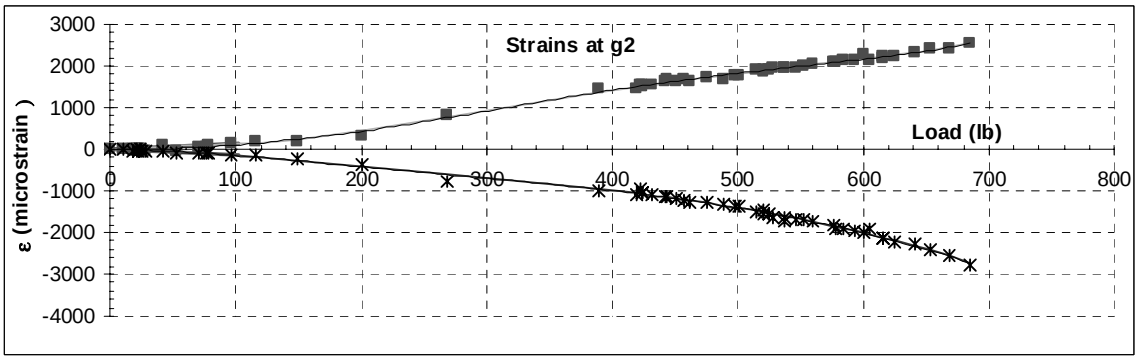

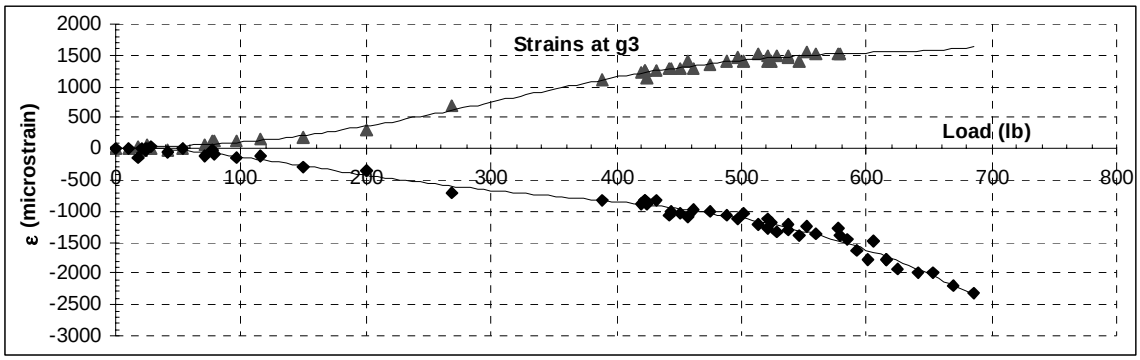
Strains at g3
Load (lb)
ε (microstrain)
2000
1500
1000
500
0
-500
-1000
-1500
-2000
-2500
-3000
0
100
200
300
400
500
600
700
800

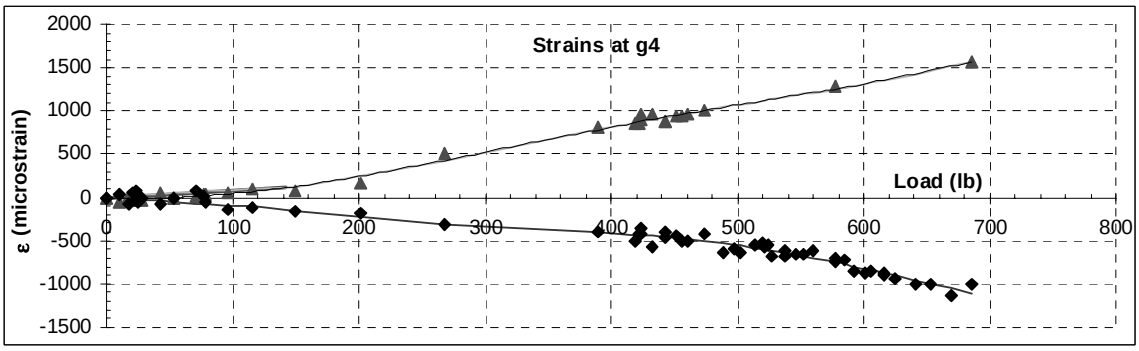
Strains at g4
Load (lb)
ε (microstrain)
2000
1500
1000
500
0
-500
-1000
-1500
0
100
200
300
400
500
600
700
800

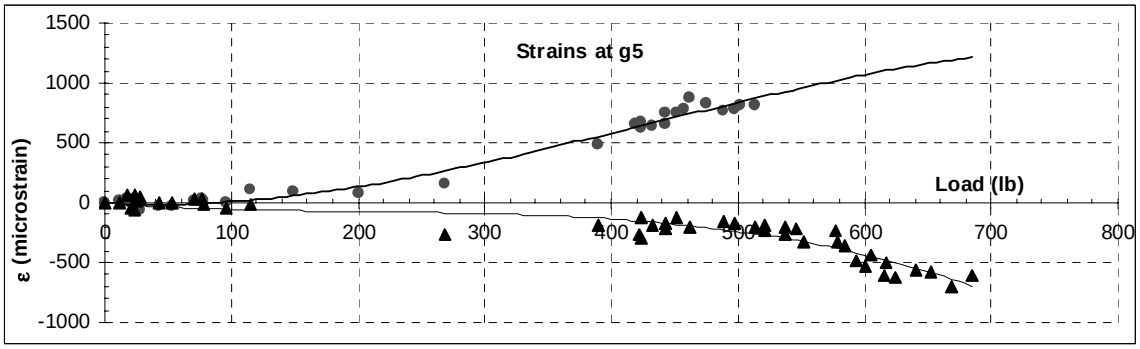
Strains at g5
Load (lb)
ε (microstrain)
1500
1000
500
0
-500
-1000
0
100
200
300
400
500
600
700
800

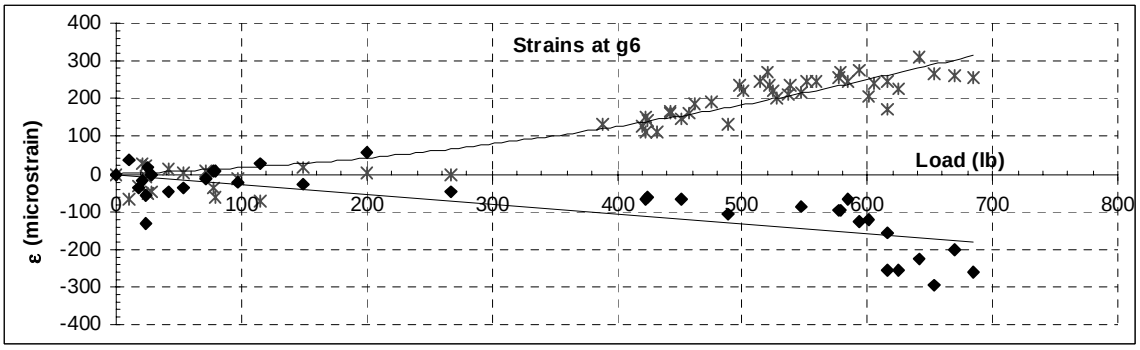
Strains at g6
Load (lb)
ε (microstrain)
400
300
200
100
0
-100
-200
-300
-400
0
100
200
300
400
500
600
700
800

**Lateral Test# L4**

**Shaft Information and Load - Displacement Data**

| qu (ksf) | 20 | |
|---|---|---|
| Elevation | Model (in) | Prototype (ft) |
| LVDT | -0.650 | -3.63 |
| Load | 0 | 0.00 |
| LVDT | 0.250 | 1.40 |
| surface | 1.183 | 6.61 |
| strain g1 | 1.183 | 6.61 |
| strain g2 | 1.734 | 9.68 |
| strain g3 | 2.285 | 12.76 |
| strain g4 | 2.837 | 15.84 |
| strain g5 | 3.388 | 18.92 |
| strain g6 | 3.939 | 21.99 |
| tip | 4.215 | 23.53 |
| Diameters | | |
| Shaft | 1.060 | 5.92 |
| Rebar cage | 0.750 | 4.19 |

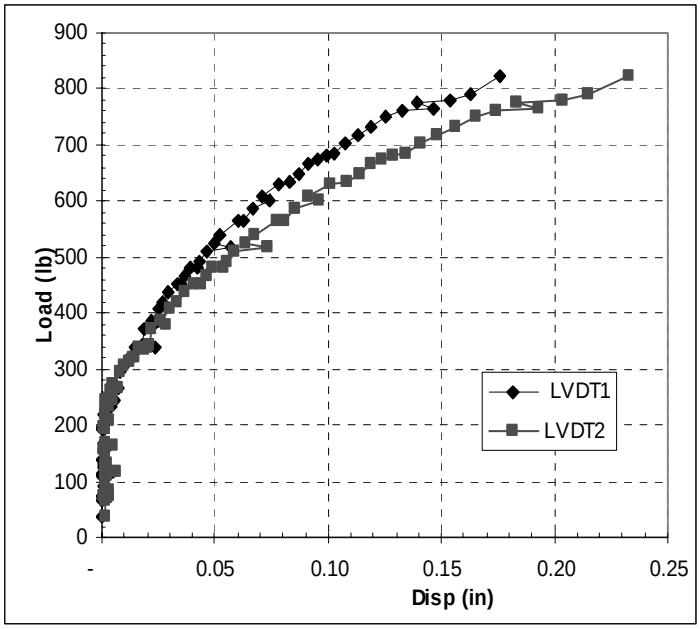


**Load - Strain Data**

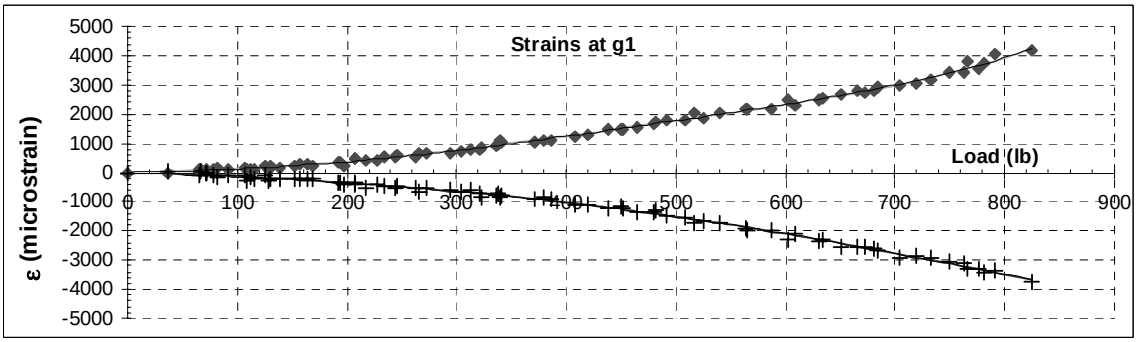


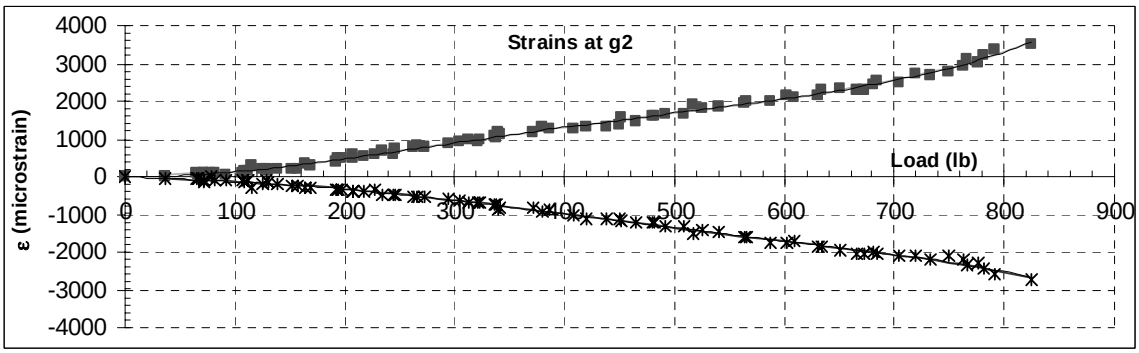

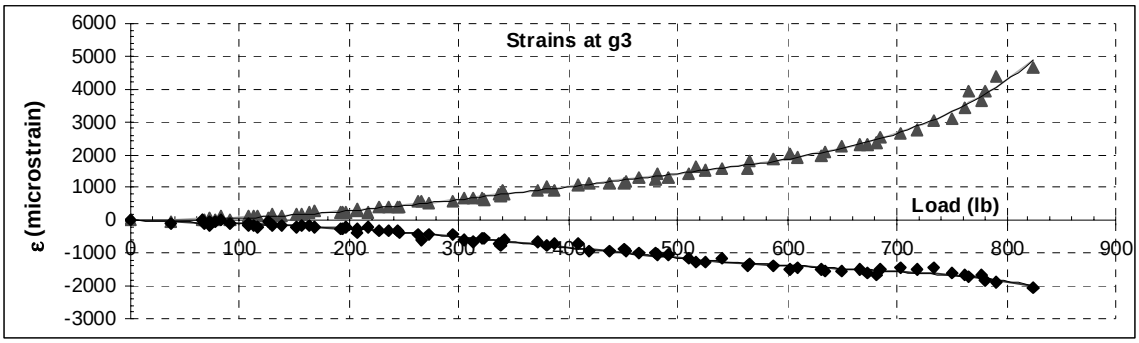
Strains at g3
ε (microstrain)
Load (lb)
6000
5000
4000
3000
2000
1000
0
-1000
-2000
-3000
0
100
200
300
400
500
600
700
800
900

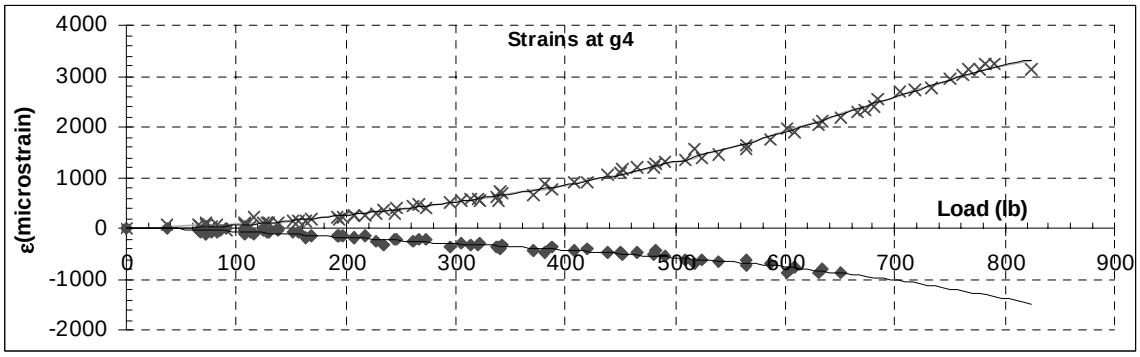
Strains at g4
ε(microstrain)
Load (lb)
4000
3000
2000
1000
0
-1000
-2000
0
100
200
300
400
500
600
700
800
900

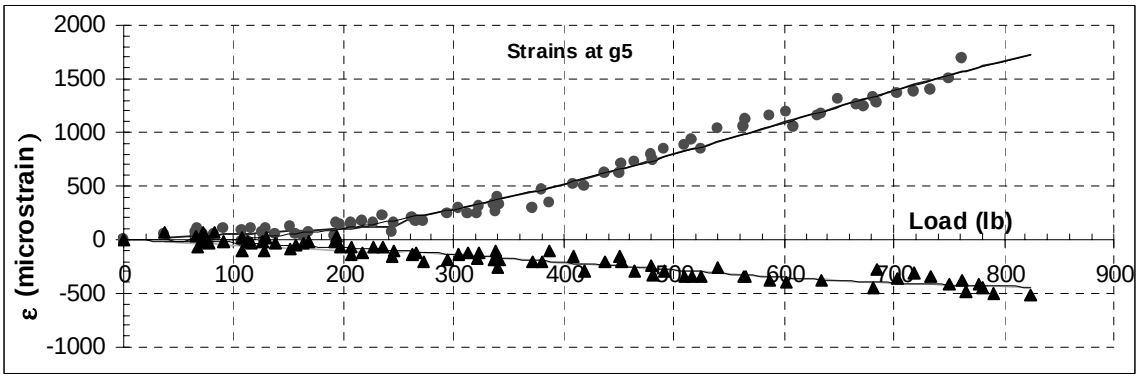
Strains at g5
ε (microstrain)
Load (lb)
2000
1500
1000
500
0
-500
-1000
0
100
200
300
400
500
600
700
800
900

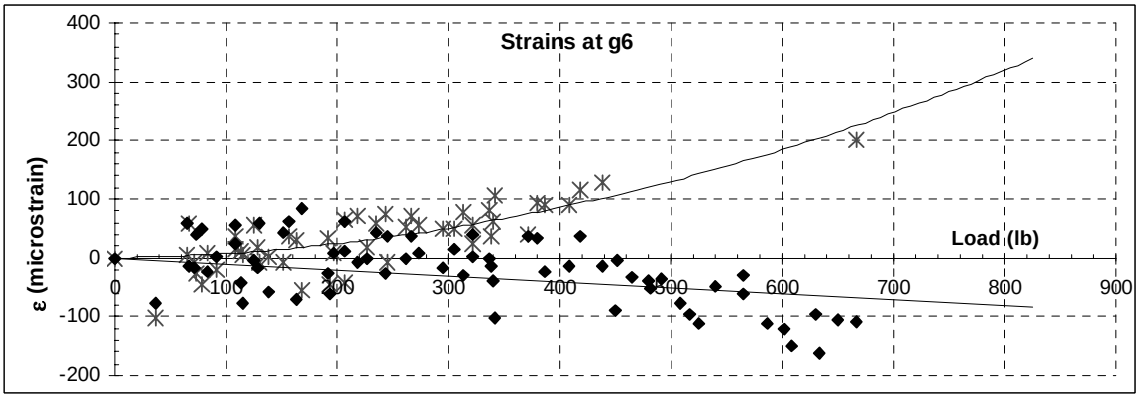
Strains at g6
ε (microstrain)
Load (lb)
400
300
200
100
0
-100
-200
0
100
200
300
400
500
600
700
800
900

**Lateral Test # L6**

**Shaft Information and Load - Displacement Data**

| qu (ksf) | 20 | |
|---|---|---|
| Elevation | Model (in) | Prototype (ft) |
| LVDT2 | -0.650 | -3.63 |
| Load | 0 | 0.00 |
| LVDT1 | 0.250 | 1.40 |
| surface | 1.183 | 6.61 |
| strain g1 | 1.183 | 6.61 |
| strain g2 | 1.734 | 9.68 |
| strain g3 | 2.285 | 12.76 |
| strain g4 | 2.837 | 15.84 |
| strain g5 | 3.388 | 18.92 |
| strain g6 | 3.939 | 21.99 |
| tip | 4.215 | 23.53 |
| Diameters | | |
| Shaft | 1.060 | 5.92 |
| Rebar cage | 0.750 | 4.19 |

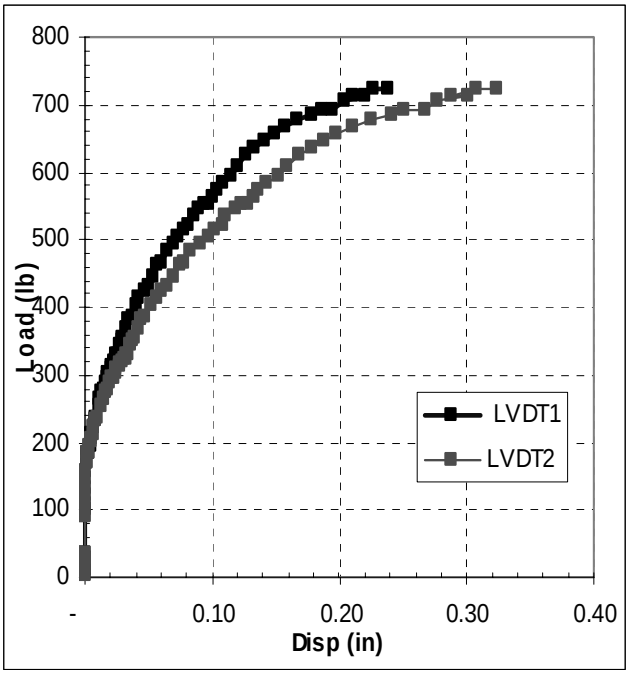


**Load - Strain Data**

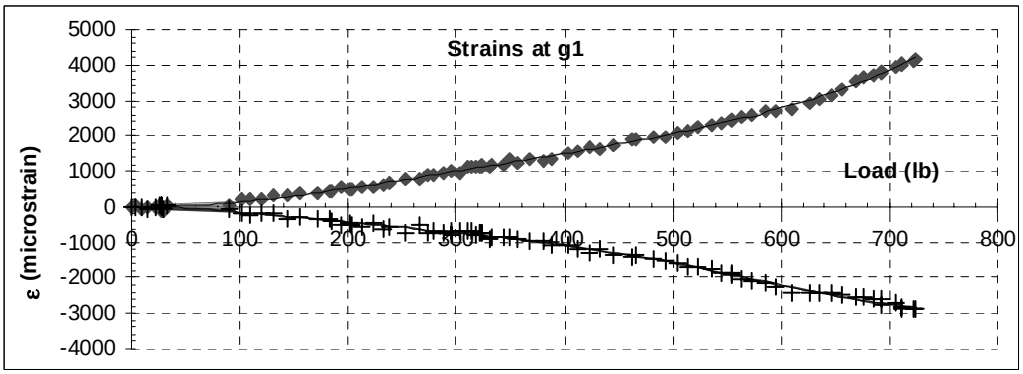


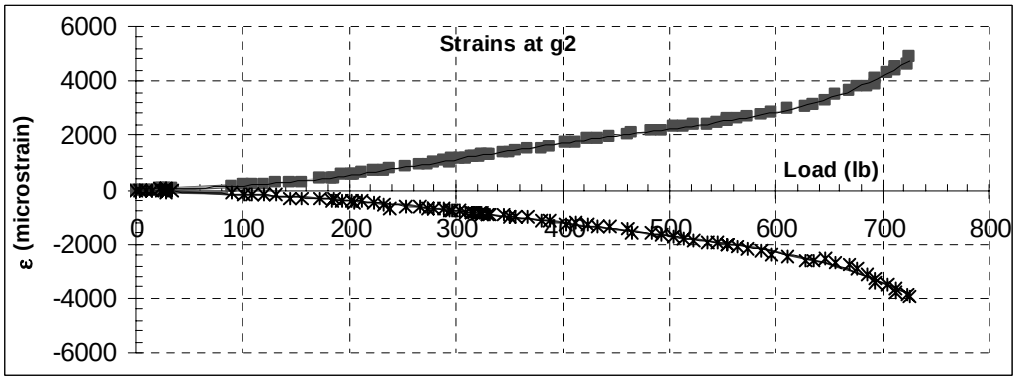

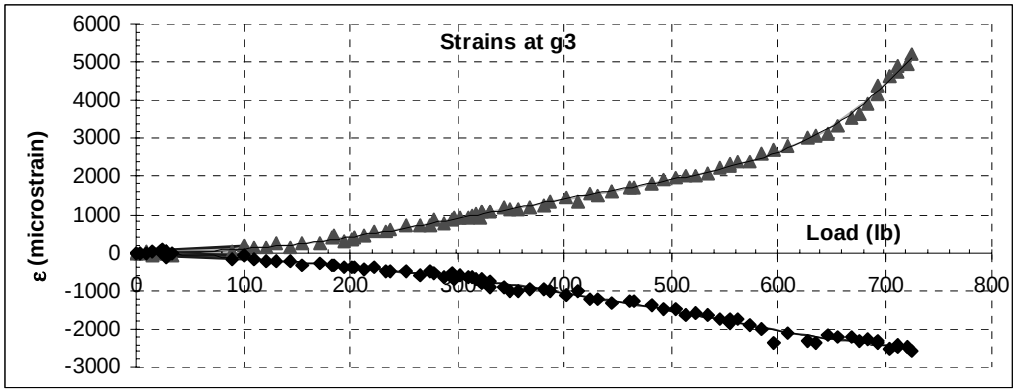
Strains at g3
ε (microstrain)
Load (lb)
6000
5000
4000
3000
2000
1000
0
-1000
-2000
-3000
0
100
200
300
400
500
600
700
800

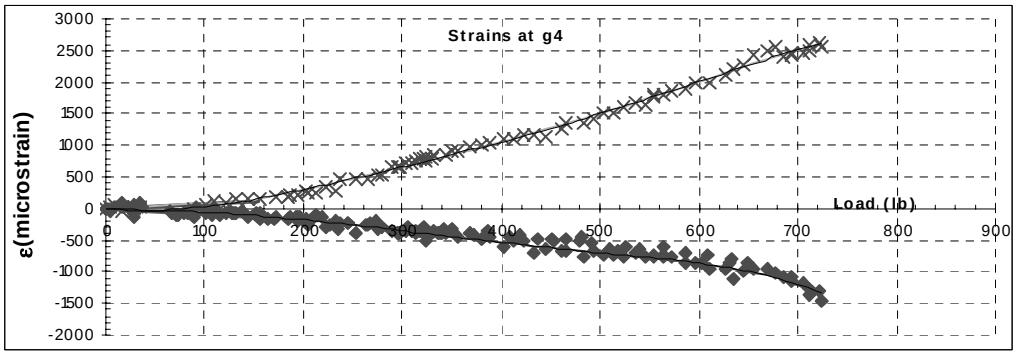
Strains at g4
ε(microstrain)
Load (lb)
3000
2500
2000
1500
1000
500
0
-500
-1000
-1500
-2000
0
100
200
300
400
500
600
700
800
900

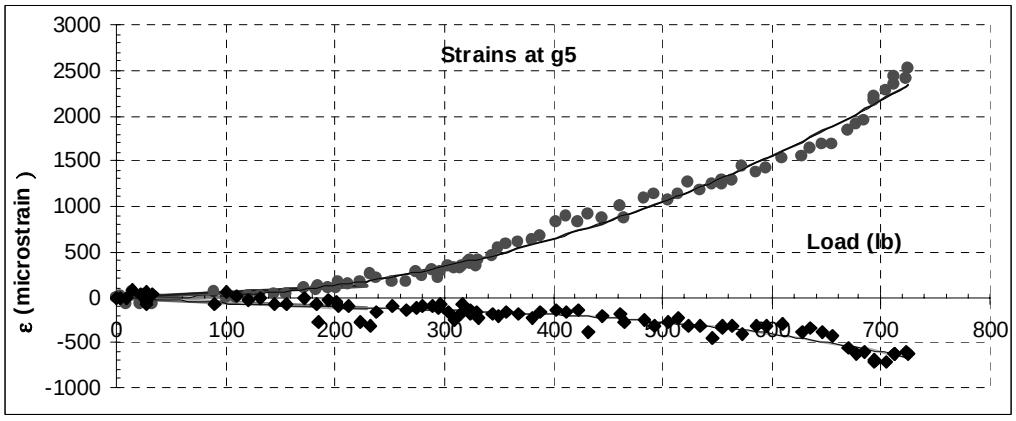
Strains at g5
ε (microstrain )
Load (lb)
3000
2500
2000
1500
1000
500
0
-500
-1000
0
100
200
300
400
500
600
700
800

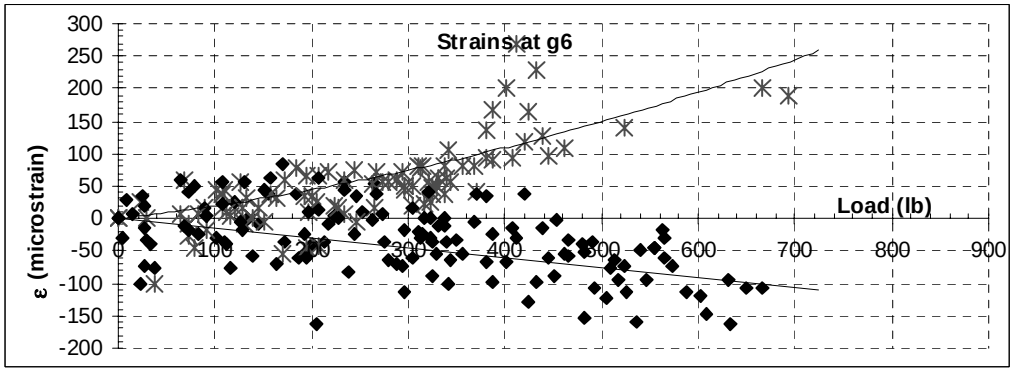
Strains at g6
ε (microstrain)
Load (lb)
300
250
200
150
100
50
0
-50
-100
-150
-200
0
100
200
300
400
500
600
700
800
900

**Lateral Test # L7**

**Shaft Information and Load - Displacement Data**

| qu (ksf) | 20 | |
|---|---|---|
| Elevation | Model (in) | Prototype (ft) |
| LVDT | -0.650 | -3.63 |
| Load | 0 | 0.00 |
| LVDT | 0.250 | 1.40 |
| surface | 1.183 | 6.61 |
| strain g1 | 1.183 | 6.61 |
| strain g2 | 1.734 | 9.68 |
| strain g3 | 2.285 | 12.76 |
| strain g4 | 2.837 | 15.84 |
| strain g5 | 3.388 | 18.92 |
| strain g6 | 3.939 | 21.99 |
| tip | 4.215 | 23.53 |
| Diameters | | |
| Shaft | 1.060 | 5.92 |
| Rebar cage | 0.750 | 4.19 |

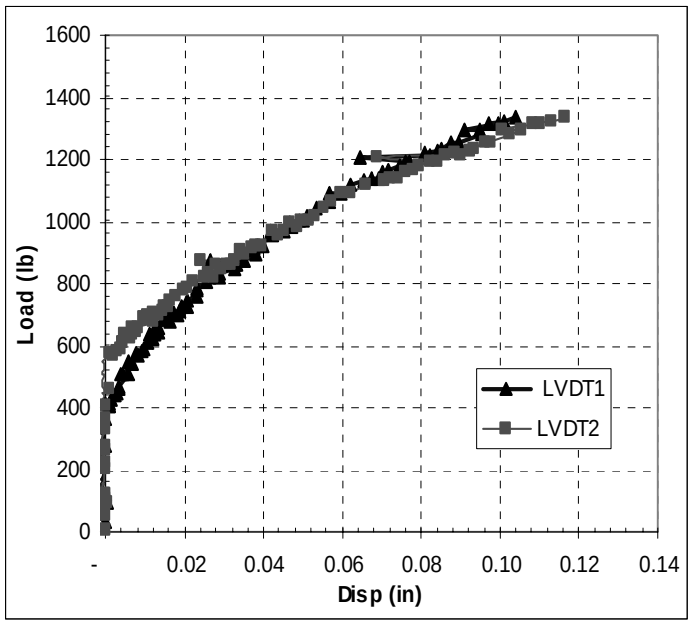


**Load - Strain Data**

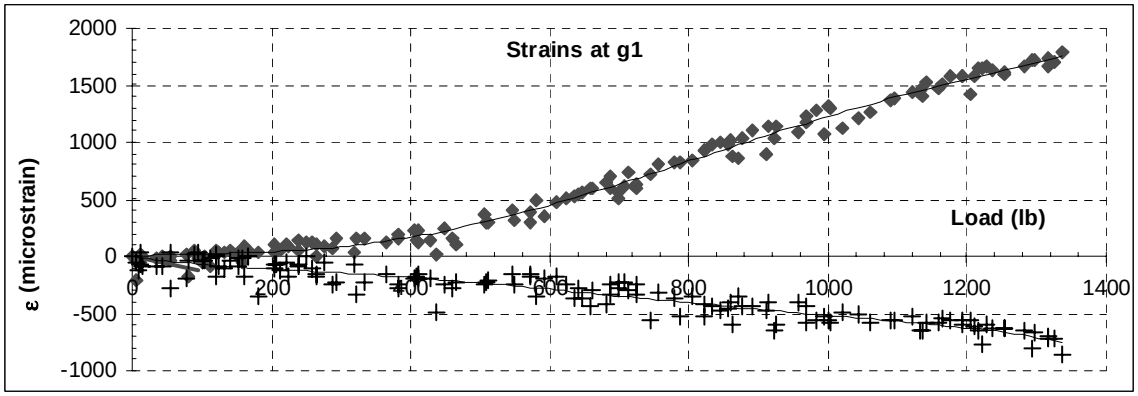


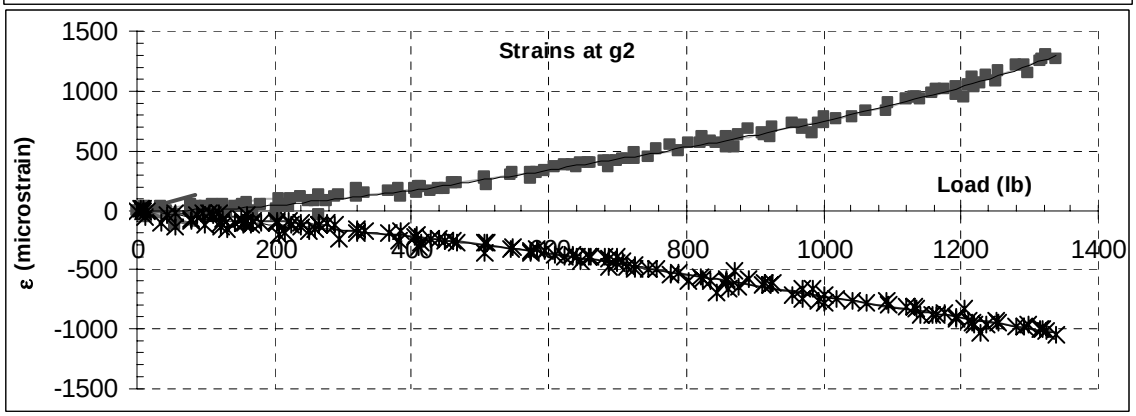

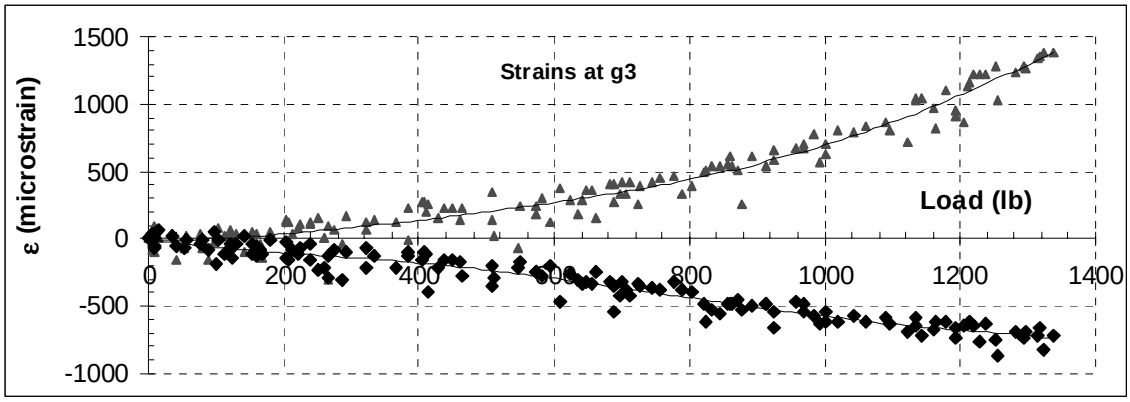
Strains at g3
ε (microstrain)
Load (lb)
1500
1000
500
0
-500
-1000
0
200
400
800
1000
1200
1400

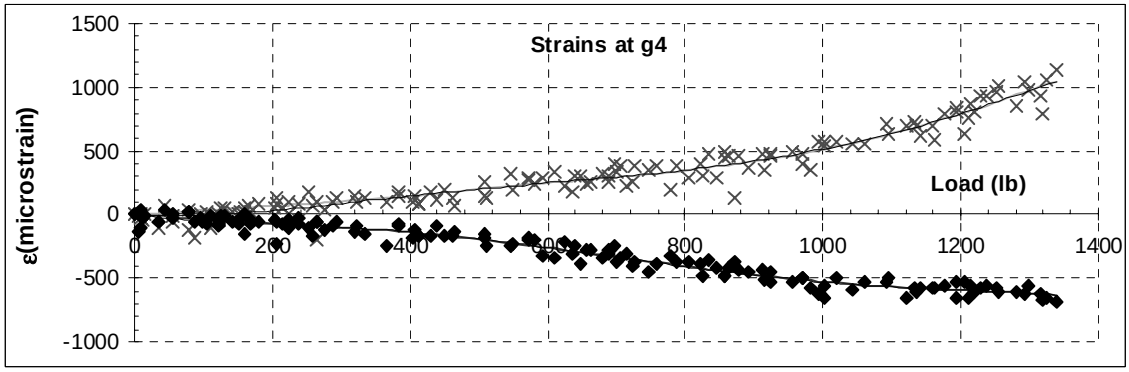
Strains at g4
ε(microstrain)
Load (lb)
1500
1000
500
0
-500
-1000
0
200
400
800
1000
1200
1400

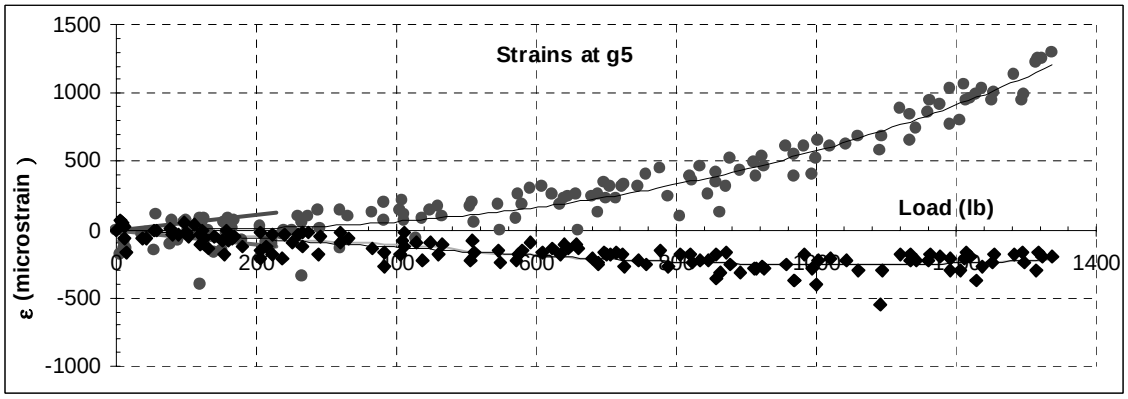
Strains at g5
ε (microstrain )
Load (lb)
1500
1000
500
0
-500
-1000
0
200
400
1400

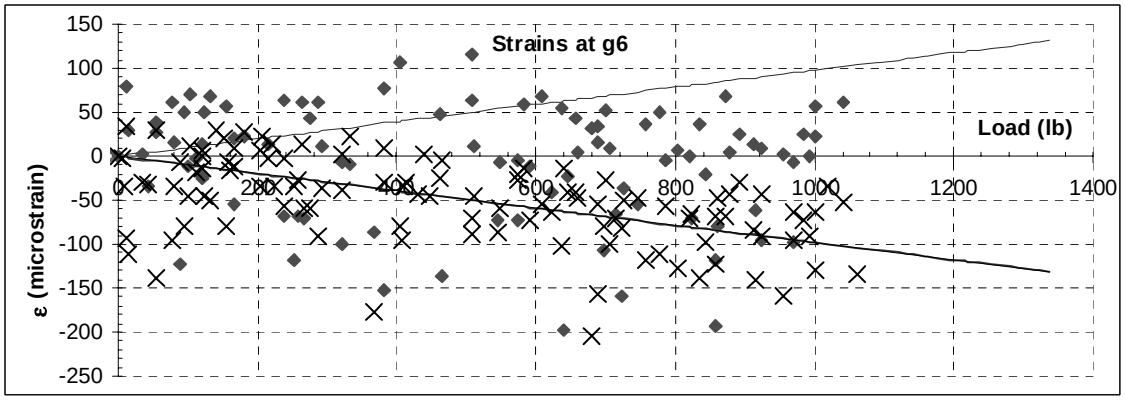
Strains at g6
ε (microstrain)
Load (lb)
150
100
50
0
-50
-100
-150
-200
-250
0
200
400
600
800
1000
1200
1400

**Lateral Test # L8**

**Shaft Information and Load - Displacement Data**

| qu (ksf) | 20 | |
|---|---|---|
| Elevation | Model (in) | Prototype (ft) |
| LVDT | -0.600 | -3.35 |
| Load | 0 | 0.00 |
| LVDT | 0.250 | 1.40 |
| surface | 1.350 | 7.54 |
| strain g1 | 1.350 | 7.54 |
| strain g2 | 2.137 | 11.93 |
| strain g3 | 2.925 | 16.33 |
| strain g4 | 3.712 | 20.73 |
| strain g5 | 4.500 | 25.13 |
| strain g6 | 5.287 | 29.52 |
| tip | 5.759 | 32.15 |
| Diameters | | |
| Shaft | 1.580 | 8.82 |
| Rebar cage | 1.310 | 7.31 |

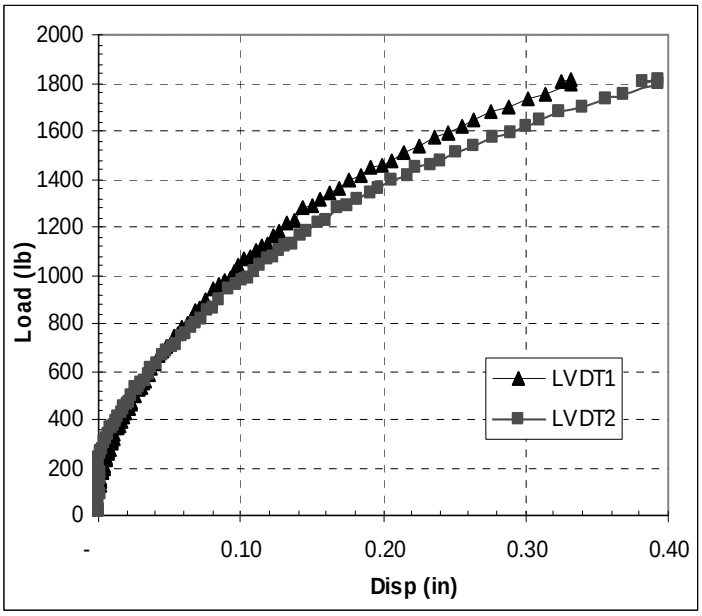


**Load - Strain data**

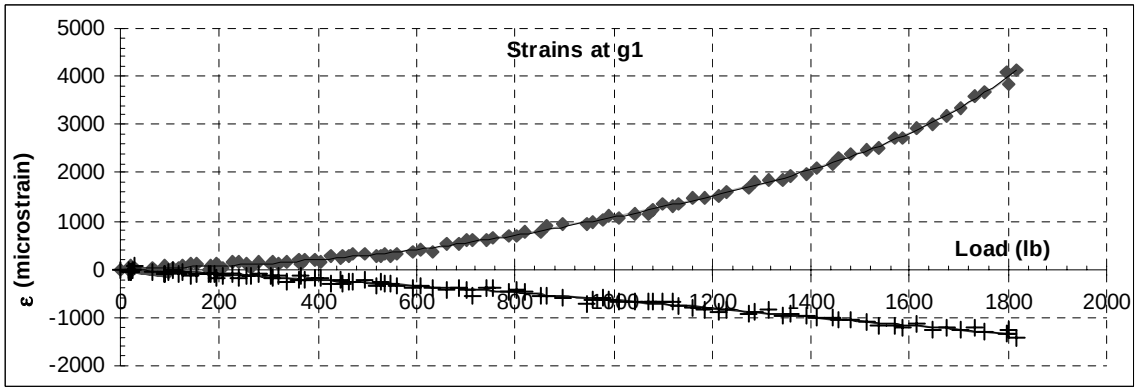


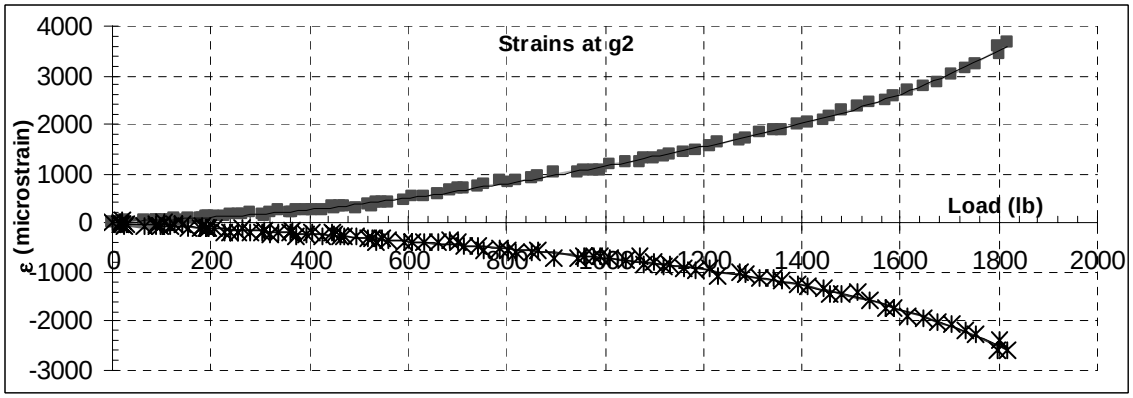

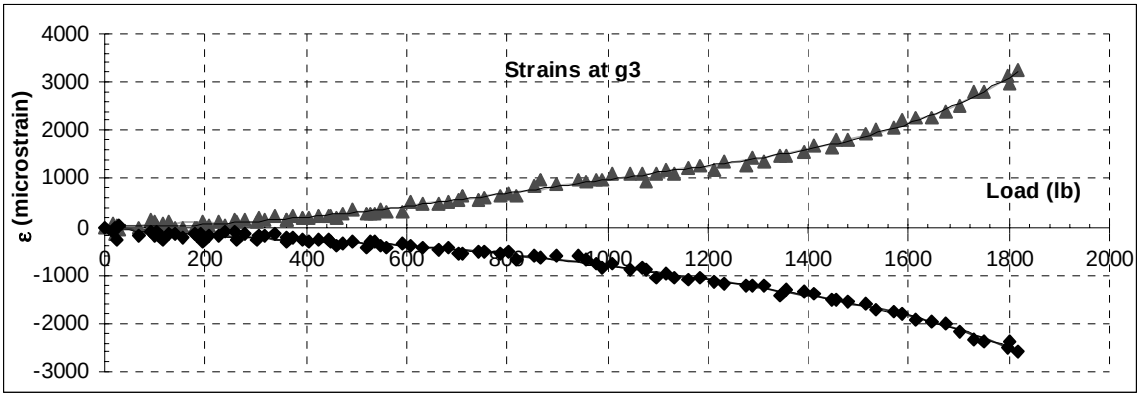
Strains at g3
ε (microstrain)
Load (lb)
4000
3000
2000
1000
0
-1000
-2000
-3000
0
200
400
600
800
1000
1200
1400
1600
1800
2000

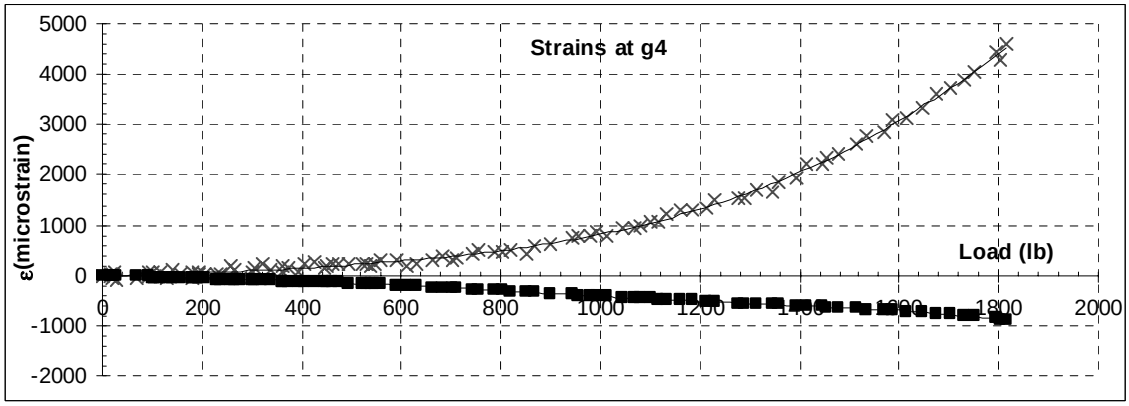
Strains at g4
ε(microstrain)
Load (lb)
5000
4000
3000
2000
1000
0
-1000
-2000
0
200
400
600
800
1000
1200
1800
2000

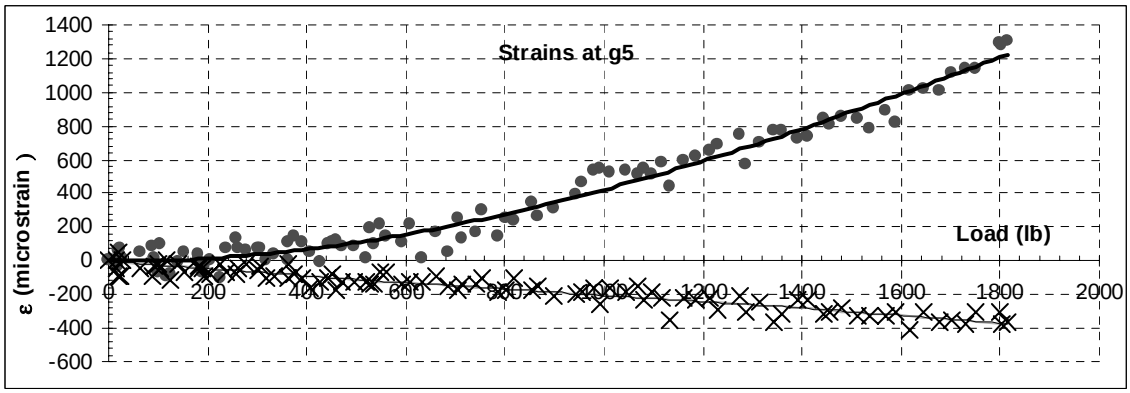
Strains at g5
ε (microstrain )
Load (lb)
1400
1200
1000
800
600
400
200
0
-200
-400
-600
0
200
400
600
1200
1400
1600
1800
2000

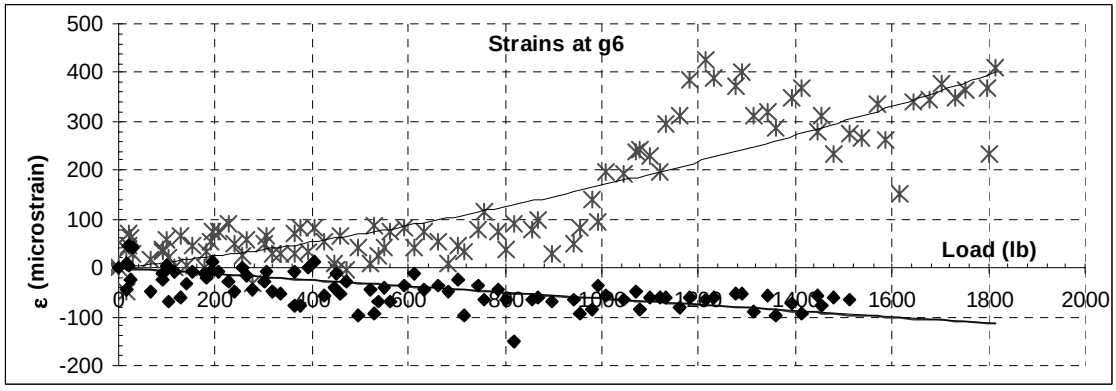
Strains at g6
ε (microstrain)
Load (lb)
500
400
300
200
100
0
-100
-200
0
200
400
600
800
1000
1200
1400
1600
1800
2000

**Lateral Test # L9**

**Shaft Information and Load - Displacement Data**

| qu (ksf) | 40 | |
|---|---|---|
| Elevation | Model (in) | Prototype (ft) |
| LVDT | -0.897 | -5.01 |
| Load | 0 | 0.00 |
| LVDT | 0.153 | 0.85 |
| surface | 1.183 | 6.61 |
| strain g1 | 1.183 | 6.61 |
| strain g2 | 1.892 | 10.56 |
| strain g3 | 2.600 | 14.52 |
| strain g4 | 3.309 | 18.48 |
| strain g5 | 4.018 | 22.43 |
| strain g6 | 4.726 | 26.39 |
| tip | 5.081 | 28.37 |
| Diameters | | |
| Shaft | 1.060 | 5.92 |
| Rebar cage | 0.750 | 4.19 |

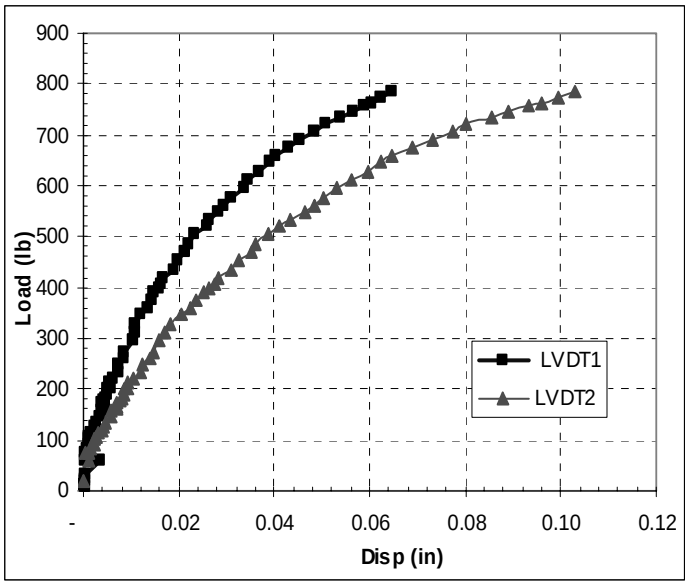


**Load - Strain Data**

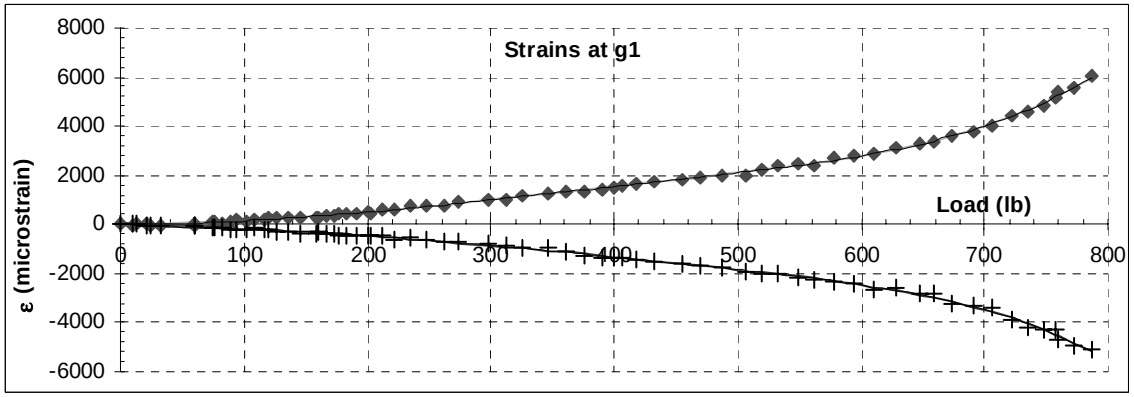


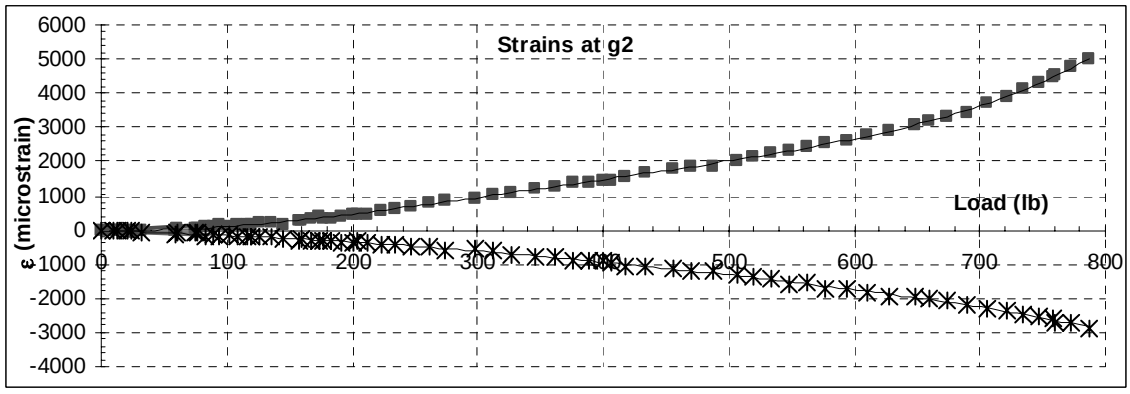

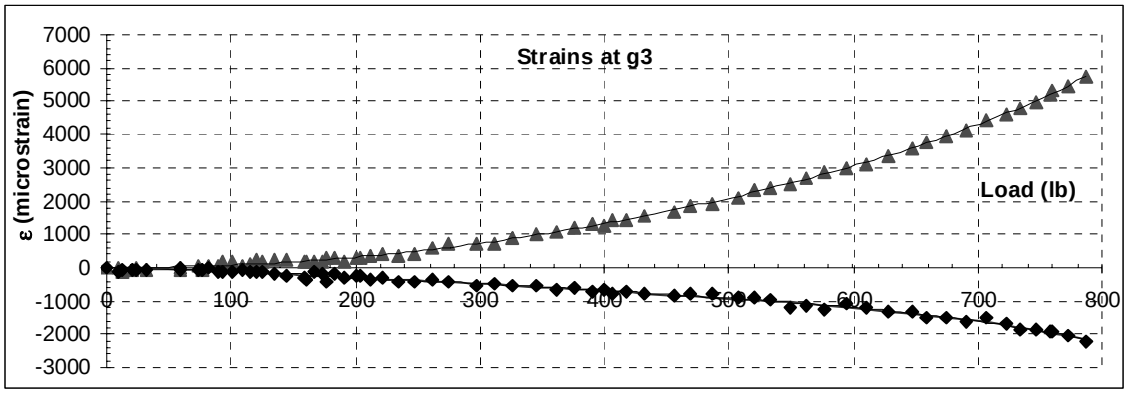
Strains at g3
ε (microstrain)
Load (lb)
7000
6000
5000
4000
3000
2000
1000
0
-1000
-2000
-3000
0
100
200
300
400
500
600
700
800

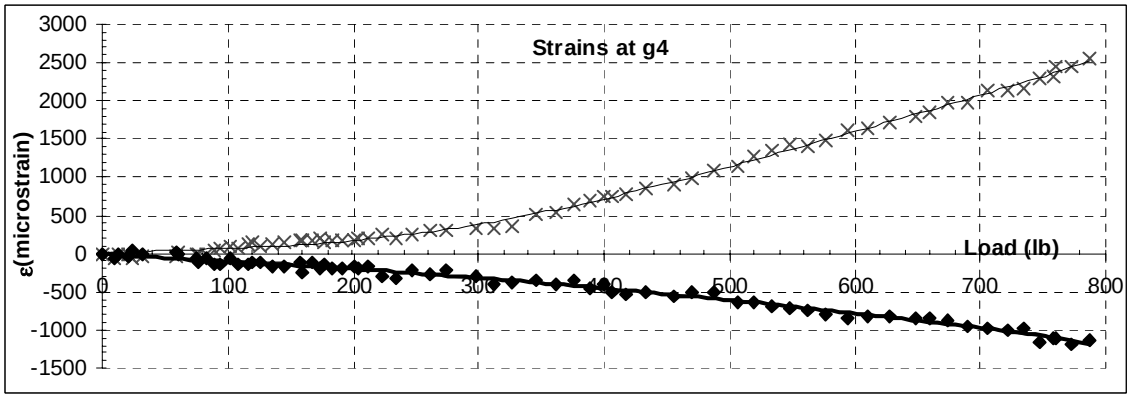
Strains at g4
ε(microstrain)
Load (lb)
3000
2500
2000
1500
1000
500
0
-500
-1000
-1500
0
100
200
300
400
500
600
700
800

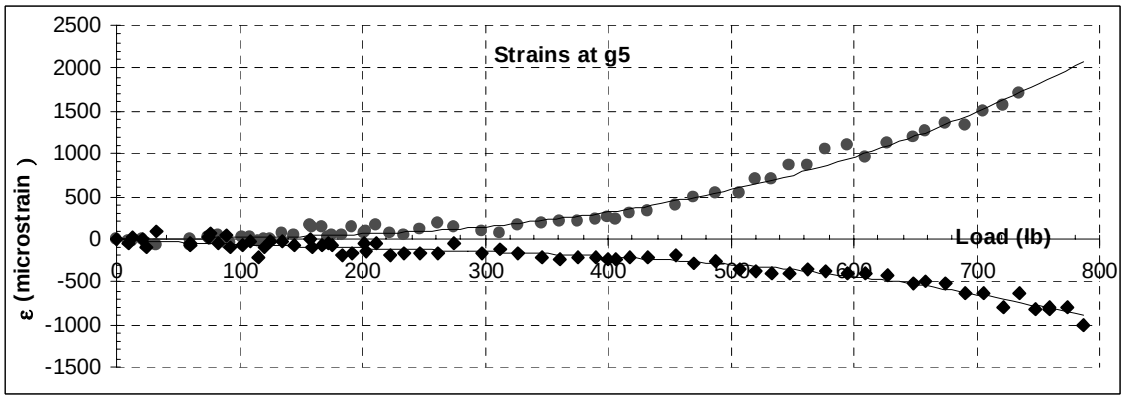
Strains at g5
ε (microstrain )
Load (lb)
2500
2000
1500
1000
500
0
-500
-1000
-1500
0
100
200
300
400
500
600
700
800

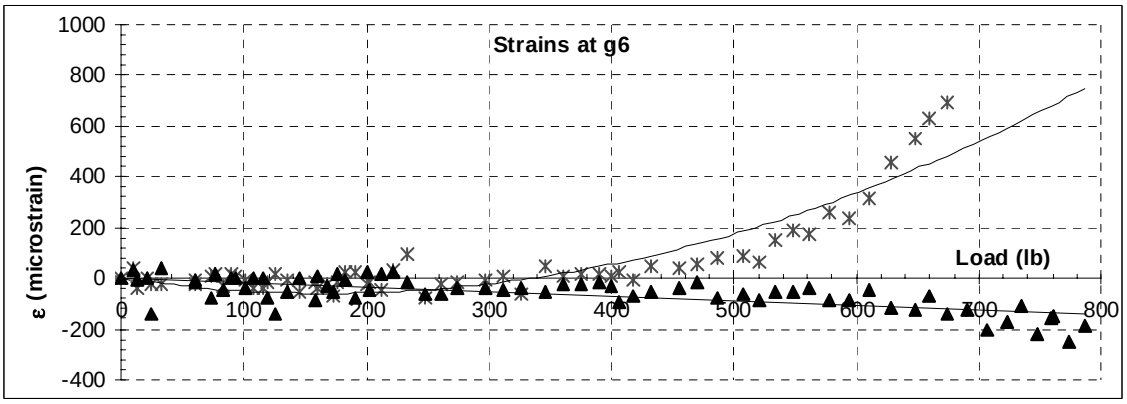
Strains at g6
ε (microstrain)
Load (lb)
1000
800
600
400
200
0
-200
-400
0
100
200
300
400
500
600
700
800

**Lateral Test # L10**

**Shaft Information and Load - Displacement Data**

| qu (ksf) | 40 | |
|---|---|---|
| Elevation | Model (in) | Prototype (ft) |
| LVDT | -0.930 | -5.19 |
| Load | 0 | 0.00 |
| LVDT | 0.060 | 0.34 |
| surface | 1.253 | 7.00 |
| strain g1 | 1.253 | 7.00 |
| strain g2 | 1.844 | 10.30 |
| strain g3 | 2.434 | 13.59 |
| strain g4 | 3.025 | 16.89 |
| strain g5 | 3.615 | 20.18 |
| strain g6 | 4.205 | 23.48 |
| tip | 4.481 | 25.02 |
| Diameters | | |
| Shaft | 1.580 | 8.82 |
| Rebar cage | 1.310 | 7.31 |

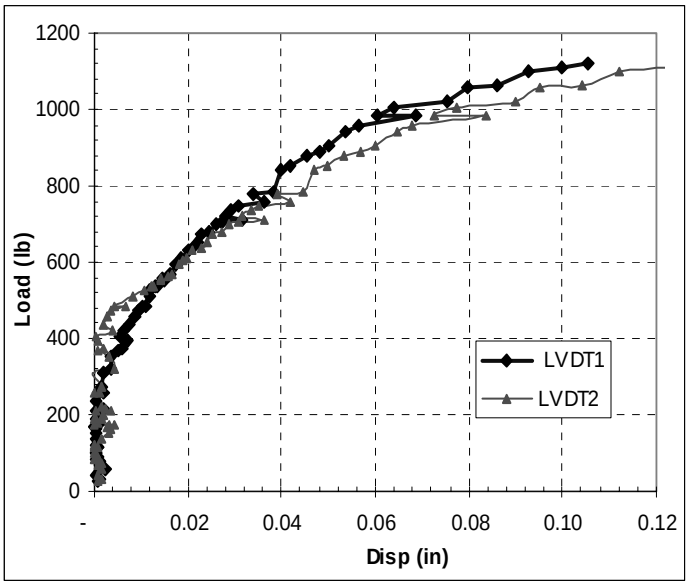


**Load - Strain Data**

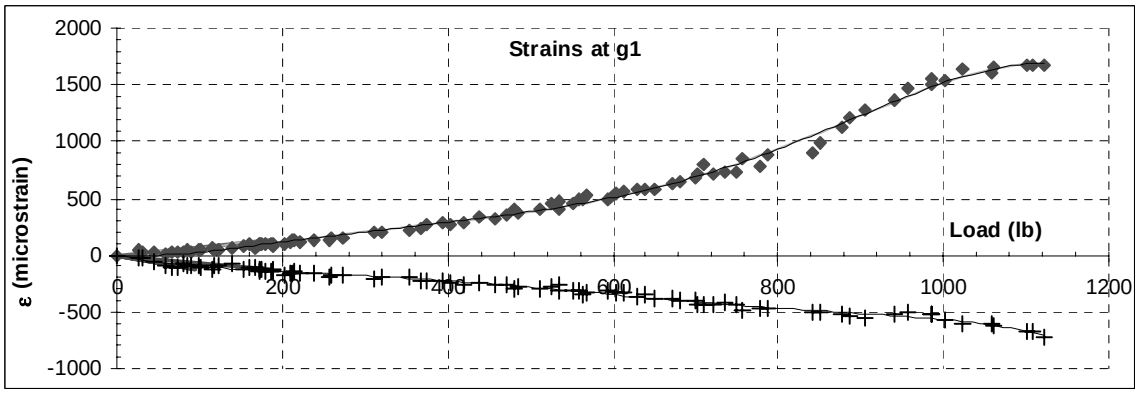


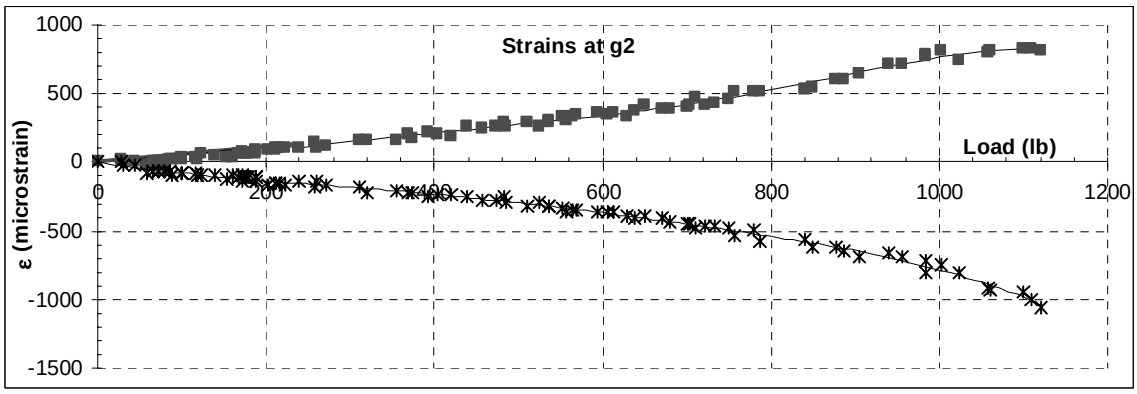

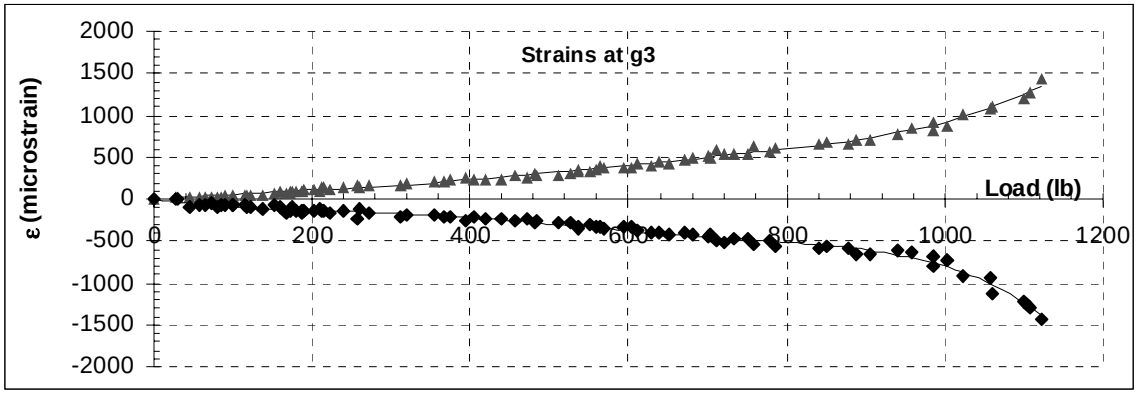
Strains at g3
ε (microstrain)
Load (lb)
2000
1500
1000
500
0
-500
-1000
-1500
-2000
0
200
400
600
800
1000
1200

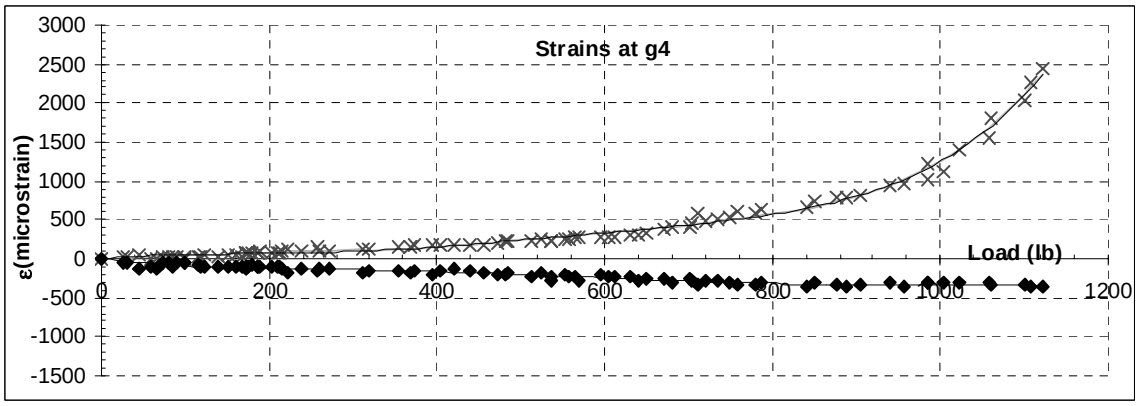
Strains at g4
ε(microstrain)
Load (lb)
3000
2500
2000
1500
1000
500
0
-500
-1000
-1500
0
200
400
600
800
1000
1200

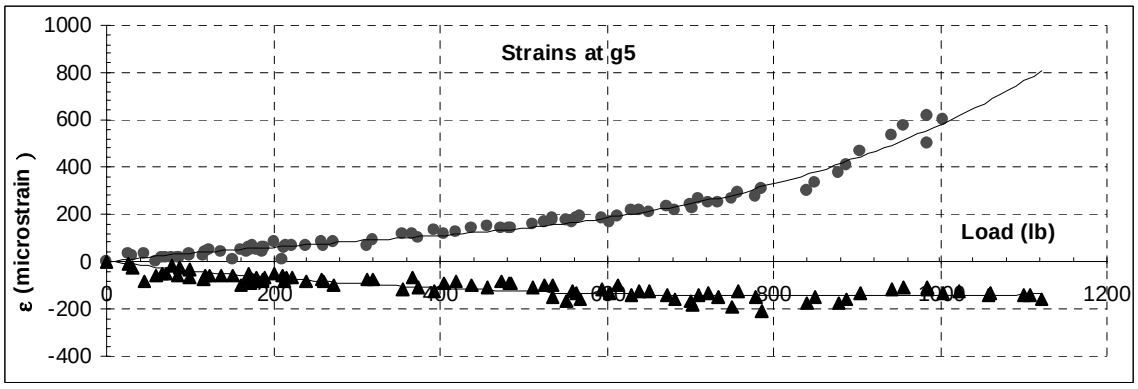
Strains at g5
ε (microstrain )
Load (lb)
1000
800
600
400
200
0
-200
-400
0
200
400
600
800
1000
1200

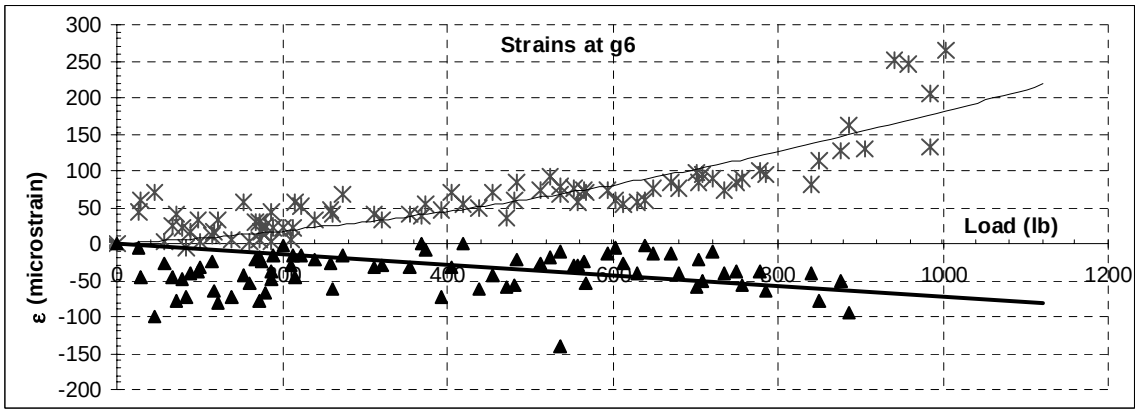
Strains at g6
ε (microstrain)
Load (lb)
300
250
200
150
100
50
0
-50
-100
-150
-200
0
200
400
600
800
1000
1200

**Lateral Test # L11**

**Shaft Information and Load - Displacement Data**

| qu (ksf) | 40 | |
|---|---|---|
| Elevation | Model (in) | Prototype (ft) |
| LVDT | -0.700 | -3.91 |
| Load | 0 | 0.00 |
| LVDT | 0.300 | 1.68 |
| surface | 1.233 | 6.88 |
| strain g1 | 1.233 | 6.88 |
| strain g2 | 1.824 | 10.18 |
| strain g3 | 2.414 | 13.48 |
| strain g4 | 3.005 | 16.78 |
| strain g5 | 3.595 | 20.07 |
| strain g6 | 4.186 | 23.37 |
| tip | 4.461 | 24.91 |
| Diameters | | |
| Shaft | 1.580 | 8.82 |
| Rebar cage | 1.310 | 7.31 |

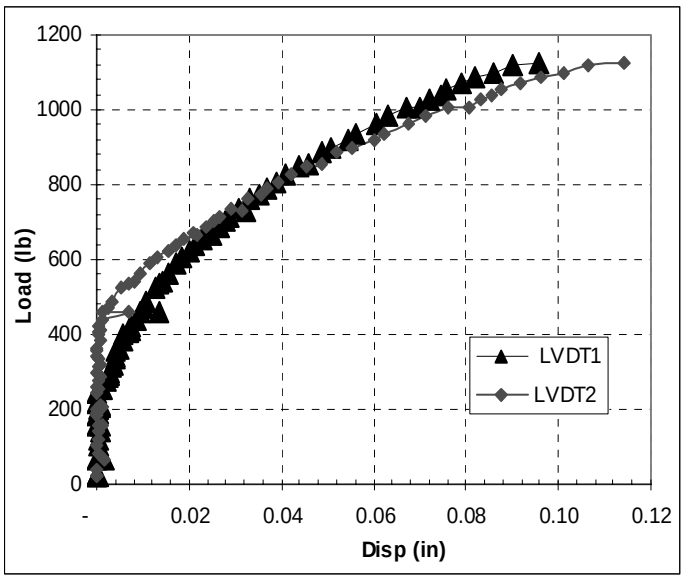


**Load - Strain Data**

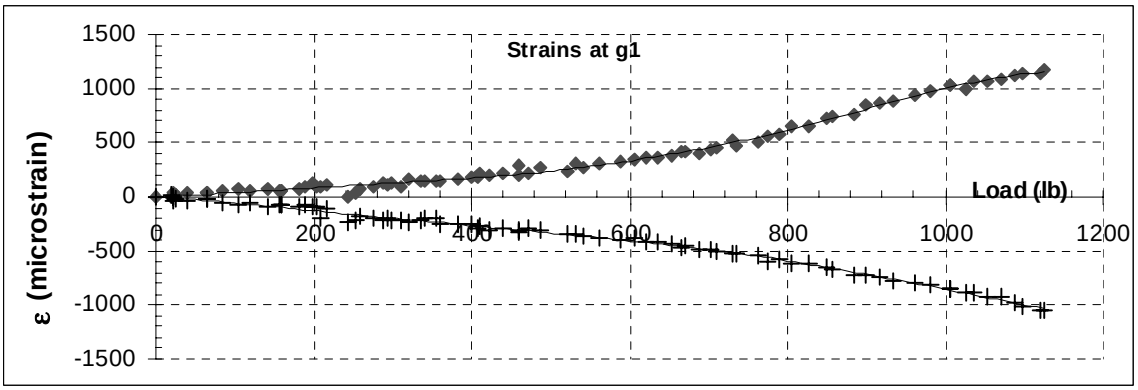


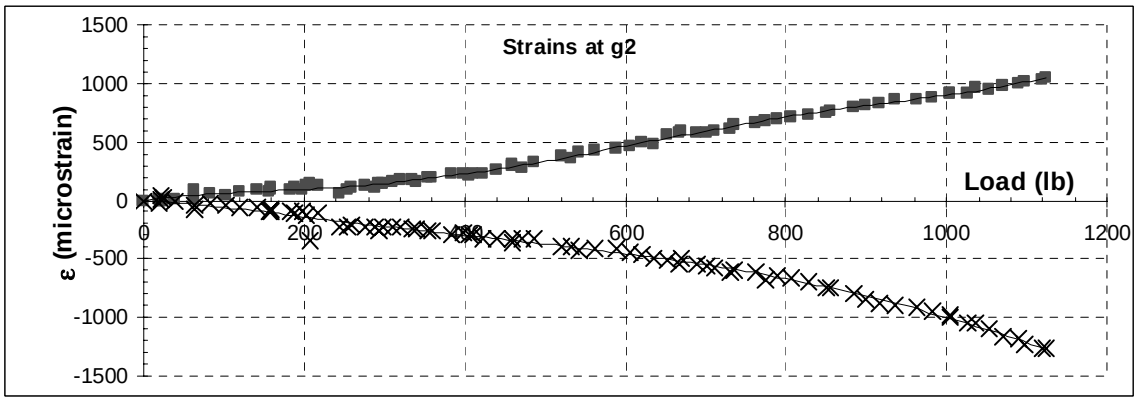

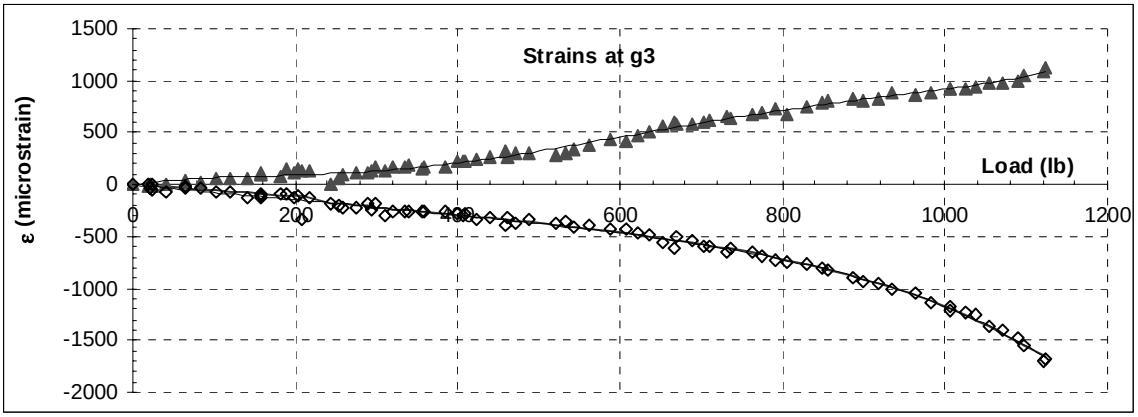
Strains at g3
ε (microstrain)
Load (lb)
1500
1000
500
0
-500
-1000
-1500
-2000
0
200
400
600
800
1000
1200

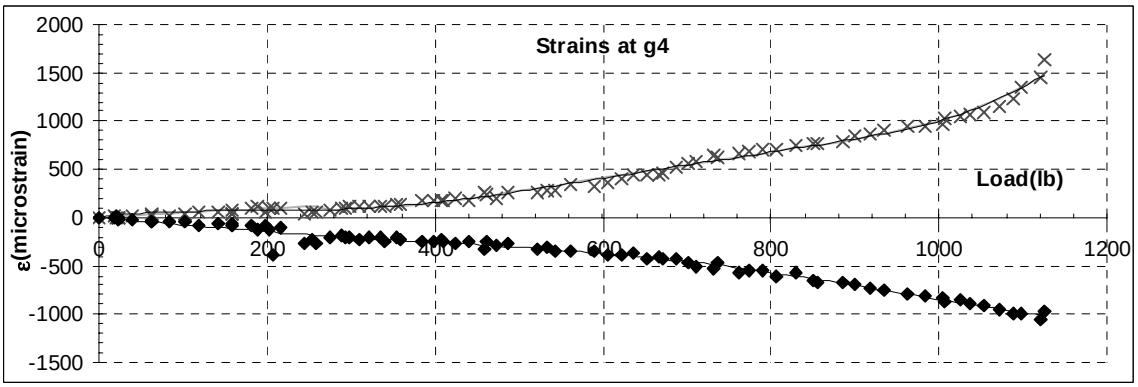
Strains at g4
ε(microstrain)
Load(lb)
2000
1500
1000
500
0
-500
-1000
-1500
0
200
400
600
800
1000
1200

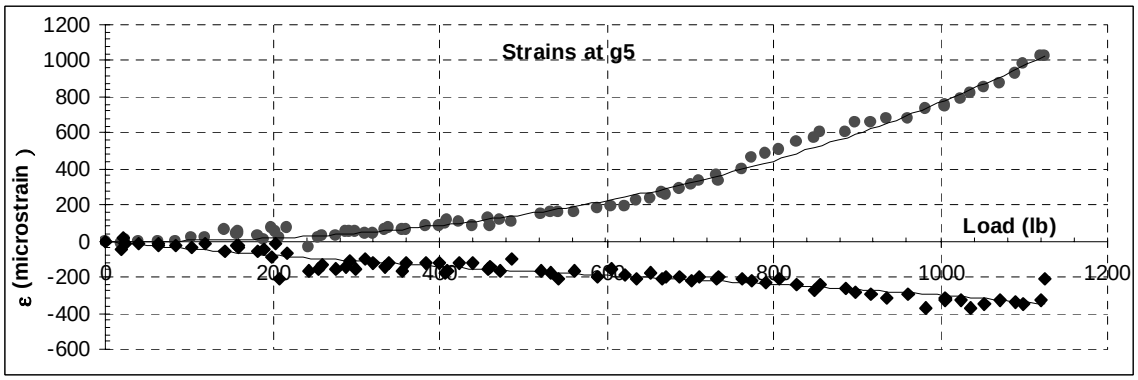
Strains at g5
ε (microstrain )
Load (lb)
1200
1000
800
600
400
200
0
-200
-400
-600
0
200
400
600
800
1000
1200

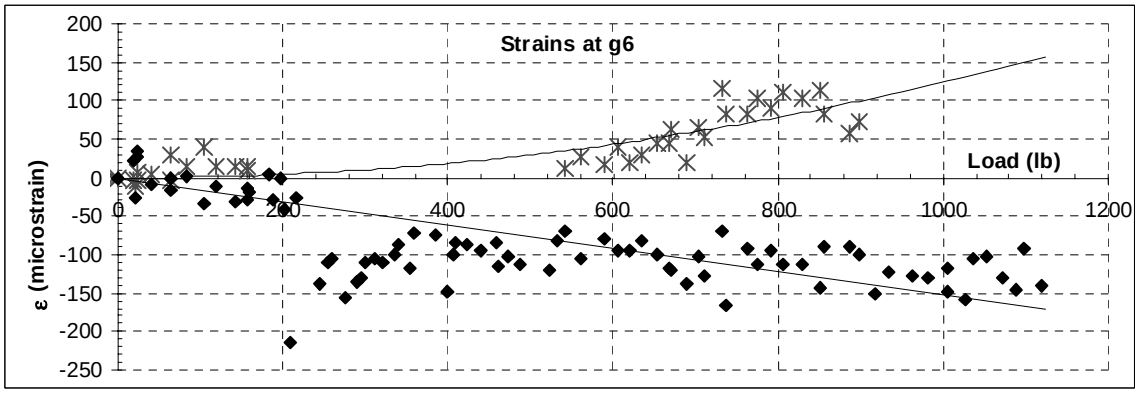
Strains at g6
ε (microstrain)
Load (lb)
200
150
100
50
0
-50
-100
-150
-200
-250
0
200
400
600
800
1000
1200

**Lateral Test # L12**

**Shaft Information and Load - Displacement Data**

| qu (ksf) | 40 | |
|---|---|---|
| Elevation | Model (in) | Prototype (ft) |
| LVDT | -0.700 | -3.91 |
| Load | 0 | 0.00 |
| LVDT | 0.300 | 1.68 |
| surface | 1.233 | 6.88 |
| strain g1 | 1.233 | 6.88 |
| strain g2 | 1.745 | 9.74 |
| strain g3 | 2.257 | 12.60 |
| strain g4 | 2.769 | 15.46 |
| strain g5 | 3.280 | 18.31 |
| strain g6 | 3.792 | 21.17 |
| tip | 4.028 | 22.49 |
| Diameters | | |
| Shaft | 1.060 | 5.92 |
| Rebar cage | 0.750 | 4.19 |

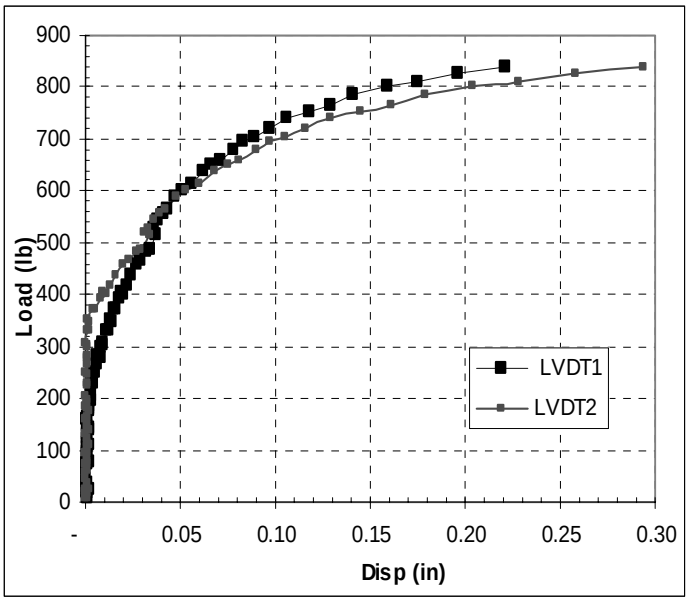


**Load - Strain Data**

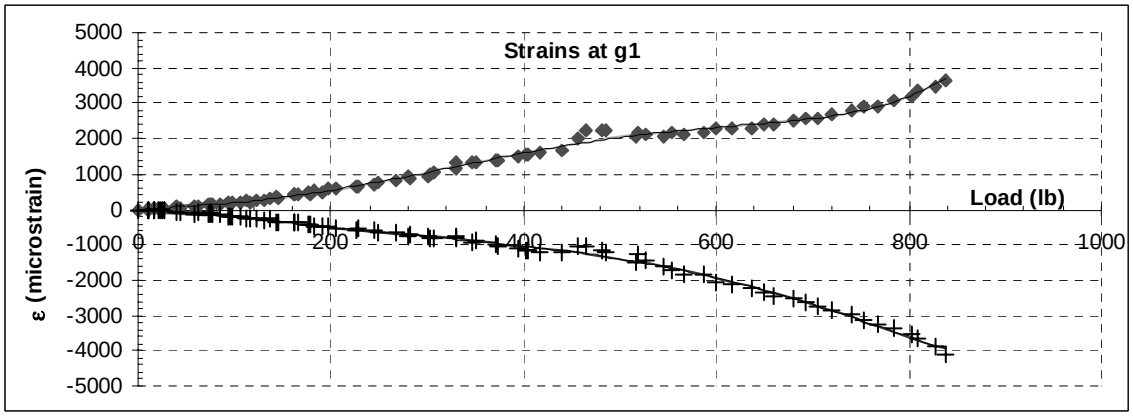


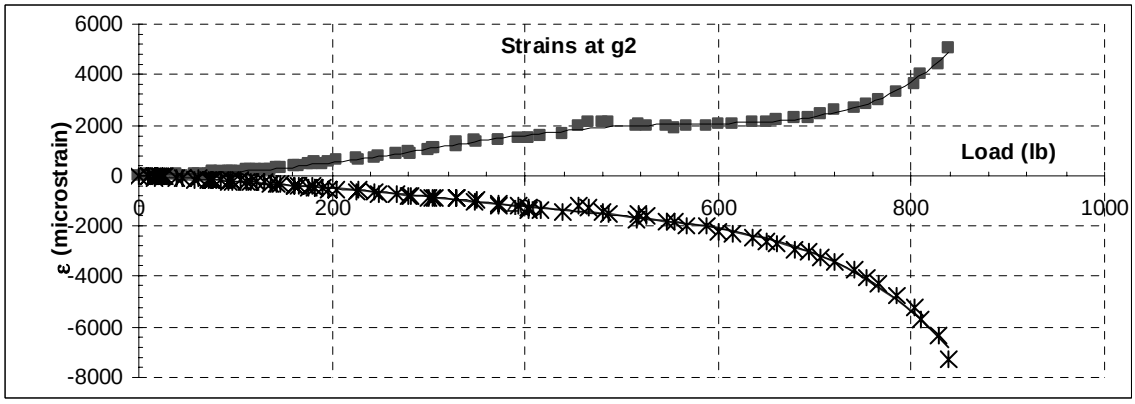

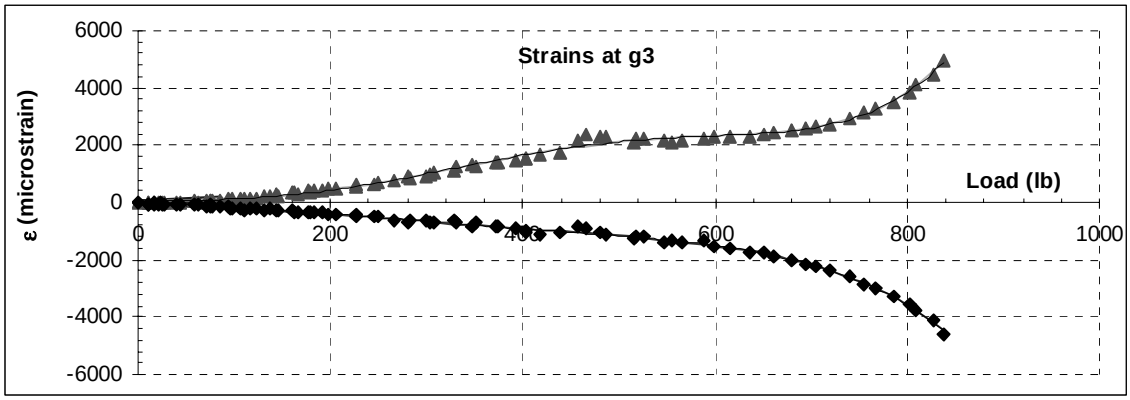
Strains at g3
ε (microstrain)
Load (lb)
6000
4000
2000
0
-2000
-4000
-6000
0
200
400
600
800
1000

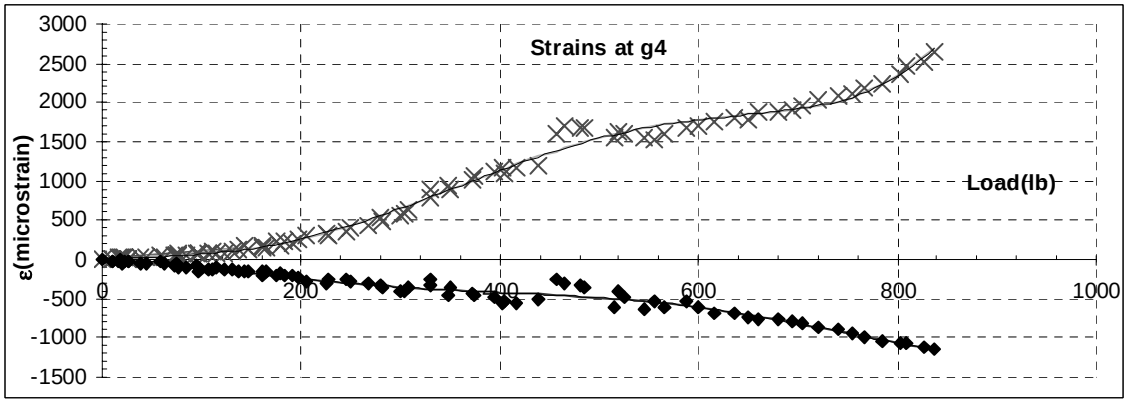
Strains at g4
ε(microstrain)
Load(lb)
3000
2500
2000
1500
1000
500
0
-500
-1000
-1500
0
200
400
600
800
1000

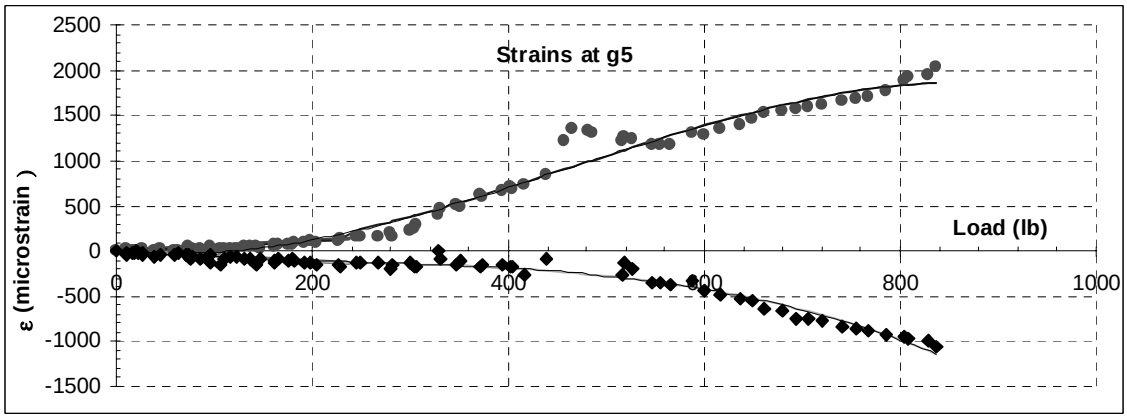
Strains at g5
ε (microstrain )
Load (lb)
2500
2000
1500
1000
500
0
-500
-1000
-1500
0
200
400
600
800
1000

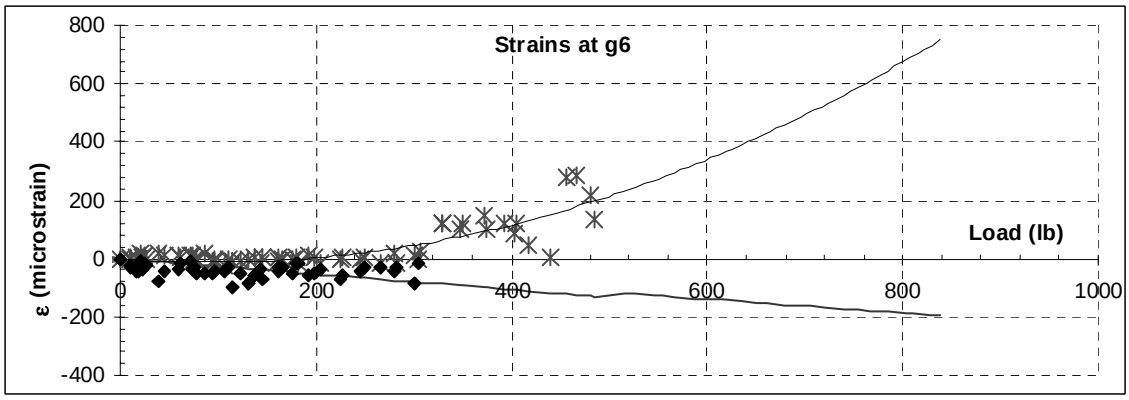
Strains at g6
ε (microstrain)
Load (lb)
800
600
400
200
0
-200
-400
0
200
400
600
800
1000

# Appendix B

## P-Y CURVES AND COMPARISON OF LATERAL DISPLACEMENTS

### Lateral Test # L1

### P-Y Curves

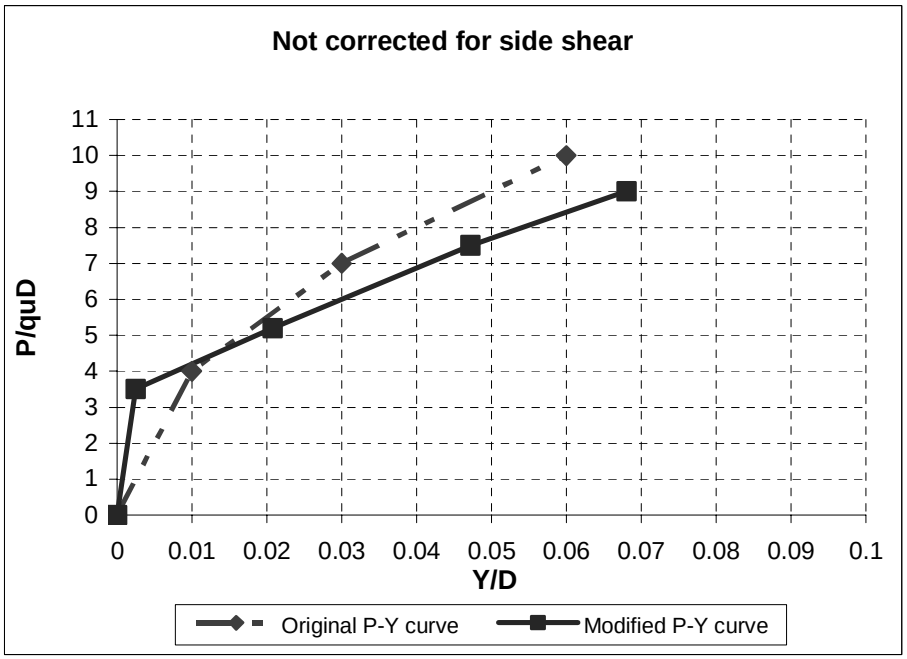


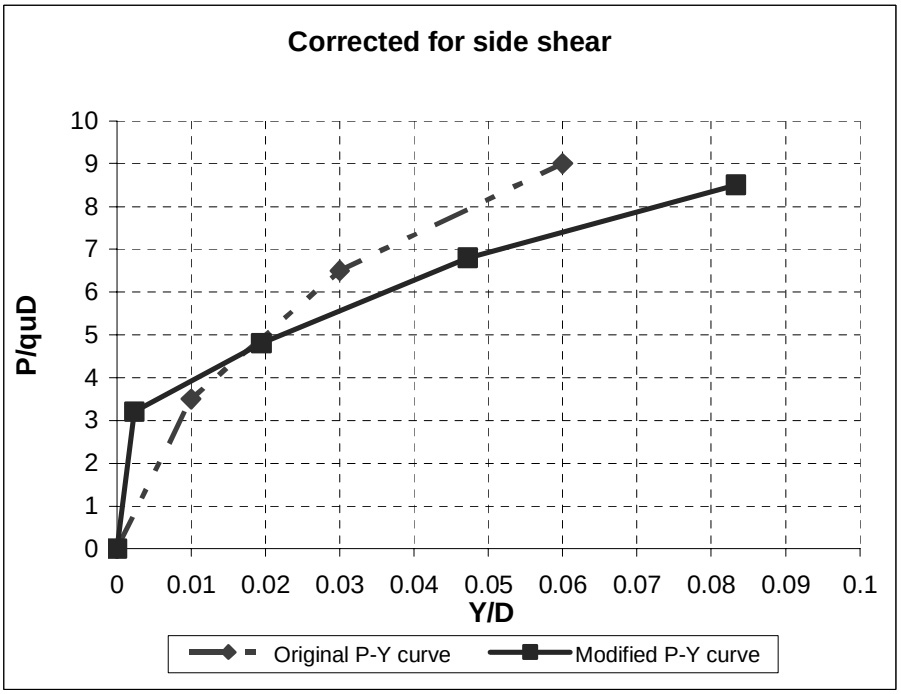

## Lateral Displacements (Not Corrected for Side Shear)

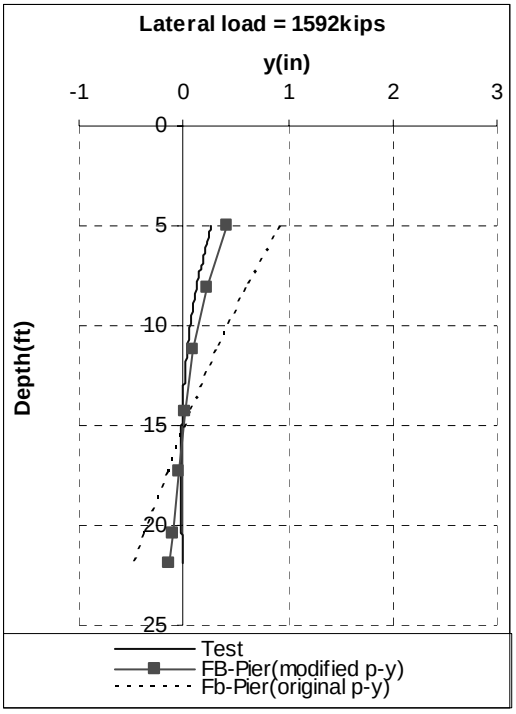


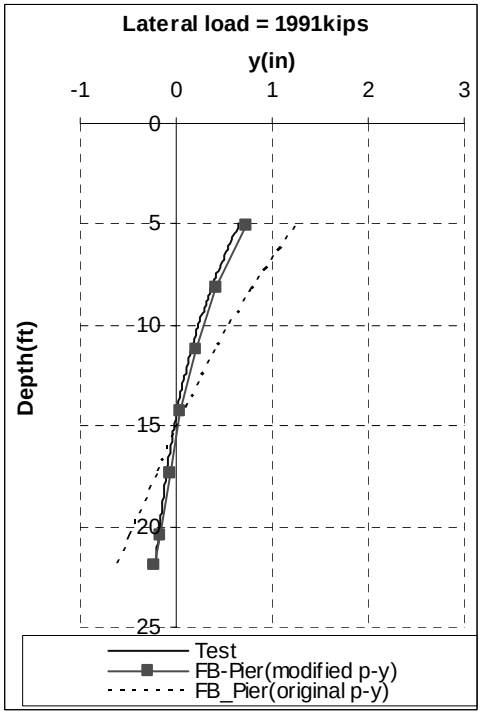


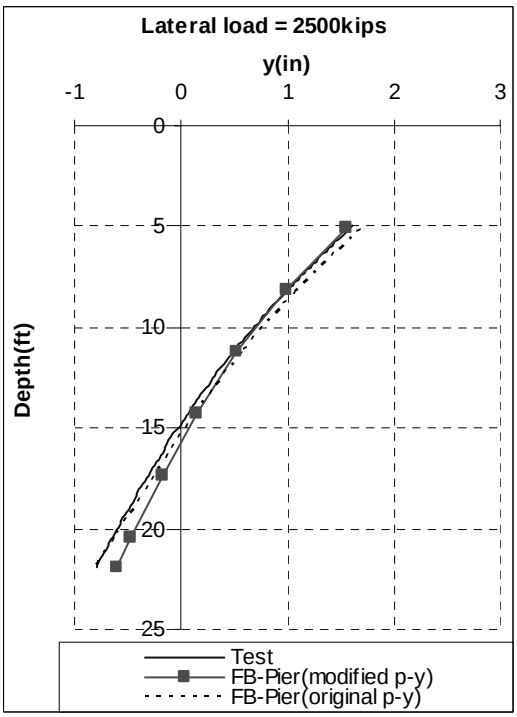


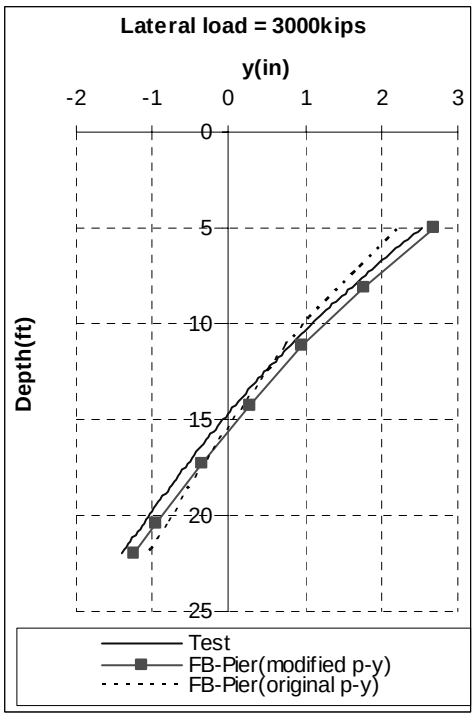

## Lateral Displacements (Corrected for Side Shear)

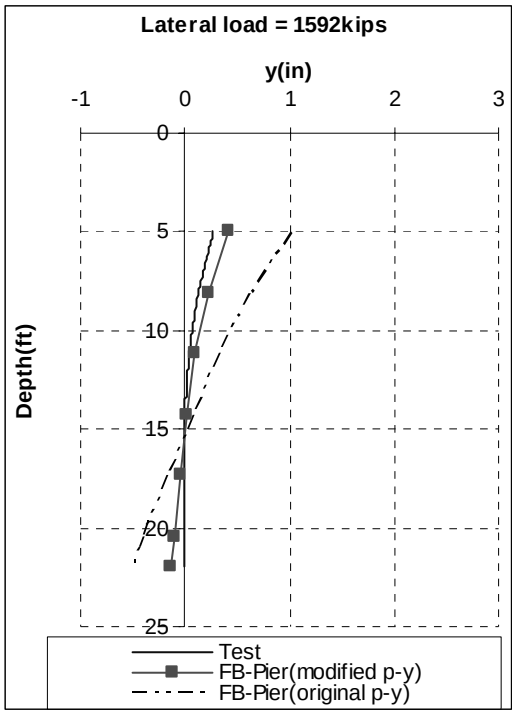


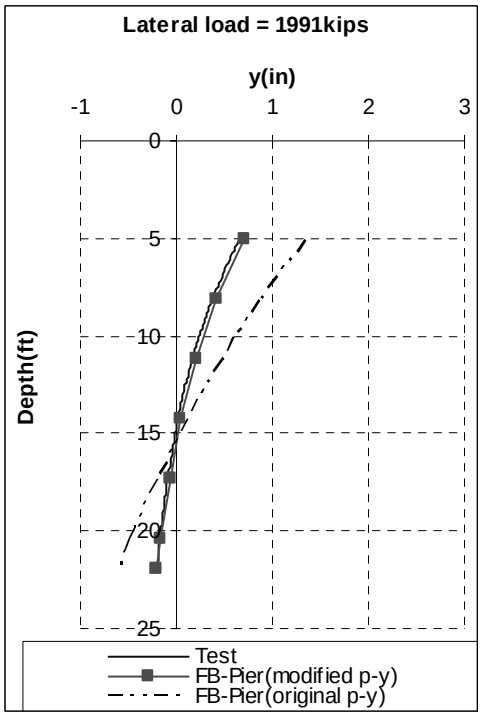


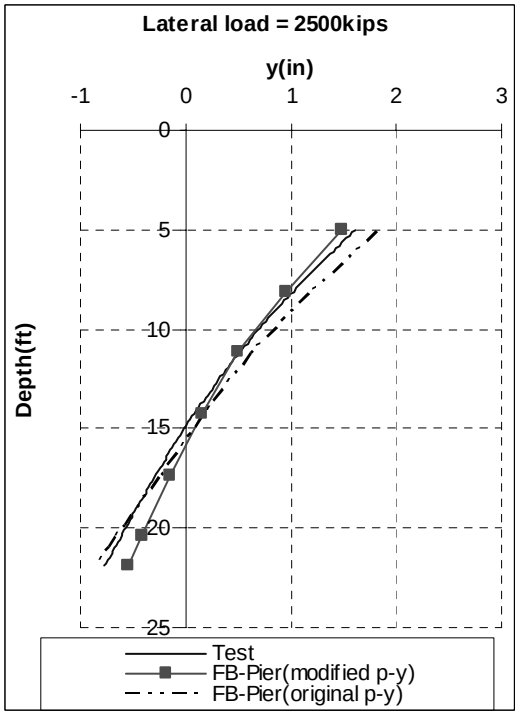


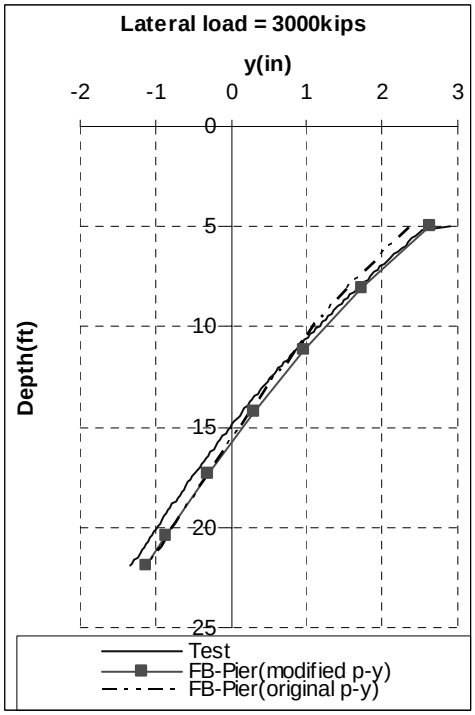

**Lateral Test # L2**

**P-Y Curves**

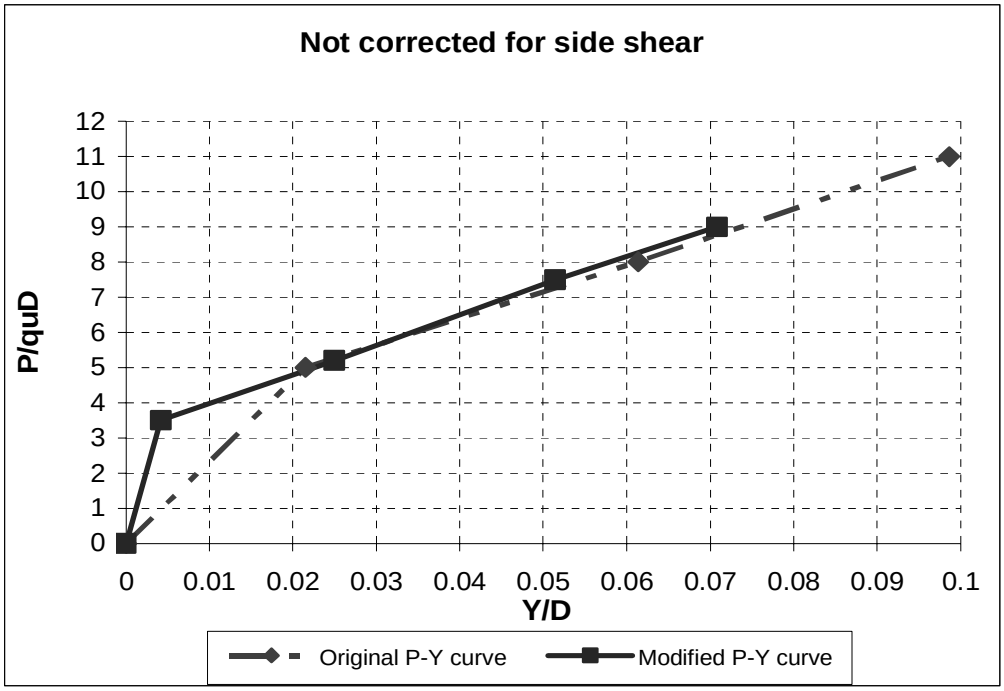


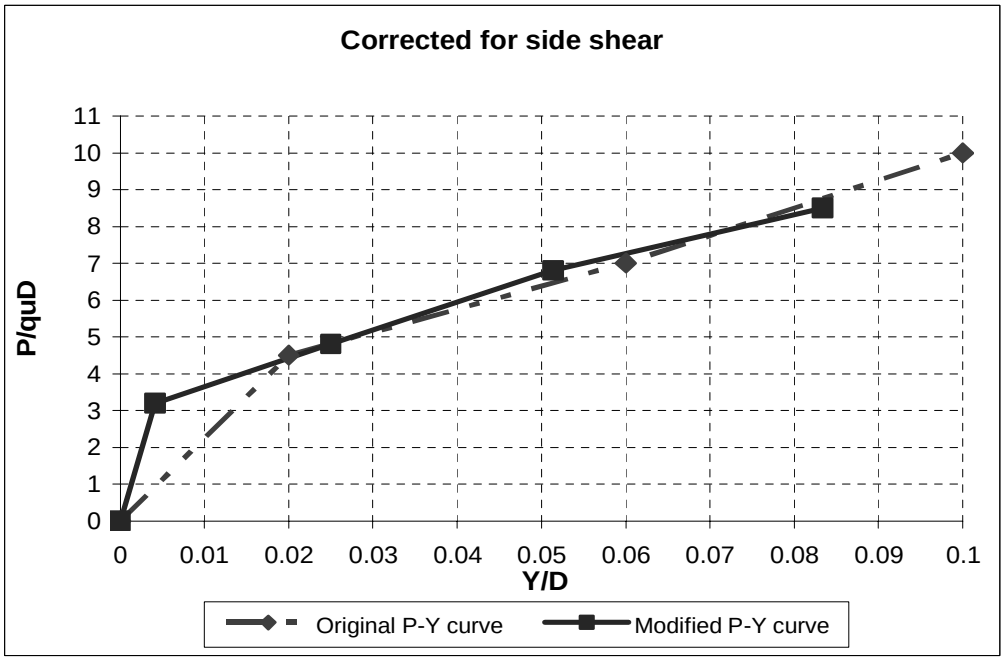

## Lateral Displacements (Not Corrected for Side Shear)

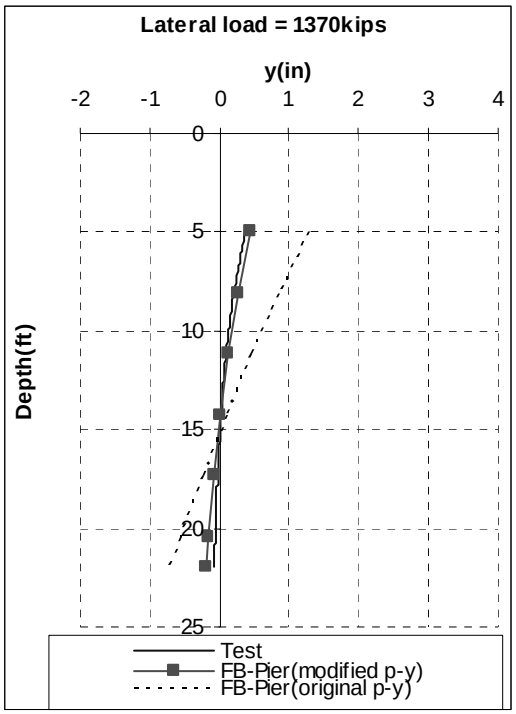


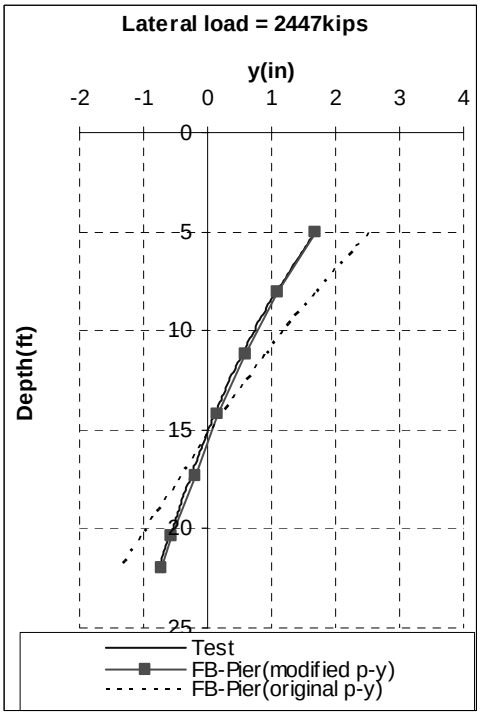


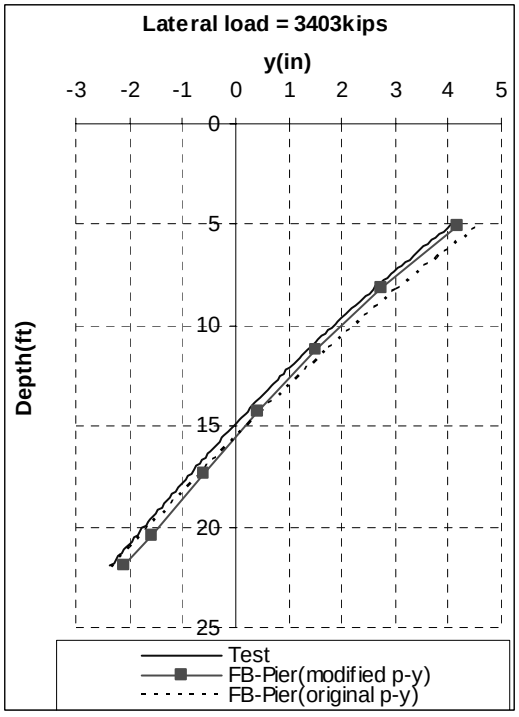

## Lateral Displacements (Corrected for Side Shear)

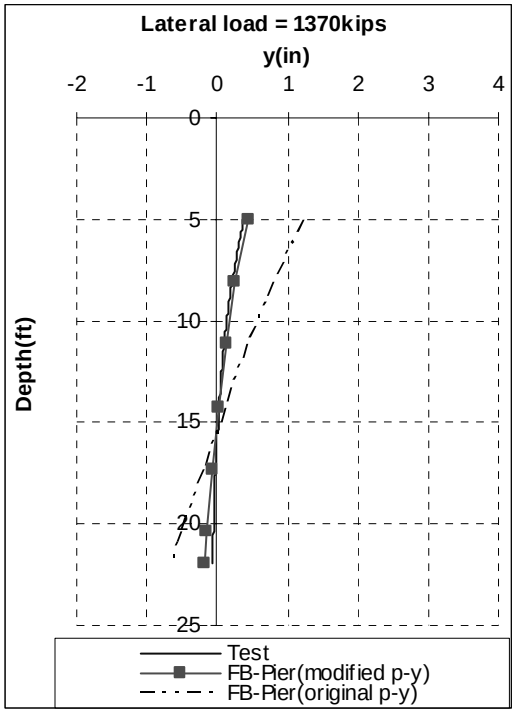


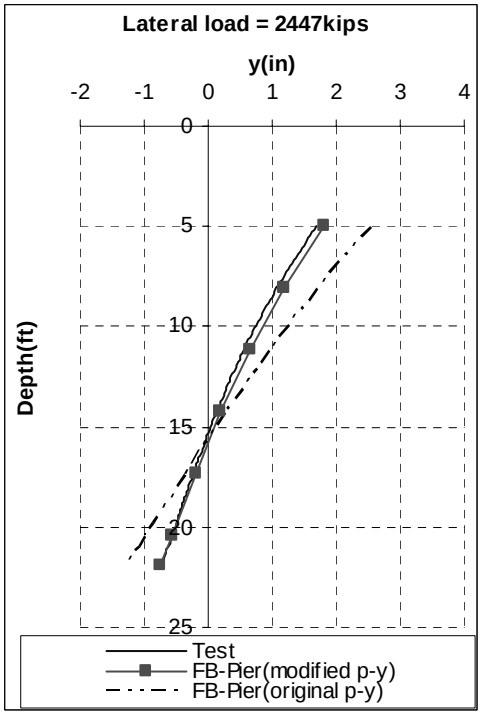


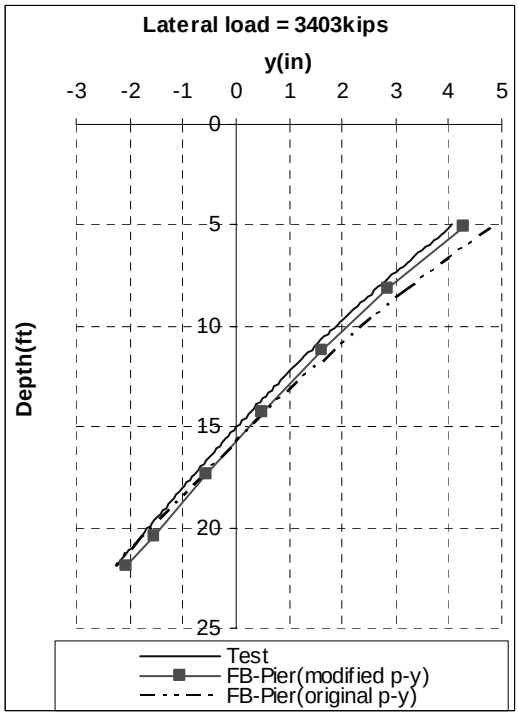

**Lateral Test # L3**

**P-Y Curves**

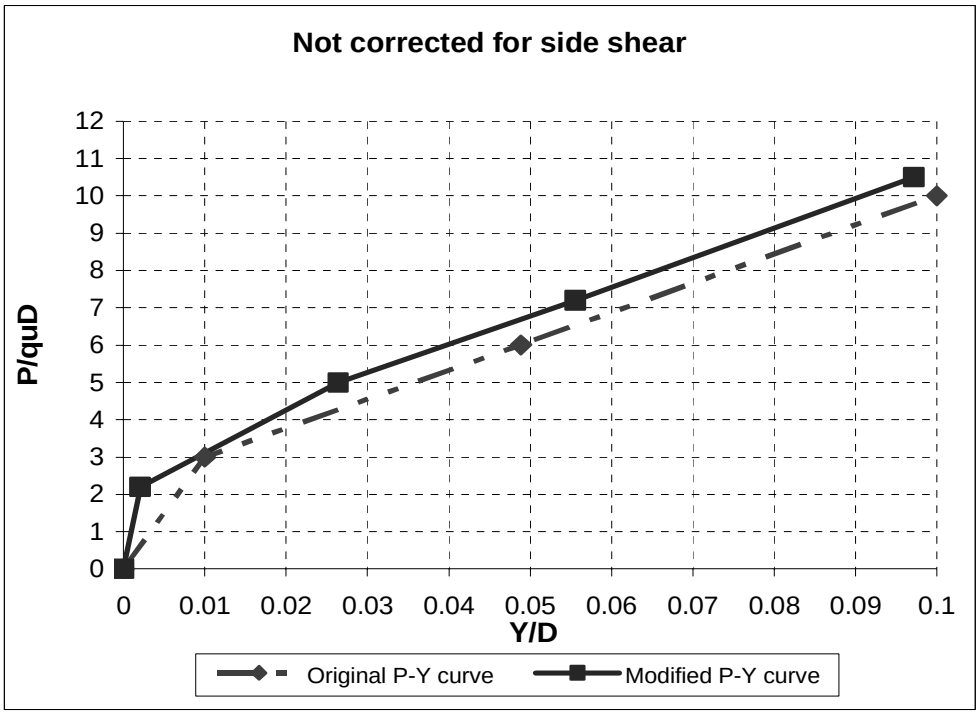


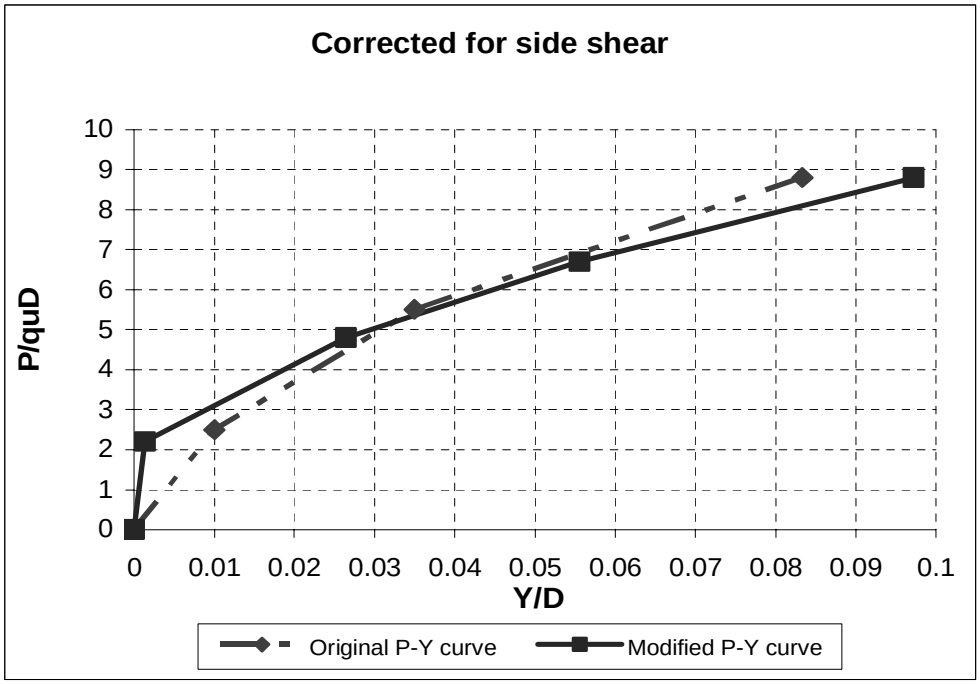

## Lateral Displacements (Not Corrected for Side Shear)

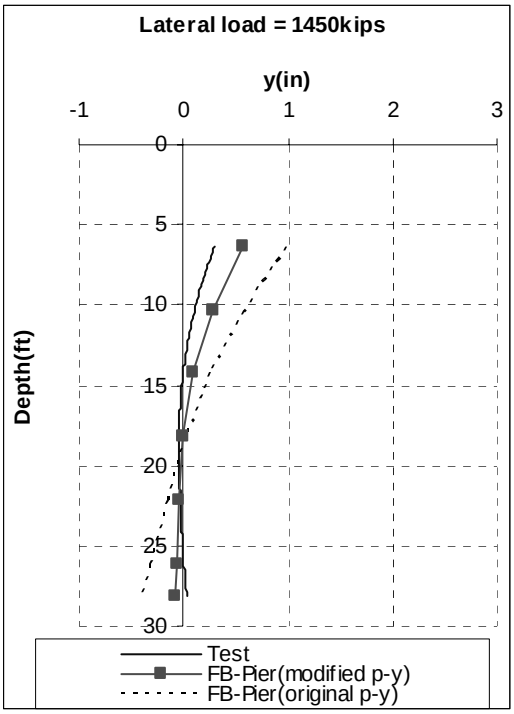


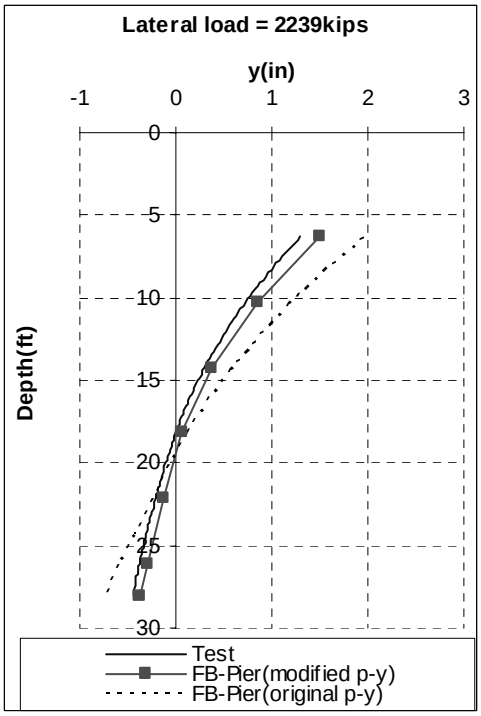


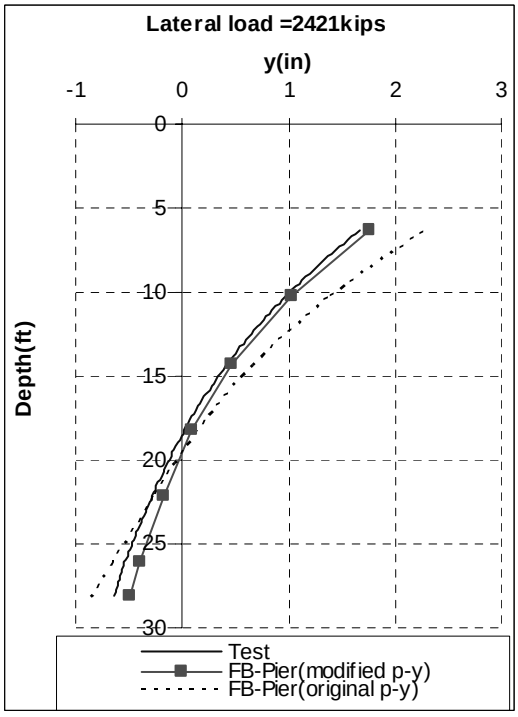


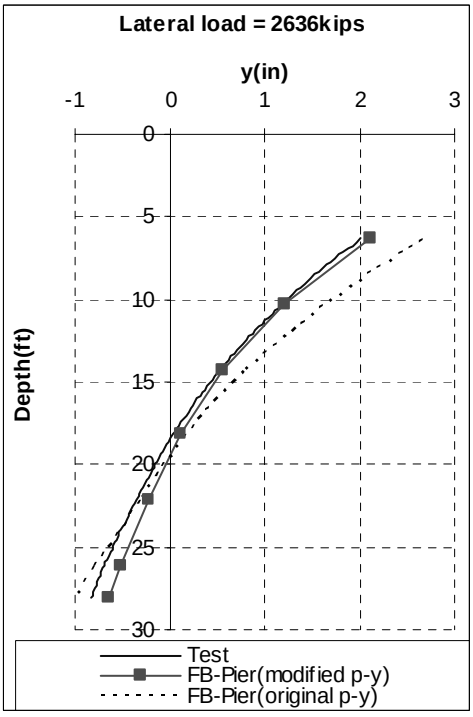

## Lateral Displacements (Corrected for Side Shear)

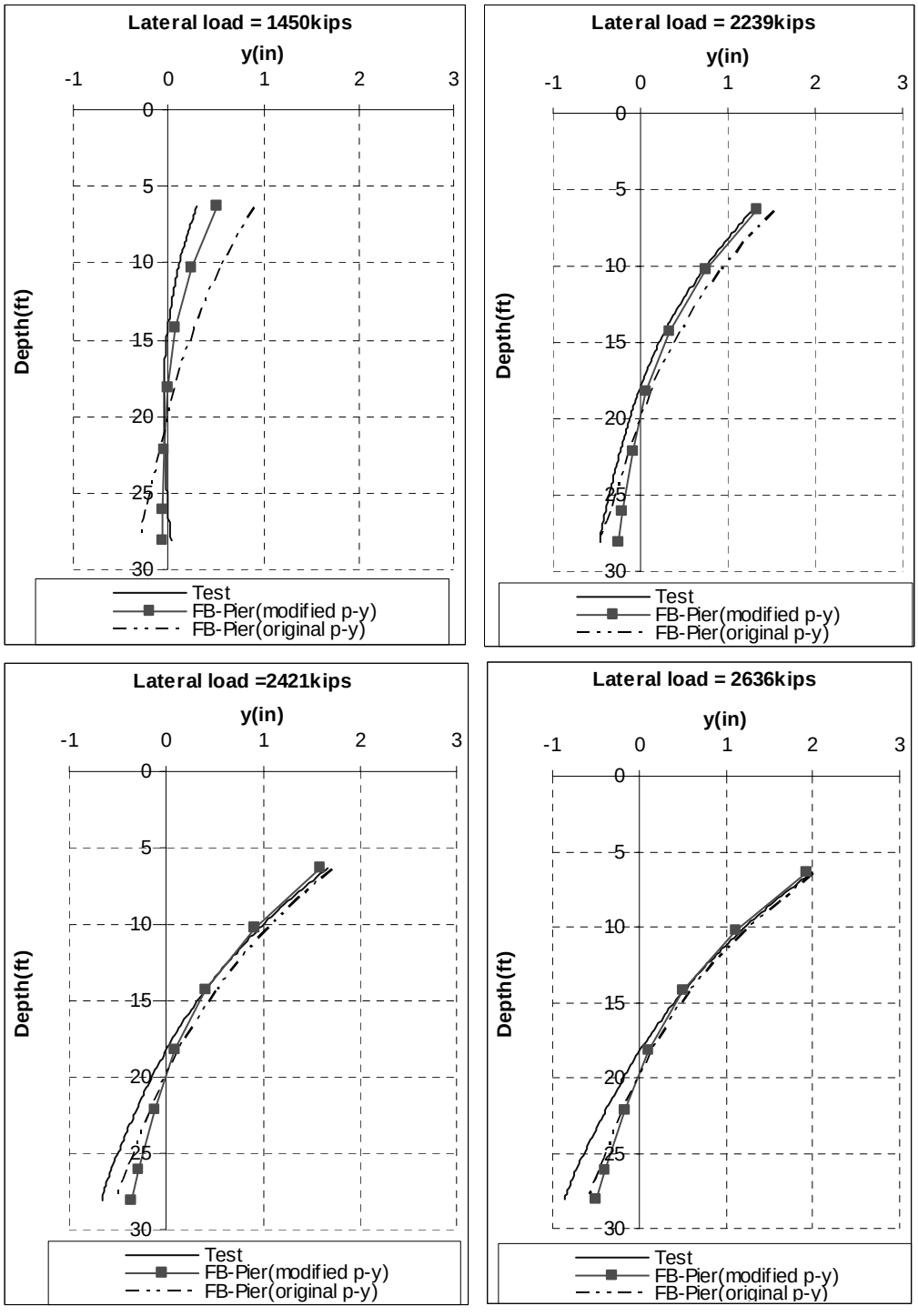

**Lateral Test # L4**

**P-Y Curves**

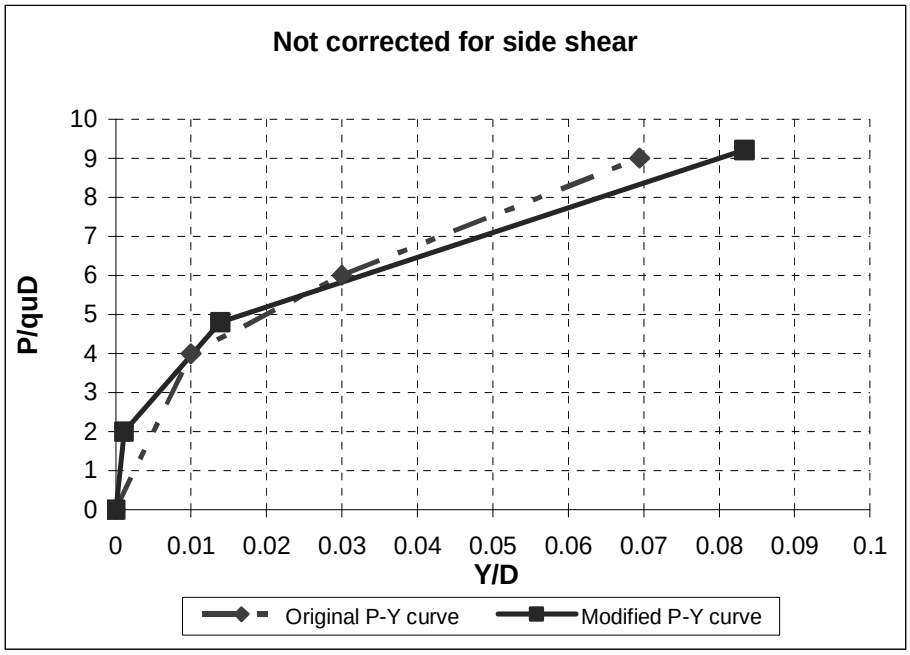


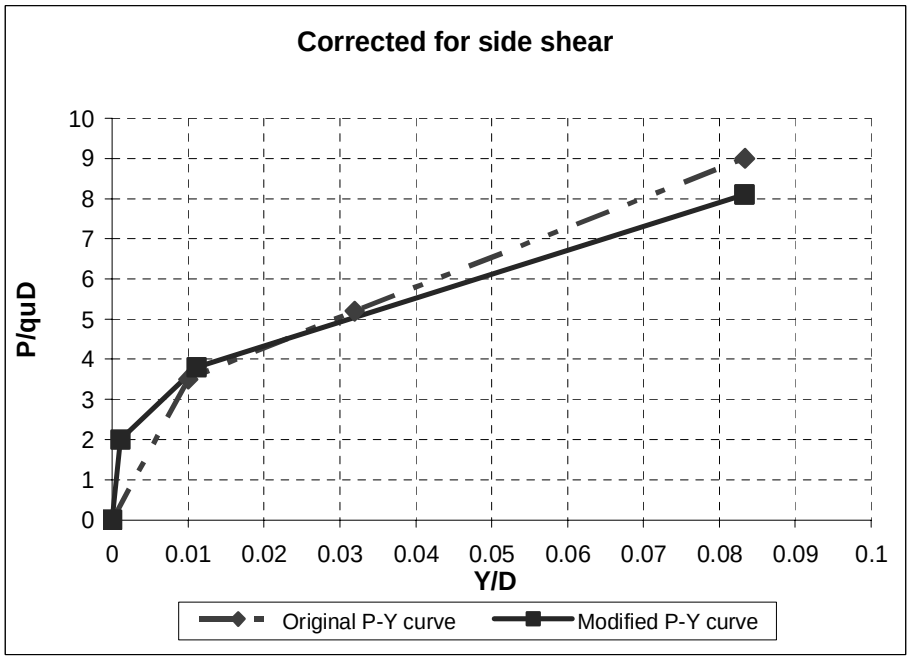

## Lateral Displacements (Not Corrected for Side Shear)

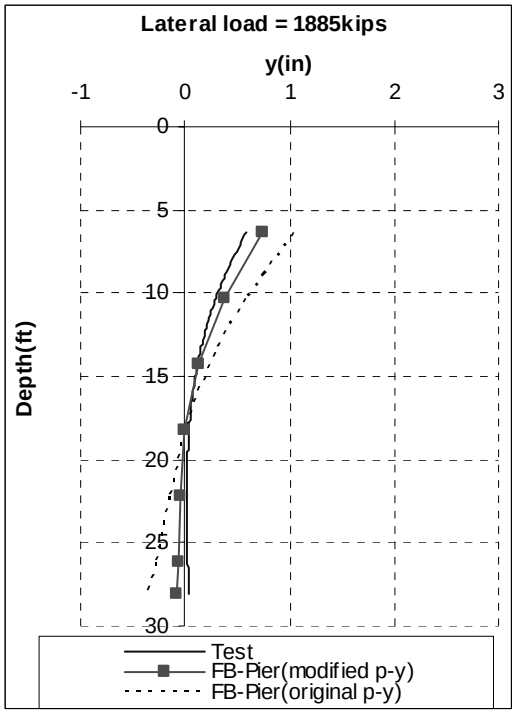


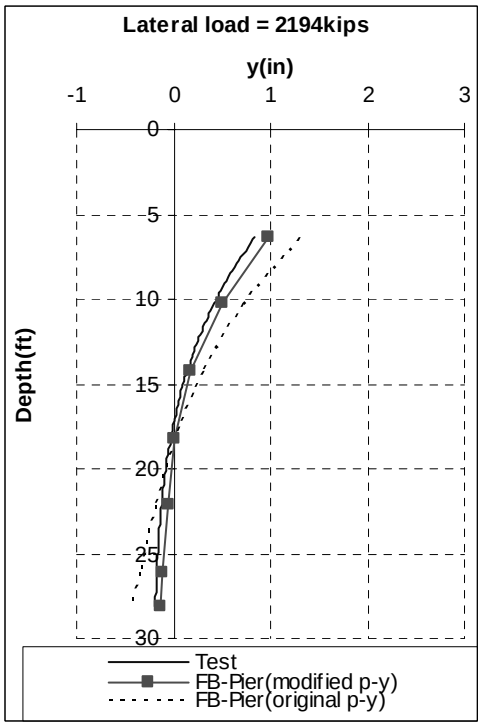


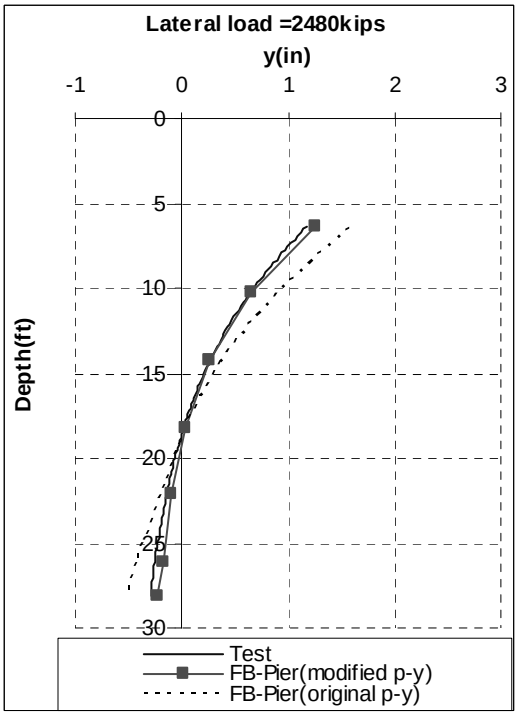


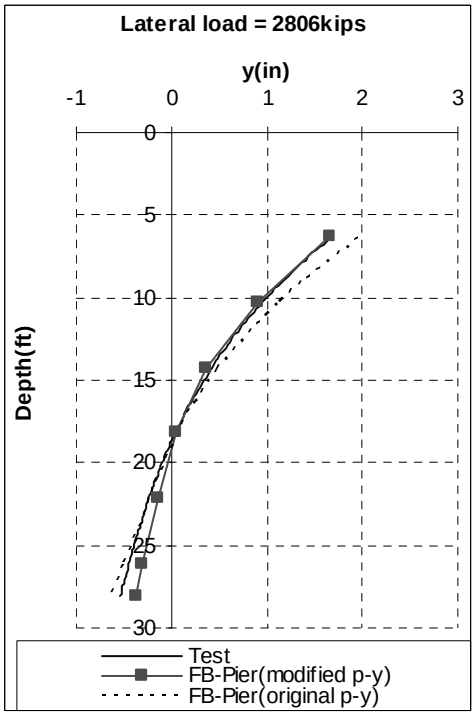

## Lateral Displacements (Corrected for Side Shear)

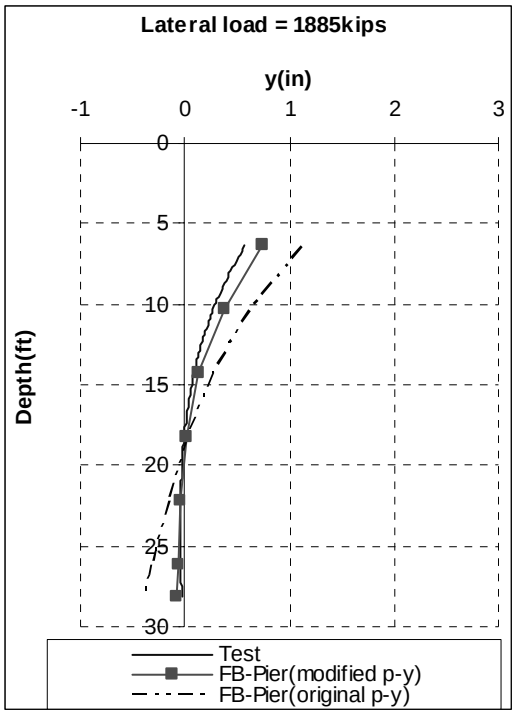


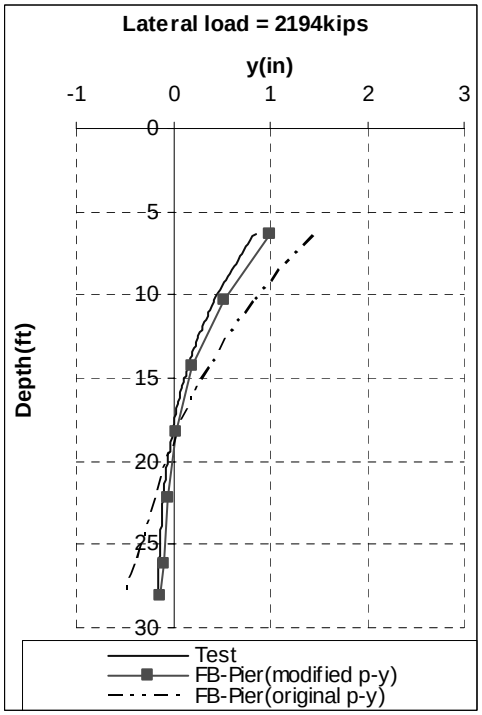


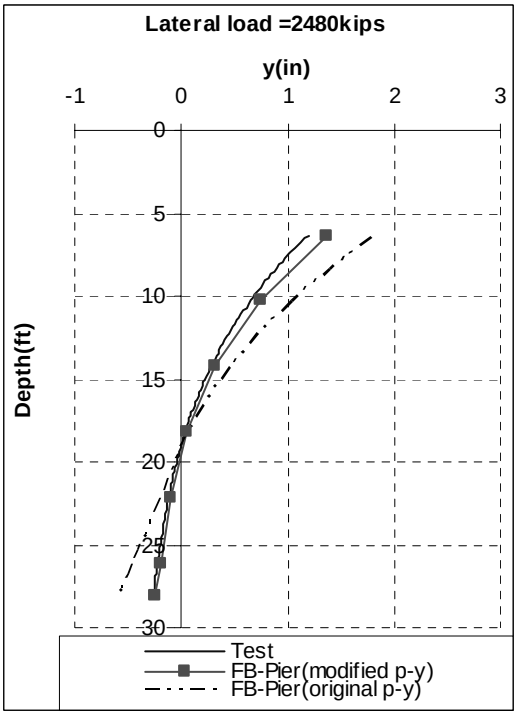


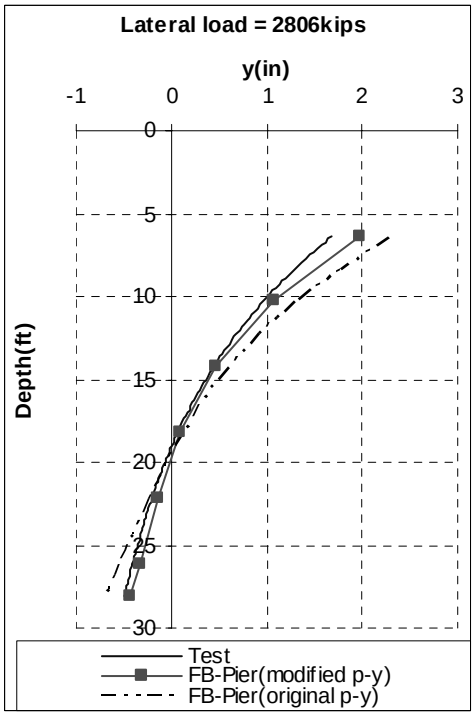

**Lateral Test # L5**

**P-Y Curves**

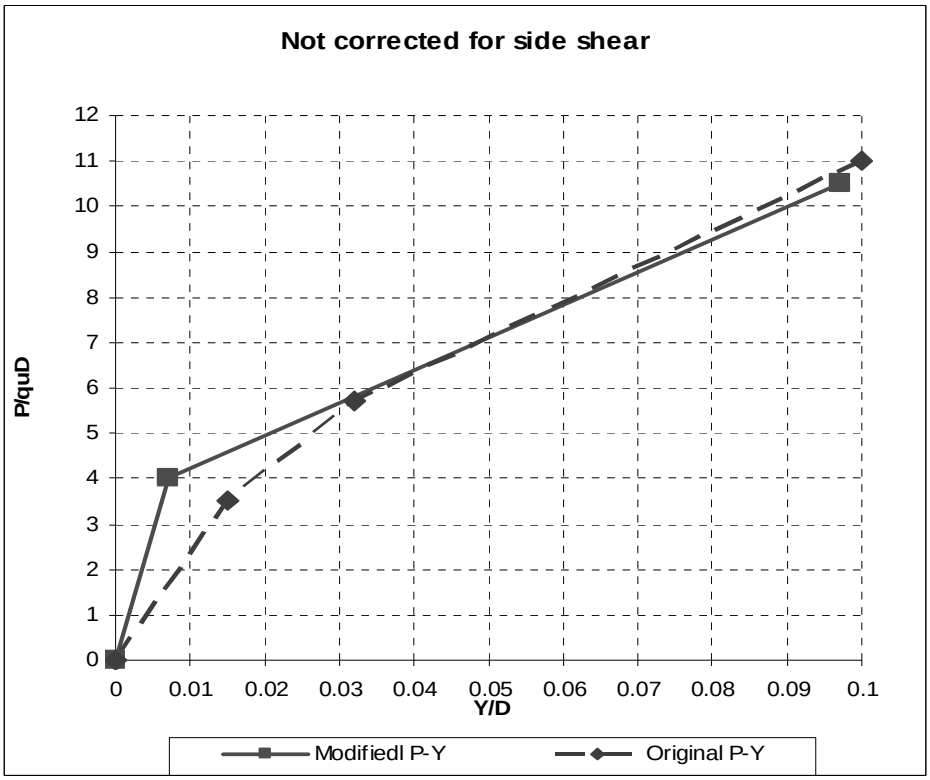


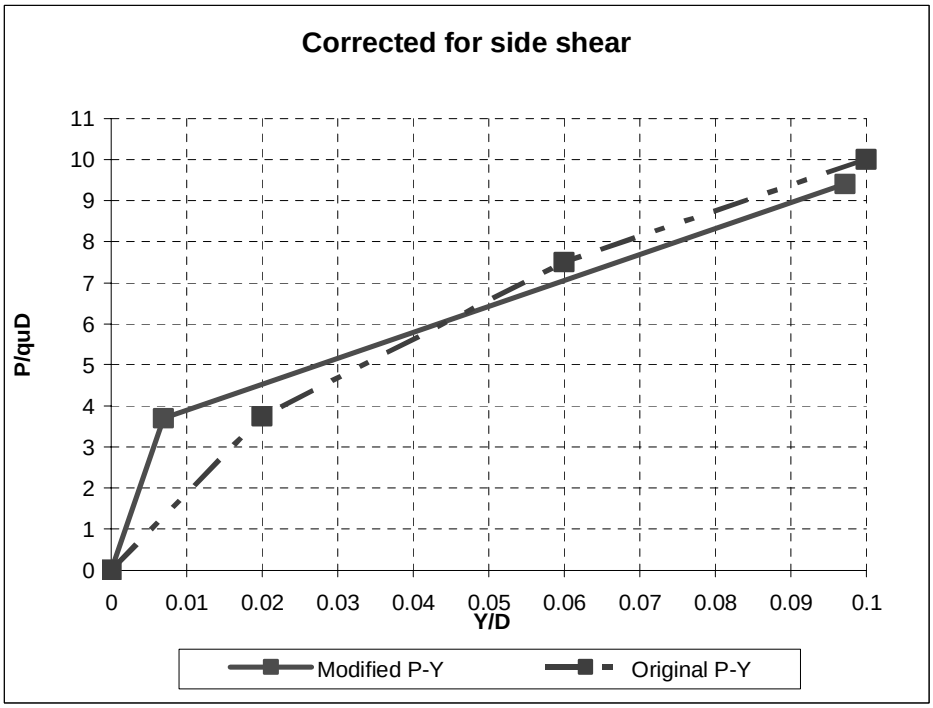

**Lateral Displacements (Not Corrected for Side Shear)**

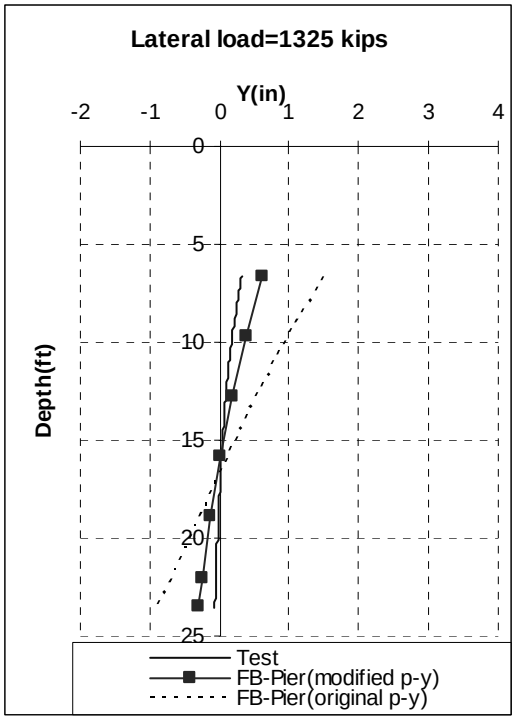


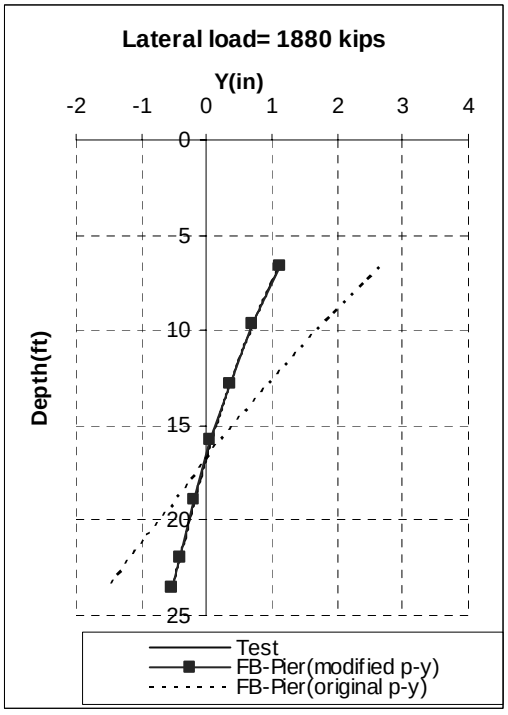


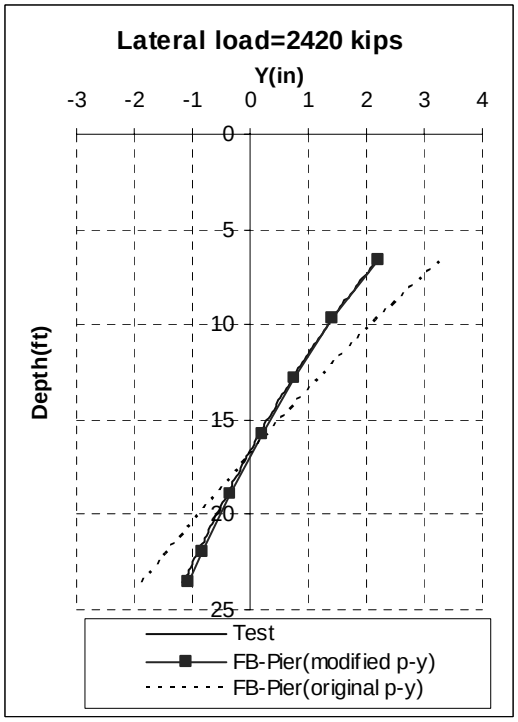


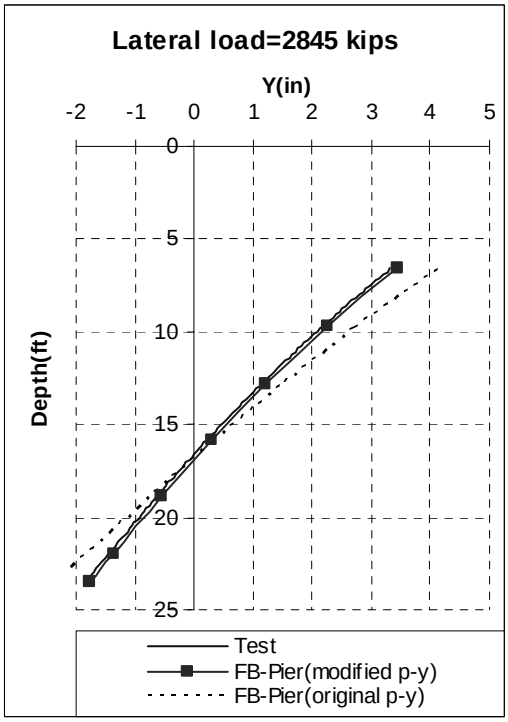

## Lateral Displacements (Corrected for Side Shear)

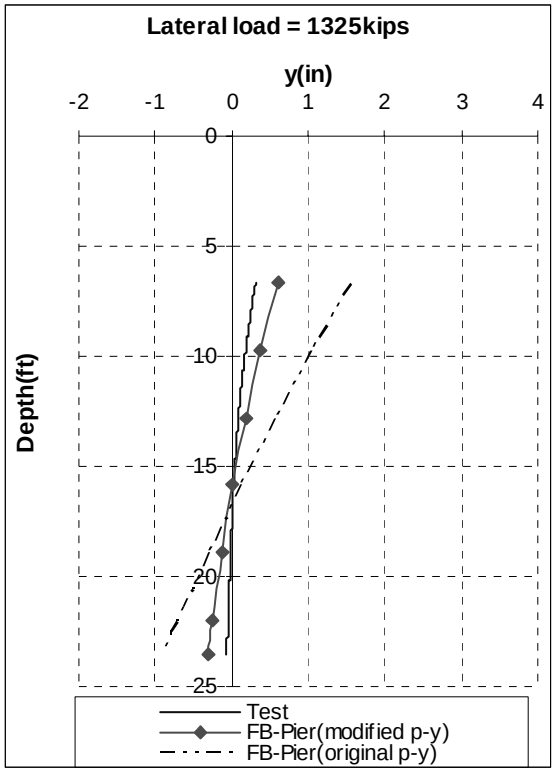


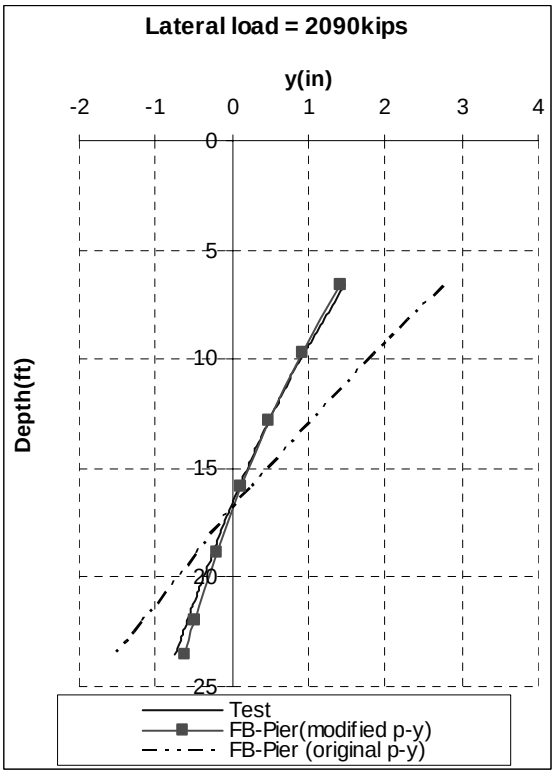


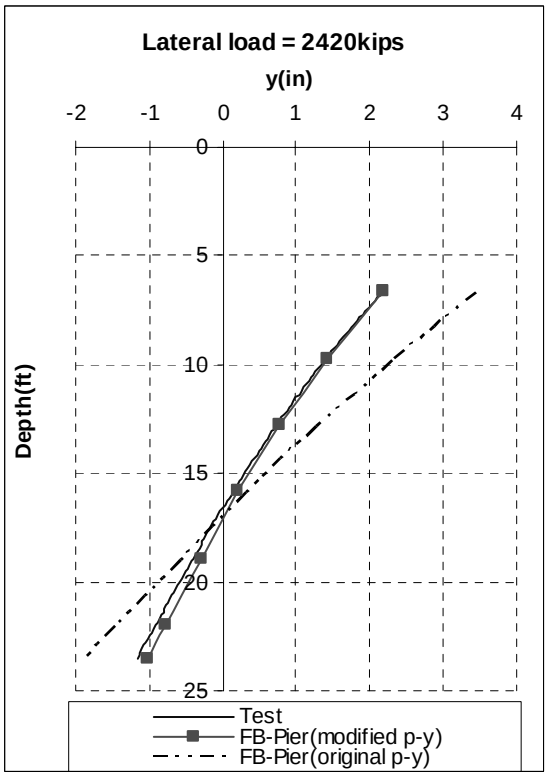


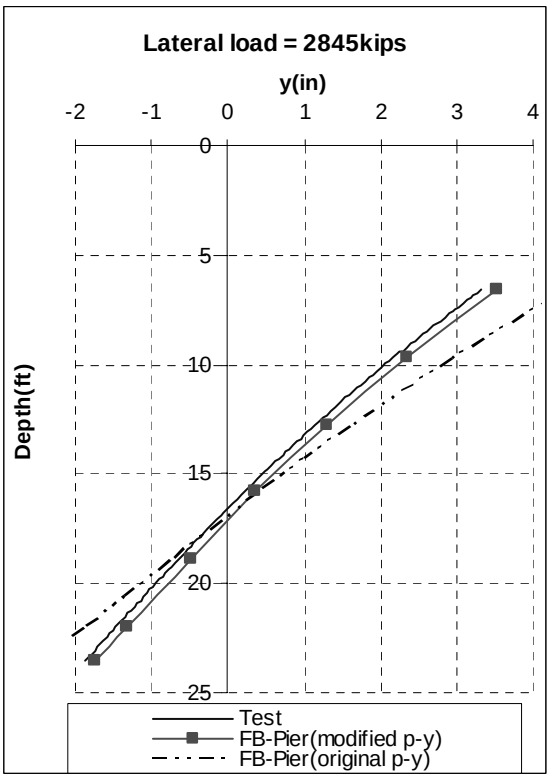

**Lateral Test # L6**

**P-Y Curves**

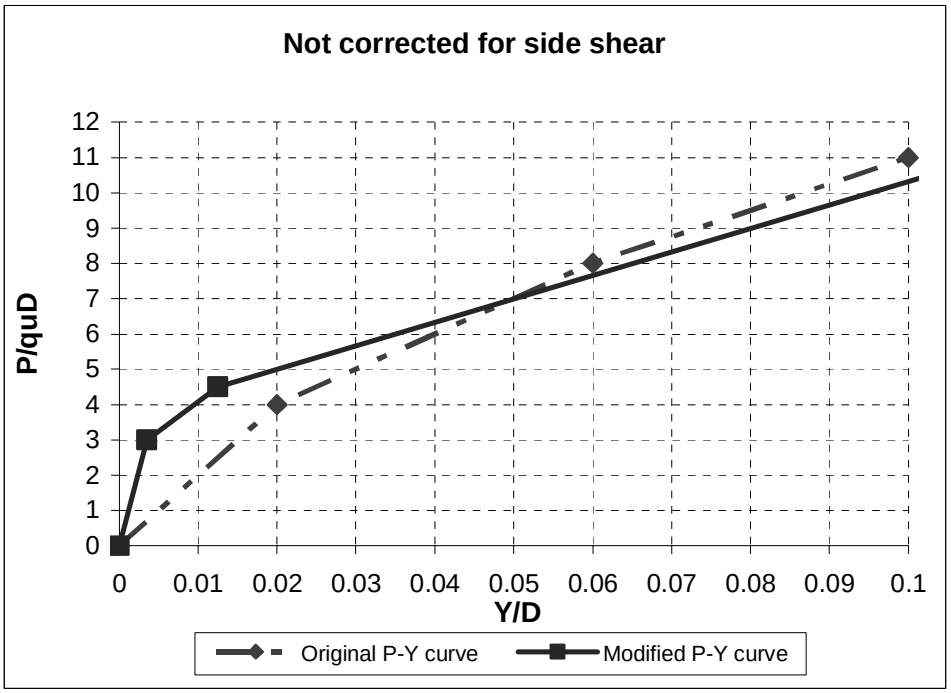


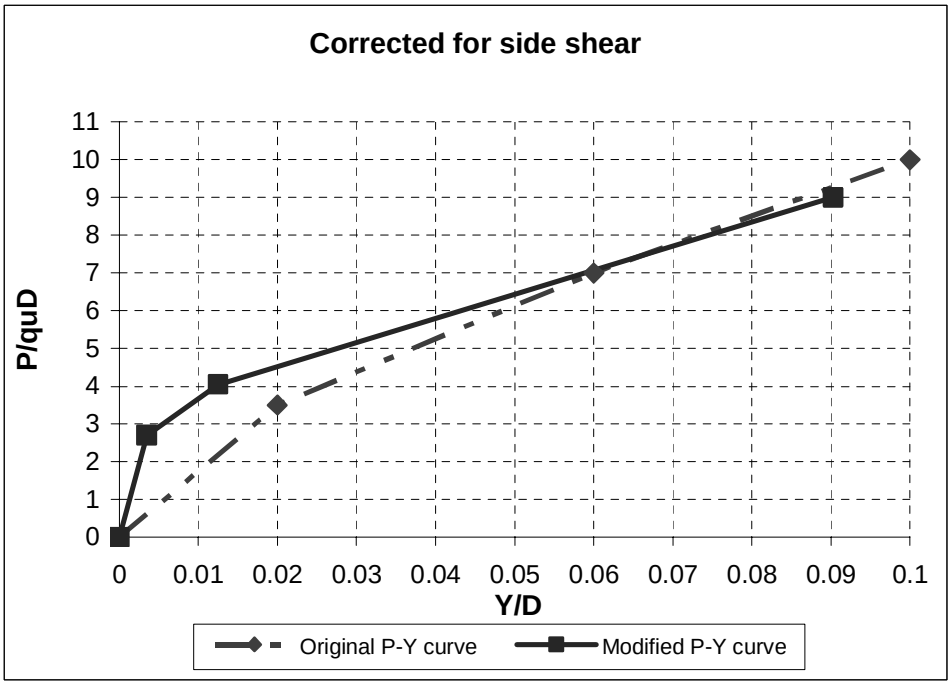

## Lateral Displacements (Not Corrected for Side Shear)

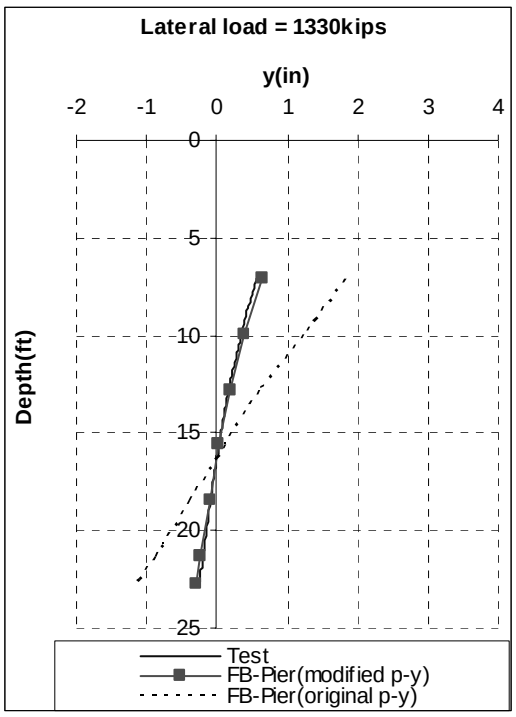


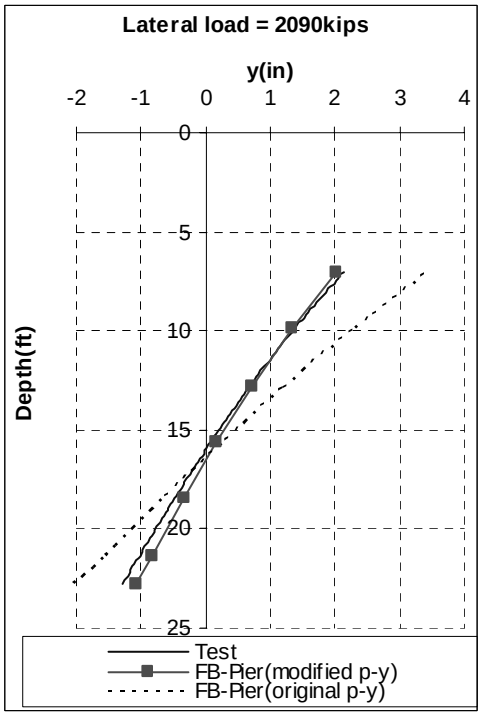


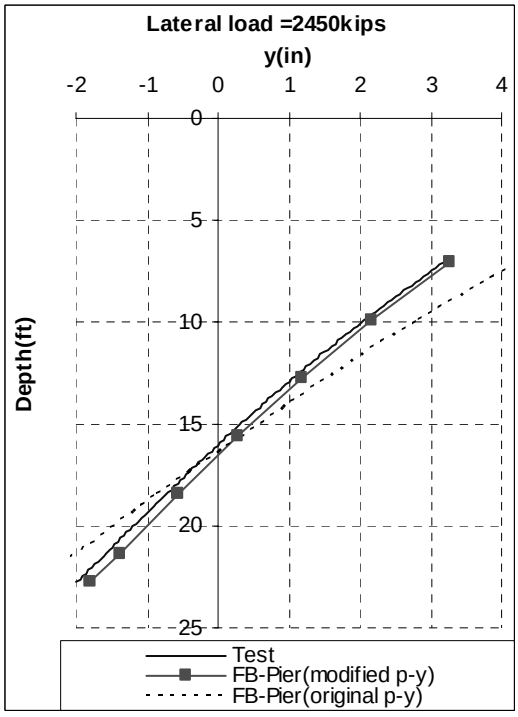


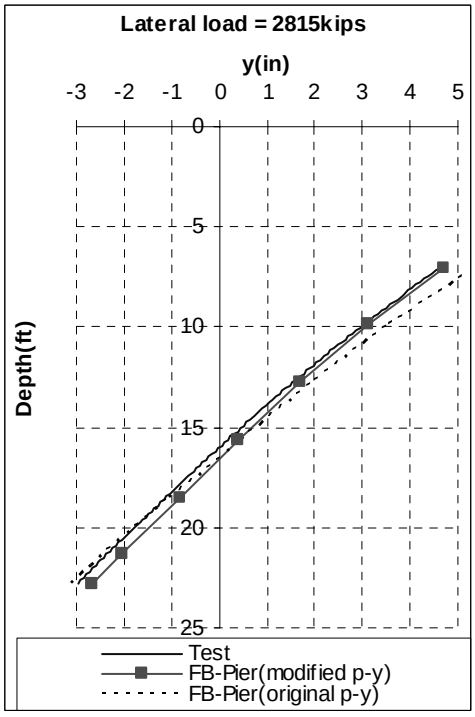

## Lateral Displacements (Corrected for Side Shear)

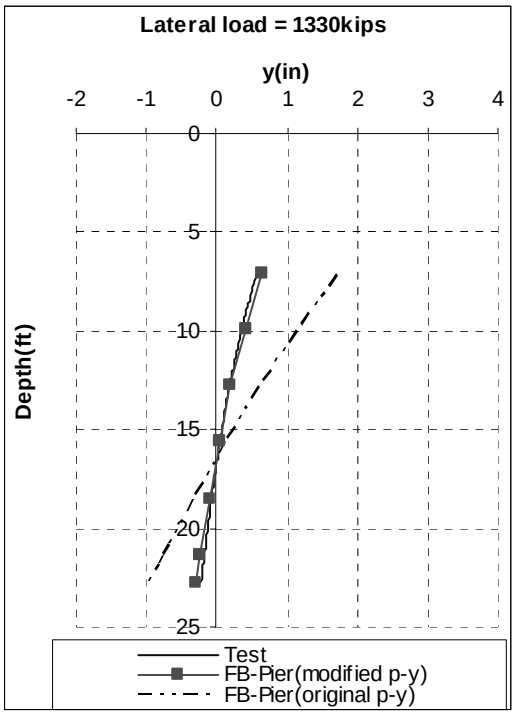


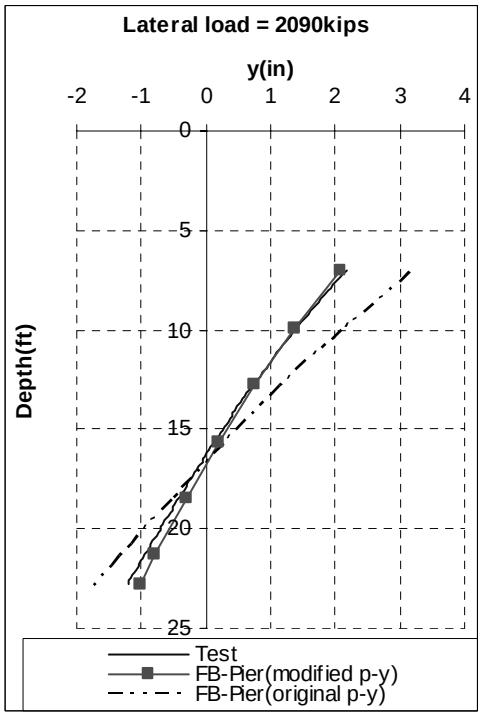


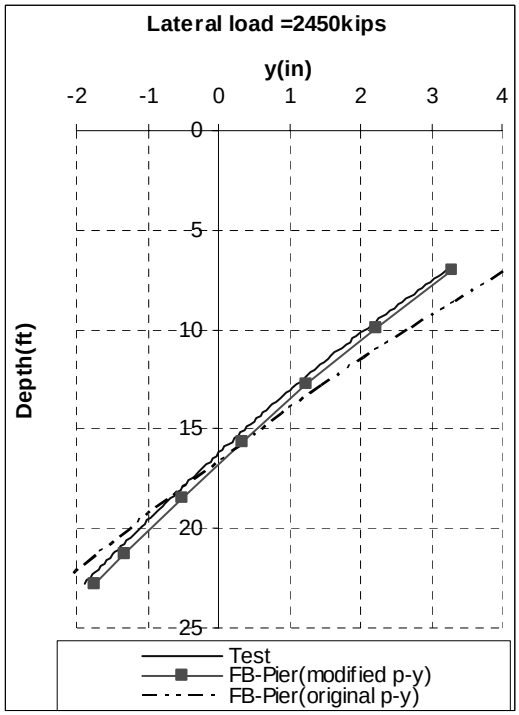


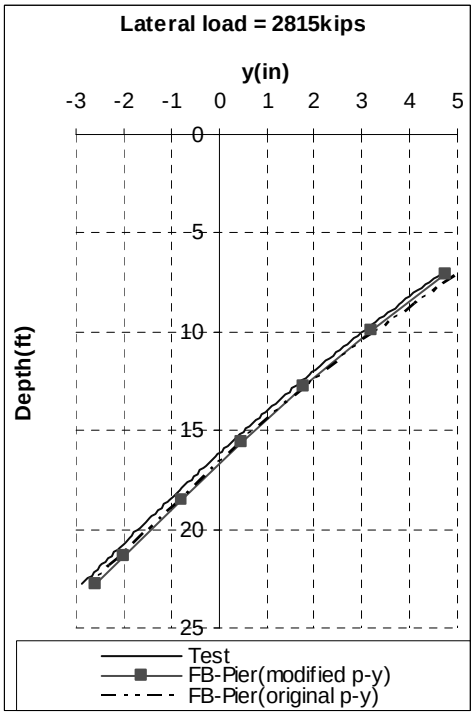

**Lateral Test # L7**

**P-Y Curves**

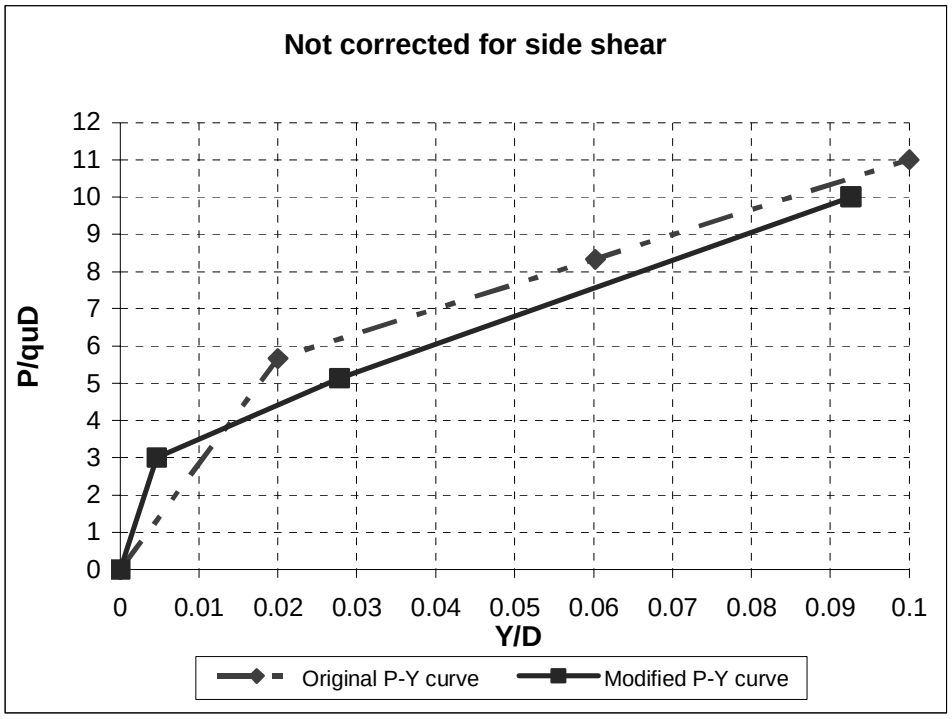


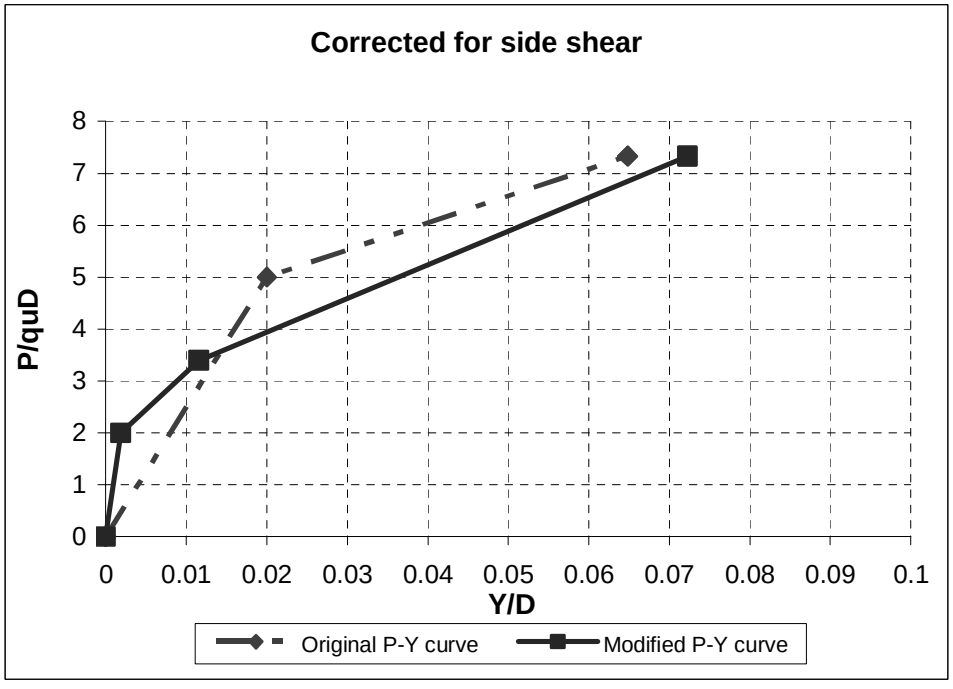

## Lateral Displacements (Not Corrected for Side Shear)

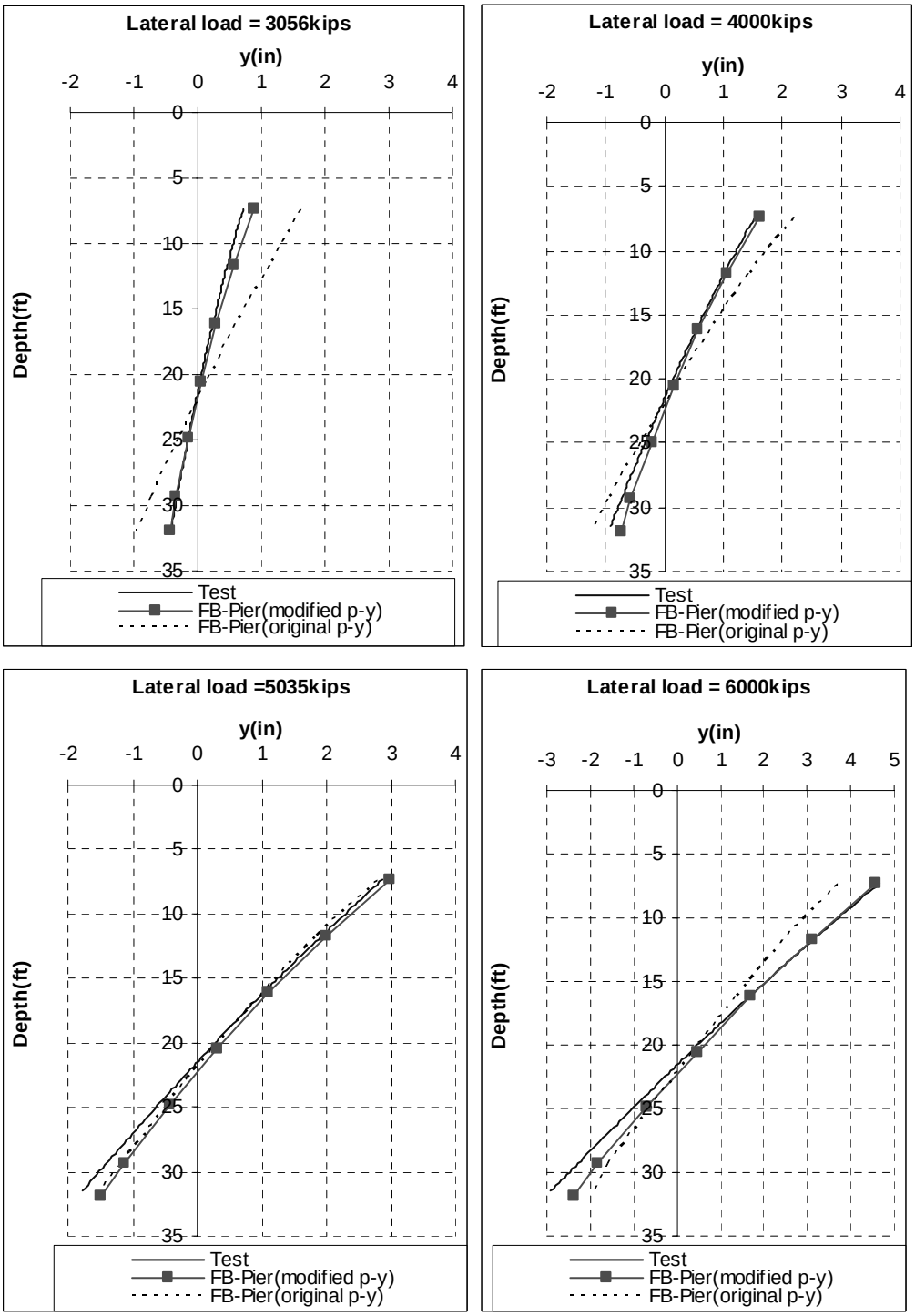

**Lateral Displacements (Corrected for Side Shear)**

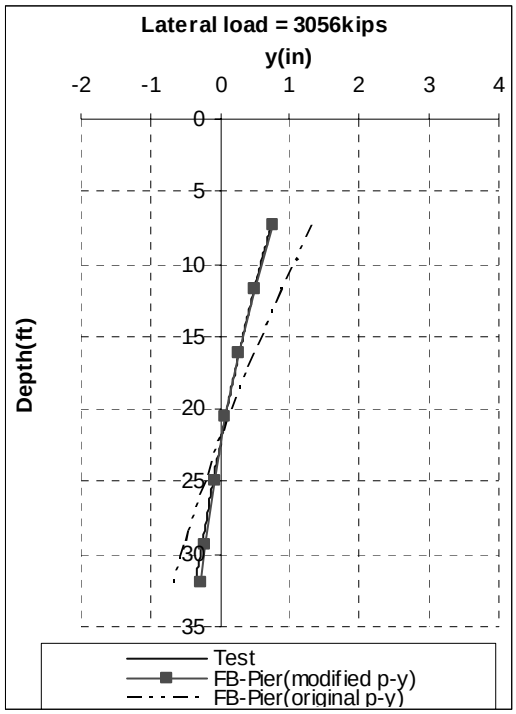


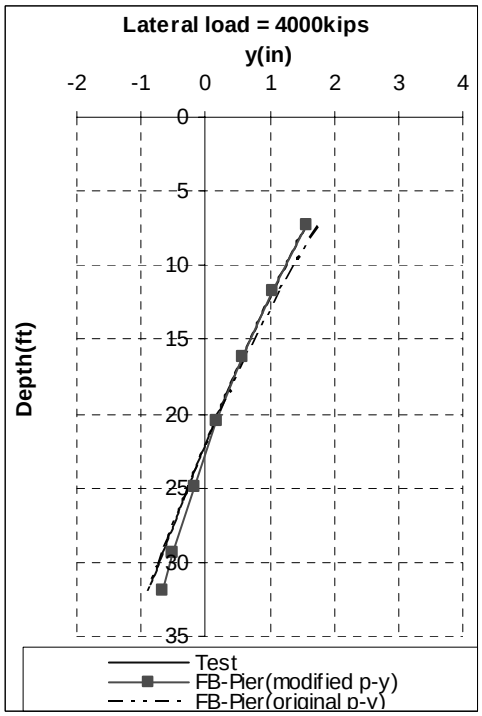


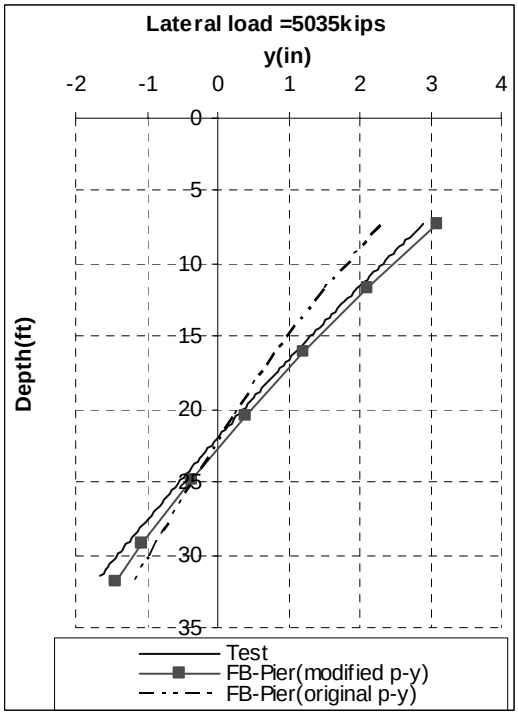


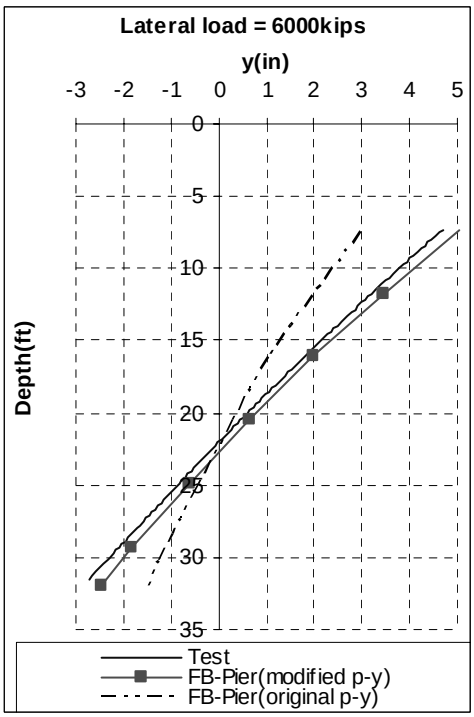

**Lateral Test # L8**

**P-Y Curves**

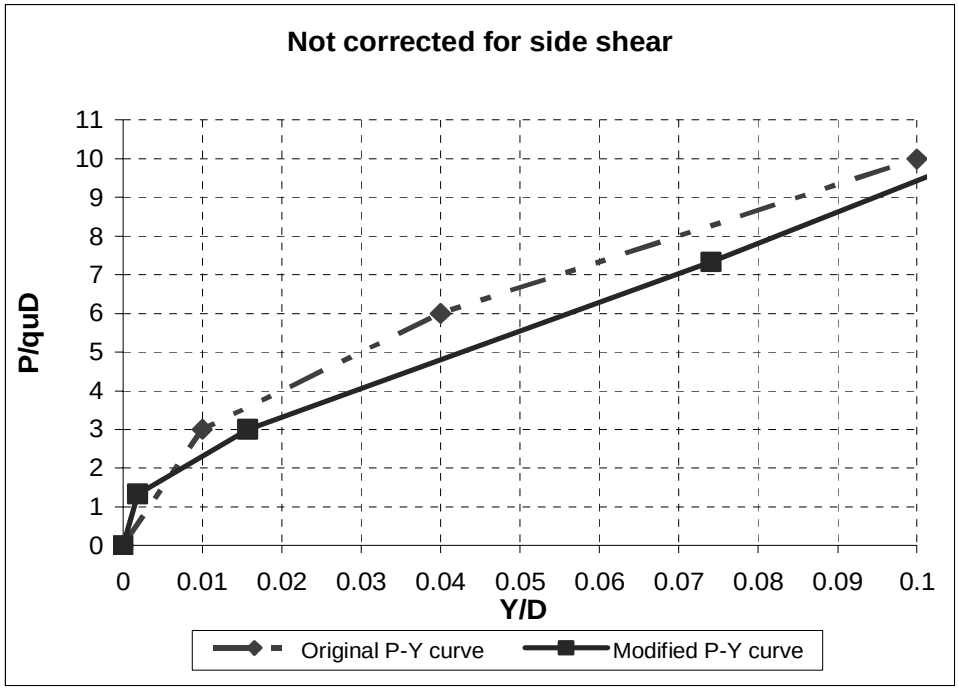


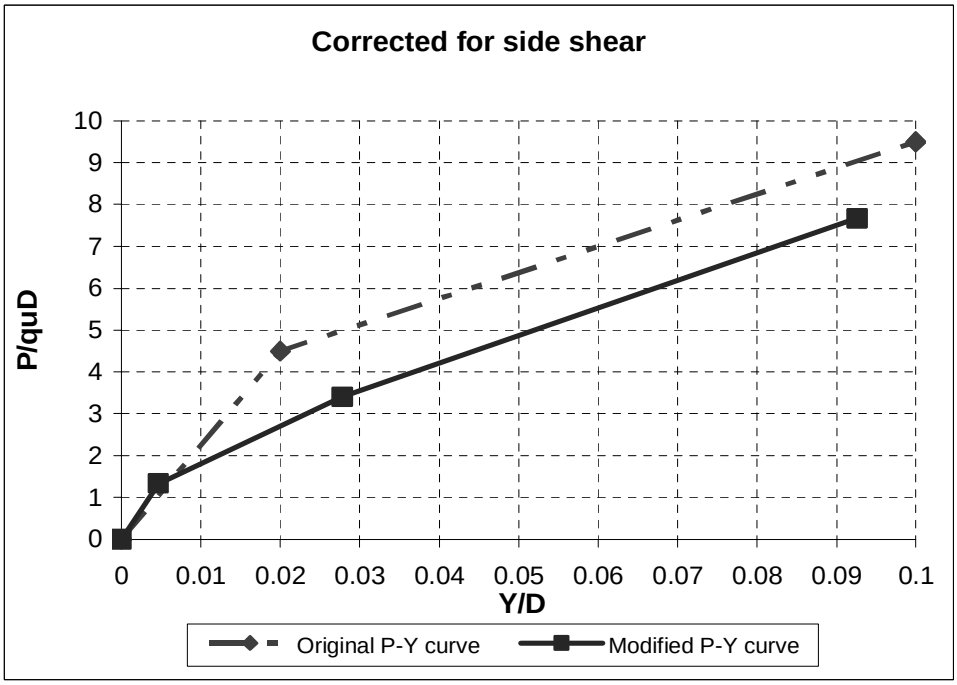

## Lateral Displacements (Not Corrected for Side Shear)

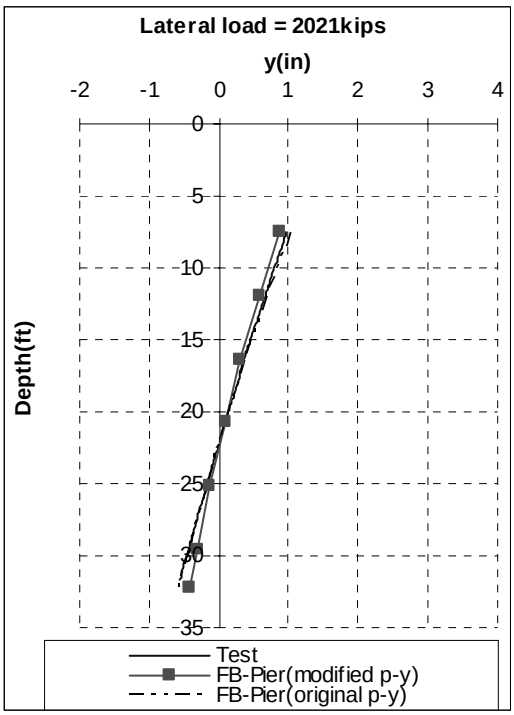


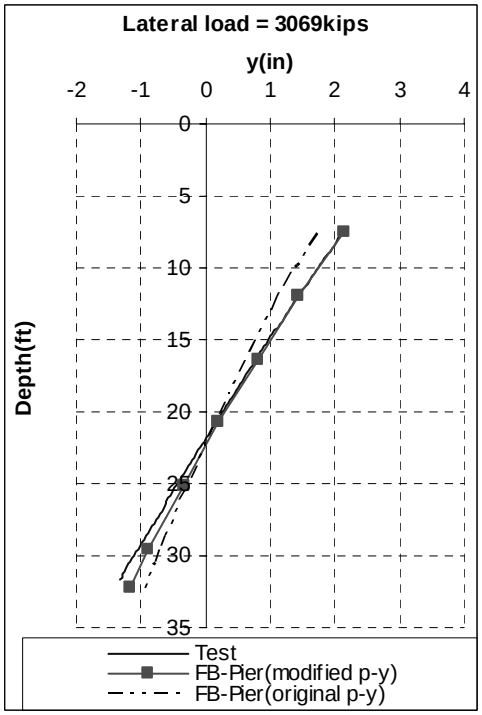


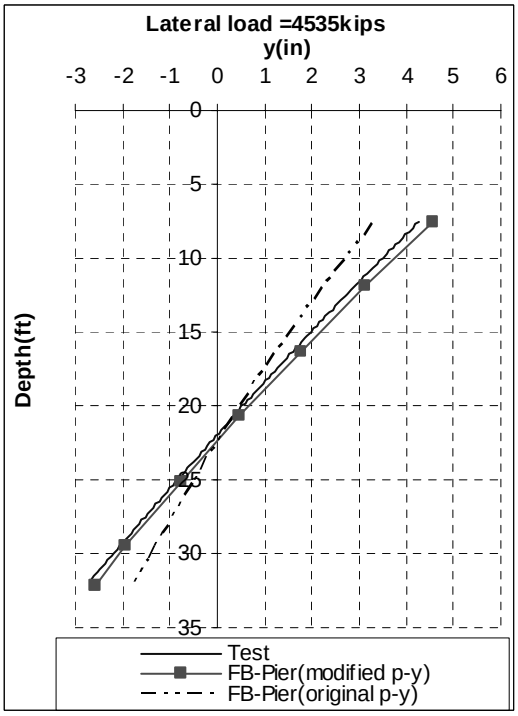


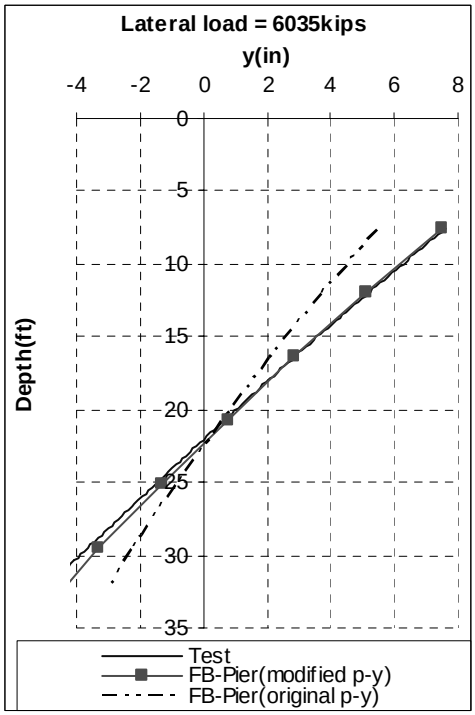

**Lateral Displacements (Corrected for Side Shear)**

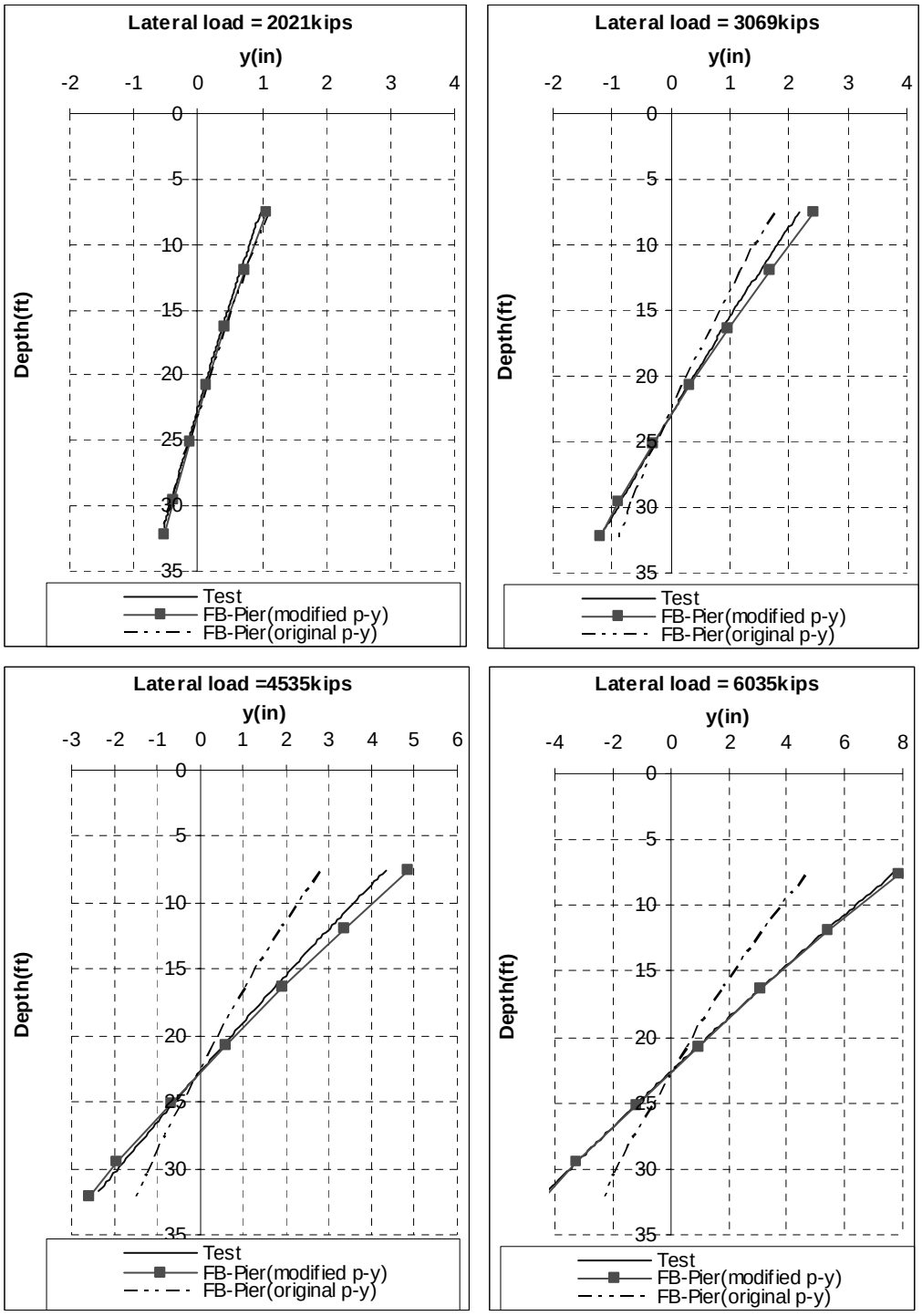

**Lateral Test # L9**

**P-Y Curves**

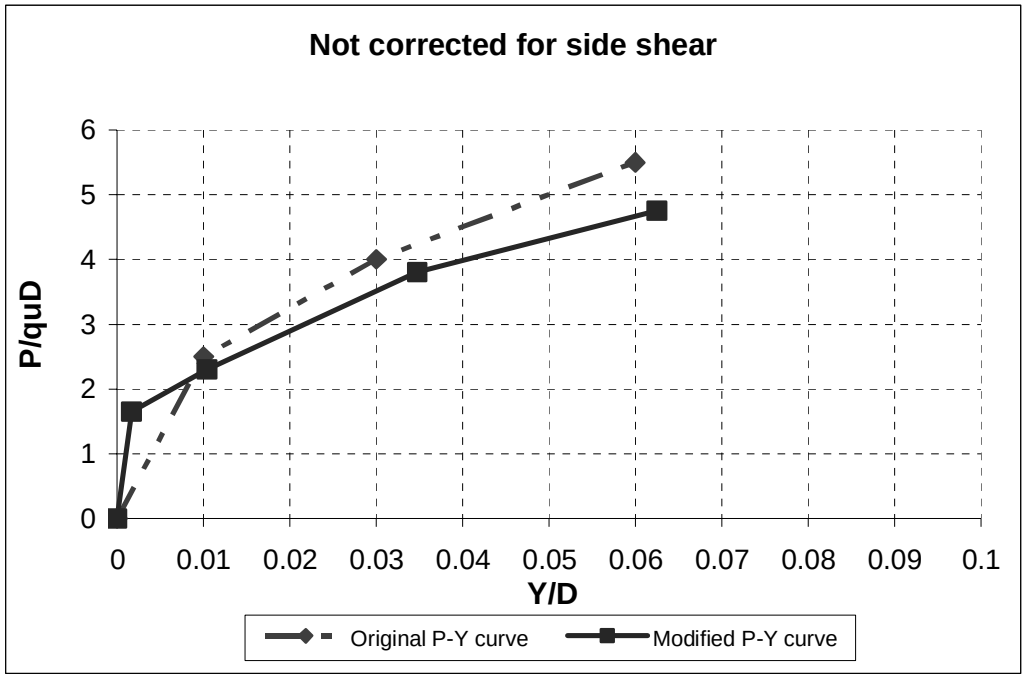


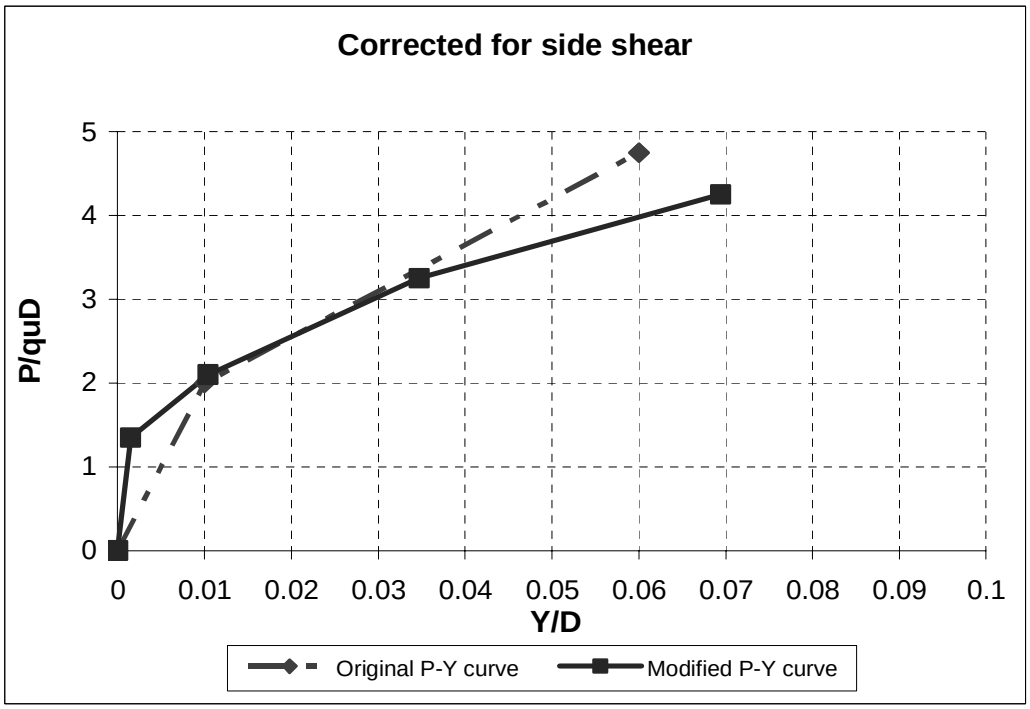

## Lateral Displacements (Not Corrected for Side Shear)

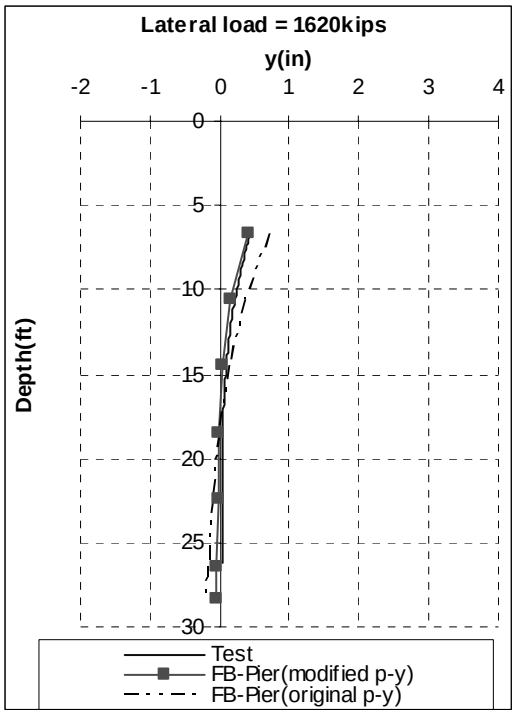


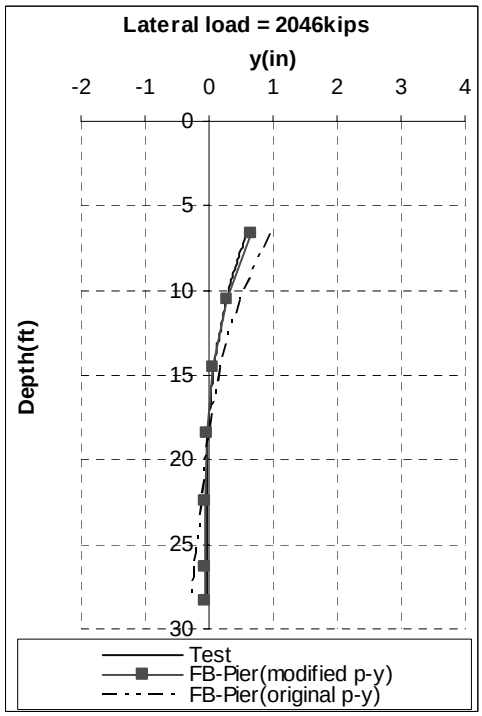


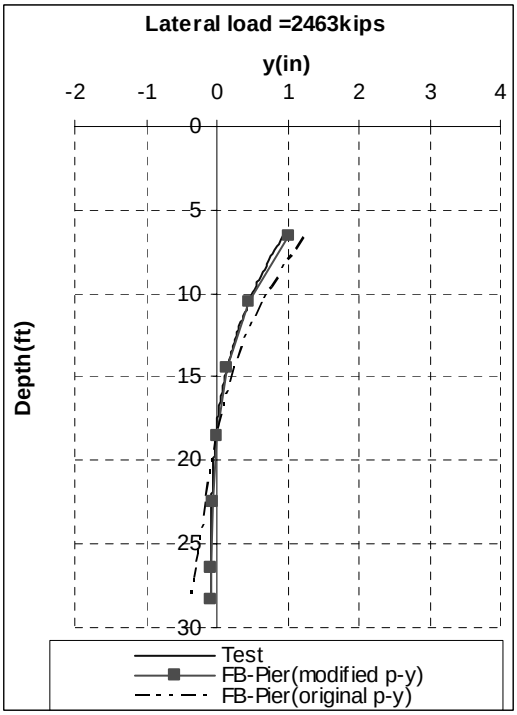


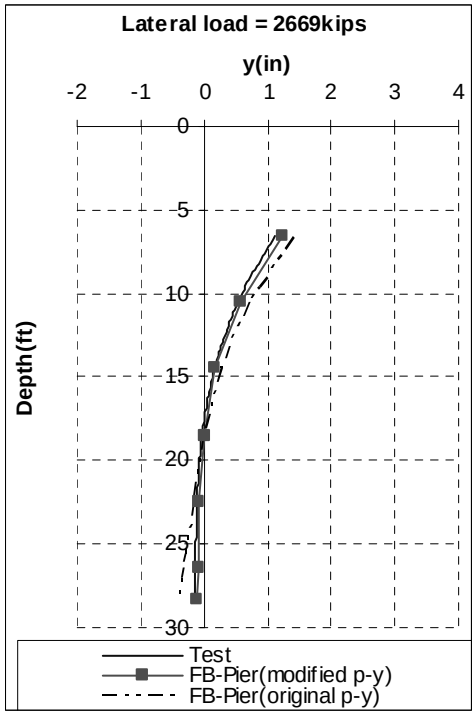

## Lateral Displacements (Corrected for Side Shear)

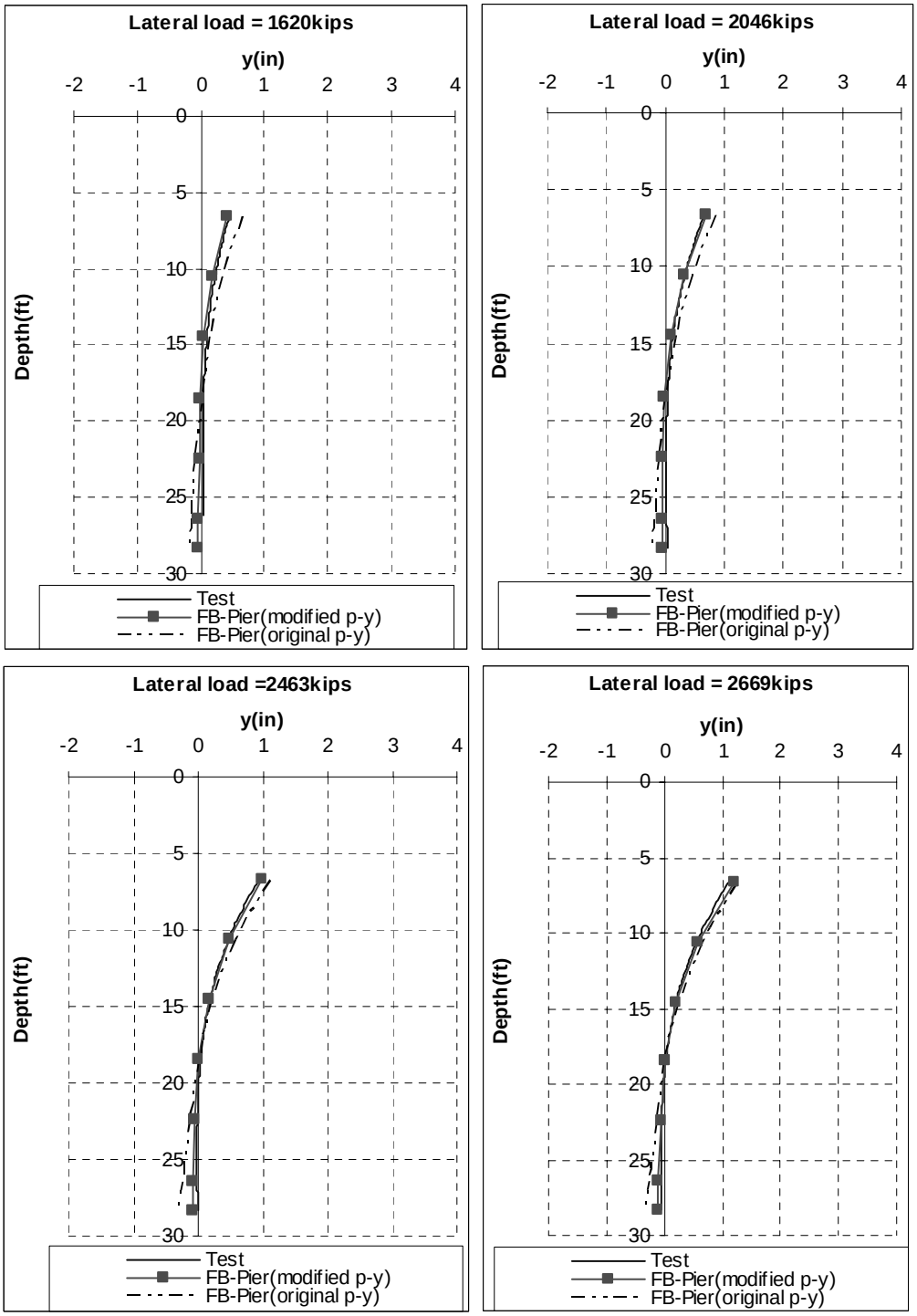

**Lateral Test # L10**

**P-Y Curves**

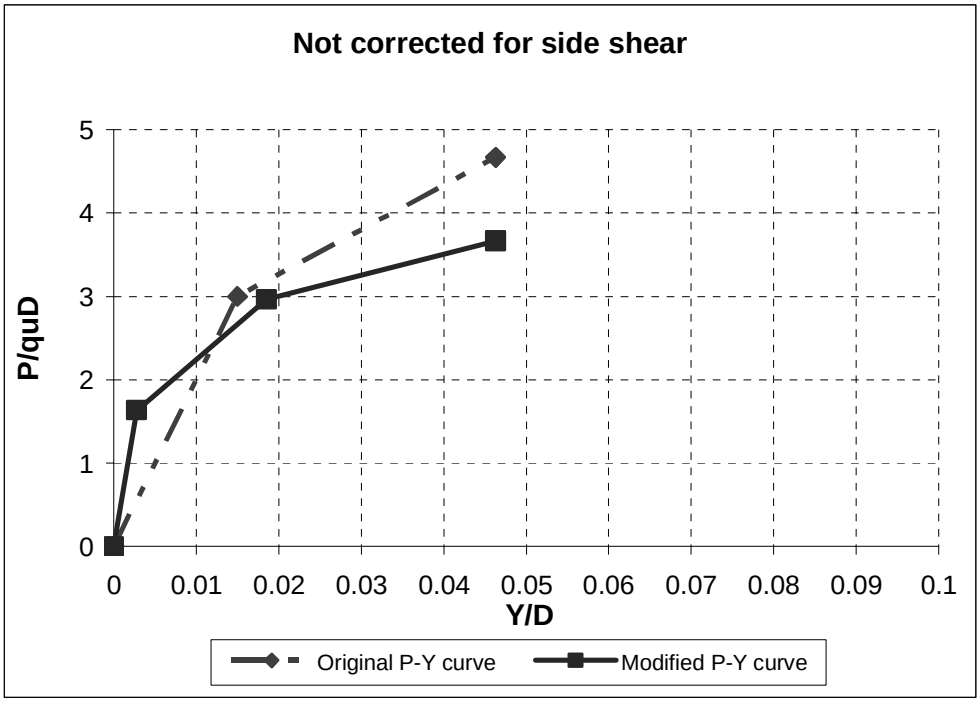


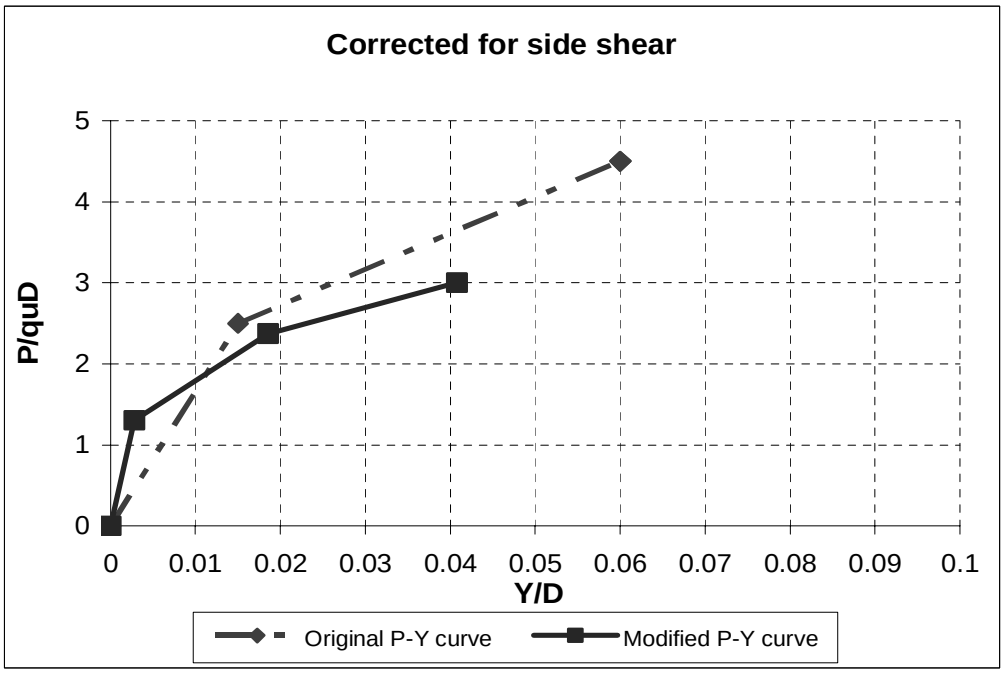

**Lateral Displacements (Not Corrected for Side Shear)**

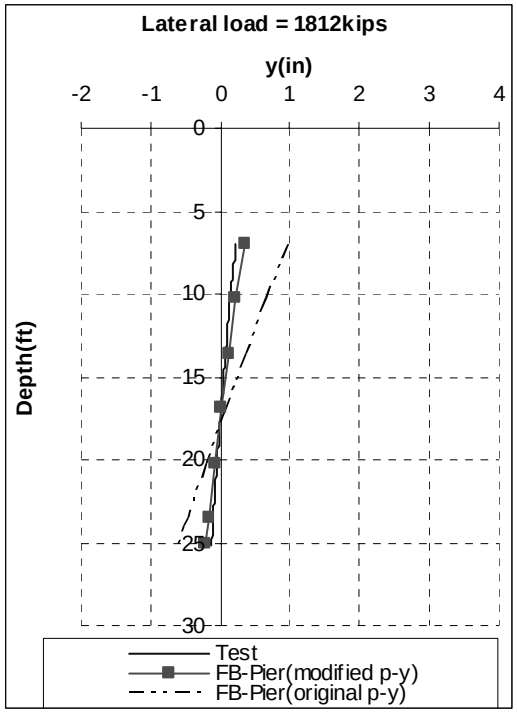


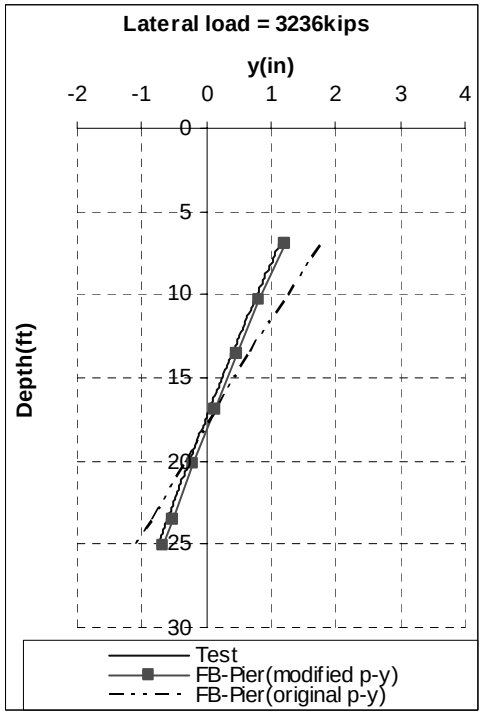


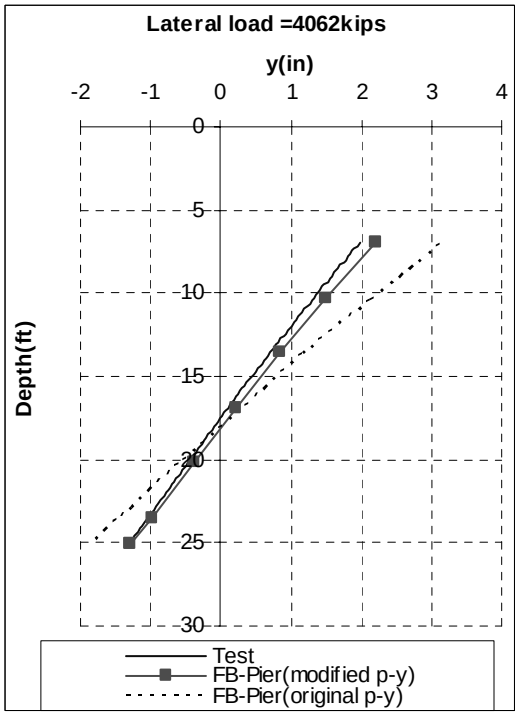


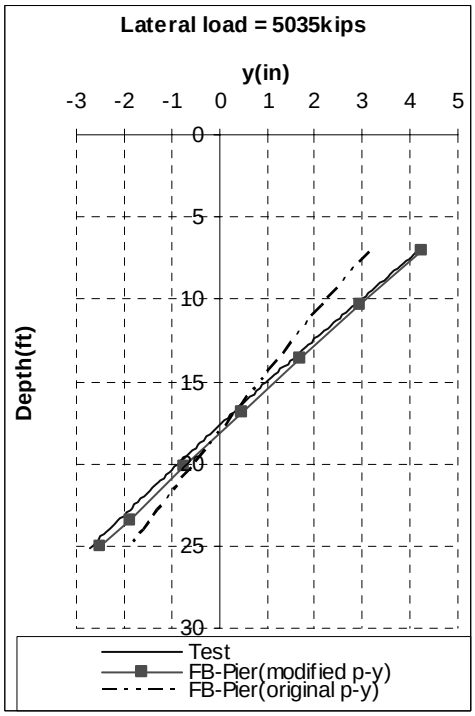

**Lateral Displacements (Corrected for Side Shear)**

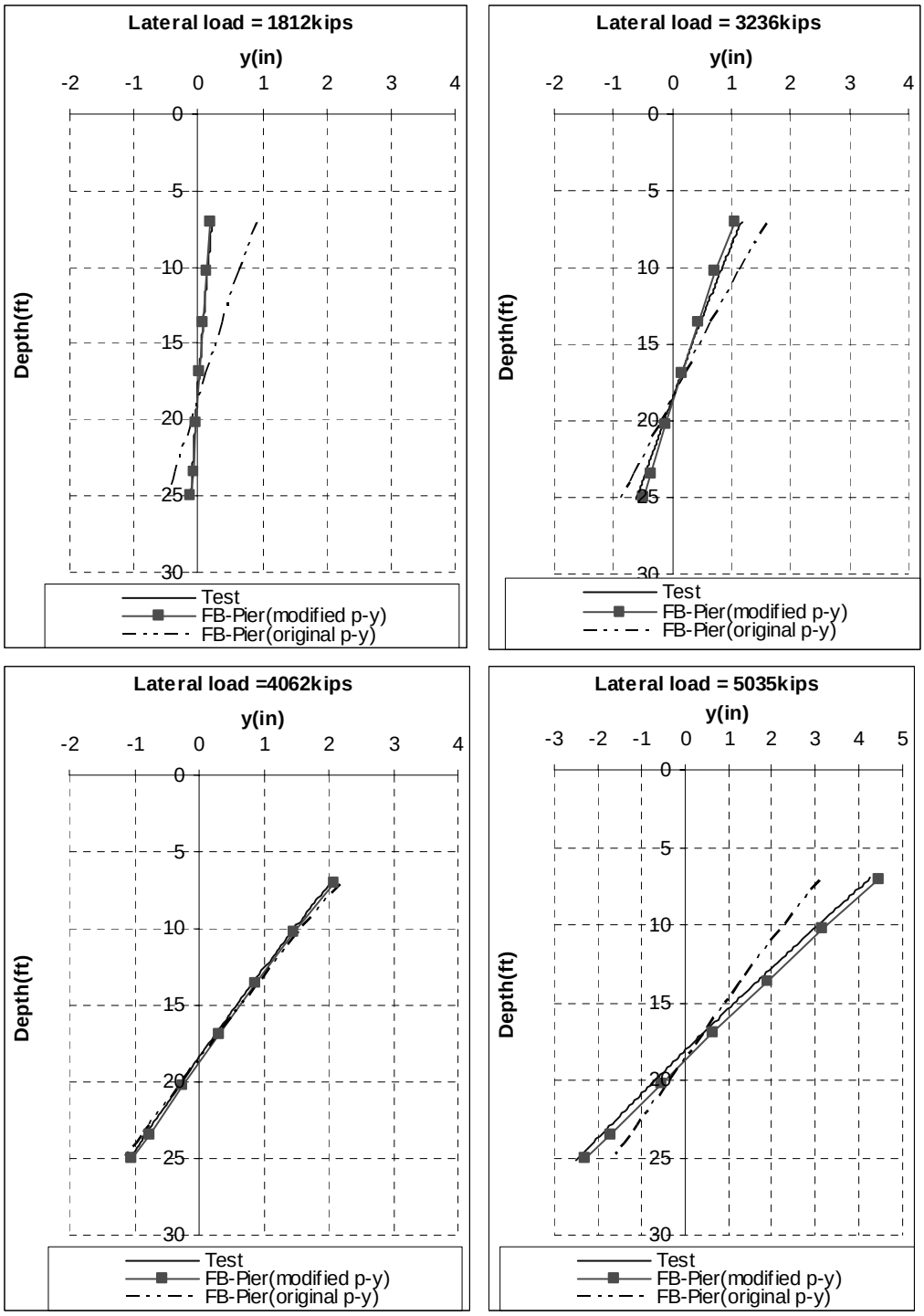

**Lateral Test # L11**

**P-Y Curves**

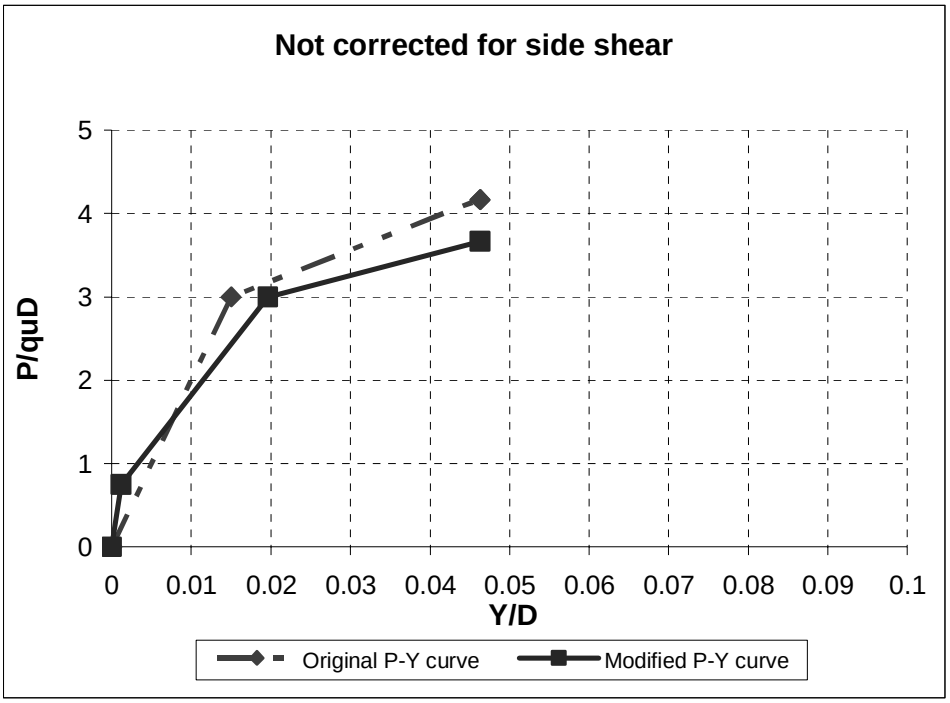


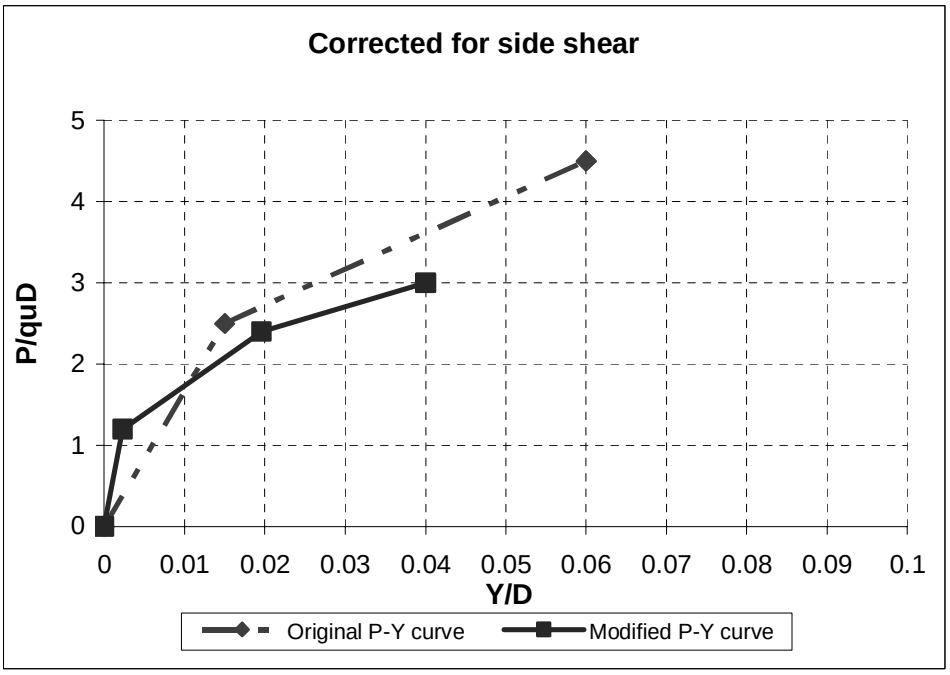

## Lateral Displacements (Not Corrected for Side Shear)

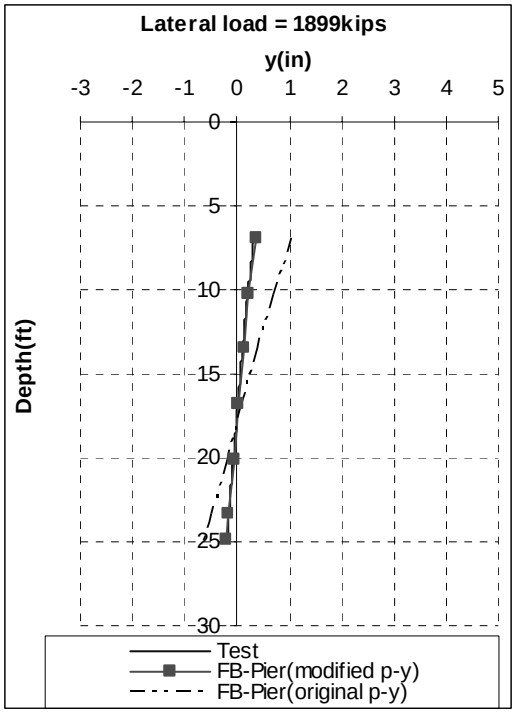


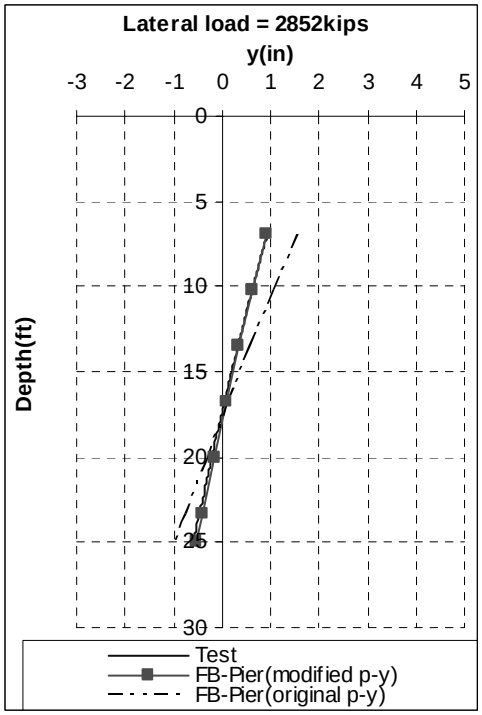


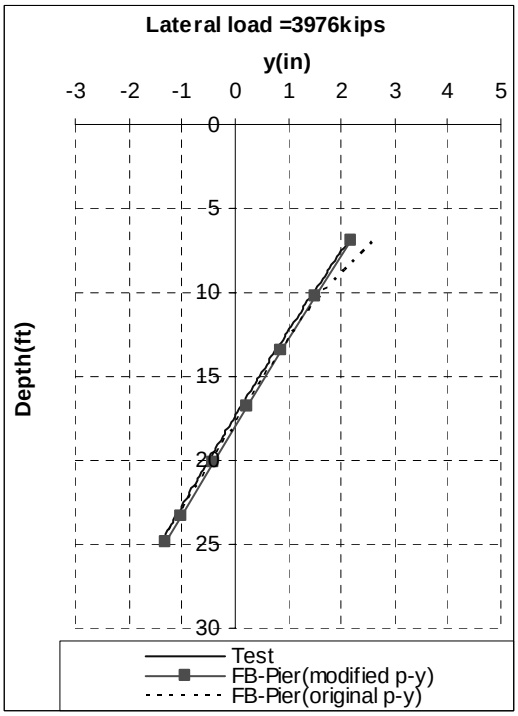


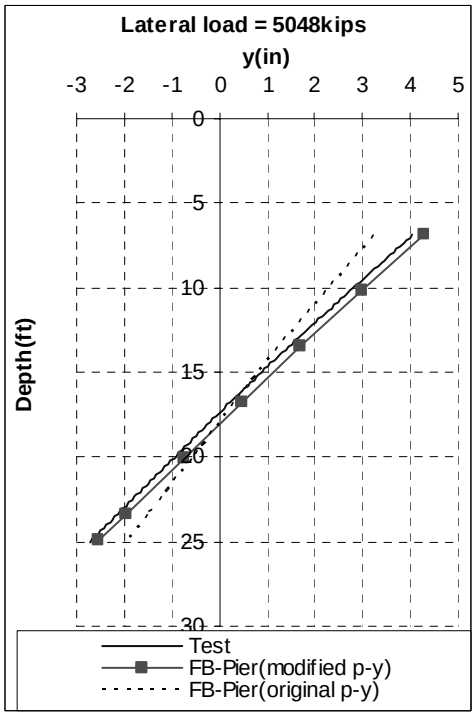

## Lateral Displacements (Corrected for Side Shear)

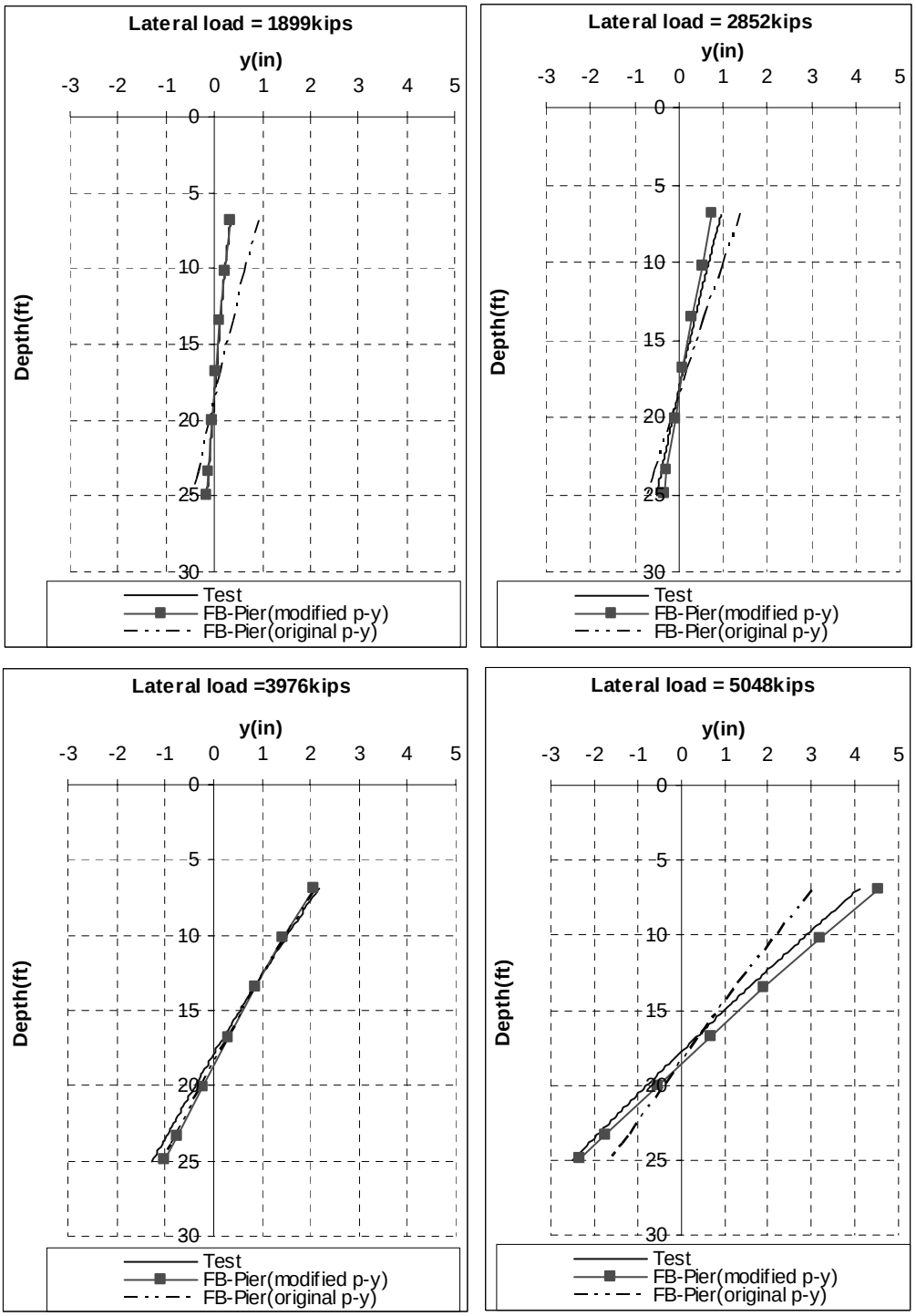

**Lateral Test # L12**

**P-Y Curves**

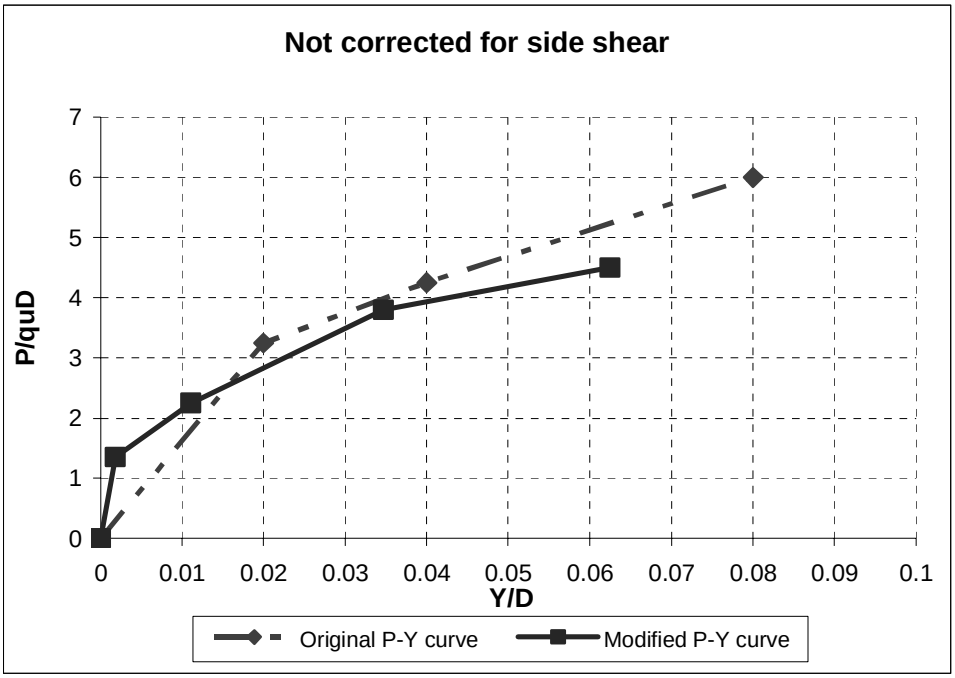


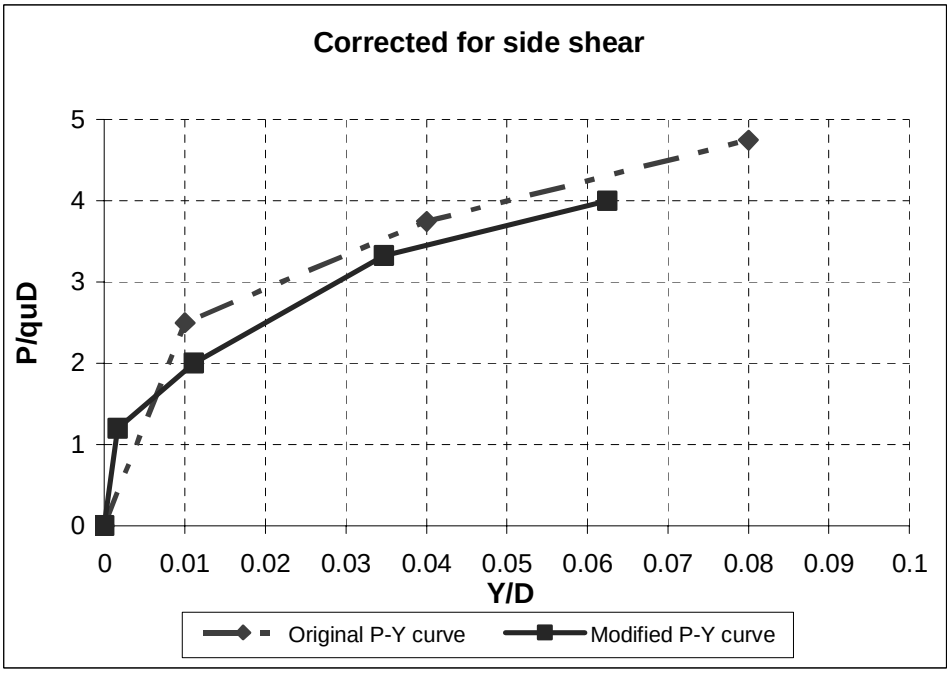

**Lateral Displacements (Not Corrected for Side Shear)**

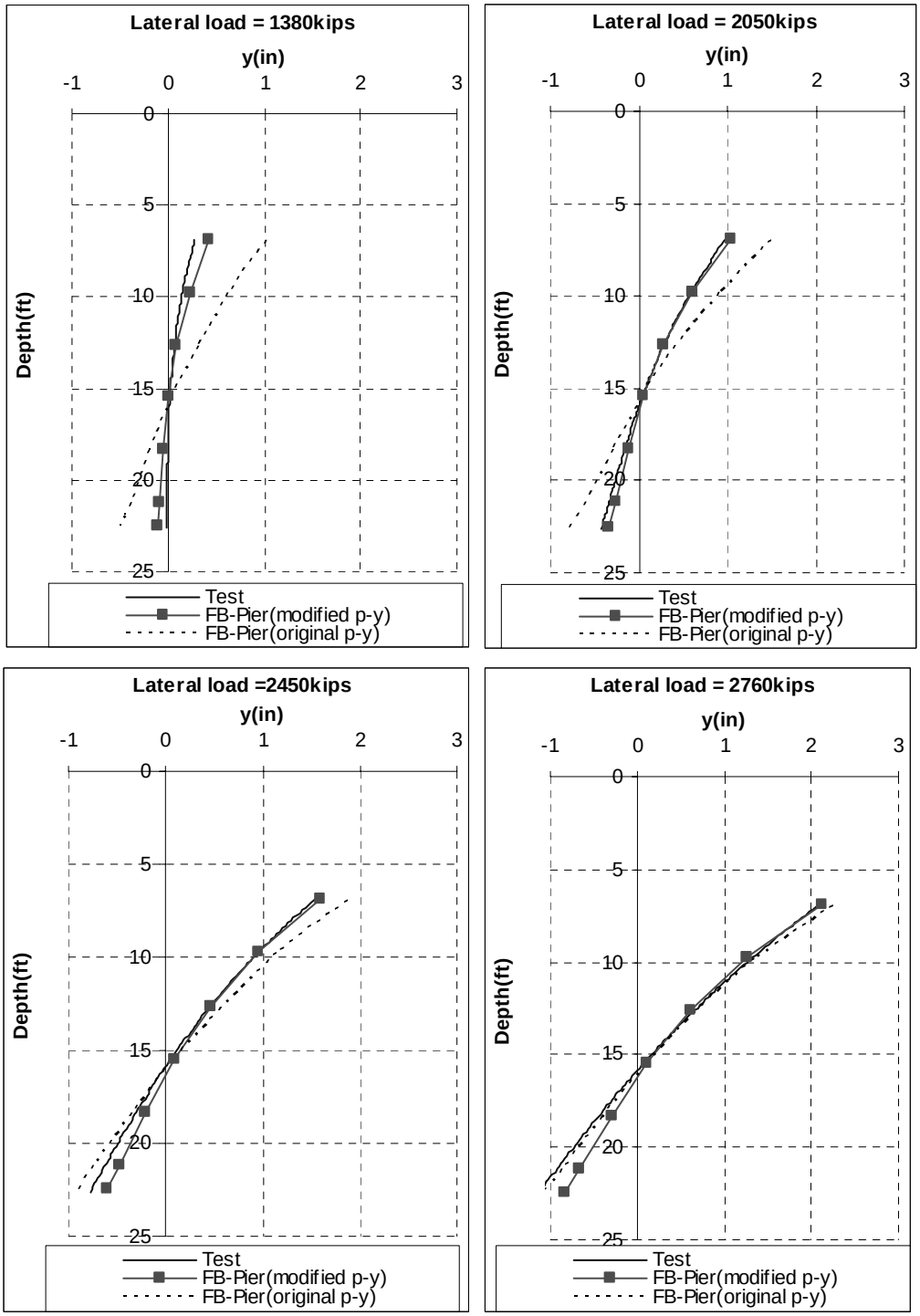

**Lateral Displacements (Corrected for Side Shear)**